Universidade do Estado do Rio de Janeiro

Centro de Tecnologia e Ciências

Faculdade de Geologia

Marco Aurélio Maia Teodoro

Petrogênese do complexo alcalino Tanguá (RJ): novo mapa litofaciológico e estudos geocronológicos e isotópicos

Rio de Janeiro

2024

Marco Aurélio Maia Teodoro

Petrogênese do complexo alcalino Tanguá (RJ): novo mapa litofaciológico e estudos geocronológicos e isotópicos

Tese apresentada, como requisito parcial para obtenção do título de Doutor, ao Programa de Pós-Graduação em Geociências, da Universidade do Estado do Rio de Janeiro. Área de concentração: Geociências.

Orientador: Prof. Dr. Anderson Costa dos Santos

Coorientador: Prof. Dr. Luiz Carlos Bertolino

Rio de Janeiro

2024

CATALOGAÇÃO NA FONTE
UERJ/REDE SIRIUS/CTCC

T314 Teodoro, Marco Aurélio Maia.
Petrogênese do complexo alcalino Tanguá (RJ): novo mapa litofaciológico e estudos geocronológicos e isotópicos / Marco Aurélio Maia Teodoro.– 2024.
177 f. : il.

Orientador: Anderson Costa dos Santos.
Coorientador: Luiz Carlos Bertolino.
Tese (Doutorado) – Universidade do Estado do Rio de Janeiro, Faculdade de Geologia**.**

1. Geologia - Teses. 2. Petrogênese - Tanguá (RJ) – Teses. 3. Rochas ígneas alcalinas – Teses. I. Santos, Anderson Costa dos. II. Bertolino, Luiz Carlos. III. Universidade do Estado do Rio de Janeiro. Faculdade de Geologia. IV. Título.

CDU: 552.11(815.3)

Bibliotecária Responsável: Priscila Freitas Araujo/ CRB-7: 7322

_____ _____

Assinatura Data

Marco Aurélio Maia Teodoro

Petrogênese do complexo alcalino Tanguá (RJ): novo mapa litofaciológico e estudos geocronológicos e isotópicos

Tese apresentada, como requisito parcial para obtenção do título de Doutor, ao Programa de Pós-Graduação em Geociências, da Universidade do Estado do Rio de Janeiro. Área de concentração: Geociências.

Aprovada em 16 de dezembro de 2024.

Orientador: Prof. Dr. Anderson Costa dos Santos

Faculdade de Geologia - UERJ

Coorientador: Prof. Dr. Luiz Carlos Bertolino

Centro de Tecnologia Mineral (CETEM)

Banca Examinadora: _____

Prof. Dr. Mauro Geraldes

Faculdade de Geologia - UERJ

_____

Prof. Dr. Werlem Holanda

Faculdade de Geologia – UERJ

_____

Prof. Dr. Tiago Amâncio Novo

Faculdade de Geologia – IGC/Universidade Federal de Minas Gerais

_____

Prof. Dr. Pedro Augusto da Silva Rosa

Faculdade de Geologia – IGC/Universidade Federal de Minas Gerais

_____

Prof. Dr. Júlio César Lopes da Silva

Instituto de Geociências – UFRRJ

Rio de Janeiro

2024

DEDICATÓRIA

Dedico esta tese aos meus pais, Maria Helena e Sebastião, que sempre me incentivaram a seguir pelo caminho dos estudos.

AGRADECIMENTOS

A caminhada do doutorado até este momento me fez vivenciar diferentes experiências e sensações, permitindo-me melhorar cada dia mais, pessoal e profissionalmente (geologicamente!). No entanto, nada disso seria possível sem o apoio de algumas pessoas que desempenharam um papel crucial durante toda essa jornada. O início desta caminhada não foi nada fácil, a felicidade da aprovação em paralelo a uma pandemia sem precedentes impediu parte das trocas e das interações presenciais (e importantes) com colegas e professores da pós. No entanto, a generosidade das pessoas se mostrou - mais uma vez - muito essencial, e mesmo com a distância BH-RJ, relações puderam ser criadas. Dessa forma, gostaria de agradecer a todos que fizeram parte desta história, direta ou indiretamente, e que deixaram sua marca neste momento.

Ao meu orientador e amigo, Prof. Dr. Anderson Costa dos Santos, por todas as discussões e ensinamentos, sempre muito técnicos, pelos incentivos e "puxões de orelha" que me permitiram seguir e buscar os conhecimentos necessários para esta conquista.

Ao meu coorientador, Prof. Dr. Luiz Carlos Bertolino, por todas as sugestões, conversas e apoio de extrema importância durante todo o meu doutorado.

Ao Prof. Dr. Hermínio, pelo apoio, conversas e orientações, especialmente no final desta jornada;

À UERJ e seus professores que foram resilientes durante a pandemia e sempre apoiaram os estudantes de pós-graduação nos momentos mais difíceis.

Aos laboratórios da universidade LGPA, LAGIR e Multilab, e todos os seus colaboradores, pela preparação das amostras e realização das análises essenciais para a concretização do meu trabalho

À FAPERJ por todo apoio financeiro e logístico durante todo o meu trabalho.

Ao Instituto SENAI de Inovação em Processamento Mineral, em Belo Horizonte/MG, pela liberação do uso da infraestrutura de preparação de amostras e análise mineralógica, essenciais para viabilizar as etapas iniciais do trabalho. Aproveito para agradecer o apoio direto dos amigos Christopher Rezende, Edileny Paula, Rayanne Bicalho, Luís Silva, Angélica Martins e André Faria durante esta etapa.

Aos meus amigos dos "Excluídos" e que a geologia me permitiu conhecer, aqui representados por Juninho, Barbariza, Carol Bueno, Vivi, Will, Mari e Victor Fraga, pelas

conversas que me permitiam relaxar, pela companhia em momentos difíceis e por todo o apoio durante esta jornada.

Aos geólogos Camilo José e Marcos Vinícius (Bombeiro) por todo o incentivo para seguir em busca deste objetivo.

Aos amigos que a UERJ, mesmo à distância, me permitiu encontrar, em especial Dan Mothé, Caio Souza, Marcos Barros e Mariana Bessa. A ajuda de vocês foi essencial.

Aos geólogos Prof. Dr. Werlem Holanda e João Pedro Alves que foram meus companheiros de campo e colegas de interpretação de dados.

Aos meus pais, Maria Helena e Sebastião, e aos meus irmãos Michelle e Marcelo que sempre foram a minha base e meus maiores incentivadores e inspirações. Aos meus sogros, Edna e Tiãozinho (*in memoriam*), aos meus cunhados, Shandilla, André e Ana Paula, por todo incentivo a continuar nessa caminhada. Aos meus sobrinhos Isaac e Gabi por trazer leveza a alguns momentos.

À Lady por (literalmente!) sempre estar ao meu lado durante os estudos em casa.

Ao meu marido, Alex Freitas, por tudo que passamos juntos durante toda esta etapa. Fazer o doutorado ao mesmo tempo que você foi um desafio e um incentivo para ambos. Muito obrigado pela paciência, pelas palavras de apoio e por estar sempre ao meu lado.

Por fim, agradeço a todos que fizeram parte desta etapa, ainda que não mencionados, mas que de alguma forma contribuíram para este trabalho e me ajudaram nesta jornada.

A ignorância afirma ou nega veementemente; a ciência duvida.

Voltaire

Educação não transforma o mundo, educação muda as pessoas.

Pessoas transformam o mundo.

Paulo Freire

RESUMO

TEODORO, Marco Aurélio Maia. **Petrogênese do complexo alcalino Tanguá (RJ)**: novo mapa litofaciológico e estudos geocronológicos e isotópicos. 2024. 177 f. Tese (Doutorado em Geociências) – Faculdade de Geologia, Universidade do Estado do Rio de Janeiro, Rio de Janeiro, 2024.

O Complexo Alcalino de Tanguá está localizado no estado do Rio de Janeiro, e encontra-se no contexto do Alinhamento Poços de Caldas – Cabo Frio (APCCF), intrudindo rochas da Faixa Ribeira. O novo mapa litofaciológico proposto para o Complexo sugere que a porção interna é formada por nefelina sienitos, divididos em central, com maior teor de analcima, e intermediário, com maior conteúdo de albita. A porção mais externa é constituída por sienitos indivisíveis, sem nefelina, e brechas magmáticas nas bordas sul e leste. Adicionalmente, fonolito e traquito ocorrem como diques que cortam as outras rochas. As rochas do maciço são classificadas como metaluminosas, e em menor proporção, como peraluminosas. De acordo com o diagrama TAS as rochas são classificadas como sienitos e fonolitos, em sua maioria, e pelo diagrama R1-R2 como fonolito, traqui-fonolito, traquito e quartzo-traquito. Os dados isotópicos de Sr-Nd mostram que os sienitos plotam entre Depleted Mantle Source (DMM) e Enriched Mantle 1 (EM1) e o fonolito entre DMM e Enriched Mantle 2 (EM2). Estes *trends* são típicos do Alinhamento e podem indicar uma mistura de fontes para estas rochas. Os parâmetros ε_{Nd} negativos (entre - 3.17 e - 2.31) e ε_{Hf}, que variam entre valores positivos e negativos (de – 17.78 e + 11.49), reforçam a participação destas fontes. A variação observada para as idades modelo Nd_{TDM} (670 - 860 Ma) é semelhante a outros complexos do APCCF e tem idade próxima aos eventos colisionais do Brasiliano. Adicionalmente, as idades modelo Hf_{TDM} apresentam uma variação maior (280 - 1570 Ma), sugerindo uma possível associação com eventos geológicos anteriores à formação da Faixa Ribeira. Os resultados de ε_{Nd} e ε_{Hf}, juntamente aos dados geoquímicos (Zr/TiO_2 *versus* SSI, e SiO_2 e ETR *versus* ε_{Nd}), sugerem um importante processo de contaminação crustal durante a formação do maciço. Este processo é evidenciado pela disposição das rochas no Complexo: nefelina sienitos no centro, associados à composição original do magma, e sienitos nas bordas, gerados pela contaminação deste pelas rochas da crosta. Além disso, o comportamento distinto dos parâmetros isotópicos (Nd e Hf) indica a presença de magmas metassomatizados e sedimentos associados a *slabs* oceânicos subduzidos durante a formação do maciço, o que é reforçado por diferentes parâmetros geoquímicos, como Th/Yb *versus* Ba/La e U/Th *versus* Th. Os estudos geocronológicos por U-Pb sugerem dois pulsos principais durante a formação do complexo, um Cenomaniano (*ca.* 95 Ma) e um Daniano-Maastrichtiano (*ca.* 60-70 Ma). Este último é sustentado por um volume maior de dados, em consonância com os estudos prévios, indicando um período principal de *emplacement*. Além disso, a idade de 94,8 Ma mostra que o modelo de pluma convencional pode não ser o mais indicado para a gênese do APCCF, por se tratar de um maciço mais velho mais a leste. De forma complementar, os diques e maciços, seguindo *trends* regionais, corroboram a importância das estruturas pré-existentes no processo de formação do Alinhamento.

Palavras-chave: alinhamento Poços de Caldas – Cabo Frio; complexo alcalino Tanguá; geocronologia por U-pb; estudo isotópico por lu-hf; Sm-Nd.

ABSTRACT

TEODORO, Marco Aurélio Maia. **Petrogenesis of the Tanguá alkaline complex (RJ)**: new lithofaciological map and geochronological and isotopic studies. 2024. 177 f. Doctoral (Thesis in Geosciences) – Faculty of Geology, State University of Rio de Janeiro, Rio de Janeiro, 2024.

The Tanguá Alkaline Complex is in the Rio de Janeiro state and is of the Poços de Caldas – Cabo Frio Alignment (PCCFA) context, intruding rocks from the Ribeira Belt. The newly proposed lithofacies map for the Complex suggests that the inner portion is predominantly composed of nepheline syenites, which are further divided into central (with higher analcime content) and intermediate (with higher albite content) types. The outermost portion comprises indivisible syenites, without nepheline, and magmatic breccias on the southern and eastern edges. Additionally, phonolite and trachyte occur as dikes cutting through the other rock types. The rocks of the massif are classified as metaluminous and, to a lesser extent, as peraluminous. According to the TAS diagram, the rocks are mainly classified as syenites and phonolites, and according to the R1-R2 diagram, as phonolite, trachy-phonolite, trachyte, and quartz-trachyte. indicate that the syenites plot between a Depleted Mantle Source (DMM) and Enriched Mantle 1 (EM1), while the phonolite plots between DMM and Enriched Mantle 2 (EM2). These trends are typical of the Alignment and may suggest a mixing of sources for these rocks. The negative ε_{Nd} parameters (between - 3.17 and - 2.31) and ε_{Hf}, which vary between positive and negative (from – 17.78 to + 11.49), further support the participation of these sources.. The variation observed for the Nd_{TDM} model ages (670 - 860 Ma) is similar to other PCCFA complexes and is close to the Brasiliano collisional events. On the other hand, the Hf_{TDM} model ages present a more significant variation (280 - 1570 Ma), which may suggest an association with geological events before the formation of the Ribeira Belt. The ε_{Nd} and ε_{Hf} results, combined with geochemical data (Zr/TiO_2 versus SSI, and SiO_2 and ETR versus ε_{Nd}), indicate significant crustal contamination during the massif's formation. This process is evidenced by the spatial distribution of the rocks within the Complex: nepheline syenites at the center, associated with the magma's original composition, and syenites at the margins, formed due to contamination by crustal rocks. Furthermore, the distinct behavior of isotopic parameters (Nd and Hf) indicates the presence of metasomatized magmas and sediments associated with oceanic slabs subducted during the massif formation, which is reinforced by different geochemical parameters, such as Th/Yb versus Ba/La and U/Th versus Th. Geochronological studies by U-Pb suggest two main pulses during the formation of the complex, a Cenomanian (*ca*. 95 Ma) and a Danian-Maastrichtian (*ca.* 60-70 Ma). The latter is supported by a larger dataset, consistent with previous studies, and indicates the primary emplacement period. The intrusion of phonolites occurred syn-genetically with the syenites of the most recent period, a relationship confirmed by field observations. Furthermore, the age of 94.8 Ma shows that the conventional plume model may not be the most suitable for the genesis of the PCCFA, as it is an older massif further east. Furthermore, the dikes and massifs following regional trends underscore the significance of pre-existing structures in the alignment's formation process.

Keywords: Poços de Caldas – Cabo Frio alignment; Tanguá alkaline complex; U-Pb geochronology; Lu-Hf; Sm-Nd isotopic.

LISTA DE FIGURAS

LISTA DE FIGURES

LISTA DE TABELAS

LISTA DE TABLES

SUMÁRIO

INTRODUÇÃO

A importância de estudar as características e a gênese das rochas alcalinas é evidente, ainda que representem menos de 1% das rochas magmáticas (LAZNICKA, 2006), contribuindo significativamente para o conhecimento geológico e a evolução do planeta. A química destes complexos alcalinos, e consequentemente sua mineralogia, os tipos de rochas encontrados, e o potencial estão diretamente ligados a diferentes fatores durante a geração dos magmas. Entre esses fatores, destacam-se: pequenas variações no grau de fusão parcial de uma fonte comum; a assimilação crustal em diferentes níveis e/ou condições físico-químicas variáveis de cristalização de fusões parentais semelhantes; e o metassomatismo de uma fonte mantélica heterogênea (AZZONE et al., 2018).

O Brasil, bem como a Plataforma Sul-Americana, apresenta diversas ocorrências deste tipo de rocha, as quais foram divididas em províncias magmáticas distintas por diferentes autores, como RICCOMINI et al. (2005). A região sudeste do Brasil, próximo à Bacia do Paraná – em especial os estados de Minas Gerais, São Paulo e Rio de Janeiro – possui cerca de 30 corpos intrusivos na forma de plútons e stocks, além de diques, e que têm idades entre aproximadamente 132 Ma e 58 Ma, com intervalo mais importante entre 91 Ma e 78 Ma (ALMEIDA, 1986; RICCOMINI et al., 2005; MOTA, 2012; GUARINO et al., 2019 e referências). Nesse contexto, encontra-se a Província Alcalina da Serra do Mar (PASM), que alguns autores classificam parte como Alinhamento Poços de Caldas – Cabo Frio (APCCF), ou ainda Lineamento Magmático Cabo Frio (ULBRICH AND GOMES, 1981; ALMEIDA, 1983; RICCOMINI et al., 2005).

O Maciço Alcalino de Tanguá está localizado no estado do Rio de Janeiro e se insere no contexto do APCCF (RICCOMINI et al., 2005), próximo aos maciços de Rio de Bonito e Soarinho. O Complexo ígneo é formado por sienitos e brechas vulcânicas, além de traquito e fonolito, que ocorrem como diques intrusivos cortando outras rochas (MOTOKI et al., 2010), com gênese associada ao magmatismo alcalino do Cretáceo-Paleógeno (RICCOMINI et al., 2005).

O aprofundamento dos estudos petrogenéticos destas rochas é essencial para o entendimento de sua formação. Nesse sentido, o presente trabalho apresenta dados incrementais e inéditos no que tange os aspectos geoquímicos, mineralógicos, geocronológicos e isotópicos, contribuindo diretamente para a evolução deste conhecimento. A relevância deste trabalho está no entendimento da evolução litosférica e dos processos

petrogenéticos associados ao Alinhamento Poços de Caldas-Cabo Frio, em especial do Complexo Alcalino Tanguá. Cabe destacar ainda, que este trabalho faz parte dos projetos Emergentes 2019 - Potencial econômico dos maciços alcalinos do Rio de Janeiro, APQ1 2019 e Entidades Estaduais 2018, todos de Edital FAPERJ, e conta com a parceria de diferentes laboratórios da Universidade do Estado do Rio de Janeiro e centros de pesquisa.

Localização e vias de acesso

O município de Tanguá está localizado na porção leste da Região Metropolitana do Rio de Janeiro e faz divisa com cidades como Rio Bonito, Itaboraí e Maricá. O acesso ao município onde está localizada a área de estudo ocorre pela rodovia BR-101, em um trajeto de aproximadamente 70 km a partir da cidade do Rio de Janeiro. Já o acesso ao Maciço de Tanguá é realizado pela rodovia BR-101, na porção sul, e pela rodovia RJ-116, na porção norte (Figura 1).

Figura 1 – Mapa de localização da área de estudo e a principal via de acesso em relação à cidade do Rio de Janeiro.

Legenda: Linhas amarelas – rodovias principais da região; Linha vermelha tracejada – acesso para chegar ao Complexo Tanguá; Linha branca tracejada – área de estudo do Complexo Tanguá. Fonte: Google Earth Pro.

Estrutura da Tese

A presente tese de doutorado, intitulada "Petrogênese do Complexo Alcalino Tanguá (RJ): novo mapa litofaciológico e estudos geocronológicos e isotópicos", encontra-se dividida em capítulos, que são:

a) Introdução – capítulo ao qual este item está vinculado, traz o contexto básico do trabalho e a localização da área de estudo;

b) Capítulo 1 – apresenta os objetivos desta tese de doutorado;

c) Capítulo 2 – indica os materiais estudados no presente trabalho, os métodos utilizados para preparação e análise, e suas respectivas condições analíticas;

d) Capítulo 3 – apresenta o contexto geológico da área, com indicações sobre a gênese de rochas magmáticas em geral e de rochas alcalinas, além de informações metalogenéticas deste grupo de rochas e sua importância econômica no contexto nacional. Além disso, o item 3.4 traz o artigo intitulado "*Poços de Caldas – Cabo Frio Alignment: A petrochronological review of a non-conventional Plume Model*". Este artigo apresenta uma revisão de dados previamente publicados sobre o contexto do Alinhamento, além de dados geocronológicos inéditos para os maciços Tinguá, Itatiaia e Morro dos Gatos.;

e) Capítulo 4 – apresenta os resultados obtidos durante o estudo de maneira detalhada e as discussões/conclusões levantadas a partir das informações coletadas. Para tal, é apresentado um segundo artigo, intitulado "*Isotopic decoupling in the Nd-Hf systems from Cenomanian-Maastrichtian Tanguá Massif syenites: inheritage from sedimentary input into a metasomatized mantle*", que foi submetido à revista Anuário do Instituto de Geociências, atualmente em revisão. Neste artigo são apresentados dados petrográficos obtidos a partir de informações de campo e microscopia óptica, resultados mineralógicos baseados em difratometria de raios X, e dados litogeoquímicos para os litotipos identificados com base nas análises anteriores. Adicionalmente, dados geocronológicos por U-Pb em zircão e de geoquímica isotópica por Lu-Hf e Sm-Nd também são expostos, alguns inéditos para o maciço. Posteriormente, com base na correlação destes resultados, e também em trabalhos anteriores, são feitas interpretações a respeito da gênese das rochas estudadas;

f) Capítulo 5 – apresenta as considerações finais, baseando-se nos capítulos anteriores e nas informações apresentadas.

1. OBJETIVOS

1.1 Gerais

Os objetivos gerais deste trabalho são o mapeamento geológico de detalhe e o estudo da intrusão alcalina de Tanguá para a determinação dos litotipos aflorantes e para o entendimento da gênese associada ao complexo.

1.2 Específicos

Os objetivos específicos do presente trabalho são:

a) Realizar mapeamento faciológico no Complexo Tanguá a fim de determinar a relação entre os litotipos, utilizando como base as informações de campo e os diferentes estudos analíticos realizados;

b) Efetuar estudos mineralógicos, petrográficos e litogeoquímicos nos litotipos aflorantes;

c) Executar estudos geocronológicos e de geoquímica isotópica, associando-os aos demais resultados, para obtenção de parâmetros petrogenéticos e refinamento dos estudos já realizados;

d) Definir características do Complexo Tanguá que permitam compreender a gênese da intrusão, sugerindo possíveis fontes e evidências dos processos de formação;

e) Correlacionar os resultados obtidos durante o trabalho aos de outros maciços alcalinos do Alinhamento Poços de Caldas-Cabo Frio presentes na literatura e, dessa forma, contribuir diretamente para o entendimento da formação desta província.

2. MATERIAIS E MÉTODOS

Durante a execução do trabalho de doutorado, foram utilizados os seguintes métodos:

- Levantamento bibliográfico;
- Trabalhos de campo para mapeamento geológico e coleta de amostras;
- Preparação de amostras
- Estudos mineralógicos e petrográficos:
    - Difratometria de Raios X;
    - Microscopia Óptica;
- Estudos litogeoquímicos:
    - Óxidos Maiores;
    - Elementos traços e terras raras (ETR);
    - Metais-base;
- Estudos geocronológicos:
    - U-Pb e Lu/Hf em zircão;
    - $^{40}Ar/^{39}Ar$ em diferentes minerais (para outros maciços);
- Estudos de geoquímica isotópica:
    - Sm/Nd e Rb/Sr (rocha total).

2.1 Campanha de campo

Para mapeamento e coleta de amostras, as campanhas de campo ocorreram em 2 datas distintas. A primeira dessas ocorreu em novembro de 2020, durante o qual foram levantados 42 pontos e coletadas 30 amostras representativas das fácies mapeadas. O segundo campo foi realizado em outubro de 2021. Neste campo foram estudados 48 pontos e coletadas cerca de 30 amostras. Dessa forma, o trabalho de campo conseguiu cobrir a maior área com acesso possível e levantou um total de 90 pontos.

2.2 **Preparação de amostras**

As amostras foram encaminhadas para o Laboratório Geológico de Processamento de Amostras (LGPA) da UERJ para diferentes tipos de preparação, a depender das análises. Paralelamente, parte das amostras foram preparadas no Laboratório de preparação de amostras do Instituto SENAI de Inovação em Processamento Mineral (ISIPM) do Centro de Inovação e Tecnologia (CIT) SENAI, em Belo Horizonte. O detalhamento de cada preparação, bem como a indicação dos laboratórios são apresentados nos itens subsequentes. Cabe ressaltar que a seleção das amostras para as diferentes análises foi baseada na localização no Complexo, a fim de cobrir a maior área possível, na representatividade do litotipo descrito em campo, nas características específicas e no grau de alteração da rocha.

2.2.1 Confecção de lâminas delgadas

Para a preparação das lâminas delgadas as rochas foram cortadas nas posições demarcadas, de forma a obter uma fatia plana (*slab*) com aproximadamente 47 x 25 x 30 mm. Após um aquecimento e impregnação com resina e acetona, o *slab* foi submetido a polimento com abrasivos diferentes granulometrias, sempre em ordem decrescente de tamanho. Após novo aquecimento, a rocha foi colada em uma lâmina de vidro previamente fosqueada para melhorar a aderência e identificada com o código da amostra, para posterior corte longitudinal a fim de se retirar o excesso. Em seguida, a rocha foi desbastada com abrasivos de diferentes granulometrias, também em ordem decrescente de tamanho, até que se tivesse uma espessura do material de 30 micra. A verificação da espessura da lâmina é feita por meio da conferência da cor de polarização cinza de quartzo e/ou feldspato (no caso do presente trabalho, somente feldspato).

Para esta etapa foram selecionadas amostras de diferentes litotipos de forma a abranger o máximo de características verificadas em campo. Esta preparação foi realizada no LGPA da UERJ e as lâminas confeccionadas tiveram sua espessura adequada, quando necessário, e foram polidas no Laboratório de Laminação do ISIPM para análise por microscopia óptica. Cabe ressaltar que todas as lâminas utilizadas foram confeccionadas com

rochas amostradas no primeiro campo devido aos prazos do laboratório por conta dos atrasos causados pela pandemia.

2.2.2 Corte e pulverização de amostras

As amostras coletadas em ambos os campos e selecionadas para estudos posteriores foram submetidas a preparações específicas a depender do tamanho, características e análise a ser executadas. Dessa forma, as amostras selecionadas foram cortadas com o uso de serra/cortadora de rochas e/ou fragmentada com o uso de martelo e bigorna até o tamanho ideal para posterior adequação granulométrica. Com o auxílio de um britador de mandíbulas foi realizada a redução da granulometria para o intervalo de 7 a 1 mm. Este material, por sua vez, foi moído em moinho de disco ou de bolas de tungstênio até atingir tamanho de grãos entre 1 mm e silte/argila, para posteriormente ser homogeneizado e quarteado, seguindo o método de rejeição dos quartos opostos do cone. Cada alíquota obtida tinha em torno de 60 gramas.

A pulverização, última etapa deste processo, foi feita em moinho de bolas utilizando cadinho e bolas de carbureto de tungstênio/inox em procedimento que dura em torno de 10 minutos. O produto gerado tem em torno de 0,25 e 0,062 mm e foi utilizado para realização das análises de litogeoquímica, isótopos e difratometria de raios X. Ressalta-se que entre os processos, os britadores e moinhos foram devidamente descontaminados com uso de material amorfo. Esta preparação foi realizada pelo LGPA/UERJ, para as análises geoquímicas e isotópicas, e pelo laboratório de preparação de amostras do ISIPM/CIT SENAI (BH), para as análises de difratometria, seguindo procedimentos internos em ambos os casos.

2.3 **Litogeoquímica**

As amostras previamente preparadas pelo LGPA foram submetidas a análise de litogeoquímica de detalhe para determinação dos teores de elementos maiores e traços, incluindo ETR, no Laboratório da ALS, no Canadá. Para o trabalho foram selecionados dois pacotes que utilizam basicamente ICP-AES (*Inductively Coupled Plasma - Atomic Emission Spectrometry* ou, em português Espectrometria de Emissão Atômica por Plasma Acoplado Indutivamente). O detalhamento dos pacotes é apresentado na Tabela 1 abaixo. A preparação das amostras enviadas para cada análise segue o padrão interno do laboratório.

As amostras estudadas pelo presente trabalho foram divididas em dois lotes, relacionados às etapas de campo. Dessa forma, para o primeiro lote foram enviadas 17 amostras de diferentes litotipos associadas principalmente à porção leste e noroeste do maciço. Para estas foram realizadas todas as análises apresentadas na Tabela 1. Após a realização do segundo campo e seleção das amostras, um novo lote com 9 amostras foi enviado para o mesmo laboratório, porém, desta vez, a seleção focou em amostras que estavam associadas à porção oeste e sul do Maciço. Devido ao alto custo das análises de metais base, os estudos litogeoquímicos deste segundo lote foram focados apenas os óxidos majoritários e os elementos traços, mantendo os métodos do primeiro lote.

Tabela 1 – Relação de elementos a serem estudados por ICP-AES e suas respectivas faixas de concentração

Óxidos Majoritários – Analitos e faixas de concentração (%)							
Analito	Concentração	Analito	Concentração	Analito	Concentração	Analito	Concentração
SiO_2	0,01 – 100	MgO	0,01 – 100	TiO_2	0,01 – 100	BaO	0,01 – 100
Al_2O_3	0,01 – 100	Na_2O	0,01 – 100	MnO	0,01 – 100	*LOI*	0,01 – 100
Fe_2O_3	0,01 – 100	K_2O	0,01 – 100	P_2O_5	0,01 – 100		
CaO	0,01 – 100	Cr_2O_3	0,002 – 100	SrO	0,01 – 100		

Elementos traços (incluindo ETRs) – Analitos e faixas de concentração (ppm)							
Analito	Concentração	Analito	Concentração	Analito	Concentração	Analito	Concentração
Ba	0,5 – 10.000	Gd	0,05 – 1.000	Rb	0,2 – 10.000	U	0,05 – 1.000
Ce	0,1 – 10.000	Hf	0,2 – 10.000	Sm	0,03 – 1.000	V	5 – 10.000
Cr	10 – 10.000	Ho	0,01 – 1.000	Sn	1 – 10.000	W	1 – 10.000
Cs	0,01 – 10.000	La	0,1 – 10.000	Sr	0,1 – 10.000	Y	0,1 – 10.000
Dy	0,05 – 1.000	Lu	0,01 – 1.000	Ta	0,1–2.500	Yb	0,03 – 1.000
Er	0,03 – 1.000	Nb	0,2 – 2.500	Tb	0,01 – 1.000	Zr	2 – 10,000
Eu	0,03 – 1.000	Nd	0,1 – 10.000	Th	0,05 – 1.000		
Ga	0,1 – 1.000	Pr	0,03 – 1.000	Tm	0,01 – 1.000		

Continuação Tabela 1

Metais Base – Analitos e faixas de concentração (ppm)							
Analito	Concentração	Analito	Concentração	Analito	Concentração	Analito	Concentração
Ag	0,5 – 100	Co	1 – 10.000	Mo	1 – 10.000	Sc	1 – 10.000
As	5 – 10.000	Cu	1 – 10.000	Ni	1 – 10.000	Tl	10 – 10,000.
Cd	0,5 – 1.000	Li	10 – 10.000	Pb	2 – 10.000	Zn	2 – 10.000

2.4 **Microscopia Óptica**

As análises foram realizadas em 11 lâminas delgadas e tiveram como foco a determinação de características em escala microscópica como identificação das fases minerais presentes, feições texturais como granulação, contatos entre grãos e microestruturas, permitindo ainda sugerir a correlação entre as amostras estudadas. A partir destes resultados, bem como os obtidos por DRX, foi possível propor a divisão das amostras em grupos de diferentes litologias que serviram como base para os estudos e as interpretações subsequentes.

As lâminas delgadas foram analisadas em microscópio trinocular Leica, modelo DM-LP, que contempla objetivas com aumento de 2.5x, 5x, 10x, 20x e 50x, e conta com sistema de iluminação transmitida e refletida, permitindo assim a identificação de minerais opacos em caso de lâminas delgadas polidas. As fotomicrografias foram obtidas com uma câmera digital acoplada à terceira objetiva do microscópio da marca Motic, modelo Moticam 10.0, juntamente ao *software* disponibilizado pela empresa *Motic Images 3.0 Plus*. Esta análise foi realizada no Laboratório de Microscopia do ISIPM/CIT SENAI (BH). Conforme mencionado no item 2.2.1, estas lâminas precisaram ser desbastadas e polidas nos laboratórios do ISIPM, em Belo Horizonte, a fim de se garantir a adequação destas para o estudo.

2.5 **Difratometria de raios X**

A técnica de difratometria de raios X obtém informações sobre as fases cristalinas presentes. A técnica faz uso da interação dos raios X emitidos por uma fonte de radiação com comprimento de onda conhecido. Após a emissão e a interação, os raios X são submetidos ao fenômeno da difração após atingir os elétrons da rede cristalina do material que está sendo

analisado. Tal fenômeno obedece a Lei de Bragg e o ângulo de incidência do feixe é igual ao do feixe difratado. Por meio das distâncias interplanares dos retículos cristalinos, é possível fazer a identificação das fases minerais presentes nas amostras.

Neste sentido, as análises por difratometria de raios X foram realizadas com o intuito de identificar as fases minerais presentes, e semiquantificá-las, haja vista que fases amorfas e em baixa quantidade não são identificadas. Além disso, os resultados foram utilizados para determinar características que permitissem divisão das rochas em grupos. Estas características, em conjunto com as análises petrográficas por microscopia óptica, possibilitaram a identificação e a classificação prévia das rochas. Tendo em vista a disponibilização facilitada do uso do equipamento, foram analisadas e semiquantificadas 39 amostras de diferentes litologias.

Os fragmentos das amostras selecionadas foram previamente preparados tal qual o item 2.2.2 ou em caso de pedaços menores (aproximadamente 3 cm), estes foram preparados diretamente em panela de pulverização de aço até atingir granulometria < 270#. Para a análise utilizou-se a técnica do pó em equipamento Shimadzu/LabX6000, do Laboratório de Raios X do ISIPM/CIT SENAI (BH), o qual apresenta tubo de raios X com radiação CuKα (λ = 1,5418Å) e sistema θ-2θ. As condições analíticas foram:

- Voltagem de leitura: 40,0 kv;
- Corrente de leitura: 30,0 mA;
- Faixa de análise: 5º a 80º (2θ);
- Passo: 0,01º (2θ);
- Velocidade: 0,5 graus/minuto
- Tempo de Leitura: 1,2 segundos

Para garantir uma maior confiabilidade estatística das análises, as leituras foram realizadas em porta amostra rotacional (*Spinner*) a uma frequência de 40 rpm. No intuito de minimizar os efeitos de orientação preferencial das diferentes fases minerais utilizou-se porta-amostra com carga contrária (*back loader holder*), desenvolvido pelo próprio laboratório, o qual possibilita que a amostra seja preparada e nivelada com o porta-amostra sem seja feita a fricção direta das partículas, o que gera essa orientação. A interpretação inicial dos dados obtidos teve como foco verificar a correlação entre os difratogramas de forma a obter grupos (*clusters*) com padrões semelhantes. Posteriormente, via *software Match*!, foi realizada a identificação e semiquantificação das fases utilizando o método de Rietveld. Esta análise foi

realizada no Laboratório de raios X do ISIPM/CIT SENAI (BH) e o *software* foi disponibilizado pelo mesmo instituto. Os difratogramas encontram-se no Apêndice D.

2.6 **Análise Isotópica de Sr e Nd**

As análises foram realizadas em seis amostras de sienito (5) e fonolito (1) previamente pulverizada pelo LGPA. Uma alíquota pulverizada de cada amostra com massa entre 25 e 50 mg foi submetida a processos de digestão ácida (HCl e HF) performados em sala limpa sob pressão de ar positiva e sistema de filtragem de ar pelo Laboratório de Geocronologia e Isótopos Radiogênicos (LAGIR), da Universidade do Estado do Rio de Janeiro (UERJ). Posteriormente, no mesmo laboratório, estas amostras foram analisadas em um espectrômetro de massa por ionização térmica (em inglês, *thermal ionization mass spectrometry* – TIMS) multicoletor modelo TRITON.

O método de separação de Sr, REE, Sm e Nd (HEILBRON et al., 2013) é realizado em coluna de troca catiônica em diferentes etapas. Os procedimentos para realização das medidas com o equipamento são descritos de maneira detalhada por VALERIANO et al. (2003). Para o Sm e Nd o processo de ionização utilizou filamento de Re, em suporte com arranjo duplo e medidos de 8 e 16 ciclos, respectivamente. Já para o Sr, o filamento usado foi de Ta, em suporte simples, e 10 ciclos para medição.

Os materiais padrões de referência utilizados foram os SRM-987 and JNdi-1 (TANAKA et al., 2000; NETO et al., 2023). As razões isotópicas foram normalizadas em $^{146}Nd/^{144}Nd = 0.7219$, $^{147}Sm/^{152}Sm = 0.5608$ e $^{88}Sr/^{86}Sr = 8.3752$. Para o tratamento dos dados e obtenção das razões iniciais e idades modelo do manto empobrecido (T_{DM}) foi utilizado o software GeoChemical Data ToolKIT (ou GCDkit).

2.7 **Análise de U-Pb e Lu-Hf em minerais datáveis**

A preparação inicial das amostras para análise geocronológica foi executada pelo LGPA da UERJ. As amostras inicialmente foram submetidas a processos de adequação granulométrica de forma a diminuir progressivamente o diâmetro das partículas. Dessa forma,

as rochas foram cominuídas em moinho de mandíbulas para obtenção de material com granulometria entre 2 e 3 cm. Posteriormente, estes fragmentos foram submetidos a um novo processo de britagem, usando britadores com mandíbulas de menor espaçamento, em que o material cominuído apresenta diâmetro de aproximadamente 1 cm. Este, por sua vez, foi submetido a processo com moinho de discos e o produto obtido levado à peneira de 100 mesh (150 µm), gerando um material retido e um passante.

Ambas as frações foram bateadas, separadamente, a fim de se adquirir concentrados de minerais pesados. Posteriormente, as amostras passaram por processo de separação magnética com uso de equipamento Frantz em diferentes intensidades, iniciando por campo mais fraco. Os produtos magnéticos foram progressivamente submetidos a intensidades mais fortes de forma a se obter diferentes tipos de concentrados e, consequentemente, tipos de minerais. Cabe destacar, que cada faixa de intensidade de campo tem a intenção de concentrar um tipo ou grupo de minerais, como titanita (1A) e zircão (2,3A). Por fim, quando necessário e com material suficiente em massa, o produto magnético é submetido a separação gravítica com uso de líquido denso (bromofórmio) com vistas a separar minerais de baixa densidade que tenham sido arrastados durante o processo de separação magnética.

Uma vez separados em diferentes concentrados magnéticos, os minerais foram catados com uso de pinça e lupa petrográfica Leica, modelo EZ4 do Laboratório de Microscopia do Instituto SENAI de Inovação em Processamento Mineral, locado no CIT SENAI. Os grãos selecionados foram colados em área selecionada de fita dupla face, previamente colada em base de molde de 25 mm. Após a seleção de todos os grãos, estes foram embutidos em resina epóxi de cura a frio em vaso de pressão a fim de se retirar as bolhas. Quando curadas as seções passaram por processo de desbaste e polimento com o uso de lixas d'águas (320 e 2000) e pastas de diamante (9 µm, 6 µm, 1 µm e ¼ µm), iniciando a mais grossa para a mais fina. Após a finalização do polimento, as seções foram analisadas em Microscópio Eletrônico de Varredura Hitachi, modelo FlexSEM 1000 II, com detector de EDS Bruker, modelo Quantax 80, e software de mineralogia automatizada AMICS, também da Bruker. A partir desta análise foi possível compreender a disposição dos diferentes minerais catados e elaborar esquemas com grãos numerados a fim de facilitar as análises geocronológicas.

Por fim, as seções foram levadas ao Laboratório Multi Usuário de Meio Ambiente e Materiais (MultiLAB) para execução das análises de interesse. Para estas, foi utilizado equipamento de ablação a laser com espectrometria de massa por plasma induzido (LA-ICP-MS em inglês) da marca Thermo Scientific e modelo Neptune plus. A partir deste equipamento foram realizadas, em cada amostra, um total de 20 *spots*/leituras, em que as 6

iniciais foram em padrão interno do laboratório com idade condizente e as demais 14 (ou 15 para o segundo lote de análises) em grãos de minerais catados, sendo realizado um tiro por grão. As condições de análise e leitura foram: *fire mode continuous*, com frequência de 6 Hz e diâmetro de ponto (*spot size*) de 40 µm. Para o tratamento inicial dos dados foi utilizado no laboratório o *software Glitter*. Para a obtenção dos diagramas de Concórdia e cálculo das idades foi utilizada a extensão do excel ISOPLOT (LUDWIG, 2003) e o site *https://www.ucl.ac.uk/* que disponibiliza a extensão ISOPLOT em linguagem R, de forma online e gratuita (VERMEESCH, 2018).

Cabe ressaltar ainda que foram apresentadas análises deste método no artigo "*Unraveling the Poços de Caldas – Cabo Frio Alignment: A petrochronological review*", que se encontram no mesmo contexto do Complexo Tanguá e são referentes aos maciços Itatiaia, Tinguá e Morro dos Gatos. Apesar da similaridade entre os procedimentos, o método de preparação e a análise destas amostras são descritos de forma detalhada no artigo em questão.

2.8 **Analíse por $^{40}Ar/^{39}Ar$**

As análises geocronológicas pelo método $^{40}Ar/^{39}Ar$ foram realizadas em amostras dos maciços Itatiaia e Tinguá, e foram utilizadas com o intuito de trazer maior robustez às informações apresentadas no artigo "*Poços de Caldas – Cabo Frio Alignment: A petrochronological review of a non-conventional Plume Model*". Desta forma, as informações sobre as amostras e a análise são apresentadas de forma detalhada no artigo.

3. CONTEXTO GEOLÓGICO

A partir deste item, serão apresentados os levantamentos bibliográficos relacionados ao trabalho, com foco na gênese de rochas magmáticas, mais especificamente as alcalinas, nos contextos geotectônicos e nas fontes mantélicas. Adicionalmente, no item 3.4, é apresentado o artigo de revisão, intitulado "*Poços de Caldas – Cabo Frio Alignment: A petrochronological review of a non-conventional Plume Model* ".

3.1 Os contextos geotectônicos e as fontes dos magmas

O conceito de tectônica das placas, introduzido na década de 70, possibilitou o entendimento da geodinâmica da crosta e do manto terrestre (CONDIE, 2016). Essa compreensão permitiu associar o magmatismo aos diferentes ambientes geotectônicos, que podem ser divididos, de forma simplificada, em intraplacas, convergentes, divergentes ou transformantes/transcorrentes. Com exceção dos ambientes transformantes, que apresentam movimentação lateral, os eventos de magmatismo estão geralmente associados aos ambientes divergentes e convergentes, e menos frequentemente aos intraplacas (Figura 2).

Figura 2 – Esquema de seção transversal indicando a geração de magmas e os ambientes tectônicos associados às placas

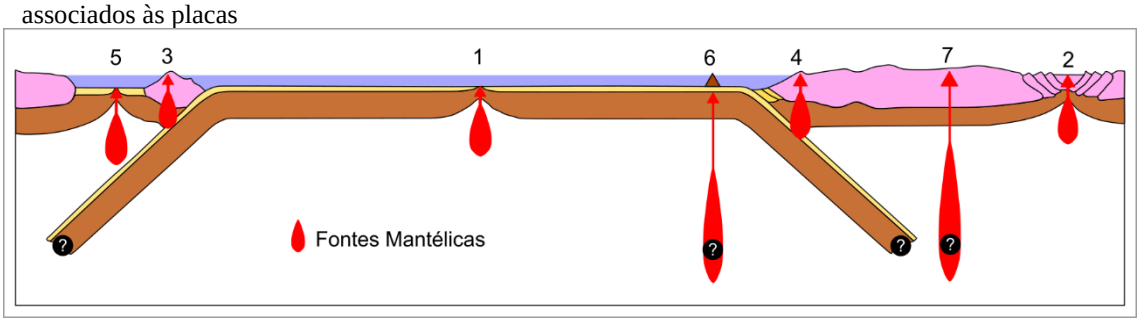

Legenda: 1 – Dorsais meso-oceânicas; 2 – Riftes continentais; 3 – Arcos de ilhas; 4 – Arcos continentais; 5 – Riftes de bacias de back-arc; 6 – Magmatismo intraplaca oceânico; 7 – Magmatismo intraplaca continental.
Fonte: modificado de WINTER (2001).

Ambientes divergentes podem ser classificados como riftes oceânicos ou riftes continentais, e ambos apresentam magmatismo específico. Os riftes oceânicos estão associados às Cadeias Meso-oceânicas, e de forma geral, o magmatismo predominante nesses

ambientes é basáltico do tipo MORB, gerado a partir da fusão parcial do manto superior por conta de processos de descompressão (ELTHON & SCARFE, 1984; KELEMEN et al., 1997; KUSHIRO, 2001). Por outro lado, os riftes continentais são caracterizados por sedimentos clásticos terrígenos imaturos e vulcanismo bimodal. Esse vulcanismo resulta da associação de magmas basálticos (toleíticos) e félsicos (WILSON, 1993; CONDIE, 2016). Um exemplo clássico desse contexto é observado na região NW da África (OUABID et al., 2021), associada ao *break-up* na margem norte do supercontinente Gondwana.

O magmatismo em ambientes convergentes, em geral, está associado aos arcos formados pela subducção das placas oceânicas (BRIGGS & MCDONOUGH, 1990). Enquanto o magmatismo de arcos de ilha gera majoritariamente uma nova crosta, os arcos continentais têm um maior retrabalhamento da crosta antiga (WANG et al., 2020). Arcos de ilhas, formados em zona de subducção intraocêanica, apresentam como rochas mais comuns basalto (toleítico e/ou cálcio-alcalino), basaltos andesíticos e andesito (ZARASVANDI et al., 2015; TSUKADA et al., 2017). Já os arcos de margem continental, formados no contexto de convergência entre crosta oceânica e crosta continental, apresentam uma ampla variedade de rochas.

Os ambientes intraplaca geralmente apresentam baixa atividade tectônica e magmática, e, por isso, sua correlação direta com a tectônica de placas não é simples. Em ambiente intraplaca o magmatismo associado a *hotspot* produz derrames basálticos e seus sistemas de enxames de diques, províncias de soleiras e intrusões máficas-ultramáficas acamadadas (YARMOLYUK et al., 2014). Uma pequena parte do magmatismo intraplaca pode estar associado à flexão ou à extensão litosférica, porém o aumento da temperatura mantélica pela presença de plumas mantélicas ou *hotspots* são a explicação da maior parte deste tipo de magmatismo (GUIMARÃES et al., 2020). Estas estruturas podem ser originadas no limite núcleo-manto, como Havaí, Galápagos, Ilhas Canárias etc. (MJELDE et al., 2010).

As rochas alcalinas, apesar de mais raras em volume quando comparada às demais rochas magmáticas, podem ocorrer em todos os ambientes tectônicos. No entanto, são mais comumente observadas em (1) riftes continentais; (2) contextos intraplaca continental e oceânica sem atividade tectônica; e (3) zonas de subducção. Destes ambientes, o primeiro é responsável pelo maior volume de rochas alcalinas continentais (WINTER, 2001). No contexto de magmatismo intraplaca de ambos os ambientes, as rochas alcalinas são comumente associadas à presença de plumas mantélicas. Este modelo é sugerido por alguns autores para a gênese das rochas do Alinhamento Poços de Caldas – Cabo Frio e da Cadeia Vitória-Trindade (*e.g.* THOMPSON et al., 1998). Para os ambientes associados à subducção

de crosta oceânicas, alguns autores destacam que a possibilidade da presença de sedimentos oceânicos e magmas metassomatizados podem trazer assinaturas muito características às rochas alcalinas (FAURE & MENSING, 2005; ROSA, 2017; QUARESMA et al., 2023).

Independentemente do contexto geotectônico, as rochas alcalinas têm sua origem comumente associada ao manto, e neste sentido, faz-se necessário o entendimento e a correlação das rochas com diferentes fontes a fim de entender sua gênese. A correlação das rochas com estas fontes é feita por meio da interpretação de dados de isotópicos de Nd, Sr e Pb, além de dados litogeoquímicos. A partir destas informações é possível indicar correlações com fontes responsáveis pela formação da rocha, ou ainda, sinalizar eventuais misturas.

De acordo com ERNST (2014), as fontes mantélicas podem ser divididas em cinco tipos principais: (1) Manto empobrecido (*Depleted Mantle – DM*) - associado a um reservatório raso de basalto meso-oceânico (NMORB), na parte superior manto, com baixos teores de elementos *Large Ion Lithophile* (LILE) (CONDIE, 2016); (2) HIMU (High μ, onde μ é a razão $^{238}U/^{204}Pb$) apresenta um elevado enriquecimento de isótopos de Pb associado à perda preferencial deste elemento durante a subducção, e um empobrecimento em Sr ($^{87}Sr/^{86}Sr$) (ERNST, 2014) (3) Focus Zone (FOZO), semelhante ao HIMU, recentemente interpretado como um componente onipresente na fonte de MORB, como um OIB produzido pela reciclagem contínua e envelhecimento da crosta oceânica não modificada (STRACKE et al., 2005; CONDIE, 2016); (4) e (5) As fontes de manto enriquecido (EM1 e EM2) caracterizadas por reservatórios com altos teores de elementos incompatíveis como Rb, Sm, U e Th em relação a Sr, Nd e Pb, quando comparados à razão do manto primitivos (CONDIE, 2016). *Enriched Mantle* 1 está possivelmente relacionado ao manto oceânico litosférico fortemente empobrecido e sedimentos antigos que são reciclados de volta para o manto (HART et al., 1992; CONDIE, 2016). Para o *Enriched Mantle* 2, as razões isotópicas estão próximas da crosta continental superior média ou de sedimentos continentais subduzidos modernos (CONDIE, 2016).

3.2 **Características das rochas alcalinas e sua gênese**

As rochas alcalinas correspondem a um pequeno volume das rochas magmáticas do planeta. Apesar disso, apresentam uma grande complexidade química e mineralógica. Essas rochas são enriquecidas em álcalis (Na_2O e K_2O) em relação à sílica, embora a proporção

entre estes constituintes não seja definida (BEST, 2013). Segundo SØRENSEN (1974) as rochas alcalinas podem ser insaturadas a saturadas e são caracterizadas por minerais como feldspatoides e/ou máficos alcalinos, mais especificamente piroxênio e anfibólio. De acordo com BEST (2013), a maior parte é subsaturada em sílica, apresenta nefelina normativa e tem feldspatoides (nefelina e leucita) em sua mineralogia modal. Além disso, as rochas alcalinas contêm altos teores de elementos incompatíveis e voláteis, como P, F, Cl, Zr, Ti, Nb, Ta e ETR (SØRENSEN, 1974).

A química altamente variada e exótica, típica deste tipo de magma, está associada à sua gênese que pode ser explicada por fusões parciais de veios metassomáticos enriquecidos nestes elementos que estão associados a peridotitos menos enriquecidos. Além disso, magmas alcalinos primitivos podem gerar novos magmas após o processo de diferenciação (BEST, 2013). Comumente controlada por tectônica extensional regional, o *emplacement* dessas rochas gera uma grande variedade de formas ígneas, em geral, de rochas evoluídas (GOMES AND COMIN-CHIARAMONTI, 2005). Uma pequena parcela de rochas alcalinas se desenvolve tipicamente em contextos intraplaca e riftes continentais em que a ressurgência do manto, localmente associado a plumas, elevam a temperatura da litosfera ou fazem com que ela se descomprima por meio de soerguimento e afinamento tectônico. Um destes fatores, ou a associação de ambos, podem levar à fusão parcial (BEST, 2013).

RICCOMINI et al. (2005) sugerem que as intrusões alcalinas do brasileiras tem o manto litosférico como principal fonte. Para as intrusões alcalinas do Alinhamento Poços de Caldas – Cabo Frio, ao qual o Complexo Tanguá está associado, diferentes intrusões possuem rochas alcalinas associadas às fontes DMM e EM (I ou II), sugerindo uma possível mistura entre elas (MOTA, 2012). Esta característica também é observada para as ilhas e os montes submarinos com rochas alcalinas associados à Cadeia Vitória-Trindade (QUARESMA et al., 2023; MAIA et al. 2021). Em conjunto com as informações isotópicas, dados geoquímicos permitem indicar também a presença de sedimentos associadas à subducção, ou processos como cristalização fracionada, saturação em sílica, assimilação crustal ou metassomatismo (FAURE & MENSING, 2005; MOTOKI et al., 2015b; ROSA, 2017, YAN & JIANG, 2019; ZHANG et al., 2019). MOTOKI et al. (2010) mostram que o Complexo Tanguá, foco do presente estudo, está associado ao contexto geotectônico intraplaca, assim como outros complexos alcalinos relacionados, e apresentam ainda assimilação de crosta continental em diferentes níveis crustais.

3.3 **Potencial Metalogenético das rochas alcalinas e sua importância econômica no Contexto Brasileiro**

As rochas alcalinas hospedam depósitos de diferentes metais e minerais industriais, dando a essas litologias um papel de destaque na indústria mineral mundial, inclusive no Brasil. Embora raras, várias intrusões de rochas alcalinas são encontradas em território brasileiro, e algumas já estão em fase de exploração e lavra. Depósitos alcalinos antigos, como os do período Arqueano, são menos frequentes do que os depósitos mais jovens. No entanto, as poucas ocorrências Arqueanas geralmente apresentam alto grau de metamorfismo (LAZNICKA, 2006). Esses depósitos alcalinos mostram teores elevados de elementos litófilos incompatíveis e metais raros como ETR + Y, fosfato, Nb, Ta, Zr, Th, U, Be e Hf (GOMES & COMIN-CHIARAMONTI, 2005; LAZNICKA, 2006).

O potencial metalogenético das rochas está associado ao seu conteúdo químico e mineralógico, e no caso das rochas alcalinas, estes fatores permitem a diferenciação de assinaturas e a classificação destas em agpaíticas e miaskíticas. De acordo SØRENSEN (1992), o termo agpaítico foi introduzido por USSING (1912) associado a uma rara suíte de nefelina sienitos peralcalinos. A diferenciação original entre esses tipos de rocha, segundo USSING (1912), se dá pelo índice agpaítico (*Agpaitic Index* – AI), definido como $(Na_2O + K_2O) > Al_2O_3$ (molar). No caso das rochas alcalinas, o maior potencial econômico dos depósitos está associado à presença de litotipos com assinatura agpaítica, associação a rochas carbonatíticas e/ou enriquecimento primário e secundário, seja por processos supergênicos ou hidrotermais (BIONDI, 2005; TORRES, 2017).

Além dos fatores químicos, a diferença entre as rochas agpaíticas e miaskíticas está relacionada à mineralogia (MARKS & MARKL, 2017). Em geral, esse último grupo tem a presença de HFSE associados a estruturas simples como zircão, ilmenita, rutilo e titanita (KHOMI͡AKOV, 1995; SØRENSEN, 1997; LE MAITRE et al., 2005; SCHILLING et al., 2009; ANDERSEN et al., 2010; MARKS et al., 2011; MARKS & MARKL, 2017). Em contrapartida, as rochas agpaíticas são nefelina sienitos peralcalinos caracterizados pela presença de minerais silicatados complexos de Na–Ca–Fe–HFSE (SCHILLING et al., 2009; GIEHL et al., 2014; SJÖQVIST, 2015; ANDERSEN et al., 2017, 2018). A eudialita é o mineral mais característico deste grupo, mas também são observados hiortdahlita, sodalita, rinkita, lavenita, rosenbuschita, aenigmatita, mosandrita, astrofilita, wöhlerita, entre outros (SØRENSEN, 1992, 1997; SCHILLING et al., 2009; MARKS et al., 2011; GIEHL; MARKS

AND NOWAK, 2014; CHAKRABARTY et al., 2016; ANDERSEN et al., 2017; MARKS & MARKL, 2017; GUARINO et al., 2019.

De acordo com o Departamento Nacional de Produção Mineral (DNPM, hoje denominado Agência Nacional de Mineração - ANM), o Brasil possui as maiores reservas de minério de Nb, correspondendo a 98,8%. Outras reservas de metais em que o país se destacou, e que se correlacionam com as rochas alcalinas, foram o tântalo (32,8%) e o ETR (17,5%). Os principais depósitos brasileiros estão na Província Ígnea do Alto Paranaíba que apresenta, já em exploração, empreendimentos minérios de fosfato, nióbio e REE como Catalão, Salitre, Tapira, Serra Negra e Araxá (AVELAR, 2018). No Brasil, os depósitos são formados por processos supergênicos ou por concentração mineral que ocorre durante um longo período de intemperismo (GOMES AND COMIN-CHIARAMONTI, 2005).

Diferentes estudos mostram também um potencial econômico de sienitos e nefelina sienitos em diferentes áreas, como rocha ornamental (COSTA, 2017) e indústria de vidro e cerâmica (SAMPAIO et al., 2008). Por conta da característica econômica brasileira, muito focada em agricultura, o nefelina sienito também tem sido estudado como fonte de potássio por meio da técnica de rochagem (SOUZA AND SCHNEIDER, 2015). Trabalhos como ROCIO et al. (2012), MORAES AND SEER (2017) e TORRES (2017) mostram a associação de nefelina sienito com depósitos de rochas alcalinas e carbonatíticas em que se tem teores consideráveis de elementos de interesse, como terras raras, fósforo, titânio e nióbio. No caso do Complexo Tanguá, observa-se um baixo potencial para exploração de ETR, em contraste com outros complexos, como Araxá e Tapira. No entanto, o Complexo apresenta outros potenciais para a indústria mineral, como o alto conteúdo de fluorita (SILVA et al., 2018), que já foi explorado no passado, e ainda o aproveitamento de rocha sienítica rica em potássio para o processo de rochagem, executado hoje pela empresa EMITANG

3.4 **Artigo 1: Poços de Caldas – Cabo Frio Alignment: A petrochronological review of a non-conventional Plume Model**

Marco Aurélio Maia Teodoro[1], Anderson Costa dos Santos[2], Luiz Carlos Bertolino[2,5], Pedro Augusto da Silva Rosa[3], Caio Rodrigues Bezerra[1], Júlio César Lopes da Silva[4], Lucas Guimarães Pereira Monteiro[1], Mariana Bessa Fagundes[1], Mauro Cesar Geraldes[2], Leticia Muniz da Costa Cardoso[1], Fred Jourdan[6]

[1] Universidade do Estado do Rio de Janeiro (UERJ), Faculdade de Geologia, Programa de Pós-graduação em Geociências. Rua São Francisco Xavier, 524 - 4° andar/bloco A, Rio de Janeiro (RJ), Brasil

[2] Universidade do Estado do Rio de Janeiro (UERJ), Faculdade de Geologia, Departamento de Mineralogia e Petrologia Ígnea. Rua São Francisco Xavier, 524 - 4° andar/bloco A, Rio de Janeiro (RJ), Brasil. Grupo Tektos e Instituto GeoAtlântico, Universidade do Estado do Rio de Janeiro

[3] Universidade Federal de Minas Gerais (UFMG), Instituto de Geociências, Departamento de Geologia. Antônio Carlos, 6627 - Pampulha, Belo Horizonte - MG, 31270-901. Centro de Pesquisas Professor Manoel Teixeira da Costa/CPMTC

[4] Departamento de Geologia, Universidade Federal do Rio de Janeiro, Rio de Janeiro (RJ), Brasil, CEP 21941-916

[5] Centro de Tecnologia Mineral, CETEM, Av. Pedro Calmon, 900, Cidade Universitária, 21941-908 Rio de Janeiro, Brasil

[6] Western Australian Argon Isotope Facility, School of Earth and Planetary Sciences and John de Laeter Centre, Curtin University, Perth, Australia

Abstract

This work reviews the Poços de Caldas – Cabo Frio Alignment (PCCFA), one of Brazil's alkaline igneous provinces, comprising syenites, phonolites, and trachytes, as well as magmatic breccias. TAS and Harker (for major and trace elements) diagrams suggest two groups based on the silica content. From the TAS diagram, it is noted that the less evolved rocks plot mainly in the tephrite/basanite and foidite fields, while the more evolved rocks predominantly fall in the phonolite and trachyte fields. In the Harker diagrams, correlations with silica can be observed for some oxides/elements, such as TiO_2, CaO, Rb, Sr, Zr, Y, and Nb. From the normalized diagrams, it is evident that the less evolved rocks exhibit low variability, indicating similar sources and petrogenetic processes. In contrast, the more evolved ones present several anomalies (Ba, Sr, Ti, Rb, Zr, and Eu), suggesting different mineral fractionations. In addition, a wide range of normalized values is observed for certain elements, such as Ba, Sr, and Pb, which may indicate distinct evolutionary processes. Sr and Nd isotopic data show show similar trends, suggesting a mixture of DMM and EM1 or DMM

and EM2 sources for the PCCFA complexes. Two new $^{40}Ar/^{39}Ar$ ages (71.55 ± 0.49 Ma and 67.31 ± 0.78 Ma) are presented for the Tinguá and Itatiaia massifs, respectively. In addition, two new U-Pb ages (69.3 ± 2.2 Ma for Tinguá and 70.4 ± 2.6 Ma for Itatiaia) are presented along with a third U-Pb age of 65 ± 2 Ma obtained for Gatos Hill, which is the first published age for this massif. The compilation of geochronological data, along with these new ages, indicates that the decrease in ages from west to east is not regular. For example, the oldest age (Itatiaia – 90.5 Ma) and the youngest age (Tinguá – 39.1 Ma) are found in more central massifs of the magmatic alignment. This feature prevents the genesis of this alignment from being attributed to a conventional plume model. In this regard, the authors suggest the presence of a plume with widespread conduits that have used preexisting structures for the intrusion the alkaline rocks, a hypothesis supported by the orientation of these magmatic bodys (massifs and dikes).

Keywords: Poços de Caldas-Cabo Frio Alignment, Lithogeochemistry, $^{40}Ar/^{39}Ar$ dating, U-Pb dating.

Resumo

Este trabalho estuda o Alinhamento Poços de Caldas – Cabo Frio (APCCF), uma das províncias ígneas alcalinas do Brasil, que é composta por diferentes tipos de sienitos, fonolitos e traquitos, além de brechas magmáticas. Os diagramas TAS e de Harker (maiores e traços) sugerem dois grupos com base no conteúdo de sílica. A partir do primeiro diagrama nota-se que as rochas menos evoluídas plotam principalmente nos campos tefrito/basanito e foidito, enquanto as mais evoluídas caem principalmente nos campos fonolito e traquito. Nos diagramas Harker correlações com sílica podem ser verificadas para alguns óxidos/elementos, como TiO_2, CaO, Rb, Sr, Zr, Y e Nb. A partir dos diagramas normalizados verifica-se que as rochas menos evoluídas apresentam baixa variabilidade, indicando fontes e processos petrogenéticos semelhantes. Já as rochas mais evoluídas apresentam diversas anomalias (como Ba, Sr, Ti, Rb, Zr e Eu), sugerindo diferentes fracionamentos minerais. Além disso, nota-se um range grande de valores normalizados para alguns elementos, como Ba, Sr e Pb, o que pode indicar processos evolutivos distintos. Os dados isotópicos de Sr e Nd mostram comportamentos semelhantes, sugerindo mistura de fontes de DMM e EM1 ou DMM e EM2

para os complexos APCCF. São apresentadas duas novas idades de $^{40}Ar/^{39}Ar$ de 71,55 ± 0,49 Ma e 67,31 ± 0,78 Ma para os maciços Tinguá e Itatiaia, respectivamente. Além disso, duas novas idades U-Pb de 69,3 ± 2,2 Ma (Tinguá) e 70,4 ± 2,6 Ma (Itatiaia) são apresentadas, além de uma terceira idade U-Pb de 65 ± 2 Ma obtida para o Maciço Morro dos Gatos, a qual é a primeira idade publicada. A compilação de dados geocronológicos, além destas novas idades, indica que a diminuição das idades de oeste para leste não é regular pois, por exemplo, as idades mais velha (Itatiaia – 90.5 Ma) e mais nova (Tinguá – 39.1 Ma) encontram-se em maciços mais centrais do alinhamento magmático. Tal característica impede que a gênese deste alinhamento seja atribuído a um modelo de pluma convencional. Neste sentido, os autores sugerem a presença de uma pluma com condutos disseminados que utilizam estruturas preexistentes para intrusão das rochas alcalinas, o que é reforçado pela orientação destes corpos magmáticas (maciços e diques).

Palavras-chave: Alinhamento Poços de Caldas-Cabo Frio; Datação $^{40}Ar/^{39}Ar$; Datação U-Pb.

3.4.1 Introduction

The Brazilian Platform has over 100 alkaline intrusion occurrences in its central-southeastern part, presenting mesozoic and cenozoic ages. GOMES & COMIN-CHIARAMONTI (2005) linked these rocks to mobile belts from the Brasiliano Cycle intruded at the Paraná Basin margins, whose emplacement is controlled by regional extensional tectonics (Figure 1). First grouped by ALMEIDA (1983) into 12 different provinces, the alkaline magmatism of the Brazilian Platform was redefined by RICCOMINI et al. (2005) based on geological, structural, and geophysical data into 15 provinces: Alto Paraguay, Ponta Grossa Arch, Valle Chico, Misiones, Central Paraguay, Amambay, Rio Apa, Rondonópolis Anteclise, Minas-Goiás, Serra do Mar, Piratini, Asunción, Cabo Frio Magmatic Lineament, Velasco and Candelária. RICCOMINI et al. (2005) suggest subdividing the Serra do Mar Province (SMP) into northern, central, and southern sectors, corresponding to the most significant areas of Cenozoic uplift along the southeastern Brazilian coast. Additionally, these authors also identified the Cabo Frio Magmatic Lineament, also known as the Poços de Caldas – Cabo Frio Alkaline Alignment (PCCFA), as a distinct province. However, other

researchers, such as GUARINO et al. (2019), continue to regard the PCCFA as part of the northern sector of the SMP.

Figure 1 – Brazilian Platform's map of the central-southeastern region alkaline provinces, associated lithologies, and main structural features.

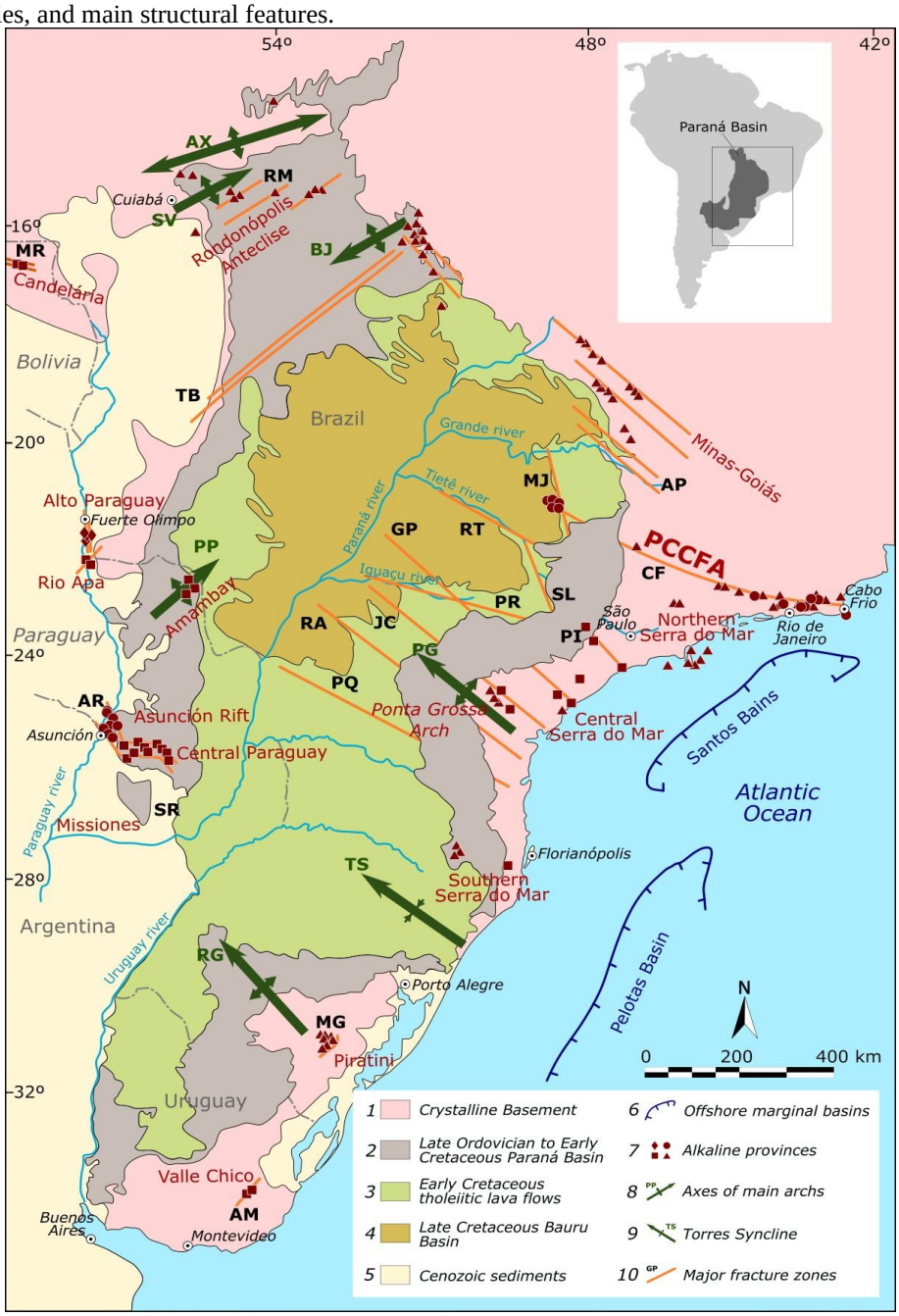

Legenda: Ages of alkaline rocks (5): Diamonds - Permian-Triassic; squares - Early Cretaceous; triangles - Late Cretaceous; and circles – Paleogene. Main arches (6): AX - Alto Xingu; SV - São Vicente; BJ - Bom Jardim de Goiás; PG - Ponta Grossa; RG - Rio Grande; PP - Ponta Porã. Major fracture zones (8) - Rifts: MR - Mercedes; RM - Rio das Mortes; MG - Moirão; SR - Santa Rosa; AR - Asunción. Lineaments: TB - Transbrasiliano; AP - Alto Paranaíba; MJ - Moji-Guaçu; CF - Cabo Frio; RT - Rio Tietê; SL - São Carlos-Leme; PR - Paranapanema; PI - Piedade; GP - Guapiara; JC - São Jerônimo-Curiúva; RA - Rio Alonzo; PQ – Rio Piquiri; AM - Santa Lucía-Aiguá-Merin).

Fonte: Modified from MILANI (1997) and RICCOMINI et al. (2005).

The SMP - PCCFA contain alkaline complexes and dike swarms, which intrude into the Proterozoic metamorphic terrains of the Ribeira Belt. These intrusions are structurally related to a fault system of the Brasiliano cycle, with ENE to EW trend (ALMEIDA, 1983; BROTZU et al., 2005; HACKSPACHER & GODOY, 1999; HEILBRON et al., 2016). This alkaline magmatism occurred from the Late Cretaceous to the Paleocene, along the ENE-EW transcurrent systems reactivated during the Gondwana break-up (ENRICH et al., 2005; GUARINO et al., 2019). According to SANTOS & HACKSPACHER (2021 and references therein), oceanic fracture zones (FZ; Figure 2A) represent areas of lithospheric weakness perpendicular to the Mid-Ocean Ridge, with faults that exhibit strike-slip movement and contain multiple intrusions linked to mantle plumes. These FZ extend into the continental crust and may be associated with the genenis of dike swarms (*e.g.*, Florianópolis and Pariquera-Açu). In this onshore context, the FZ is also linked with the Southeast Brazilian Meso-Cenozoic tectomagmatism, including the PCCFA.

This paper compiles and presents previously published data on the PCCFA, focusing on petrochronological aspects of alkaline massifs and other magmatic bodies, such as dikes. This review facilitates correlating the alkaline complexes' genesis with existing models (fault reactivation and mantle plumes) to unravel the emplacement of the PCCFA complexes. Additionally, new $^{40}Ar/^{39}Ar$ and U-Pb data for Tinguá and Itatiaia massifs, covering various syenitic facies (amphibole- and biotite-bearing syenite and biotite- and amphibole-bearing nepheline syenite), as well as U-Pb data for monzonite from Morro dos Gatos Hill, are presented to support this investigation.

3.4.2 The Poços de Caldas – Cabo Frio Alignment (PCCFA) definition and geological content

The SMP is defined by two alignments with distinct structural characteristics (ENRICH et al., 2005): 1) an alignment along the Brazilian coast following the Santos fault; and 2) the Cabo Frio Alignment associated with structural rifting systems. The Precambrian-oriented structures possibly controlled the shapes and directions of these intrusions during emplacement, generating elongated bodies from NE to NNE (RICCOMINI et al., 2005), which has been confirmed by magnetometry data (FERREIRa, 2018).

The PCCFA is a slightly curved magmatic province with a WNW-ESE trend that stretches for about 1,150 km, from Jaboticabal (São Paulo State) to the coastline of Cabo Frio

(Rio de Janeiro State). The Alignment has 26 alkaline intrusive centers with stocks, massifs, plugs, and many alkaline dikes (RICCOMINI et al., 2005). The complexes mainly comprise alkali- and nepheline syenites, with quartz-bearing syenites and granite occurrences (BROTZU et al., 2005). The ages of these alkaline intrusions vary between 84 Ma and 39 Ma (Figure 3, Table 1 and Supplementary Material), indicating a decreasing age from west to east (Rosa, 2017), although nonlinear (SANTOS & HACKSPACHER, 2021).

Alkaline dikes in the alignment present two groups with distinct geochemical characteristics (BROTZU et al., 2005): 1) strongly silica-undersaturated (basanites, foidites, and a succession from tephrites to phonolites); and 2) weakly silica-undersaturated (alkali basalts to trachytes). According to MACEDO et al. (2022 and references therein), the lamprophyres occur as dykes or sills intruding rocks of the Paleoproterozoic metamorphic basement. These dykes tend to follow structures with NE-SW to ENE-WSW directions and may be related to the parental magmas of more evolved alkaline rocks (e.g., syenites). Furthermore, although rare, locally these dykes may be crosscuted by felsic alkaline dykes (e.g., Cabo Frio Island – MOTOKI et al. 2008).

3.4.2.1 PCCFA genetic models

Two models for genesis of the PCCFA are intensely debated. The first model associates the magmatism with a mantle plume activity, suggesting that the intrusions' alignment results from the relative plate movement over the plume (THOMPSON et al., 1998). This hypothesis is supported by geological events and geochronological data, which suggest a decrease towards the east. According to THOMPSON et al. (1998), the Tristan and Trindade mantle plumes were beneath or close to southeastern Brazil at *ca.* 135 Ma and *ca.* 85 Ma, respectively, reinforcing this model. Additionally, these authors suggested the existence of a sub-lithospheric plume head with a radius of about 600 km, which started to impact the continental lithosphere in the Cretaceous period.

The second model correlates the alkaline emplacement with reactivation of subcrustal faults and then with lithospheric refertilization (ROCHA-JÚNIOR et al., 2020), caused by the mantle's partial melting, followed by the melt infiltration through fracture zones (ALMEIDA, 1991). According to RICCOMINI et al. (2005 and references therein), this reactivation is linked to the South Atlantic opening in three stages: 1) the rift stage, 2) the ocean stage, and

3) contemporary to the continental taphrogenic basin installation in southeastern Brazil. They concluded that crustal discontinuities control the alkaline magmatism, and its development is linked to the main onshore sedimentary basins (Figure 2B), such as the Taubaté and Resende basins (THOMAZ FILHO et al., 2005).

Figure 2 – A) Schematic map of southeast Brazil and the southwest Atlantic Ocean with fracture zones, tectonic lineaments, and the Mid-Atlantic Ridge correlating with the alkaline intrusions in the onshore and offshore contexts; B) Map of intrusions of the PCCFA and the SMP in the north sector, and regional geological features and structures associated with the southeastern Brazilian Platform.

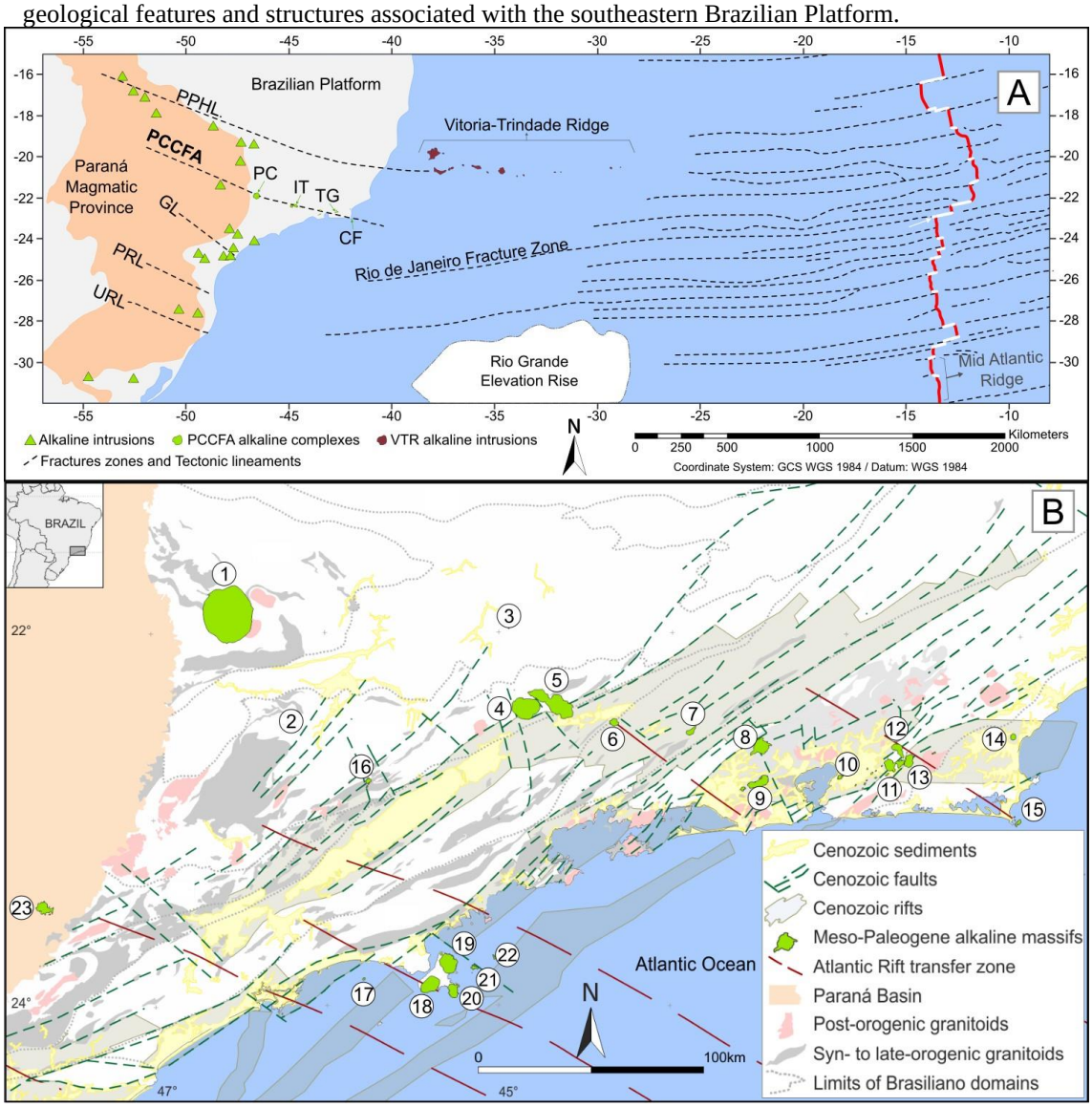

Legenda: A) AB – Abrolhos Bank; CF - Cabo Frio Complex; DB - Davis Bank; GL - Guapiara Lineament; IT - Itatiaia Complex; MVFZ – Martin Vaz Fracture Zone; MVI – Martin Vaz Archipelago; PC - Poços de Caldas Complex; PCCFA – Poços de Caldas – Cabo Frio Alignment; PRL - Piquiri River Lineament; RGFZ - Rio Grande Fracture Zone; RJFZ - Rio de Janeiro Fracture Zone; RJTF - Rio de Janeiro Transform Fault; SHFZ - Santa Helena Fracture Zone; TG - Tanguá Complex; TI – Trindade Island; URL - Uruguay River Lineament; VTFZ - Vitória-Trindade Fracture Zone. B) Alkaline massifs: 1 - Poços de Caldas; 2 - Bom Repouso; 3 - Caxambú; 4 - Passa Quatro; 5 - Itatiaia; 6 - Morro Redondo; 7 - Serra dos Tomazes; 8 - Tinguá; 9 - Mendanha-Mapicuru; 10 - Itaúna; 11 - Tanguá; 12 - Soarinho; 13 - Rio Bonito; 14 - Morro de São João; 15 - Cabo Frio; 16 - Ponte Nova; 17 - Monte de Trigo; 18 - São Sebastião; 19 - Serraria; 20 - Mirante; 21 - Búzios; 22 - Vitória; and 23 - SMP Ipanema near occurrence.

Fonte: A) Modified from SANTOS AND HACKSPACHER (2021); B) Data were compiled from the CPRM public database, and the map was modified based on ROSA & RUBERTI (2018) and THOMPSON et al. (1998).

Table 1 – Statistical summary of geochronological data for the main PCCFA complexes, considering all analytical methods. Data sources include AMARAL et al. (1967), BIONDI (2005), DECKART et al. (1998), FERRARI (2001), MOTA (2012), MOTOKI et al. (2013, 2010), NETTO et al. (2005), SILVA et al. (2018, 2020), SILVA (2019), SMITH et al. (1999), SONOKI & GARDA (1988), THOMPSON et al. (1998), and from present work (see Supplementary Material for details, such as method, used material/rock and the associated reference). n: number of data; The table provides the following information: the minimum represents the lowest geochronological value for each massif; the median is the central value of the data set when arranged in ascending order; and the maximum represents the highest geochronological value.

Massifs	n	Minimum (Ma)	Median (Ma)	Maximum (Ma)
Poços de Caldas	67	54.2	76.3	89.3
Passa Quatro	4	66.7	70.4	77.0
Itatiaia	26	64.6	69.6	90.5
Morro Redondo	15	67.2	72.6	79.8
Tinguá	8	39.1	66.5	71.6
Mendanha	24	54.2	71.5	81.8
Tanguá	8	65.0	68.2	74.0
Rio Bonito	10	65.0	65.3	83.9
Soarinho	4	58.0	59.0	61.8
Morro dos Gatos	1	65.4	65.4	65.4
Morro do São João	4	60.1	63.1	64.9
Cabo Frio	5	50.0	54.0	72.4

Figure 3 – Boxplot diagram of geochronological data of the main PCCFA alkaline complexes arranged from west to east obtained by $^{40}K/^{40}Ar$, U-Pb, and $^{40}Ar/^{39}Ar$ methods. The massifs are presented from left to right in the following order: Poços de Caldas, Passa Quatro, Itatiaia, Morro Redondo, Tinguá, Mendanha, Tanguá, Rio Bonito, Soarinho, Morro dos Gatos, Morro do São João and Cabo Frio. This interval is skipped when the massif has no age obtained by the specific method.

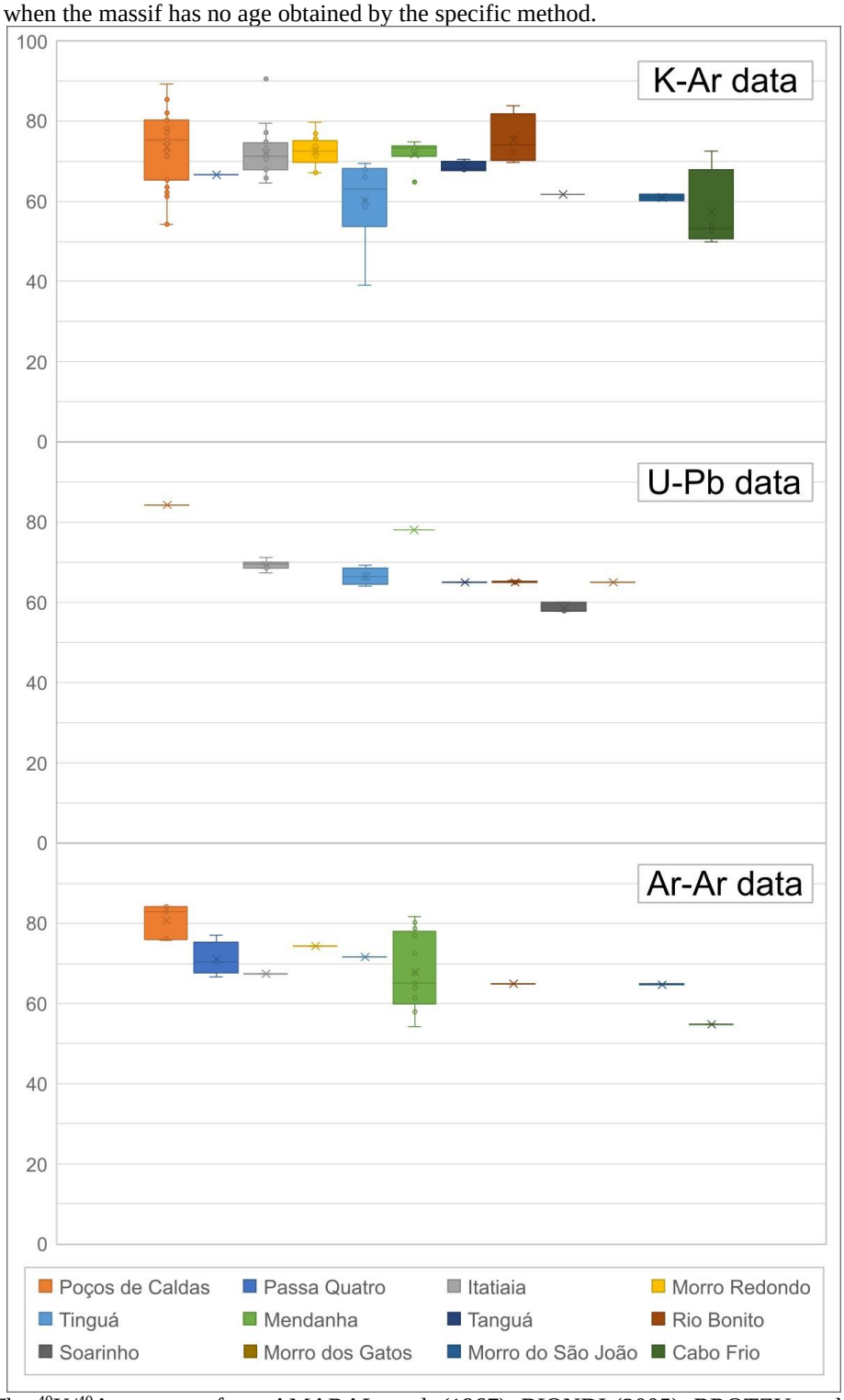

Fonte: The $^{40}K/^{40}Ar$ ages are from AMARAL et al. (1967), BIONDI (2005), BROTZU et al. (1989), BUSHEE (1971), MONTES-LAUAR et al. (1995), RIBEIRO FILHO AND CORDANI (1966), SONOKI AND GARDA (1988), THOMPSON et al. (1998), ULBRICH et al. (2002). The U-Pb are from ROSA (2017), SILVA (2019), SILVA et al. (2020, 2023), TAKENAKA (2014). The $^{40}Ar/^{39}Ar$ ages are from Brotzu et al. (1992), DECKART et al. (1998), FERRARI (2001), MONTES-LAUAR et al. (1995), MONTES-LAUAR AND PACCA (1988), MOTA

(2012), MOTOKI et al. (2013), SHEA (1992), SILVA et al. (2015), SILVA et al. (2020), SONOKI & GARDA (1988), ULBRICH et al. (2002), VLACH et al. (2003), and from present work.

3.4.3 Methodology

3.4.3.1 U-Pb Geochronology

The samples analyzed were selected based on their representativeness of the correlated massif and their low degree of alteration. Additionally, other samples had been selected for analysis; however, it was not possible to obtain zircon grains for the study due to insufficient quantities or the absence of the mineral. Prior to geochronological analysis, petrographic studies were conducted on the selected samples, which will be presented together.

The new geochronological data it was obtained from zircon crystals from rocks processed and prepared in the Geological Sample Processing Laboratory (LGPA) of Rio de Janeiro State University (UERJ). Milling was used to reduce the particle size, followed by magnetic separation (Frantz), to concentrate the mineral of interest (zircon) into a dense liquid. The mineral concentrate was later taken to the Multilab Laboratory at UERJ, where the zircon crystals were collected using a stereomicroscope. The crystals were mounted on an epoxy resin to obtain zircon cathodoluminescence images and conduct the U-Pb analyses.

A New Finningan Neptune MC-ICP-MS system was coupled to an excimer laser ablation device in the Multilab Laboratory for U-Pb analyses. This laser device features a camera that allows conducting a detailed analysis from the ablation of the crystal using a laser spot with a diameter between 80 and 100 μm. For the analyses, the frequency was 5 Hz, and the energy variation was 80% to 100%. Helium gas was used for carriage in the laser ablation, while argon gas was used in ICP-MS. Two different standards were used for the analyses: GJ-1 from JACKSON et al. (2004) and 91500 from WIEDENBECK et al. (1995).

3.4.3.2 $^{40}Ar/^{39}Ar$ Radioisotopic data

Fresh biotite from the nepheline syenite of the Itatiaia Complex and amphibole from the syenite of the Tinguá Complex were selected. These minerals were separated using a Frantz magnetic separator and then hand-picked under a stereomicroscope. The selected amphibole minerals were leached in diluted HF for one minute and then thoroughly rinsed with distilled water in an ultrasonic cleaner.

Samples were loaded into two large aluminum disc wells. These wells were bracketed by small wells, including Fish Canyon sanidine used as a neutron flux monitor, for which an age of 28.03 ± 0.08 Ma was adopted (JOURDAN & RENNE, 2007). The discs were Cd-shielded (to minimize undesirable nuclear interference reactions) and irradiated for 25 hours in Hamilton University's McMaster nuclear reactor (Canada) in position 5C. The J-values were 0.0091820 ± 0.0000266 (Tinguá Complex) and 0.0090200 ± 0.0000496 (Itatiaia Complex). Mass discrimination was monitored using an automated air pipette, which indicated a mean value of 1.00583 ± 0.00322 per dalton (atomic mass unit). The correction factors for interfering isotopes were $(^{39}Ar/^{37}Ar)_{Ca}$ = 7.30x10^{-4} (± 11%), $(^{36}Ar/^{37}Ar)_{Ca}$ = 2.82x10^{-4} (± 1%) and $(^{40}Ar/^{39}Ar)_{K}$ = 6.76x10^{-4} (± 32%).

The $^{40}Ar/^{39}Ar$ analyses were performed at the Western Australian Argon Isotope Facility of Curtin University. The amphibole aliquot was step-heated using a 110 W Spectron Laser System, with a continuous Nd-YAG (IR; 1064 nm) laser rastered across either single large grains or multigrain aliquots wrapped in zero-blank niobium foil, throughout approximately 1 mn to ensure a homogeneously distributed temperature. The biotite aliquot was step-heated in a double vacuum high-frequency Pond Engineering furnace. The gas was purified in a stainless steel extraction line using three SAES AP10 getters and a liquid nitrogen condensation trap. Ar isotopes were measured in static mode using an MAP 215-50 mass spectrometer (resolution of *ca*. 450; sensitivity of 4x10^{-14} mol/V) with a Balzers SEV 217 electron multiplier, mostly using 9 to 10 peak-hopping cycles. The data acquisition was performed using the Argus program by M.O. McWilliams and was run under a LabView environment.

The raw data were processed using the ArArCALC software (KOPPERS, 2002), and the ages were calculated using the decay constants recommended by RENNE et al. (2011). Blanks were monitored every 3 to 4 steps. All parameters and relative abundance values are provided in the Supplementary Material.

3.4.4 Results

3.4.4.1 PCCFA Complexes review and new geochronological data

Based on recent works, we compiled geological, petrographic, mineralogical, and geochronological data for the PCCFA alkaline complexes. The data are presented according to their geographical position, from west to east, in the following sections. The main rock types found in each massif and their associated mineralogy are summarized in Table 2, while the lithogeochemical, geochronological, and isotopic data are provided in the Supplementary Material.

Table 2 - Summary of the main lithologies observed in the primary massifs of the PCCFA, along with their major and accessory minerals. This information was compiled from studies by BROTZU et al. (1989; 1992; 2007); ENRICH et al. (2005); GERALDES et al. (2013); GUARINO et al. (2019; 2021); MOTA (2012); MOTOKI et al. (2010; 2013); ROSA & RUBERTI (2018); SILVA et al. (2015); SILVA et al. (2018; 2023); SILVA (2019); SILVEIRA et al. (2005); and VALENÇA (1980).

Massif	Main rocks	Minerals	
		Major	Accessory
Poços de Caldas	Nepheline syenite, phonolite and pyroclastic rocks	Alkali feldspar, nepheline and clinopyroxene	Sodalite, amphibole, titanite, apatite, biotite, and eudialyte
Passa Quatro	Nepheline syenite, breccia and phonolite	Alkali feldspar, nepheline, plagioclase, amphibole, pyroxene, biotite	Titanite, apatite, Ti-magnetite, låvenite, and eudialyte
Itatiaia	Syenite, nepheline syenite, phonolite, nephelinite, nordmarkite, granite, trachyte, monzonite, trachybasalt, and melagabbro	Alkali feldspar, nepheline, clinopyroxene, amphibole, biotite, titanite, apatite, zircon, titanomagnetite, sodalite, quartz (in quartz syenites)	Ilmenite, låvenite, hiortdahlite, astrophyllite, and catapleiite
Morro Redondo	Alkali syenite, nepheline syenite, trachyte, and phonolite	Alkali feldspar and nepheline	Nepheline, plagioclase, hornblende, biotite, titanite, apatite, and opaques
Tinguá	Syenite, nepheline syenite and phonolite	Alkali feldspar and nepheline	Amphibole, titanite, apatite, and opaques
Mendanha	Syenite, trachyte, breccia, lapillite, and phonolite	Alkali feldspar, nepheline, plagioclase, and hornblende	Biotite, scapolite, muscovite, carbonate, zircon, apatite, augite, and opaque
Tanguá	Syenite, nepheline syenite, breccia, trachyte and phonolite	Alkali feldspar, nepheline, amphibole, and biotite	Magnetite, titanite and apatite
Rio Bonito	Syenite, nepheline syenite, breccia, trachyte and phonolite	Alkali feldspar and nepheline	Hornblende, clinopyroxene, biotite, opaques, titanite, apatite,

Massif	Main rocks	Minerals	
		Major	**Accessory**
			and zircon
Soarinho	Syenite, quartz syenite, quartz monzonite, breccia and nordmarkite	Alkali feldspar, plagioclase and biotite	Quartz (in quartz-bearing rocks), amphibole and opaque
Morro dos Gatos	Alkaline syenite, nepheline syenite, monzonite, trachyte, gabbros and pyroclastic rock	Alkali feldspar, plagioclase, clinopyroxene, and biotite	Quartz, apatite and magnetite
Morro do São João	Alkaline syenite, nepheline syenite, clinopyroxenite and alkaline gabbro	Alkali feldspar and nepheline	Biotite, amphibole, clinopyroxene, titanite, apatite, Ti-magnetite and melanite garnet
Cabo Frio	Alkaline syenite, nepheline syenite, phonolite, trachyte, and breccia	Alkaline feldspar, nepheline, clinopyroxene, amphibole, and biotite	Magnetite, titanite and apatite

3.4.4.1.1 Poços de Caldas Complex (MG)

The Poços de Caldas Complex (Figure 4A) is circular and the largest in Brazil (*ca.* 800 km² - ULBRICH et al., 2005). The massif comprises nepheline syenites and phonolites, with relevant quantities of strongly agpaitic rock types, pyroclastic rocks, and remnants of lava flows, the last being formed by mafic-ultramafic rocks from the Serra Geral Formation (ULBRICH et al., 2005). Nepheline syenite rocks are medium- to coarse-grained, generally with hypidiomorphic textures, and contain large and microperthitic alkali feldspar macrocrystals (oikocrysts), which enclose different chadacrysts such as nepheline, clinopyroxene and titanite among others. Nepheline syenites' major minerals consist of alkali feldspar, nepheline and clinopyroxene (aegirine to sodic augite), and the main accessory phases are sodalite, amphibole, titanite, apatite, biotite and eudialyte. The phonolites are texturally diverse, presenting subaphyric to seriate porphyritic characteristics, with fine-grained to medium-grained groundmass. Alkali feldspar and nepheline are the main phenocrysts, but clinopyroxene and amphibole are also observed (GUARINO et al., 2021).

The first geochronological study yielded ages between 87 and 109 Ma and was performed on zircon crystals from phonolitic dikes that cross-cut nepheline syenites using the lead-alpha method (DUTRA, 1966). The several rocks analyzed by ULBRICH et al. (2002) showed $^{40}K/^{40}Ar$ ages ranging from 54.2 to 89.3 Ma. The Rb/Sr data (whole-rock) showed isochron ages of 78.6 ± 6.6 Ma for nepheline syenites and 76.6 ± 2.6 Ma for hydrothermally altered syenite (ULBRICH et al., 2002). SHEA (1992) presented two $^{40}Ar/^{39}Ar$ readings of

biotite from a lamprophyre dike, which crosscut phonolites and syenites, which are the primary rocks of the massif, and even breccias in the Osamo Utsumi Mine. These analyses yielding ages of 75.6 ± 0.6 and 76.2 ± 1.6 Ma from mica phenocryst and groundmass mica, respectively. The $^{40}Ar/^{39}Ar$ plateau ages were determined for a phlopogite from carbonatitic dikes, which is a late hydrothermal veins, varying between 83.5 ± 0.1 Ma and 84.3 ± 0.1 Ma. These data suggesting a minimum age for mineral crystalization and vein formation (VLACH et al., 2003). See Supplementary Material for details of these geochronological data.

Figure 4 – A) Simplified geological map of the Poços de Caldas Complex (ULBRICH, 1984); B) Simplified map of the Itatiaia alkaline massif with sectors.

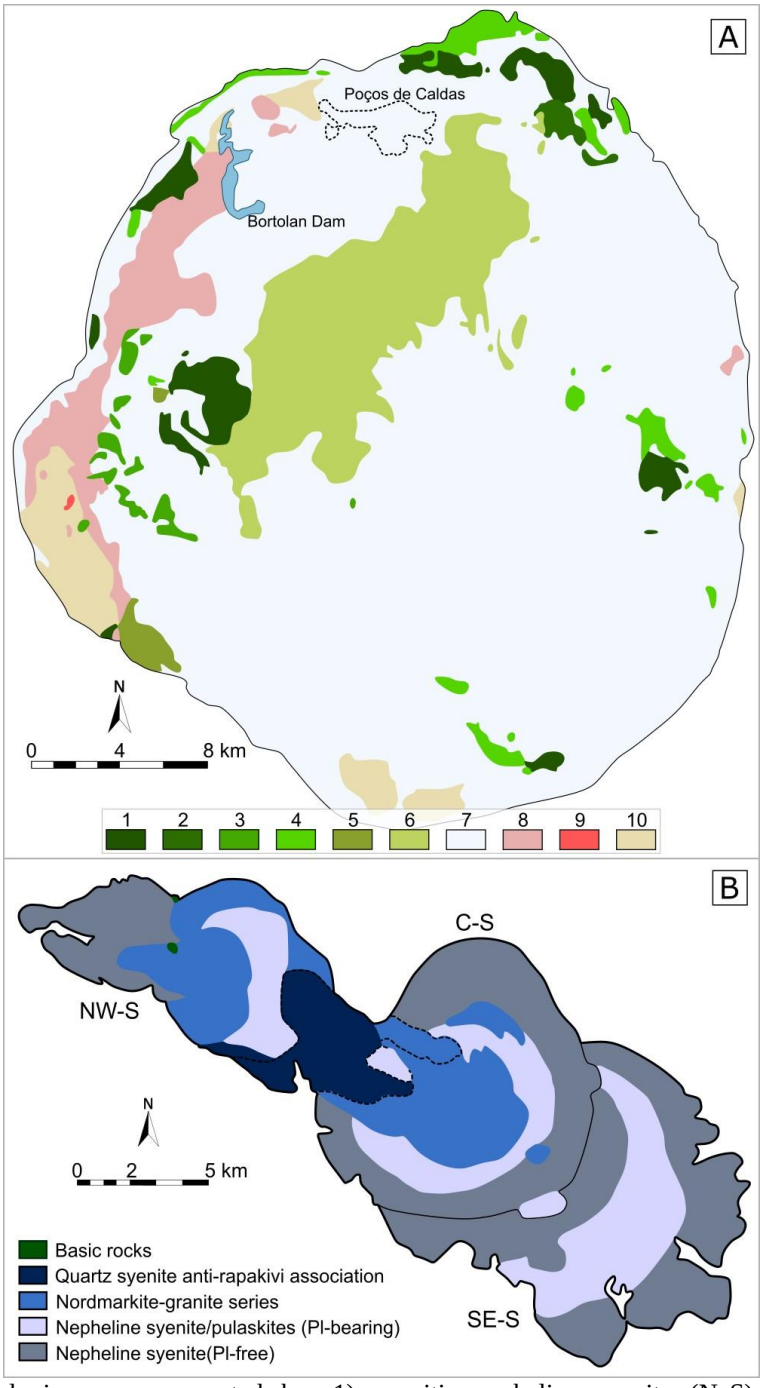

Legenda: Lithologies are represented by: 1) agpaitic nepheline syenite (NeS); 2) NeS with pseudoleucite; 3) porphyritic NeS; 4) gray NeS; 5) biotite-bearing NeS; 6) NeS, Pedreira type; 7) tinguaites and phonolites, undifferentiated; 8) volcaniclastic deposits (to the W, Vale do Quartel strip); 9) diabase, Serra Geral Formation; 10) sandstones and related sedimentary rocks, Paraná Basin; 11) undifferentiated basement.

Fonte: A) Modified from ULBRICH et al. (2005); B) Modified from ROSA AND RUBERTI (2018).

3.4.4.1.2 Passa Quatro Complex

The Passa Quatro Complex (*ca*. 165 km²) has a subcircular geometry and consists of a ring- and plug-like body (CHIESSI, 2004; GUARINO et al., 2019), featuring more silica-undersaturated and peralkaline rocks than the Itatiaia Complex itself (GUARINO et al., 2019). The complex predominantly comprises nepheline syenites, which are intruded by alkaline polymictic breccias and phonolite dikes. The nepheline syenite is medium to coarse-grained and has hypidiomorphic to slightly porphyritic textures. The mineral composition includes alkali feldspar and variable amounts of nepheline, with plagioclase occurring in some rocks. Mafic minerals such as amphibole, pyroxene, and biotite occur as accessories, and sodalite and analcime are rare (BROTZU et al., 1992; ENRICH et al. 2005; GUARINO et al., 2019). Locally cumulus or flow textures involving large alkali feldspar grains.

According to ENRICH et al. (2005), the phonolite dikes can be divided into three types based on texture and mineralogy. The first type has an aphanitic texture and contains sanidine, nepheline, clinopyroxene, amphibole, and titanite as the main minerals. The second type exhibits a porphyritic texture with phenocrysts of sanidine, biotite, opaque minerals, and occasional pseudoleucite, along with apatite and titanite as accessory minerals (miaskitic type). Lastly, the third type is also porphyritic, featuring phenocrysts of sanidine and nepheline, with clinopyroxene, amphibole, and titanite in a matrix of similar mineralogy (agpaitic type).

Few geochronological analyses have been reported regarding the Passa Quatro Complex. The $^{40}K/^{40}Ar$ age in amphibole from nepheline syenite yielded an age of 66.7 ± 3.3 Ma (RIBEIRO FILHO & CORDANI, 1966, recalculated by SONOKI & GARDA, 1988). The Rb-Sr isochron (whole-rock) showed an age of 70.43 ± 0.5 Ma (MONTES-LAUAR et al., 1995) and an age of 77 ± 3 Ma (BROTZU et al., 1992), both performed in nepheline syenites. The details of these data are in the Supplementary Material.

3.4.4.1.3 Itatiaia Complex

The Itatiaia complex (*ca.* 215 km^2) has a roughly NW-SE ellipsoidal body (Figure 4B) with an association of plug- or dike-type intrusions in the complex's external part

(MELLUSO et al., 2017), as well as moon-shaped units (ROSA & RUBERTI, 2018). According to these last authors, the intrusion can be subdivided into three sectors based on the association of structures and lithotypes: Southeastern Sector (SE-S), Central Sector (C-S), and Northwest Sector (NW-S).

The SE-S comprises nepheline syenites, biotite hornblende nepheline syenite, sodalite nepheline syenite, and aegirine nepheline foyaitic syenite, with miaskitic to agpaitic signatures, besides dikes of phonolite and nephelinite. The C-S has a ring-like structure, which was intruded in part of the southeastern sector, with a neck-like structure formed in the transition area to the northwestern sector. The sector shows nepheline syenite (with an agpaitic assemblage), nordmarkite, alkali feldspar granite, quartz alkali feldspar syenite, and trachytes. The NW-S comprises quartz and nepheline syenites, trachytes, monzonite, trachybasalt, and a metasomatized cumulative melagabbro with an unclear structure and intrusion relationships (ROSA & RUBERTI, 2018).

According to ROSA & RUBERTI (2018), the nepheline-bearing syenites comprise nepheline, alkali feldspar, clinopyroxenes, hornblende, biotite, titanite, apatite, zircon, titanomagnetite, sodalite and ± ilmenite. The agpaitic minerals locally observed are låvenite, hiortdahlite, astrophyllite, and catapleiite, with arfvedsonite and aegirine. Quartz-bearing syenites comprise mainly quartz, alkali feldspar, clinopyroxene, richterite/ferro-richterite, biotite, titanite, and titanomagnetite. Apatite, ilmenite and chevkinite can be observed.

The first geochronological analyses were carried out by AMARAL et al. (1967 and recalculated by SONOKI & GARDA, 1988), and have an average age of 68 Ma ($^{40}K/^{40}Ar$ age), using biotite (5) and barkevikite (1) from nepheline- and quartz syenites. Other $^{40}K/^{40}Ar$ data varied between 64.6 ± 1.0 and 90.5 ± 2.2 Ma and were obtained using different minerals of nepheline syenites (SONOKI & GARDA, 1988). More recent studies obtained from U-Pb data (zircon) yielded ages varying between 71.26 ± 0.29 to 67.47 ± 0.25 Ma, using several syenites (ROSA, 2017). See Supplementary Material for details.

3.4.4.1.4 Morro Redondo Complex

The Morro Redondo Complex (*ca.* 8 Km²) has a subcircular shape. VALENÇA et al. (1983) indicated a mineral zoning for syenitic mass. The central zone has slightly high

proportions of nepheline and amphiboles compared to the outermost zones (BROTZU et al., 1989).

The complex comprises syenites (nepheline- and alkali- with nepheline) and trachytic to phonolitic breccias (MOTA, 2012). Nepheline syenites are medium- to coarse-grained rocks and locally show inequigranular or cumulatic textures (BROTZU et al., 1989; MOTA, 2012). The main mineral is K-feldspar in ripiform euhedral crystals, while plagioclase and hornblende are also observed. Nepheline-bearing alkali syenites are coarse-grained and have cumulatic (BROTZU et al., 1989) and inequigranular textures. K-feldspar is the main mineral present in these rocks (*ca*. 75%), but hornblende, biotite, nepheline, titanite, apatite, and opaques are also observed. Trachytes have a porphyritic texture with aphanitic groundmass and K-feldspar phenocrysts. The groundmass comprises K-feldspar, clay minerals, opaques, and apatite. Xenoliths and iron oxides surrounding vugs can also be found in the trachytes (MOTA, 2012).

The $^{40}K/^{40}Ar$ age in amphibole from nepheline syenites yielded an age of 67.2 ± 4.0 Ma for the Morro Redondo Complex (RIBEIRO FILHO & CORDANI, 1966, recalculated by SONOKI & GARDA, 1988). BROTZU et al. (1989) analyzed biotite, amphibole, and whole-rock from syenites, alkali- and nepheline syenites, and phonolites. The study yielding $^{40}K/^{40}Ar$ ages between 68.0 ± 4.9 Ma and 79.8 ± 3.4 Ma. Additionally, hornblende $^{40}Ar/^{39}Ar$ data obtained from nepheline syenites yielded an age of 74.38 ± 0.50 (2σ) Ma (plateau age - MOTA, 2012). See Supplementary Material for details.

3.4.4.1.5 Tinguá Complex

The Tinguá Complex (*ca. 50* km²) with subcircular shape and the massif comprises syenites and phonolites. Nepheline syenite is a coarse-grained rock composed of K-feldspar and nepheline, with amphibole, titanite, apatite, and opaques as accessories. Phonolite is fine-grained, even microcrystalline-grained, and has a microporphyritic texture. Ripiform K-feldspar phenocrysts and square/hexagonal nepheline are observed, and acicular amphibole, opaques, and titanite occur as accessories (SILVA, 2019). Some earlier studies (*e.g.* SONOKI AND GARDA, 1988) refer to the presence of a rock type called tinguaite (as in other massifs of the PCCFA), although this term is now obsolete. The term was introduced by Rosenbusch in 1887 to describe the texture of a subvolcanic phonolite composed of alkali feldspar,

nepheline with or without other feldspathoids, aegirine, and sometimes biotite (LE MAITRE et al., 2002; ULBRICH et al., 2005).

The $^{40}K/^{40}Ar$ analyses yielded ages of 60.1 ± 2.6 Ma (mafic minerals) and 67.9 ± 3.9 Ma (biotite), both performed on nepheline syenite (AMARAL et al., 1967, recalculated by SONOKI & GARDA, 1988). These last authors also showed a $^{40}K/^{40}Ar$ date of 39.1 ± 3.4 Ma based on whole-rock analysis of tinguaite (phonolite). The U-Pb ages in zircons from nepheline syenites yielding ages of 67 ± 4 Ma, 64 ± 2 Ma, and 66 ± 3 Ma (SILVA, 2019). All these ages are in the Supplementary Material.

3.4.4.1.6 Mendanha

The Mendanha Complex (Figure 5A) is formed by morphological elevations, and two main intrusions are observed: 1) the Mendanha alkaline massif and 2) the Marapicu massif. The Mendanha massif comprises syenites embedded in gneisses and different types of porphyritic trachytes, breccias, lapillites, and agglomerates. Trachytic lavas intercalated with breccias in subhorizontal layers and pumps with sudden cooling surfaces are observed, suggesting mixed magmatism (SILVEIRA et al., 2005).

The Marapicu lithotypes are classified into two facie categories: 1) syenitic and 2) phonolitic. The syenitic facies comprise alkali feldspar, nepheline, plagioclase, and hornblende. Biotite, scapolite, muscovite, carbonate, zircon, apatite, augite, and opaque (mainly magnetite) are accessory minerals. The phonolitic facies are divided into two groups based on phenocryst contents: the first one is represented by phenocrysts of alkali feldspar, nepheline, and hornblende; the second one is composed of phenocrysts of sanidine and nepheline, with some occurrences of biotite phenocrysts (SILVA et al., 2015).

The $^{40}K/^{40}Ar$ dating of hornblende, biotite and groundmass range from 64.9 ± 1.6 to 74.9 ± 3.3 Ma (SONOKI & GARDA, 1988). Fission track data showed an age range of 65.3 Ma to 66.5 Ma (NETTO et al., 2005). According to MOTA (2012), the $^{40}Ar/^{39}Ar$ analyses yielded an age of 64.12 ± 0.40 (2σ) Ma of biotite (plateau age) and an age of 58.55 ± 0.45 Ma for a lamprophyre dike (whole-rock - plateau age). Other $^{40}Ar/^{39}Ar$ age studies were carried out in different minerals (hornblende, biotite, and phlogopite, or whole-rock), yielding ages varying between 54.2 ± 2.8 and 81.8 ± 1.8 Ma (DECKART et al., 1998; FERRARI, 2001;

SMITH et al., 2001). Detailed geochronological data can be found in the Supplementary Material.

Figure 5 – A) Geological map of the Mendanha Complex; B) Morro dos Gatos Alkaline Hill Geological map; C) Magmatic facies map of the Morro de São João Alkaline Complex; D) Geological map of Cabo Frio Island.

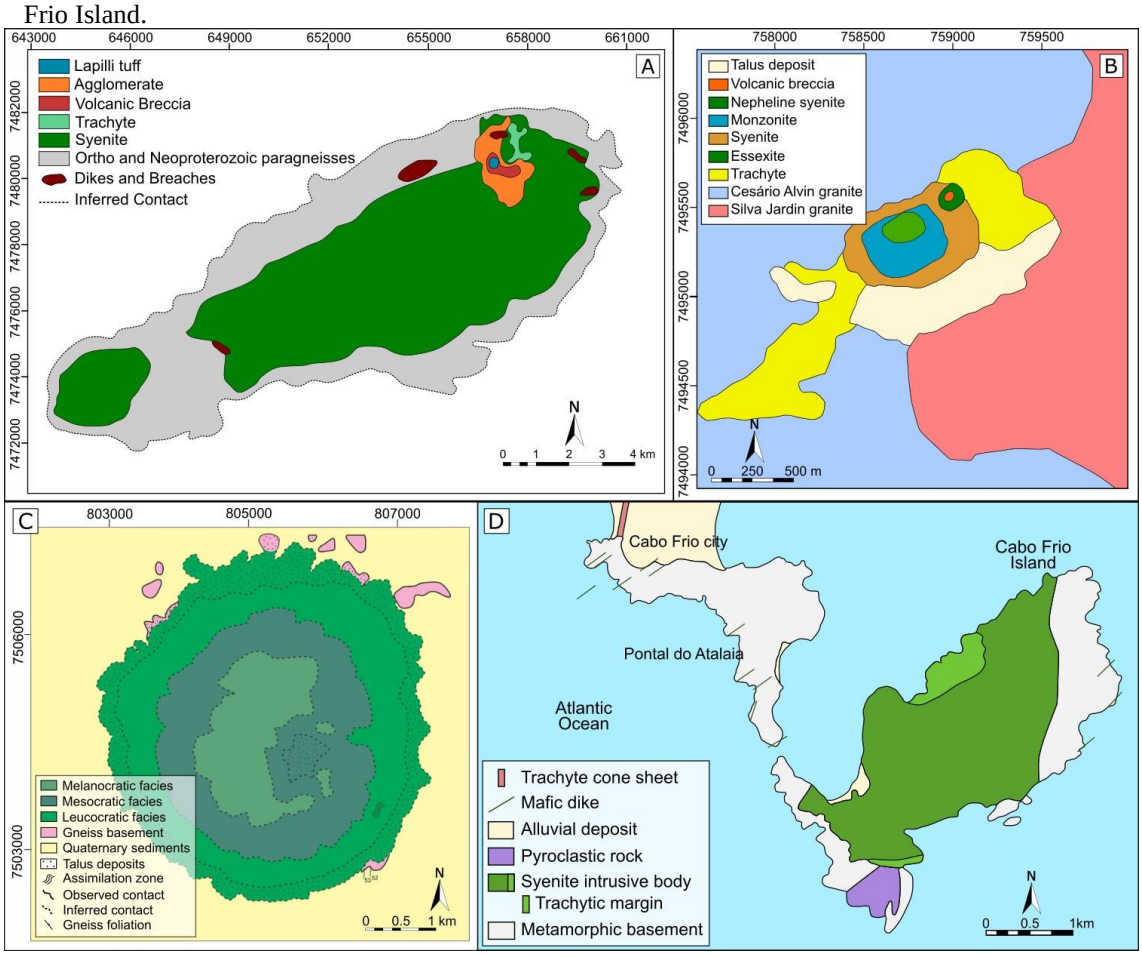

Fonte: A) Modified from MOTA (2012); B) Modified from MONTEIRO (2021); Modified from FAGUNDES (2020); B) Proposed by SICHEL et al. (2008) obtained in MOTOKI et al. (2008).

3.4.4.1.7 Tanguá

The Tanguá Complex (*ca.* 50 Km²) comprises syenites, volcanic breccias and dikes of trachyte and phonolite (MOTOKI et al., 2010). VALENÇA (1980) proposed a concentric division according to its mineralogical and textural characteristics, split into lower, middle, and upper syenite, besides the brecciated zones. The lowest zone is in contact with the metamorphic basement, has no pseudoleucite, and has the lowest content of nepheline, while

both increase toward the upper zone. Similar behaviors are observed for textural features towards the center. On the other hand, the content of orthoclase, biotite, and plagioclase decreases towards the upper zone.

Nepheline syenites are coarse-grained, with alkali feldspar, nepheline and amphibole as the main minerals, while magnetite, titanite and apatite occur as accessories (MOTOKI et al., 2010). Alkaline syenites have a porphyritic texture with alkali feldspar phenocrysts, and also comprise nepheline, amphibole, and biotite, with magnetite, titanite, and apatite as accessories (MOTOKI et al., 2010). Phonolite is observed as dikes, crosscutting syenitic bodies, or tabular xenoliths in the nepheline syenite magma (MOTOKI et al., 2010). Fluorite-bearing hydrothermal veins, often parallel to the dikes, are observed in the massif (SILVA et al., 2018).

The $^{40}K/^{40}Ar$ ages are 68.4 ± 2.3 Ma (amphibole) and 67.8 ± 1.9 Ma (K-feldspar), both from syenite (CORDANI & TEIXEIRA, 1979, recalculated by SONOKI & GARDA, 1988). The Rb-Sr whole-rock analyses yielded an intrusive age of 66.8 Ma for a nepheline syenite (MOTOKI et al., 2010). SILVA et al. (2018) used the (U-Th)/He method with fluorites from hydrothermal veins to obtain hydrothermal ages between 0.11 ± 0.02 Ma and 74.1 ± 2.8 Ma. The U-Pb analyses of zircon crystals from nepheline syenite yielded an age of 65 ± 1 Ma (2σ - SILVA, 2023). The Supplementary Material provides more details regarding the geochronological data.

3.4.4.1.8 Rio Bonito

The Rio Bonito Complex (*ca.* 29 km²) exhibits concentric zoning with lower, middle, and upper syenitic facies (VALENÇA, 1980). In the lower zones outcrops syenites with lower nepheline content and higher orthoclase content. The upper zone, however, consists of syenite richer in nepheline, making this massif zoning similar to Tanguá Complex. Additionally, magmatic breccias are exposed in the western portion of the massif.

The massif comprises nepheline syenite and alkali feldspar syenite, dikes of trachyte and phonolite crosscutting the others lithotypes, and volcanic breccias (SILVA et al., 2020). Nepheline syenites, the main rock types in the complex, are coarse-grained and comprise alkali feldspar and nepheline as major minerals and hornblende, clinopyroxene, biotite, opaques, titanite, apatite, and zircon as accessories. The alkali syenite without nepheline is

mainly found in the intrusion borders and the subvolcanic breccias outcrop in the western part of the massif (VALENÇA, 1980).

The first results of $^{40}K/^{40}Ar$ analyses of K-feldspars varied between 69.7 Ma and 83.9 Ma from nepheline syenite (AMARAL et al., 1967, recalculated by SONOKI & GARDA, 1988). The U-Pb analyses of zircon crystals from nepheline syenite yielded ages of 65.47 ± 0.60 Ma and 65.18 ± 0.60 Ma (SILVA et al., 2020). The $^{40}Ar/^{39}Ar$ dating showed similar results, yielding ages of 65.03 ± 0.70 Ma (biotite) and 65.03 ± 0.46 Ma (amphibole), both from nepheline syenite (SILVA et al., 2020). For additional information on the geochronological data, see the Supplementary Material.

3.4.4.1.9 Soarinho

The Soarinho Complex is mildly silica-oversaturated to saturated and is split into two zones: 1) the north zone (W-E orientation), which is composed of quartz-bearing syenites, quartz-bearing monzonite, and less saturated syenites; and 2) the south zone (N-S orientation), which comprises breccias and saturated syenites (VALENÇA, 1980). According to SONOKI & GARDA (1988), some rocks are described as nordmarkite.

The quartz syenites have porphyritic textures and fine- to medium-grained matrix with coarse phenocrysts (rounded orthoclase phenocrysts and plagioclase laths). Monzonites are medium- to coarse-grained rocks with mesocratic characteristics and comprise plagioclase, K-feldspar, and biotite as major minerals and quartz as accessory. The alkali-feldspar syenite is medium- to coarse-grained, mainly composed of anhedral to ripiform K-feldspar, with amphibole and opaque minerals as accessories (SILVA et al., 2023).

The $^{40}K/^{40}Ar$ aging (biotite) of nordmarkite yielded a result of 61.8 ± 2.5 Ma (CORDANI & TEIXEIRA, 1979, recalculated by SONOKI & GARDA, 1988). The U-Pb ages using zircon crystals are 58 ± 2 Ma for quartz syenite, 60 ± 2 Ma for monzonite, and 58 ± 2 Ma for alkali-feldspar syenite (SILVA et al., 2023). See Supplementary Material for details.

3.4.4.1.10 Morro dos Gatos Alkaline Hill

The Morro dos Gatos Alkaline Hill (less than 0.5 km² - Monteiro, 2021) is a semicircular outcrop (Figure 5B), with rocks showing a varying concentric shape (alkaline gabbros) towards the core (biotite syenites - MONTEIRO, 2021). According to GERALDES et al. (2013), the Morro dos Gatos body intrudes into the Silva Jardim granite, most of the hill, while the alkaline rocks outcrop in the western portion.

This latter portion consists of rocks that range from syenite to monzonite, characterized by coarse grain size, equigranular texture, and the absence of evident mineral orientation. Trachyte occurs in two generations: the first is found in the western portion and its abrupt contact with other rocks indicates that this rock is not associated with a lava flow or dike; the second is associated with dikes that cut through the main intrusion. Breccia dikes are also observed cutting through the Morro dos Gatos body (GERALDES et al., 2013).

The same authors indicate that the alkaline rocks of the massif are primarily composed of alkali feldspar, plagioclase, clinopyroxene, and biotite, with quartz, apatite, and magnetite occurring as accessory minerals. Additionally, nepheline and amphibole are not found. No previous geochronological studies have been conducted on the alkaline rocks of the Morro dos Gatos Complex.

3.4.4.1.11 Morro do São João Alkaline Complex

The Morro de São João Alkaline Complex (MSJ – *ca.* 10 km²) has circular shape (Figure 5C) and conical body with *ca*. 4 km diameter, with the top dissected by weathering processes. FAGUNDES (2020) proposed a magmatic faciological map of the MSJ, which presents three main facie types 1) leucocratic facies, 2) mesocratic facies (with mingling features), and 3) melanocratic facies.

The complex mainly comprises melanocratic nepheline syenites (shonkinite) and nepheline syenites, subordinate clinopyroxenites, and alkaline gabbros (BROTZU et al., 2007). The melanocratic nepheline syenites and nepheline syenites are crosscut by thin tabular intrusions, ranging from phonotephrite to phonolitic compositions, while the mafic-ultramafic rocks are classified as cumulates. The cumulate rocks have clinopyroxene, apatite, titanite,

and Ti-magnetite as cumulus phases, and the intercumulus phases are biotite, amphibole, alkali feldspar, and nepheline (< 1 vol%). The alkali gabbros have less clinopyroxene, apatite, titanite, and Ti-magnetite. The felsic phases include plagioclase as an early phase and alkali feldspar as interstitial minerals. The felsic rocks are alkali syenites and nepheline syenites and comprise interstitial nepheline and alkali feldspar with rare plagioclase cores. The accessory phases are titanite, apatite, Ti-magnetite, and melanite garnet.

The $^{40}K/^{40}Ar$ data indicated an age of 61.6 ± 1.5 Ma for nepheline syenite whole-rock and an age of 60.1 ± 2.1 Ma using K-feldspar from malignite (AMARAL et al., 1967, recalculated by SONOKI & GARDA, 1988). MOTA (2012) reported a $^{40}Ar/^{39}Ar$ age of hornblende from nepheline syenite of 64.86 ± 0.61 Ma. See Supplementary Material for details.

3.4.4.1.12 Cabo Frio Island

The Cabo Frio Island (Figure 5D) is the easternmost complex and comprises nepheline syenite and alkaline syenite plutons, which are crosscut by phonolite, trachyte, lamprophyre dikes, and subvolcanic breccia (MOTOKI et al., 2013). According to these authors, the main rock in the massif is coarse-grained nepheline syenite, which comprises alkaline feldspar, nepheline, clinopyroxene, amphibole, and biotite as major minerals, with magnetite, titanite and apatite accessories. The alkaline syenite has similar major minerals, including alkali-feldspar, clinopyroxene and amphibole. Additionally, it is worth noting that host rock xenoliths show signs of plastic deformation.

Another rock linked to Cabo Frio Island is the pulaskite (nepheline-bearing alkali feldspar syenite – LE MAITRE et al.,2002). This lithotype is described as a medium-grained rock, with alkali feldspar and biotite as the main minerals, and smaller amounts of barkevikite, sodalite, and nepheline. Apatite, sphene, and magnetite occur as accessory minerals (AMARAL et al., 1967). The pyroclastic body of Cabo Frio Island is a subvolcanic conduit (SICHEL et al., 2008), which is heavily weathered (MOTOKI et al., 2008).

The $^{40}K/^{40}Ar$ geochronological data show ages of *ca*. 50 Ma and 52.6 ± 2.0 Ma for whole-rock tinguaites (phonolites), 54.0 ± 2.6 Ma for biotite from pulaskite, and 72.4 ± 2.9 Ma for alkali feldspar from tinguaite (AMARAL et al., 1967, recalculated by SONOKI & GARDA, 1988). The $^{40}Ar/^{39}Ar$ data yielded an age of 54.83 ± 0.35 Ma for biotite crystal from

nepheline syenite (MOTOKI et al., 2013). Refer to the Supplementary Material for further details on the geochronological data.

3.4.4.2 New geochronological data

This study contributes to the understanding of the PCCFA by providing new geochronological data (U-Pb and $^{40}Ar/^{39}Ar$) for the Itatiaia, Tinguá, and Morro dos Gatos massifs. The new ages are presented in the same order as in the previous section, from west to east, starting with the results from the U-Pb method and subsequently, where available, the data from the $^{40}Ar/^{39}Ar$ method. In addition to these data, the petrographic analysis results of the studied samples by U-Pb are also presented. All these ages, along with important information, are summarized in Table 3. For more detailed data of these ages, as well as to review the zircons analyzed using the U-Pb method, see the Supplementary Material.

For the Itatiaia massif, a sample of syenite (ITA 30A; Figure 6A) was studied using the U-Pb method. This rock is medium to coarse-grained, has inequigranular texture, and contains subhedral to anhedral crystals of perthitic feldspar, hornblende, and aegirine (Figure 6B). Minor minerals include biotite, titanite, and quartz, while zircon, apatite, and opaque minerals are identified as accessory minerals. The U-Pb analyses of the zircons yielded an age of 70.2 ± 2.7 Ma (MSWD = 0.2; P = 0.65 - Figure 6C).

The $^{40}Ar/^{39}Ar$ analysis was performed on biotite crystals from a biotite- and amphibole-bearing nepheline syenite sample (ITA 22A). This study obtained an age of 67.31 ± 0.78 Ma (MSWD = 1.5 - Figure 7A), slightly younger than the age determined by U-Pb. Compared to previously conducted geochronological analyses, the obtained ages for Itatiaia Complex fall within the same range, indicating consistency between the studies.

For the Tinguá massif, a nepheline syenite sample (TIG 04E; Figure 6D) medium- to coarse-grained and with gray color was studied using the U-Pb method. The rock is inequigranular and comprises subhedral to anhedral crystals of perthitic feldspar and nepheline (Figure 6E). Minor minerals include hornblende and aegirine, while accessory minerals include titanite, opaque, zircon, and apatite. The U-Pb results yielded an age of 69.3 ± 2.2 Ma (MSWD = 0.00021 - Figure 6F).

The $^{40}Ar/^{39}Ar$ study was conducted on hornblende crystals obtained from an amphibole- and biotite-bearing syenite (TIG-01). The analysis yielded an age of 71.55 ± 0.49

Ma (MSWD = 1.12 - Figure 7B), slightly older than the first age. When compared to previous studies, all the newly presented ages are older, suggesting that the massif formed earlier than previously known (*ca.* 3.5 Ma), primarily due to the Ar-Ar result.

Finally, a monzonite sample (MDG 03B; Figure 6G) with coarse-grained and equigranular texture and mesocratic feature was selected for the Morro dos Gatos massif. The rock predominantly comprises plagioclase, K-feldspar, biotite, and clinopyroxene, with quartz, apatite, and opaque minerals as accessory minerals (Figure 6H). The U-Pb analysis of zircons from this sample provided an age of 65.4 ± 2 Ma (MSWD = 1.13 - Figure 6I), marking the first age determination for this massif.

Table 3 – Summary table of the ages presented in this study for the Itatiaia, Tinguá, and Morro dos Gatos complexes, obtained using U-Pb and $^{40}Ar/^{39}Ar$ methods.

Complex	Method	Age (Ma)	Rock	Comment
Itatiaia	U-Pb	70.2 ± 2.7	Syenite	27 zircon grains were analyzed, and 18 grains were used to obtain the age
	$^{40}Ar/^{39}Ar$	67.31 ± 0.78	Nepheline syenite	Biotite grains were analyzed
Tinguá	U-Pb	69.3 ± 2.2	Nepheline syenite	27 zircon grains were analyzed, and 18 grains were used to obtain the age
	$^{40}Ar/^{39}Ar$	71.55 ± 0.49	Syenite	Hornblende grains were analyzed
Morro dos Gatos	U-Pb	65.4 ± 2	Monzonite	18 zircon grains were analyzed, and 8 grains were used to obtain the age

Figure 6 - A-C) Itatiaia Massif: A) Photograph of the sample analyzed by U-Pb; B) Photomicrograph of the sample showing the presence of alkali feldspar (fsp) associated with hornblende (hbl), titanite (ttn), and opaque minerals (opc); C) U-Pb Concordia age diagram of zircon crystals from Itatiaia Massif. D-F) Tinguá Massif: D) Photograph of the sample analyzed by U-Pb; E) Photomicrograph of the sample showing the presence of alkali feldspar and nepheline (ne) associated with apatite (ap); F) U-Pb Concordia age diagram of zircon crystals from Tinguá Massif. G-I) Morro dos Gatos Alkaline Hill: G) Photograph of the sample analyzed by U-Pb; H) Photomicrograph of the sample showing the presence of alkali feldspar, plagioclase (pl), biotite (bt), and opaque minerals; I) U-Pb Concordia age diagram of zircon crystals from Morro dos Gatos Alkaline Hill.

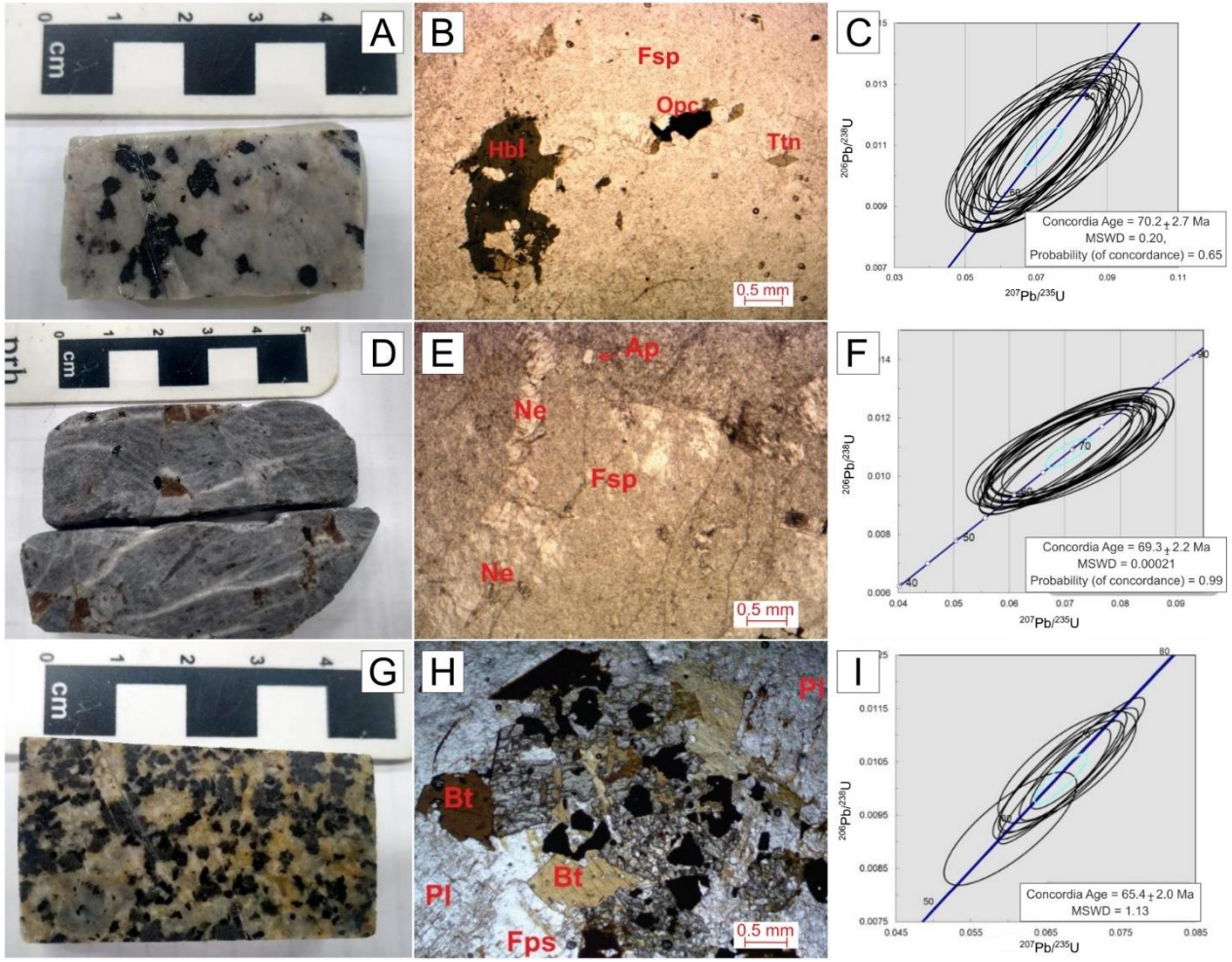

Figure 7 - $^{40}Ar/^{39}Ar$ step-heating diagram: A) Biotite of the Itatiaia massif; B) Hornblende crystal from the Tinguá massif.

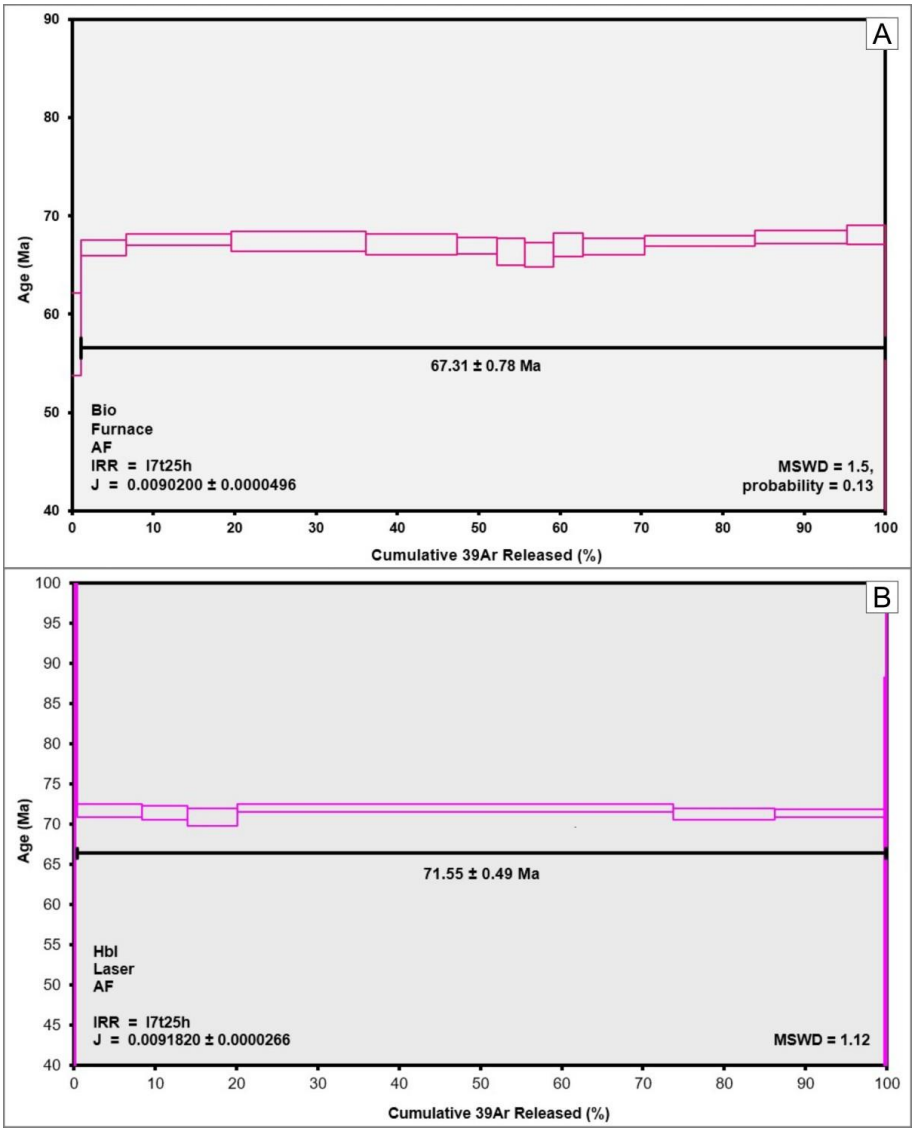

3.4.4.3 Lithogeochemistry

The lithogeochemical data gathered in this study are fully presented in the Supplementary Material. The total lithogeochemical results by lithology for each complex, along with classifications based on information provided by previous studies, are summarized in Table 4. However, to ensure the quality of the information, a filter was applied to the results when compared to the SiO_2 content. In these cases, samples were selected in which the oxides Na_2O and K_2O, in addition to silica, were not missing, and the total sum of the analyses was above 97%.

From various diagrams (Figure 8 to Figure 10), it can be observed that silica can be used to categorize rocks into two broad groups: 1) those with lower silica content (ranging from ca. 35 wt.% - to 50 wt.%); 2) those with higher silica content (ranging from 50 wt.% to *ca.* 75 wt.%). The less evolved rocks are associated with leucitite, tephrite, and basanite (Poços de Caldas Massif), and the more evolved ones are syenites and phonolites (GUARINO et al., 2021). Some rocks from the Itatiaia Massif exhibit high silica contents and can be classified as silica-oversaturated (ROSA & RUBERTI, 2018).

Table 4 - Number of lithogeochemical samples classified by lithology for the PCCFA complexes. The samples classified in this table as “not defined” are associated with those presented as acronyms by the authors, which could not be directly categorized, and with results in which the samples were not classified individually. See the Supplementary Material for result details.

Rock/Lithotype	Complexes								
	Poços de Caldas	Itatiaia	Morro Redondo	Mendanha	Tanguá	Rio Bonito	Soarinho	Morro de São João	Cabo Frio Island
Nepheline syenite	49	37	12	0	0	0	0	2	22
Alkaline syenite	0	0	0	0	0	0	0	0	7
Quartz syenite	0	29	0	0	0	0	0	0	0
Phonolite	62	0	2	0	0	0	0	0	17
Monzonite	0	1	0	0	0	0	0	0	0
Lamprophyre	2	0	0	0	0	0	0	0	0
Leucitite	8	0	0	0	0	0	0	0	0
Tephrite	9	0	0	0	0	0	0	0	0
Basanite	3	0	0	0	0	0	0	0	0
Foidite	0	4	0	0	0	0	0	0	0
Mafurite	0	1	0	0	0	0	0	0	0
Trachyte	0	4	4	0	0	0	0	0	7
Melagabbro	0	1	0	0	0	0	0	0	0
Not Defined	0	5	6	10	16	23	16	13	11
Total Complex	133	82	24	10	16	23	16	15	64

In the TAS diagram (Figure 8) the less evolved samples predominantly plot within the tephrite/basanite or foidite fields, with a smaller number in the phono-tephrite, trachy-basalt, and basalt fields. Notably, these rocks, particularly those associated with the Poços de Caldas Complex, exhibit a positive correlation. On the other hand, the more evolved rocks are primarily classified as phonolite or trachyte, with some classified as tephri-phonolite, trachy-andesite, basaltic trachy-andesite, or rhyolite. A distinguishing feature of these silica-rich samples is that some rocks show positive correlations (e.g., Cabo Frio Island, between trachy-andesite and trachyte), but overall, most samples display a negative correlation. Another notable observation is a clear gap between the less evolved and more evolved rocks, with no intermediate results.

In the Harker diagrams for major elements (Figure 9), several correlations (mostly negatives) are observed compared to silica content. The Harker diagrams for TiO_2 and CaO show a negative correlation, with the less evolved rocks having a more vertical slope. For the Al_2O_3 diagram, the silica-depleted rocks exhibit a positive correlation, while the silica-enriched ones show a negative correlation. However, any interpretation of this behavior, along with the data dispersion for Na_2O and K_2O, should be approached cautiously because these oxides can be heavily influenced by the weathering of these rocks. Figure 10 presents Harker diagrams for trace elements relative to silica. In this case, in addition to the previously mentioned filter, trace element analyses with concentrations significantly higher than the others (possible outliers) were excluded to avoid distorting the data's overall trends (see the Supplementary Material for the complete data). These results show a slight negative correlation in the less evolved rocks from Poços de Caldas for elements such as Rb, Sr, Zr, Y, and Nb. The data are more scattered for the more evolved rocks, but positive correlations can still be noted for Rb and Nb in the Itatiaia rocks.

Figure 8 - TAS diagram (Total alkali versus SiO_2) by LE BAS et al. (1986) for the major PCCFA alkaline complexes.

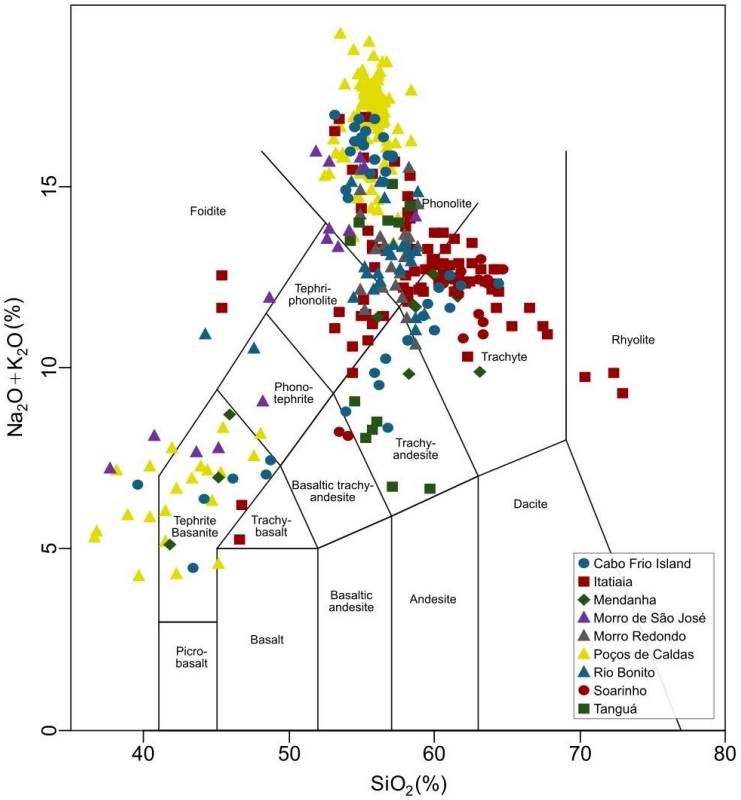

Fonte: Data from ARAÚJO (1995), GUARINO et al. (2021), MOTA (2012), MOTOKI et al. (2013, 2015), ROSA & RUBERTI (2018), and SCHORSCHER & SHEA (1992).

The normalized diagrams (Figure 11 and Figure 12) are presented by complex, and in some cases, the results are divided into two figures to facilitate visualization. Additionally, the data are presented as ranges, showing the maximum and minimum values found for each lithology within each complex. This approach allows for clear observation of the variations in results reported in previous studies.

The trace elements normalized to the primitive mantle (MCDONOUGH & SUN, 1995) reveal negative anomalies for Ba, Sr, P, and Ti in the more evolved rocks (Figure 11). Positive anomalies are less frequent and are associated with Rb, Ba, Sr, Pb, and Zr. Certain elements show significant differences in the normalized data across lithotypes, such as Ba and Sr in the three lithotypes of the Itatiaia Complex, Ba in the nepheline syenite and phonolite, and Pb in the phonolite, both in the Poços de Caldas Complex. The less evolved rocks (lines - Figure 11B) exhibit low variation in element content, with notable U and Pb anomalies.

The REE normalized to the primitive mantle (MCDONOUGH & SUN, 1995 - Figure 12) indicate that all complexes are characterized by an enrichment in light REE (La_N/Yb_N =

5.0 – 230.2 and La_N/Sm_N = 2.4 – 450.3). The heavy REE displays distinct descending or ascending patterns, regardless of the specific alkaline complex. The Eu anomaly is the most prevalent and is be observed in nearly all complexes, with either negative or positive behavior in the more evolved rocks. Both the presence (negative and/or positive) and absence of the Eu anomaly can be observed within a single lithology of a single massif, such as in the nepheline syenites from the Cabo Frio Island, Itatiaia, Morro Redondo, and Rio Bonito complexes (see Supplementary Material). Significant differences in minimum and maximum values are also observed for certain lithotypes, such as the nepheline syenite and phonolite from the Poços de Caldas Complex, as well as among the different lithologies of the Itatiaia and Rio Bonito complexes. The less evolved rocks (lines - Figure 12B) show less variation in REE content, and Eu anomalies are rare.

Figure 9 – Harker's diagram for major elements (% by weight) for the major PCCFA alkaline complexes.

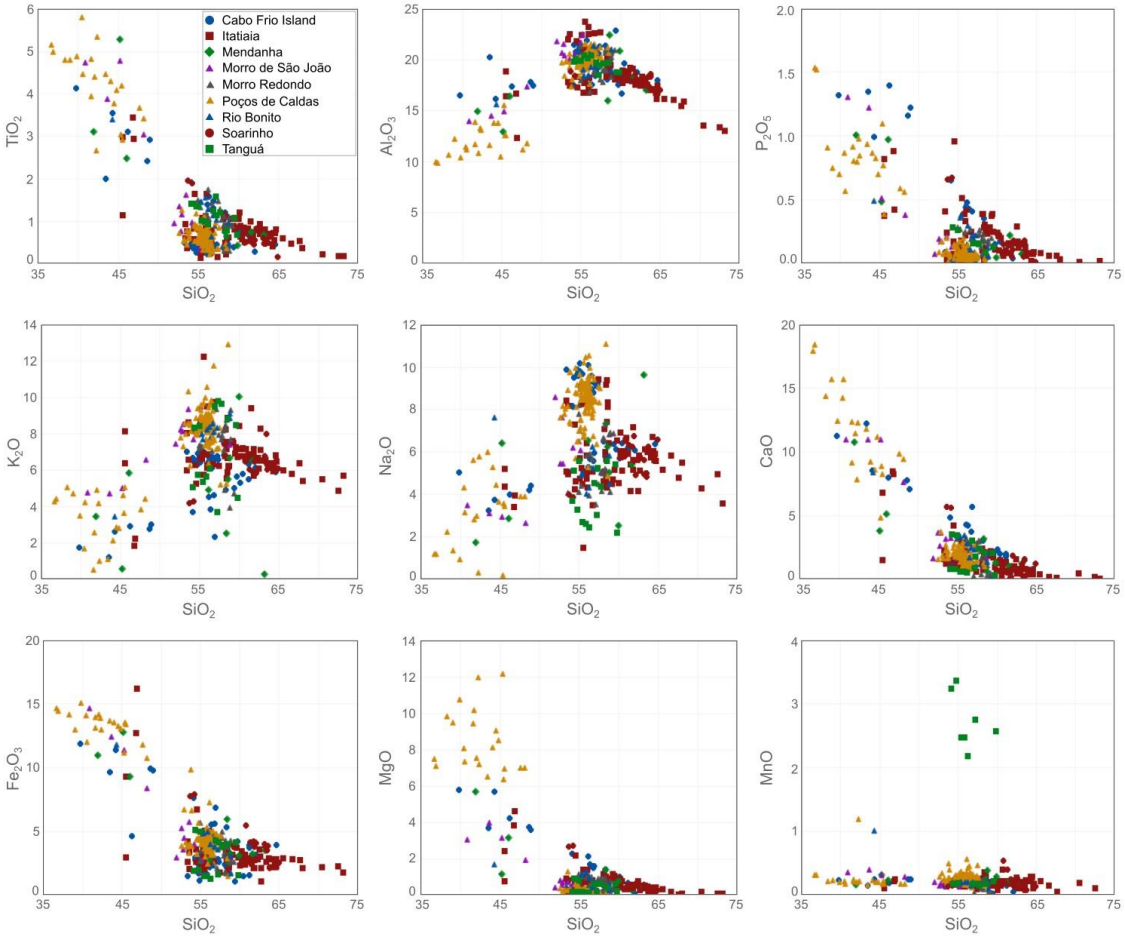

Fonte: Data were obtained by ARAÚJO (1995), GUARINO et al. (2021), MOTA (2012), MOTOKI et al. (2013, 2015b), ROSA AND RUBERTI (2018), SCHORSCHER AND SHEA (1992).

Figure 10 - Harker diagram for trace elements (ppm) for the major PCCFA alkaline complexes.

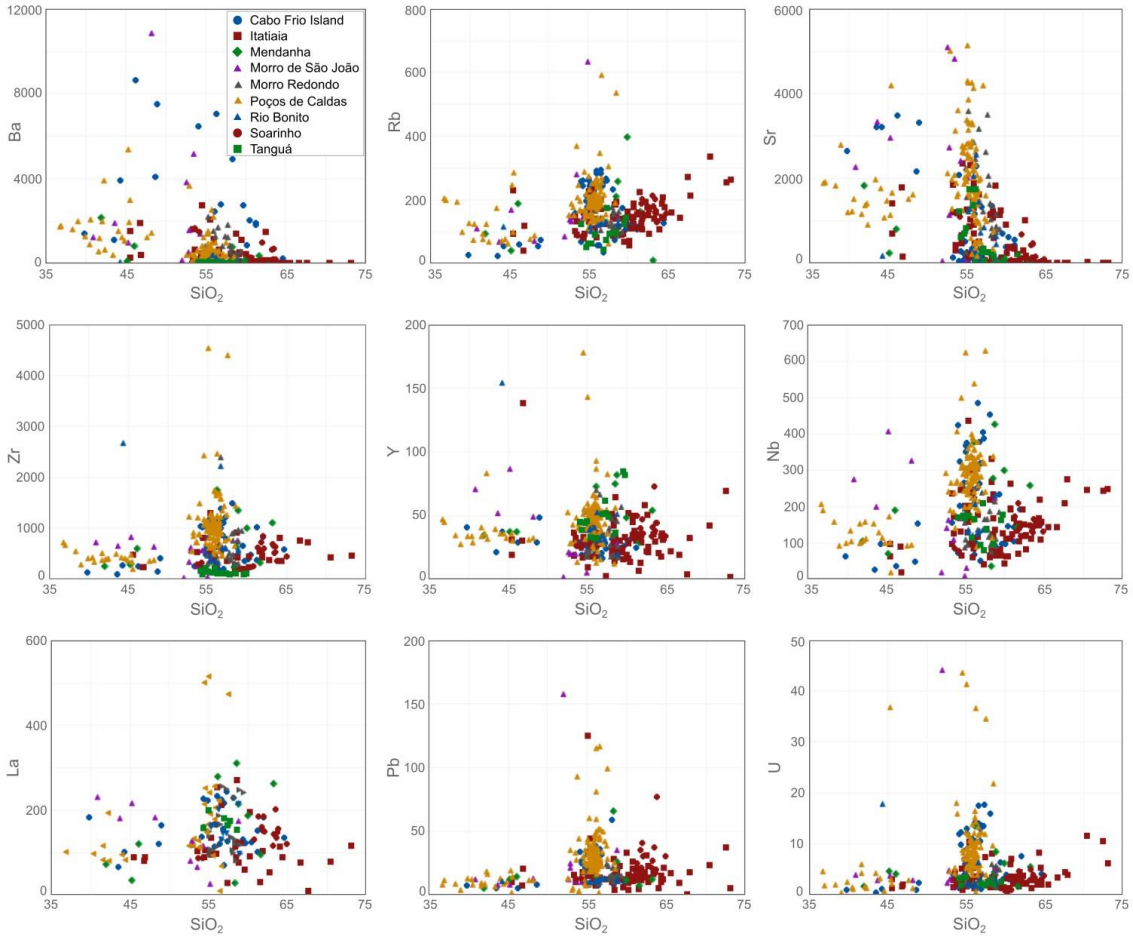

Fonte: Data from ARAÚJO (1995), GUARINO et al. (2021), MOTA (2012), MOTOKI et al. (2013, 2015), ROSA & RUBERTI (2018), and SCHORSCHER & SHEA (1992).

Figure 11 – Primitive Mantle normalized elements (MCDONOUGH AND SUN, 1995) for the mainly PCCFA alkaline complexes. A-B) Poços de Caldas complex; C-D) Itatiaia complex; E) Morro Redondo complex; F) Mendanha complex (according to MOTA (2012), all identified lithotypes on the massif were analyzed: syenites, trachytes, breccias, and lamprophyre dike. However, the author did not classify the samples by lithotypes); G) Tanguá complex; H) Soarinho complex. I) Rio Bonito complex; J) Morro do São João complex (according to MOTA (2012), all identified lithotypes on the massif were analyzed: syenites, malignite, shonkinite, and gabbro. However, the author did not classify the samples by lithotypes); and K-L) Cabo Frio Complex.

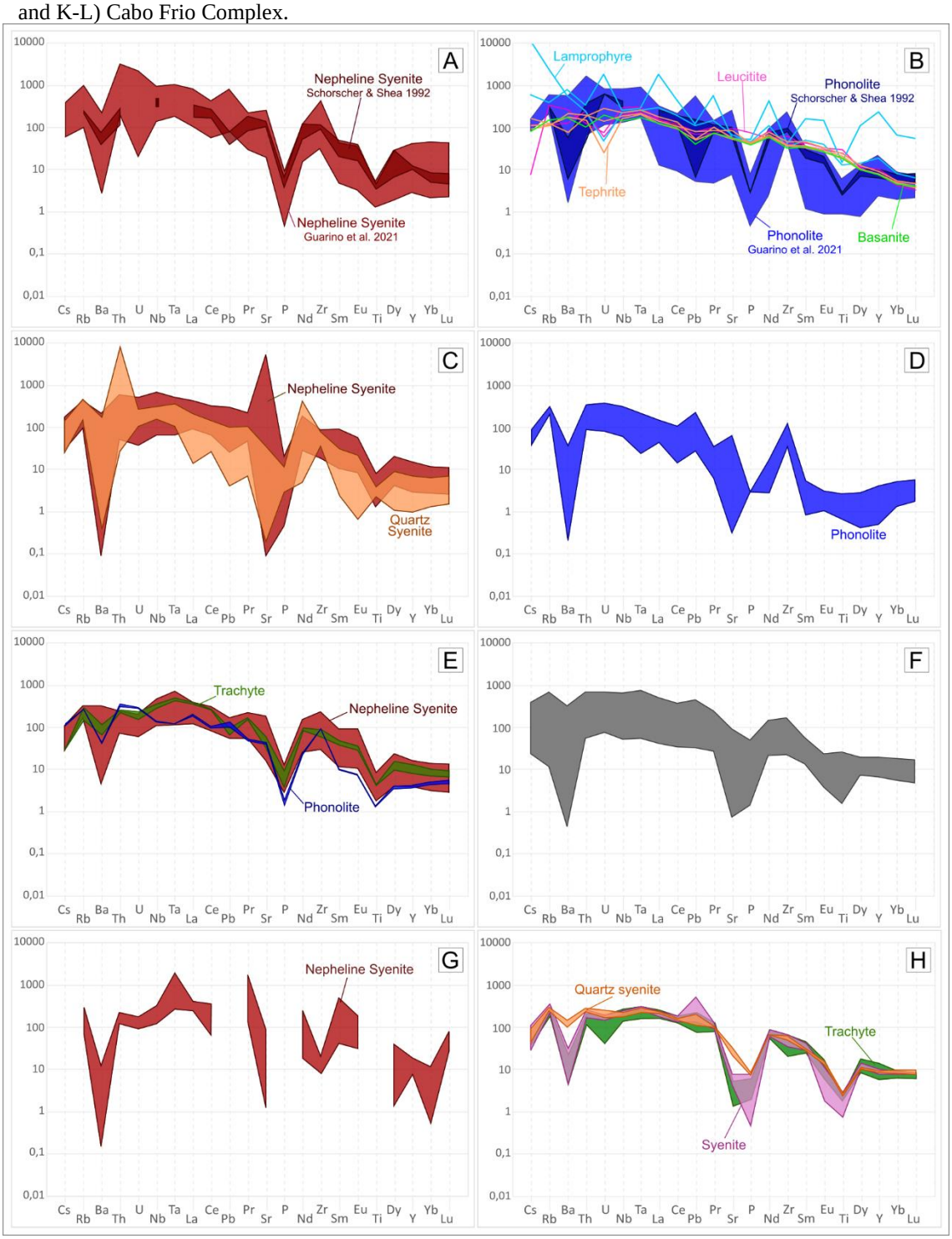

Fonte: The geochemical analyses were performed by GUARINO et al. (2021), MOTA (2012), MOTOKI et al. (2015b), ROSA (2017), SCHORSCHER AND SHEA (1992), and SILVA (2019).

Figure 11 (continued)

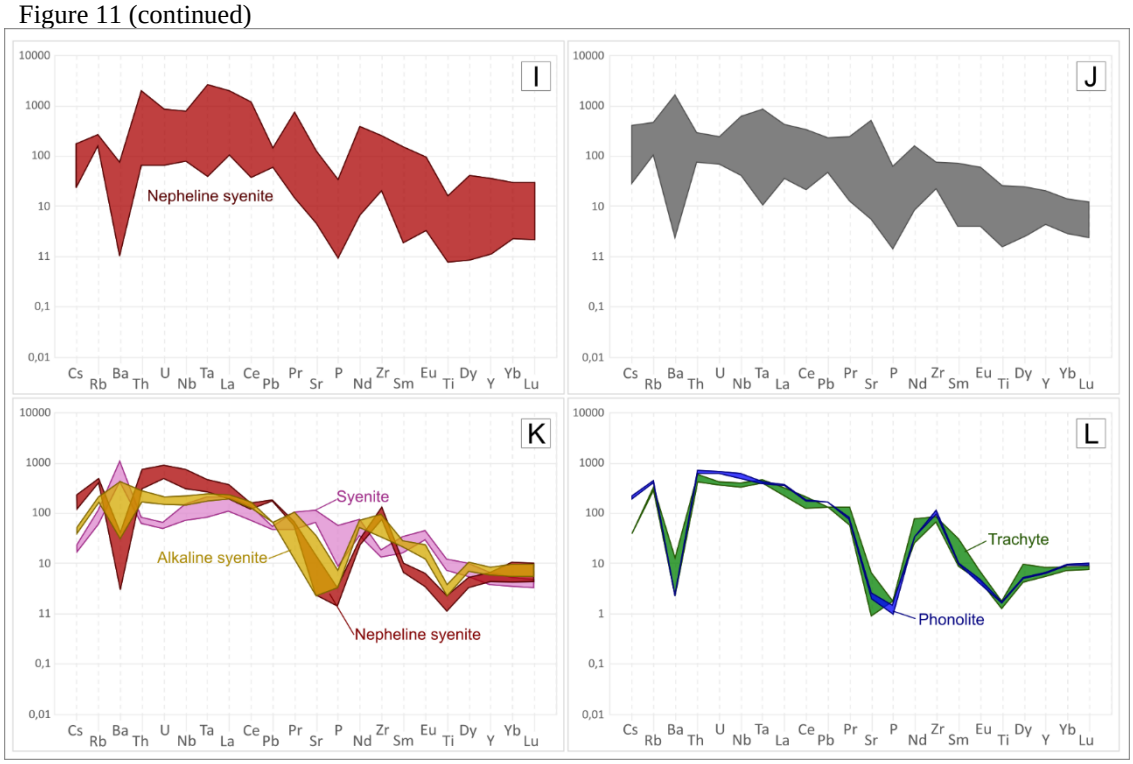

Figure 12 – Primitive mantle normalized rare earth elements (MCDONOUGH AND SUN, 1995) for the mainly PCCFA alkaline complexes. A-B) Poços de Caldas complex; C-D) Itatiaia complex; E) Morro Redondo complex; F) Mendanha complex (according to MOTA (2012), all identified lithotypes on the massif were analyzed: syenites, trachytes, breccias, and lamprophyre dike. However, the author did not classify the samples by lithotypes); G) Tanguá complex; H) Soarinho complex; I) Rio Bonito complex; J) Morro do São João complex (according to MOTA (2012), all identified lithotypes on the massif were analyzed: syenites, malignite, shonkinite, and gabbro. However, the author did not classify the samples by lithotypes); and K-L) Cabo Frio Complex.

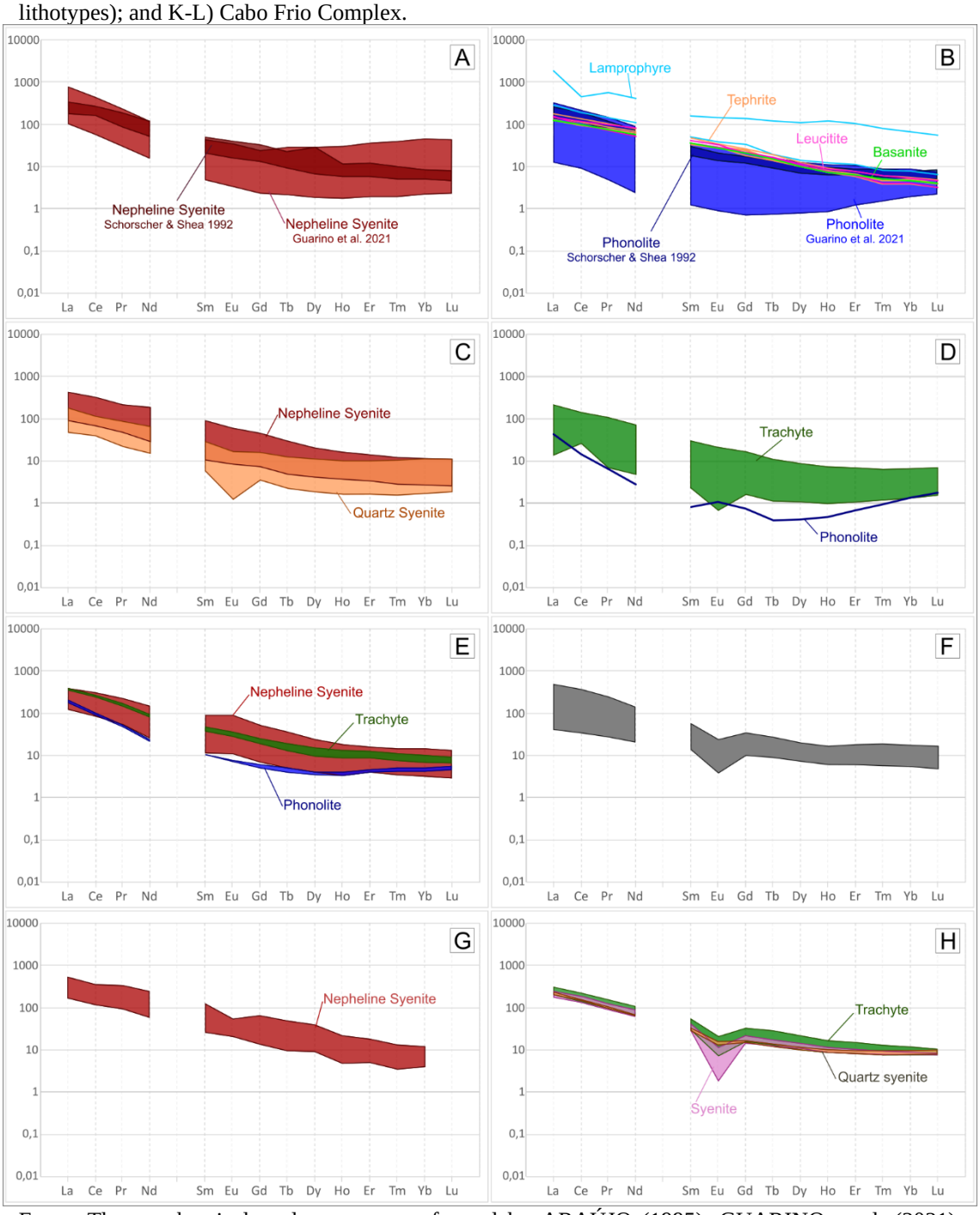

Fonte: The geochemical analyses were performed by ARAÚJO (1995), GUARINO et al. (2021), MOTA (2012), MOTOKI et al. (2015b), ROSA (2017), SCHORSCHER AND SHEA (1992), and SILVA (2019).

Figure 12 (continued)

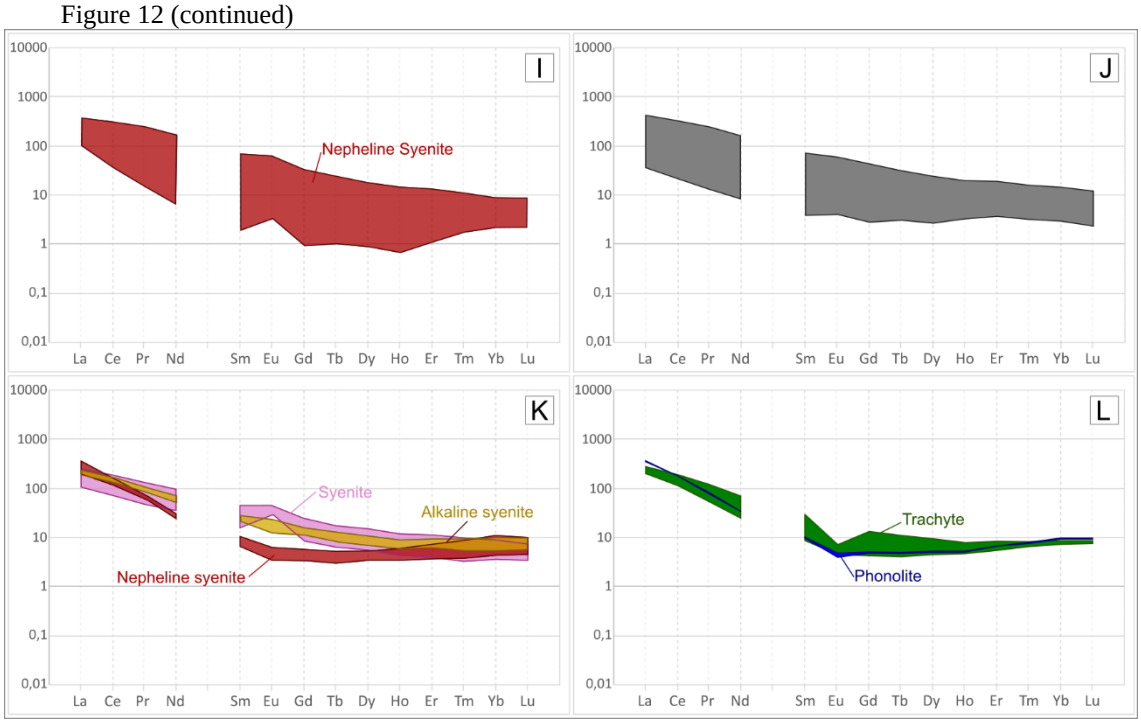

3.4.4.4 Isotopic Geochemistry

The compiled isotopic geochemistry data are provided in the Supplementary Material. Table 5 summarizes the data collected in this study, showing the number of isotope results per massif, along with their minimum and maximum values. Figure 13 presents a boxplot diagram of the analyses performed for the massifs. It can be observed that the $^{87}Sr/^{86}Sr_{(i)}$ ratios for the Mendanha and Tanguá complexes show the greatest variability, unlike the more consistent behavior of the other massifs. In contrast, the Morro Redondo, Poços de Caldas, and Morro de São João complexes are the only that display results classified as outliers. The largest variations for the $^{143}Nd/^{144}Nd_{(i)}$ ratios are associated with the Mendanha, Itatiaia, and Poços de Caldas complexes. At the same time, the smallest range is found in the Morro de São João and Morro Redondo complexes.

Table 5 - Summary of isotopic ratios ($^{87}Sr/^{86}Sr_{(i)}$ e $^{143}Nd/^{144}Nd_{(i)}$) for different massifs of the PCCFA. The table presents the number of data points collected and the minimum and maximum values. The data were obtained from the works of BROTZU et al. (2007), GUARINO et al. (2021), MOTA (2012), MOTOKI et al. (2010), ROSA (2017), SICHEL et al. (2012), THOMPSON et al. (1998), and ULBRICH et al. (2003).

Massif/Complex	$^{87}Sr/^{86}Sr_{(i)}$			$^{143}Nd/^{144}Nd_{(i)}$		
	Number	**Minimum**	**Maximum**	**Number**	**Minimum**	**Maximum**
Poços de Caldas	20	0.70443	0.70912	20	0.512360	0.512560
Itatiaia	14	0.70469	0.70643	18	0.512223	0.512560
Morro Redondo	9	0.70565	0.71042	9	0.512344	0.512400
Mendanha	12	0.70471	0.72347	14	0.512177	0.512600
Morro do São João	15	0.70490	0.70985	15	0.512333	0.512428
Soarinho	2	0.70492	0.70498	2	0.512460	0.512510
Tanguá	4	0.70620	0.71280	0	0.000000	0.000000
Rio Bonito	4	0.70510	0.70520	0	0.000000	0.000000
Cabo Frio	4	0.70419	0.70490	3	0.512420	0.512500

Figure 13 - Boxplot showing the variation in isotopic ratios ($^{87}Sr/^{86}Sr_{(i)}$ and $^{143}Nd/^{144}Nd_{(i)}$) for different massifs of the PCCFA.

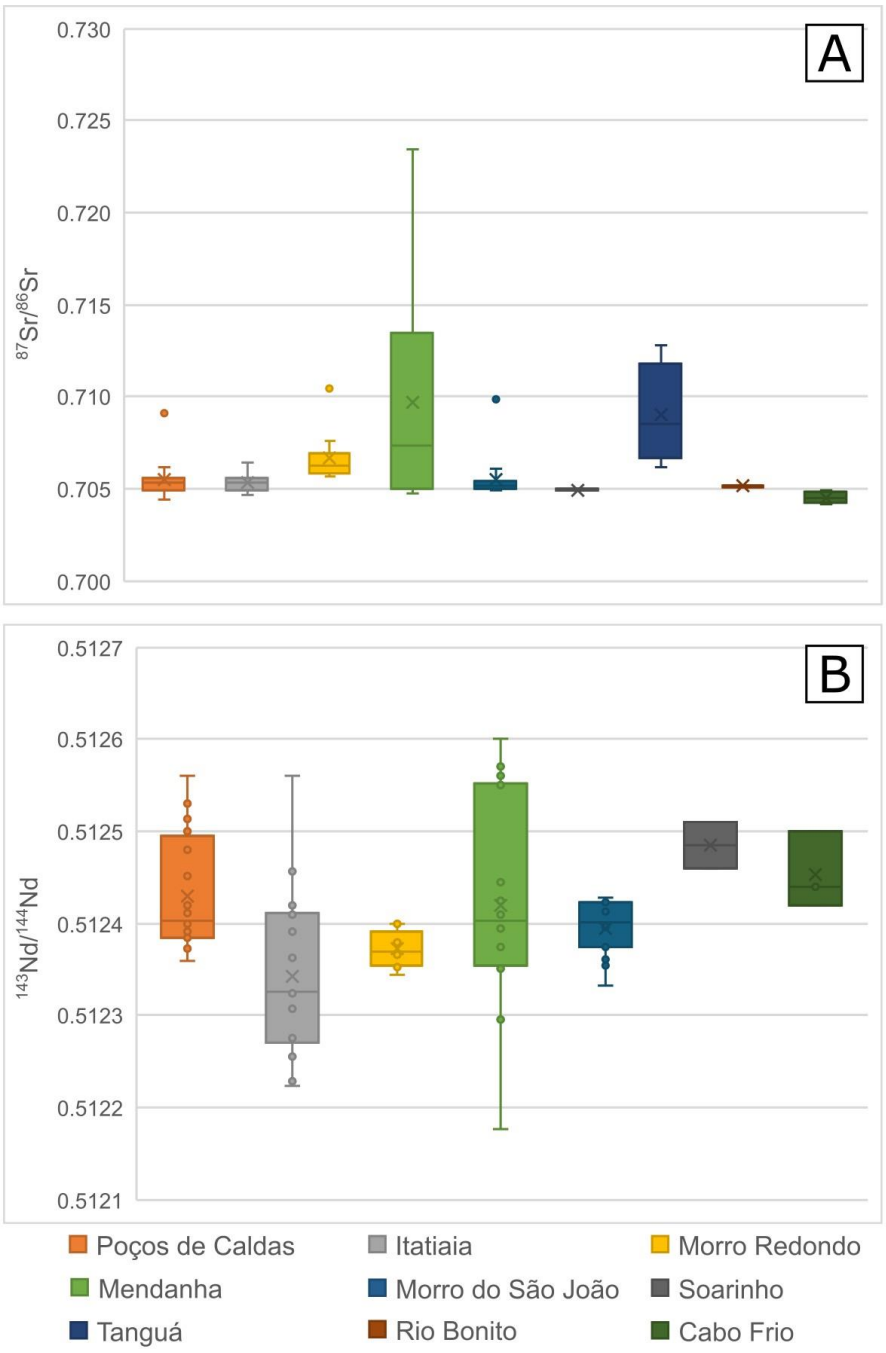

Fonte: The data were obtained from the works of BROTZU et al. (2007), GUARINO et al. (2021), MOTA (2012), MOTOKI et al. (2010), ROSA (2017), SICHEL et al. (2012), THOMPSON et al. (1998), and ULBRICH et al. (2003).

According to THOMPSON et al. (1998), the Poços de Caldas alkaline massif has $^{87}Sr/^{86}Sr_{(i)}$ ratios from 0.70474 to 0.70487, $^{143}Nd/^{144}Nd_{(i)}$ ratios from 0.51243 to 0.51246, and ε_{Nd} from - 2.14 to - 1.43. Additionally, GUARINO et al. (2021) studied different lithotypes of

the Poços de Caldas Complex: the nepheline syenites have $^{87}Sr/^{86}Sr_{(i)}$ ratios ranging between 0.70503 and 0.70540, and ε_{Nd} between - 3.9 and - 2.5; the phonolites have $^{87}Sr/^{86}Sr_{(i)}$ data varying from 0.70511 to 0.70527 and ε_{Nd} from - 3.4 to - 3.2; and basic-ultrabasic lavas have a slightly less radiogenic $^{87}Sr/^{86}Sr_{(i)}$ ratios, ranging from 0.70440 to 0.70498 and ε_{Nd} from – 3.7 to – 1.2.

ROSA (2017) indicated that the Itatiaia Complex rocks have $^{87}Sr/^{86}Sr_{(i)}$ ratios ranging from 0.70469 to 0.70503 for the S-SE sector and 0.70533 and 0.70643 for the S-C and S-NW sectors, respectively. The $^{143}Nd/^{144}Nd_{(i)}$ ratios vary from 0.512409 to 0.512362 for the S-SE sector, and for the S-C and S-NW sectors, the values range from 0.512329 to 0.512223. The Morro Redondo Complex has $^{87}Sr/^{86}Sr_{(i)}$ ratios ranging from 0.70565 to 0.71042 and $^{143}Nd/^{144}Nd_{(i)}$ from 0.51234 to 0.51240 (MOTA, 2012). For Mendanha Complex, this last author indicated that the $^{87}Sr/^{86}Sr_{(i)}$ ratios vary between 0.70514 and 0.72347, $^{143}Nd/^{144}Nd_{(i)}$ between 0.512180 and 0.512445, and ε_{Nd} between - 8.99 and - 3.77. The dikes of Mendanha Complex have $^{87}Sr/^{86}Sr_{(i)}$ ratios ranging from 0.70455 to 0.70820, $^{143}Nd/^{144}Nd_{(i)}$ from 0.51250 to 0.51255, and εNd from - 0.85 to - 0.07 (THOMPSON et al., 1998).

The Tanguá massif has $^{87}Sr/^{86}Sr_{(i)}$ ratio between 0.7062 (MOTOKI et al., 2010; SICHEL et al., 2012), more radiogenic than Soarinho dikes, which have $^{87}Sr/^{86}Sr_{(i)}$ ratios of 0.70484 and 0.70494, $^{143}Nd/^{144}Nd_{(i)}$ ratios of 0.51247 and 0.51241, and ε_{Nd} of - 1.60 and - 2.86 (THOMPSON et al., 1998). For MSJ, moderate radiogenic ratios were obtained for the $^{87}Sr/^{86}Sr_{(i)}$ (between 0.7049 and 0.7061) and low for the $^{143}Nd/^{144}Nd_{(i)}$ (between 0.512361 and 0.512428). The ε_{Nd} values vary between - 4.03 and - 5.54 (MOTA et al., 2009). The Cabo Frio dikes have $^{87}Sr/^{86}Sr_{(i)}$ ratios ranging from 0.70404 to 0.70460, $^{143}Nd/^{144}Nd_{(i)}$ from 0.51239 to 0.51247, and ε_{Nd} from - 3.56 to - 1.90 (THOMPSON et al., 1998).

3.4.5 Discussion

The PCCFA Alkaline Province mainly comprises nepheline syenites, syenites, phonolites, and trachytes. GUARINO et al. (2019) suggest that the similarity between the massifs of this alignment in terms of major and trace elements may indicate mantle sources that are similar both geochemically and isotopically. The occurrence of less evolved rocks (leucitite, tephrite, and basanite) and more evolved ones (syenites, phonolites, and trachytes) in the same complex, such as Poços de Caldas, can be attributed to fractional crystallization

processes, as suggested by GUARINO et al. (2019). The most evolved rocks range from silica-undersaturated (nepheline syenite) to silica-supersaturated (quartz-syenite), which are associated with crustal contamination processes, allowing them to cross the thermal barrier, as observed in the Itatiaia and Soarinho complexes (*e.g.*, ROSA, 2017 and SILVA et al., 2023).

According to MOTOKI et al. (2015), several massifs have pyroclastic volcanic conduits, primarily filled with welded tuff breccia. These breccias, which are outcropped preferentially at the intrusion edges, are polymictic (containing massif and host-rock fragments) and may feature a syenitic matrix and compositional zoning of fragments (*e.g.*, Mota, 2012, and Silva, 2019). The increasing content of alkaline rock fragments closer to the intrusion suggests that some pulses intruded into coller alkaline rock, brecciating it.

Correlations between silica and oxides, such as TiO_2, and P_2O_5, may indicate the mineral fractionation of rocks, such as titanite and apatite. This further supported by trace element anomalies, such as Ba, Sr, Rb, and Zr. The same lithology within a massif can exhibit a wide range of values in normalized diagrams (Figure 11 and Figure 12), suggesting that the rocks may have undergone different evolutionary processes during the formation of the complexes. Studies like those by MOTOKI et al. (2015) and ROSA (2017) suggest the presence of crustal assimilation processes during emplacement, which could account for these variations. Additionally, the Eu anomaly is associated with europium's ability to replace Ca, indicating fractionation into plagioclase and suggesting distinct REDOX conditions in the magma crystallization. Hence, the presence of positive and negative anomalies in the PCCFA massifs (or even the absence of anomalies), within the same complex and lithology, reinforce the idea of changing conditions and plagioclase fractionation during the massif evolution (see Eu/Eu* in the Supplementary Material). For the slight compositional difference of less evolved rocks (normalized data) indicates similar sources and petrogenetic processes as suggested, as noted by GUARINO et al. (2021). Additionally, the U and Pb anomalies may indicate zircon fractionation, while the absence of the Eu anomaly suggests that plagioclase fractionation did not occur during the formation of these rocks.

Sr- and Nd-isotopic data from the PCCFA complexes show close ranges, with trends between DMM and EM1 or DMM and EM2 (Figure 14), suggesting pre-eruptive isotopic homogeneity and a source mixture. Some authors have linked the genesis of these massifs to the context of a broad lithospheric mantle (*e.g.*, RICCOMINI et al., 2005; GUARINO et al., 2021; and ULBRICH et al., 2003), an enriched mantle (*e.g.*, SILVA, 2019), or even a variable contribution of both depleted and enriched sources (GORDON et al., 2023). GUARINO et al. (2021) demonstrated that the difference observed for the Sr-Nd isotopic composition within

the PCCFA is associated with a lithospheric mantle rich in highly potassium-metasomatized liquid.

According to WILLBOLD & STRACKE (2010 and references therein), different continental crust types may be involved with magma generation from sources classified as Enriched Mantle (EM). Using Eu/Eu* and $^{87}Sr/^{86}Sr$ data, it is possible to infer the participation of either lower or upper continental crust. The authors argued that the involvement of crustal sediments associated with the oceanic crust plays a significant role in the formation of these enriched sources. This view is supported by ROSA (2017), who, based on Sr-Nd-Pb isotopic signatures, described a normal mantle from which melting influenced crustal contamination during its evolution.

Figure 14 – $^{143}Nd/^{144}Nd$ versus $^{87}Sr/^{86}Sr$ diagram of alkaline complexes associated with PCCFA for mantle source correlation. The isotopic data were obtained by BROTZU et al. (2007), GUARINO et al. (2021), MOTA (2012), ROSA (2017), THOMPSON et al. (1998), and ULBRICH et al. (2003).

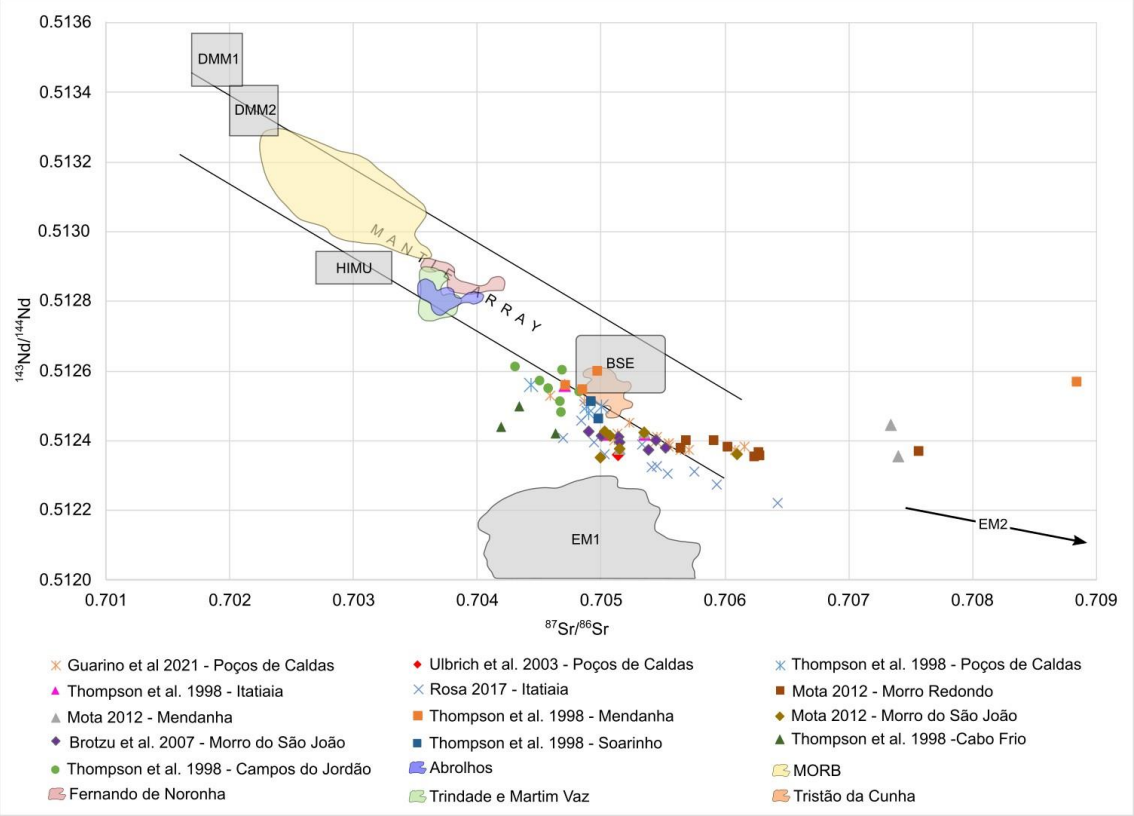

Fonte: Modified from MOTA (2012).

Although some authors emphasize that the PCCFA rocks are not cogenetic and not linked to mantle plumes (*e.g.*, RICCOMINI et al., 2005; GUARINO et al., 2021), certain features – such as possible decrease in age towards the east and specific isotopic signatures -

may indicate a plume-related origin (THOMPSON et al., 1998). Tomographic data reveal a potential correlation between onshore and offshore structures linked with shallow mantle plumes, further supporting this last model (CELLI et al., 2020). Regardless of the model, the structural control of magmatism in the South American alkaline provinces is evident. The relationship of these preexisting structures with the magmatic intrusions is supported by the dikes' and massifs' orientation and reinforced by similar structural fracture zones in the onshore and offshore contexts (RICCOMINI et al, 2005; SANTOS & HACKSPACHER, 2021).

Based on previous and new geochronological data, certain characteristics of the PCCFA genesis can be identified. The new U-Pb (70.2 ± 2.7 Ma) and $^{40}Ar/^{39}Ar$ (67.31 ± 0.78 Ma) ages of the Itatiaia massif fall within the intermediate range of previously published ones. On the other hand, the new ages obtained for the Tinguá massif by the U-Pb (69.3 ± 2.2 Ma) and $^{40}Ar/^{39}Ar$ (71.55 ± 0.49 Ma) methods are the oldest yet identified for the complex. Since U-Pb (Figure 3B) and $^{40}Ar/^{39}Ar$ (Figure 3C) data are still more restricted, $^{40}K/^{40}Ar$ results (Figure 3A) for a few samples were also used to complement the interpretations. These methods data of some massifs were combined in Figure 15A, which used previously published ages and new ones for several massifs (Poços de Caldas, Passa Quatro, Itatiaia, Tinguá, Tanguá, Soarinho, and Cabo Frio). Additionally, an aerial satellite image (Figure 15B), and a topographic profile (Figure 15C) display the distances between these massifs. The data show a possible age-decreasing trend (Figure 15A) from west (Poços de Caldas Complex) to east (Cabo Frio Complex), consistent with the stationary plume model (THOMPSON et al., 1998; and THOMAZ FILHO et al., 2005). However, some ages highlight the non-regressive age concept.

The Itatiaia and Tinguá complexes, located in the central portion of the alignment, show the oldest (90.5 ± 2.2 Ma) and youngest (39.1 ± 3.4 Ma) PCCFA ages published, respectively. Besides that, some Poços de Caldas Complex ages are contemporaneous with those of the Cabo Frio Complex, respectively the westernmost and easternmost massifs of the alignment. When considering only the U-Pb and $^{40}Ar/^{39}Ar$ ages (Figure 3), which are more precise and recent, contemporaneous results are observed for the Tinguá, Mendanha, Tanguá, Rio Bonito, Morro dos Gatos, and Morro do São João complexes (from west to east).

In summary, the geochronological data suggest no clear pattern of gradual decrease in age towards the eastern region, and massifs in different geographic locations may exhibit contemporaneous ages. The geochronological data variability for the same massif reinforces

the presence of different pulses during the complexes' emplacement, as suggested by Rosa & Ruberti (2018).

These geochronological characteristics imply that the PCCFA genesis cannot be associated with a conventional mantle plume (*e.g.*, Hawaii hotspot), with an evolution from west to east. An alternative hypothesis involves an unconventional plume that splits into distinct conduits, dividing in different directions, as suggested by COURLLIOT et al. (2003) and TSEKHMISTRENKO et al. (2021). These diffuse intrusions may have taken advantage of pre-existing structures to reach the surface, which could explain the observed age distribution and structural orientations. However, further studies are required to confirm that this new concept applies to the PCCFA, and this indication should be taken as a suggestion for further works.

Figure 15 – Image comparing the ages of the Poços de Caldas, Passa Quatro, Itatiaia, Tinguá, Tanguá, Soarinho, and Cabo Frio complexes, with the geographic positioning and topographic profile: A) The geochronological data were obtained by the $^{40}K/^{40}Ar$, U-Pb and $^{40}Ar/^{39}Ar$ based on the works: AMARAL et al. (1967); BIONDI (2005); BROTZU et al. (1989); BROTZU et al. (1992); BUSHEE (1971); DECKART et al. (1998); FERRARI (2001); MONTES-LAUAR AND PACCA (1988); MONTES-LAUAR et al. (1995); MOTA (2012); MOTOKI et al. (2013); RIBEIRO FILHO AND CORDANI (1966); SHEA (1992); SILVA (2019); SILVA et al. (2020, 2023); SONOKI AND GARDA (1988); TAKENAKA (2014); THOMPSON et al. (1998); ULBRICH et al. (2002); VLACH et al. (2003) and from present work; B) The geographical position of the selected complexes to indicate the distance between them and the position in the PCCFA context; C) Topographic profile evolution, from the Poços de Caldas Complex to the Cabo Frio Complex. The last two images were obtained from Google Earth Pro.

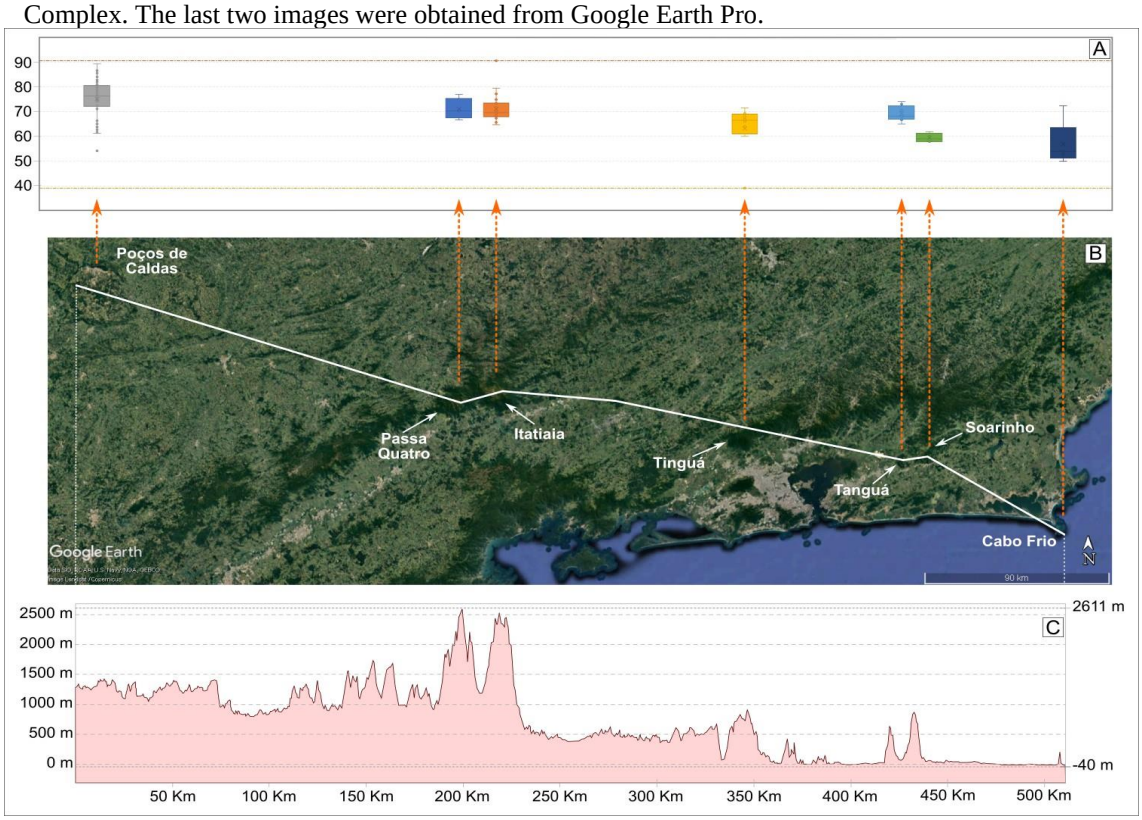

3.4.6 Concluding remarks

1. The PCCFA massifs have similar lithotypes, predominantly comprising nepheline syenites, syenites, phonolites, and trachytes, which are generally silica-undersaturated. However, some massifs are also composed of less evolved rocks, which present low chemical variability, suggesting similar sources and petrogenetic processes. The presence of silica-oversaturated rocks in the Itatiaia and Soarinho massifs may be linked to crustal contamination, indicating that the magma crossed the thermal barrier. This is reinforced by Sr-Nd-Pb isotopic signatures. The Eu anomalies for more evolved rocks suggest distinct REDOX conditions and different plagioclase fractionation behavior during the magma rise and the complexes' genesis, which is not observed in the less evolved rocks.

2. Isotopic data indicate a possible mixing of DMM and EM1 magma sources or DMM and EM2. The involvement of metasomatized rocks and crustal sediments is also associated with the genesis of the complexes' magma.

3. The new Tinguá massif ages (69.3 ± 2.2 Ma by U-Pb and 71.55 ± 0.49 Ma by $^{40}Ar/^{39}Ar$) indicated that it is older than previously thought. The Itatiaia geochronological data (70.2 ± 2.7 Ma by U-Pb and 67.31 ± 0.78 Ma by $^{40}Ar/^{39}Ar$) are consistent with earlier findings. Additionally, the first published age data for the Morro dos Gatos massif (65.4 ± 2 Ma using the U-Pb method) suggest a contemporaneous genesis with other massifs.

4. Although the geochronological data trend decreases gradually towards the east, the overall distribution indicates that the conventional stationary plume model may not fully explain the alignment genesis. A hypothesis for the first model is the presence of a mantle plume with distinct conduits, which used these regional structures for the massif emplacement, reinforcing the importance of these structures. However, further studies are required to confirm this suggestion for PCCFA genesis.

3.4.7 Acknowledgements

This work was supported by CNPq (ProTrindade Program) [Process number. 557146/2009-7]; the MCT/CNPq project [number 26/2009]; and FAPERJ [Entidades Estaduais 2018 number 210.297/2018; APQ1 2019 number 210.179/2019; JCNE 2022 number 201.469/2022]. The corresponding author thanks Rio de Janeiro State University for supporting and encouraging his research and FAPERJ for the doctoral fellowship. MSc. Marco Aurélio Maia Teodoro thanks Prof. Dr. Anderson and Prof. Dr. Luiz Bertolino for all the teaching, support, and suggestions during this work. All authors thank the journal's editors and reviewers.

4. RESULTADOS E DISCUSSÕES

Este item apresenta os resultados analíticos obtidos durante o trabalho de doutorado e que são expostos no artigo *Isotopic decoupling in the Nd-Hf systems from Cenomanian-Maastrichtian/Danian Tanguá Massif syenites: inheritance from sedimentary input into a metasomatized mantle,* submetido à revista Anuário do Instituto de Geociências. Neste artigo são expostas as informações petrográficas levantadas nas campanhas de campo e nos estudos de microscopia óptica e difratometria de raios X, além dos resultados litogeoquímicos, geocronológicos e de geoquímica isotópica. A partir destas informações é feita uma nova proposição de mapa litofaciológico, bem como são realizadas interpretações e contribuições no que tange a classificação das rochas e a petrogênese do complexo. Os resultados analíticos enviados pelos laboratórios são expostos entre o APÊNDICE A e o APÊNDICE G.

4.1 Artigo 2: Isotopic decoupling in the Nd-Hf systems from Cenomanian-Maastrichtian Tanguá Massif syenites: inheritage from sedimentary input into a metasomatized mantle.

Desacoplamento isotópico nos sistemas Nd-Hf dos sienitos do Maciço Tanguá do Cenomaniano-Maastrichtiano/Daniano: herança de entrada sedimentar em um manto metasomatizado

Marco Aurélio Maia Teodoro[1], Anderson Costa dos Santos[2], Luiz Carlos Bertolino[2,3] Claudio Valeriano[2], Mauro Geraldes[2], Henrique Bruno[2]

1 Universidade do Estado do Rio de Janeiro (UERJ), Faculdade de Geologia, Programa de Pós-graduação em Geociências. Rua São Francisco Xavier, 524 - 4° andar/bloco A, Rio de Janeiro (RJ), Brasil

2 Universidade do Estado do Rio de Janeiro (UERJ), Faculdade de Geologia, Departamento de Mineralogia e Petrologia Ígnea. Rua São Francisco Xavier, 524 - 4° andar/bloco A, Rio de Janeiro (RJ), Brasil. Grupo Tektos e Instituto GeoAtlântico, Universidade do Estado do Rio de Janeiro

3 Centro de Tecnologia Mineral, CETEM, Av. Pedro Calmon, 900, Cidade Universitária, 21941-908 Rio de Janeiro, Brasil

Abstract

The Tanguá Complex (TC) is an alkaline intrusion that is part of the Poços de Caldas-Cabo Frio Alignment (PCCFA), which has more than 25 intrusive bodies and follows a WNW-ESE trend, stretching over 1000 km in Brazil's southeast. This work brings a new perspective on the TC features and genesis based on new fieldwork mapping and mineralogical, petrographic, lithogeochemical, geochronological, and isotopic data. A new lithofaciological map is proposed for the Tanguá Complex, which is divided into five main parts: i) central nepheline syenite; ii) intermediate nepheline syenite; iii) syenite, the outermost part of the massif; iv) breccias; v) indivisible nepheline-bearing syenite. In addition, phonolites and trachytes occur as dikes crosscutting the complex. According to U-Pb geochronological data, the Tanguá Complex has two distinct age groups: an older one, with Cenomanian age, and a younger one, with Danian-Maastrichtian age (*ca*. 60-70 Ma), which is similar to previous studies. However, the first group has the oldest age (94.8 Ma - syenite) obtained for the massif and the PCCFA, suggesting that the conventional plume model may not be the most appropriate explanation for the province formation. Sr-Nd and Lu-Hf isotopic signatures indicate that the syenites and nepheline-syenites plot in the DMM-EMI array, while the phonolite in the DMM-EMII array. Several geochemical and isotopic correlations (e.g., SSI, Zr/TiO_2, REE sum, and ε_{Nd}) reinforce the significant role of crustal contamination during the massif's genesis. Additionally, the geochemical ratios Rb/Sr, Ba/Rb, and K/Rb suggest that the magma responsible for Complex genesis was metasomatized, which is also indicated for other massifs in the Alignment. The ratios of Th/Yb, Ba/La, U/Th, Th/La, and Sm/La, along with the Nd-Hf isotopic decoupling, indicate the involvement of oceanic sediments, which may be linked to EMI sources and confirm metasomatized melts. These features suggest that the magmas were generated with contributions from subducted slabs associated with the Brazilian Orogeny and Ribeira Belt formation, as indicated by the model ages obtained from Nd-Hf systems.

Keywords: Tanguá Alkaline Massif; U-Pb dating; Lu-Hf and Sm-Nd isotopes.

Resumo

O Complexo Tanguá (CT) é uma intrusão alcalina que faz parte do Alinhamento Poços de Caldas-Cabo Frio (APCCF), que possui mais de 25 corpos intrusivos e segue uma direção WNW-ESE, estendendo-se por mais de 1000 km no sudeste do Brasil. Este trabalho traz uma nova perspectiva sobre as feições e a gênese do CT com base em novo mapeamento de campo e dados mineralógicos, petrográficos, litogeoquímicos, geocronológicos e isotópicos. Um novo mapa litofaciológico é proposto para o Complexo Tanguá, que é dividido em cinco partes principais: i) nefelina sienito central; ii) nefelina sienito intermediário; iii) sienito, a parte mais externa do maciço; iv) brechas; v) nefelina sienito indivisível. Além disso, fonolitos e traquitos ocorrem como diques que cortam o complexo. De acordo com dados geocronológicos U-Pb, o Complexo Tanguá possui dois grupos com idades distintas: um mais antigo, com idade Cenomaniana, e um mais novo, com idade Daniano-Maastrichtiana (*ca*. 60-70 Ma), o qual é semelhante a estudos anteriores. O primeiro grupo, porém, possui a idade (94,8 Ma - sienito) mais antiga já obtida para o maciço e o APCCF, sugerindo que o modelo de pluma convencional pode não ser a explicação mais apropriada para a formação da província. As assinaturas isotópicas Sr-Nd e Lu-Hf sugerem que os sienitos e nefelina-sienitos são plotados no *trend* DMM-EMI, enquanto os fonolitos caem no *trend* DMM-EMII. Várias correlações geoquímicas e isotópicas (*ca*. SSI, Zr/TiO_2, soma de REE e ε_{Nd}) reforçam o papel significativo da contaminação crustal durante a gênese do maciço. Além disso, as razões geoquímicas Rb/Sr, Ba/Rb e K/Rb sugerem que o magma responsável pela gênese do complexo foi metassomatizado, o que também é indicado para outros maciços no alinhamento. As razões de Th/Yb, Ba/La, U/Th, Th/La e Sm/La, juntamente com o desacoplamento isotópico Nd-Hf, indicam o envolvimento de sedimentos oceânicos, os quais podem estar ligados a fontes de EMI e confirmam *melts* metassomatizados. Essas características sugerem que os magmas foram gerados com contribuições de placas subduzidas associadas à orogenia Brasiliana e na formação do Cinturão Ribeira, conforme indicado pelas idades do modelo obtidas dos sistemas Nd-Hf.

Palavras-chave: Maciço Alcalino Tanguá; Datação U-Pb; Isótopos Lu-Hf e Sm-Nd

4.1.1 Introduction

The Brazilian Platform hosts over a hundred alkaline complexes, ranging from the Permian-Triassic to the Paleogene age, which are mostly found in the mobile belts in the Paraná Basin edges, such as the Brasília and Ribeira Belts (ENRICH et al., 2005; HEILBRON et al., 2016; RICCOMINI et al., 2005; ROSA & RUBERTI, 2018). The latter regional geological feature presents a NE trend (HASUI et al., 1975; HEILBRON et al., 2000, 2004, 2008; TROUW et al., 2000) and it is formed by different units such as Archean to Paleoproterozoic basement, metasediment rock units from Paleo to Neoproterozoic Age and Neoproterozoic granites (HEILBRON et al., 2016). According to HEILBRON et al. (2020), the Ribeira Belt presents two distinct magmatic arc systems during its evolution, an internal one aged between 650 and 595 Ma and an external one with two stages of evolution, an intra-oceanic one aged between 860 – 760 Ma and a newer aged between 640 – 605 Ma, which is Japan arc-type. The stages associated with the external system add a considerable volume to the crust.

The Serra do Mar Province (SMP - ALMEIDA, 1983) shows alkaline massifs and dike swarms intruding the Proterozoic Ribeira Belt metamorphic terrains, which are associated with the Brasiliano Cycle fault-related magmatism (ALMEIDA, 1983; BROTZU et al., 2005; HACKSPACHER AND GODOY, 1999; MACHADO et al., 1996; HEILBRON et al., 2016). Riccomini et al. (2005) suggested a new division of the SMP into two provinces: 1) Serra do Mar following the Brazilian cost along the Santos fault, and 2) Poços de Caldas – Cabo Frio Alignment (PPCFA) corresponding to the northern portion of the previous SMP associated with structural rifting systems (ALMEIDA AND CARNEIRO, 1998; ALVES, 1996; ALVES AND GOMES, 2001; ALMEIDA, 1991; SADOWSKI AND DIAS NETTO, 1981).

The PCCFA is classified as a magmatic alignment with 26 intrusive centers and approximately 1,150 km long (Figure 16A-B). It covers part of southeastern Brazil and is formed by stocks, plugs, and dikes (ALMEIDA, 1986, 1983; ALMEIDA et al., 1996; Motoki et al., 2008; RICCOMINI et al., 2005; SILVA et al., 2018; THOMAZ FILHO AND RODRIGUES, 1999; MELLUSO et al., 2017; ROSA & RUBERTI, 2018). The origin of this region is still a topic of debate. Some researchers connect it to partial mantle melting due to the reactivation of existing fault systems (e.g., RICCOMINI et al., 2005) to a mantle plume beneath the continental crust (e.g., THOMPSON et al., 1998).

The Tanguá Complex (TC) is in Rio de Janeiro State, Brazil, and is an alkaline massif in the eastern part of PPCFA, near the Soarinho and Rio Bonito massifs (Figure 16B-C), which present similar lithologies and ages to TC. The complex comprises syenites, breccias, and dikes of phonolite and trachyte, which crosscut the syenitic rocks (MOTOKI et al., 2010). VALENÇA (1980) conducted detailed petrographic work and initially divided the massif into concentric zones based on mineralogy. Previous geochronological studies show that the TC rocks are between Maastrichtian and Danian Ages, between 65 Ma and 68.4 Ma (CORDANI AND TEIXEIRA, 1979; Silva, 2023; SONOKI & GARDA, 1988). However, further geochronological data and studies focusing on its petrogenetic evolution are still needed for the TC. MOTOKI et al. (2015b) proposed that crustal contamination processes played a crucial role in forming the massif, contributing an estimated 20% to 30%. SILVA (2019) showed that the Lu-Hf data indicated a mantle provenance for the Tanguá Complex, reinforced by the enrichment of light REE. Sm-Nd studies performed in other PCCFA massifs generally plot between depleted mantle (DMM) and enriched mantle I (EMI) or between DMM and enriched mantle II (EMII) components, suggesting a source mixture for the liquid provenance, demonstrating a variable composition before melt (*e.g.*, asthenospheric mantle, continental sediments, and SCLM - GUARINO et al., 2021; GORDON et al., 2023; RICCOMINI et al., 2005; SILVA 2015; 2019; ULBRICH et al., 2003). In addition, GUARINO et al. (2021) further reinforced the association of rocks from the PCCFA mantle rich in metasomatized fluids.

This paper is a detailed study of the Tanguá Complex aimed at making the previous petrographic and lithogeochemical studies more robust. It includes petrographic and mineralogical contributions and satellite image interpretations to delineate lineaments to propose a new lithofaciological map for the complex. This study presents a new perspective on massif formation by analyzing lithotype samples using lithogeochemistry data, new geochronological U-Pb ages, and isotopic geochemistry (Lu-Hf and Sr-Nd). The findings contribute to our understanding of the geological genesis of the massif and its implications for the PCCFA. This study also examines the potential connection between the formation of the Tanguá massif and metasomatized melts originating from subducted oceanic sediments, as well as a possible correlation with the regional structures of the Ribeira Belt.

4.1.2 Tectonic framework

The Ribeira Belt, along with the Brasília and Araçuaí Belts, is situated on the border of the São Francisco Craton in the southeastern region of Brazil. It is formed by a series of Brasiliano folds linked with granitogenesis and metamorphism, which have impacted Meso- to Neoproterozoic sediments and the Paleoproterozoic basement (ALMEIDA, 1976; HEILBRON et al., 2016). The Ribeira Orogen was formed by diachronous microcontinent collisions between 620 Ma and 510 Ma, developing structures with NW-verging (HEILBRON et al., 2016). The Ribeira Belt and part of the Brasília Belt, including the Socorro Nappe, the Apiaí Domain, and the Eastern Terrain, are affected by intrusions of alkaline bodies and dikes from the PCCFA. This last province is made up of nepheline syenites, syenites, quartz syenites, phonolites, and trachytes, which generally have a potassium affinity (MELLUSO et al., 2017; RICCOMINI et al., 2005; ROSA & RUBERTI, 2018; SILVA et al., 2018).

The PCCFA forms a curved WNW-ESE shape alignment, containing alkaline complexes and dike swarms aged between 84 and 39 Ma (RICCOMINI et al., 2005; ROSA & RUBERTI, 2018). This magmatism is linked to a transcurrent system reactivated during the breakup of the Gondwana continent (ENRICH et al., 2005; GUARINO et al., 2019) and is also associated with oceanic fracture zones (FZ), as suggested by SANTOS AND HACKSPACHER (2021 and references therein). The alkaline dikes related to the alignment are oriented according to the ENE to EW fault systems (BROTZU et al., 2005) and some complexes, such as Itatiaia (*e.g.*, ROSA & RUBERTI, 2018).

Two models are proposed for the complexes and dikes genesis of the PCCFA. The first model associates its genesis with the presence of a conventional mantle plume moving relatively from west to east, showing an age decreasing towards east (GIBSON et al., 1995; HERZ, 1977; SADOWSKI AND DIAS NETTO, 1981; THOMAZ FILHO et al., 2005; THOMPSON et al., 1998; VANDECAR et al., 1995). In this proposal, a plume with a head of approximately 600 km would have been located beneath the continental lithosphere of the Brazilian region, impinging it during the Cretaceous Period (CEULENEER et al., 1993; COURTNEY AND WHITE, 1986; WATSON AND MCKENZIE, 1991). The relative movement of the plume caused the intrusions to shift eastward, leading to the formation of the PCCFA extending to the Cabo Frio region (VANDECAR et al., 1995; THOMPSON et al., 1998). The second proposed model is associated with partial melting resulting from the

reactivation of pre-existing structures (ALMEIDA, 1991; ALVES et al., 2006; FERRARI, 2001; RICCOMINI et al., 2005; ZALÁN & OLIVEIRA, 2005). These studies have all highlighted the importance of these geological formations and their association with alkaline massifs and dike settings and concluded that the geochronological evidence does not support the existence of a conventional plume. In addition to this structural control, THOMAZ FILHO et al. (2005) also emphasized that the alkaline magmatism of the Brazilian Platform is related to the main onshore sedimentary basins, such as Taubaté, Resende and Volta Redonda Basins.

Figure 16 – A) Regional map of the southeast part of South America highlighting the link between the Paraná Basin and Alkaline occurrences and indicating the PCCFA positioning; B) PCCFA map with the associated regional geological structures; C) Geological map associated with Tanguá, Soarinho, and Rio Bonito massifs

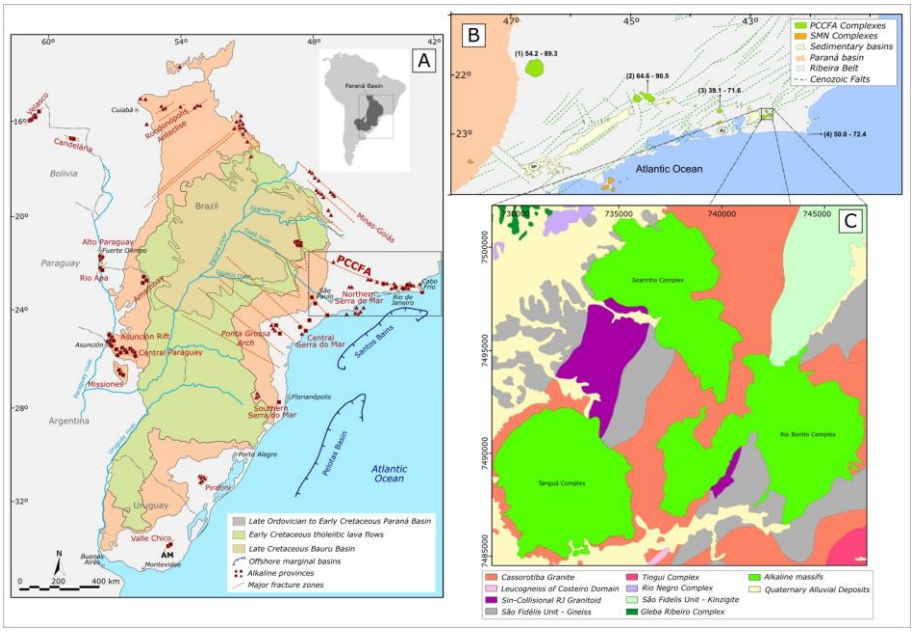

Legenda: Alkaline massifs (B): 1 - Poços de Caldas; 2 - Itatiaia; 3 - Tinguá; 4 - Cabo Frio Island.
Fonte: A) Modified from RICCOMINI et al. (2005); B) Modified from ROSA & RUBERTI (2018) and THOMPSON et al. (1998); C) Modified from HEILBRON et al. 2016

4.1.2.1 Tanguá Complex geological setting

The Tanguá Complex comprises leucocratic syenites, mostly feldspathic, and locally are observed breccia, phonolite, and trachyte. These rocks have similar mineralogy but differ in content and grain size. Additionally, *in situ* outcrops occur in the massif, but rounded fragments of several sizes are commonly observed.

VALENÇA (1980) proposed a concentric zoning of the massif into three parts, along with the magmatic breccia located in the eastern and southeastern parts of the intrusion. The central zone, the upper syenite, has a higher content of pseudoleucite and nepheline and a coarse-grained texture. All these features decrease towards the edges. In the lower syenite zone, which is in contact with the host rocks, pseudoleucite cannot be found, and nepheline is rare.

In addition to the main lithotypes, the massif presents dikes of phonolite and trachyte compositions, which crosscut all syenitic rocks (GERALDES et al., 2009; MOTOKI et al., 2010). The breccias are found in the massif's edges and crosscut the syenitic complex and basement rocks, associated with later magmatic conduits (GERALDES et al., 2013; HEINECK & RAPOSO,1981; MOTOKI et al. 2015a). Other lithologies within the massif do not exhibit any evident organization.

4.1.3 Materials and methods

The Tanguá Complex samples used in this study were collected during two fieldwork campaigns. The sample selection for the analyses considered the rock's representativeness and distribution in the massif, as well as the weathering degree. After being selected, the samples were prepared according to specific analysis requirements in two different laboratories: i) the Geological Sample Processing Laboratory (LGPA) located at the State University of Rio de Janeiro (UERJ) for petrography, geochemistry of the first field samples, geochronology and isotopic analyses; ii) and the Sample Preparation Laboratory of the SENAI Institute of Innovation in Mineral Processing (ISIPM) located in the Innovation and Technology Center (CIT) SENAI, for X-ray diffractometry, geochronology (zircon grains selection and mount) and geochemistry of the second field samples.

4.1.3.1 Lithogeochemistry

The studied samples were split into two stages according to the fieldwork campaigns. These analyses were performed in the ALS Laboratory (Canada) using Inductively Coupled

Plasma - Atomic Emission Spectrometry (ICP-AES), and the oxides/elements and their detection ranges are presented in Table 6. It is worth noting that the base metals were not analyzed for the samples from the second stage. In total, 26 samples of several lithologies were analyzed: 17 from the first field and 9 from the second field.

Table 6 – Elements studied by ICP-AES and the analyzable concentration ranges.

Major Oxides / Ranges (wt%)							
Oxides	Ranges	Oxides	Ranges	Oxides	Ranges	Oxides	Ranges
SiO_2	0.01 – 100	MgO	0.01 – 100	TiO_2	0.01 – 100	BaO	0.01 – 100
Al_2O_3	0.01 – 100	Na_2O	0.01 – 100	MnO	0.01 – 100	*LOI*	0.01 – 100
Fe_2O_3	0.01 – 100	K_2O	0.01 – 100	P_2O_5	0.01 – 100		
CaO	0.01 – 100	Cr_2O_3	0.002 – 100	SrO	0.01 – 100		

Traces elements / Ranges (ppm)							
Elements	Ranges	Elements	Ranges	Elements	Ranges	Elements	Ranges
Ba	0.5 – 10 000	Gd	0.05 – 1 000	Rb	0.2 – 10 000	U	0.05 – 1 000
Ce	0.1 – 10 000	Hf	0.2 – 10 000	Sm	0.03 – 1 000	V	5 – 10 000
Cr	10 – 10 000	Ho	0.01 – 1 000	Sn	1 – 10 000	W	1 – 10 000
Cs	0.01 – 10 000	La	0.1 – 10 000	Sr	0.1 – 10 000	Y	0.1 – 10 000
Dy	0.05 – 1 000	Lu	0.01 – 1 000	Ta	0.1–2 500	Yb	0.03 – 1 000
Er	0.03 – 1 000	Nb	0.2 – 2 500	Tb	0.01 – 1 000	Zr	2 – 10 000
Eu	0.03 – 1 000	Nd	0.1 – 10 000	Th	0.05 – 1 000		
Ga	0.1 – 1 000	Pr	0.03 – 1 000	Tm	0.01 – 1 000		

Base Metals / Ranges (ppm)							
Elements	Ranges	Elements	Ranges	Elements	Ranges	Elements	Ranges
Ag	0.5 – 100	Co	1 – 10 000	Mo	1 – 10 000	Sc	1 – 10 000
As	5 – 10 000	Cu	1 – 10 000	Ni	1 – 10 000	Tl	10 – 10 000
Cd	0.5 – 1 000	Li	10 – 10 000	Pb	2 – 10 000	Zn	2 – 10 000

4.1.3.2 Optical Microscopy

For the optical microscopy analysis, 11 samples were studied to identify mineral phases, textures, and structures, and these analyses were conducted at the ISIPM Microscopy Laboratory. The petrographic thin sections were made at LGPA, and the thickness and polishing improvement was performed at the ISIPM Laboratory when necessary. A Leica trinocular optical microscope, model DM-LP, equipped with various objectives (2.5x, 5x, 10x, 20x, and 50x) and a transmitted and reflected illumination system, was used for this study. A Motic digital camera, model Moticam 10.0, and its corresponding software were used to capture the photomicrographs.

4.1.3.3 X-ray diffraction

The analyses were carried out using the powder method on Shimadzu/LabX6000 equipment at the ISIPM X-ray Laboratory at CIT SENAI in Belo Horizonte/Brazil. The equipment has an X-ray tube with CuKα radiation (λ = 1.5418 Å) and a θ-2θ system, in addition to a 40 rpm sample rotational system and back loader holder to minimize the minerals' preferential orientation. For the study, a voltage of 40 kV and a current of 30 mA were used. The analysis range was from 5º to 80º (2θ), with a step of 0.01º (2θ), a speed of 0.5 degrees/minute, and a reading time of 1.2 seconds. The diffractograms obtained were compared and interpreted to identify and quantify the phases by the Rietveld method using the Match! Software.

4.1.3.4 Sr- and Nd- Isotope Analyses

The Laboratory of Geochronology and Radiogenic Isotopes (LAGIR) at UERJ in Rio de Janeiro, Brazil, analyzed five syenite samples and one phonolite using the Sr-Nd method. An aliquot of 25 to 50 grams of the previously pulverized sample was digested with acid (HCl and HF) in a clean room with a controlled environment, positive air pressure, and an air filtration system. For the analyses, a Thermal Ionization Mass Spectrometry (TIMS) multicollector, the TRITON model, was used (see Valeriano et al., 2003). The Sr and Nd separation method was carried out following the processes presented by Heilbron et al. (2013).

For Sm and Nd, the ionization process used a Re filament on a double support arrangement and measured 8 and 16 cycles, respectively. For Sr, the filament used was Ta, on a single support, and 10 cycles for measurement. The standard reference materials used were SRM-987 and JNdi-1 (Tanaka et al., 2000). Isotopic ratios were normalized to $^{146}Nd/^{144}Nd$ = 0.7219, $^{147}Sm/^{152}Sm$ = 0.5608 and $^{88}Sr/^{86}Sr$ = 8.3752. The GeoChemical Data ToolKit (GCDkit) software was used to process the measured data and obtain the other results.

4.1.3.5 U-Pb and Lu-Hf Analyses

For the analyses, the samples were submitted to grain size process adjustment processes to reduce particle size and then to magnetic separation processes with Frantz equipment to separate concentrates of different minerals in the LAGIR laboratory. After this last process, zircon grains were selected using a Leica microscope, model EZ4 from the ISIPM Microscopy Laboratory. These grains were glued to a 25 mm mold base with double-sided tape and subsequently mounted with epoxy resin. After drying, these mounts were ground and polished using sandpaper and diamond pastes to expose the grains.

The zircon grains were imaged using a Hitachi Scanning Electron Microscope, FlexSEM 1000 II model, with a Bruker EDS detector, at ISIPM/CIT in Belo Horizonte. The analyses were performed at the Multi-User Environment and Materials Laboratory (Multilab) in Rio de Janeiro, Brazil. Laser Ablation equipment from Thermo Scientific with Induced Plasma Mass Spectrometry (LA-ICP-MS), Neptune Plus model, were used for the analyses. Readings were acquired using the laboratory's internal standard before each analysis. According to the internal procedures, the first analysis stage used 14 zircon grains, while the second used 15. The analyses and reading conditions were fire mode continuous, with a frequency of 6 Hz and a spot size of 40 µm. Glitter software was used to process the data, and the Excel extension ISOPLOT (LUDWIG, 2003) was used to construct the Concordia-type diagrams (TERA & WASSERBURG, 1972).

4.1.4 Results

4.1.4.1 Preliminary surveys and correlation with previous work

A preliminary assessment of the structures was carried out based on previous TC works (*e.g.*, HEINECK & RAPOSO, 1981; MOTOKI et al., 2015a; SILVA, 2019; VALENÇA, 1980) and from other PCCFA complexes, such as Itatiaia (ROSA & RUBERTI, 2018) and Mendanha (MOTA, 2012; MOTOKI et al., 2008). ROSA & RUBERTI (2018) suggested that the alkaline complexes from PCCFA may have circular or half-moon structures

associated with different lithotypes or even distinct magmatic pulses. By analyzing satellite images using ArcGIS world imagery, circular or half-moon structures were identified in the Tanguá Complex, which helps in the initial massif categorization (Figure 17A). Additionally, repetitive linear structures corresponded to the four fracture families observed during the field campaign (Figure 16A-C).

Figure 17 – A) Map delimiting the Tanguá Complex contour (HEILBRON et al., 2016) on a satellite image (Base World Imagery) indicating the presence of half-moon, circular (light blue lines), and linear structures in the massif. Datum: WGS 1984 (UTM – Zone 23S); B) Ros diagram indicating families of fractures that coincide with regional structures according to colors; C) Schmidt great circles diagram with the same families of fractures indicating the directions and dips.

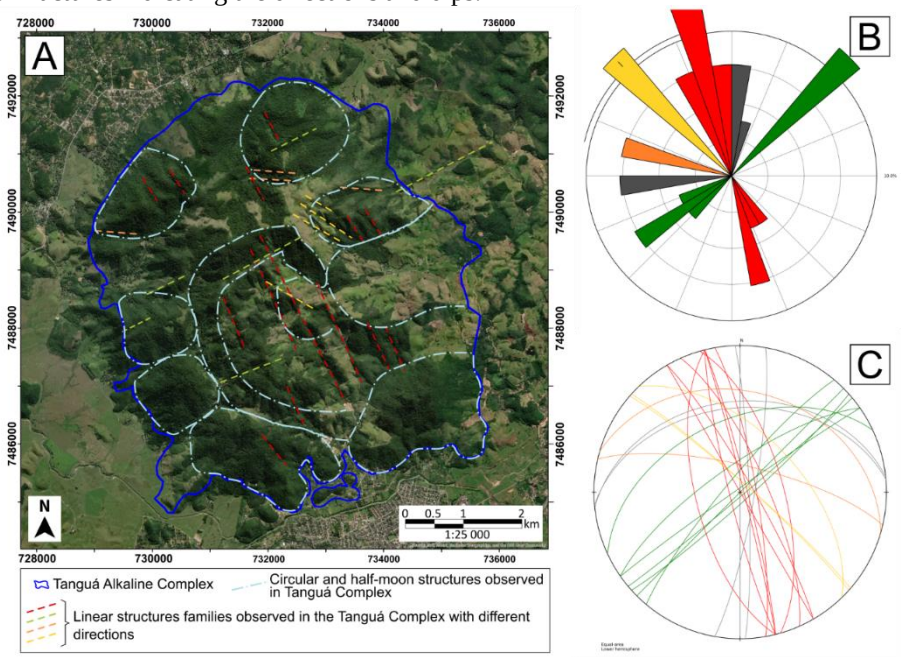

Legenda: The linear structures indicating the presence of four families of fractures: i) NNW-SSE (red); ii) NW-SE (yellow); iii) WNW-ESSE (orange); and iv) NE-SW (green).

4.1.4.2 New lithofaciological division proposal for the Tanguá Complex

Based on previous complex structures and results from petrography and X-ray diffractometry studies, it is possible to propose a new lithofaciological map for the Tanguá Complex (Figure 18). The classification comprises five units: 1) central nepheline syenite, 2) intermediate nepheline syenite, 3) syenite, 4) breccias, and 5) indivisible nepheline syenite. Generally, the breccias are mostly found on the southern and eastern edges of the massif. The syenitic zones are almost concentric, with syenite at the edge and nepheline syenite in the

central portion. It is worth highlighting the presence of a nepheline syenite zone with a half-moon-shape between the most central and outermost zones. The indivisible nepheline-bearing syenite zone is identified in the NW portion of the massif. The details of the lithotypes observed in the complex are present in the further items.

Figure 18 – Lithofaciological map of the Tanguá Alkaline Complex, showing the outcropping lithotypes at each surveyed point and linear structures. Datum: WGS 1984 (UTM – Zone 23S).

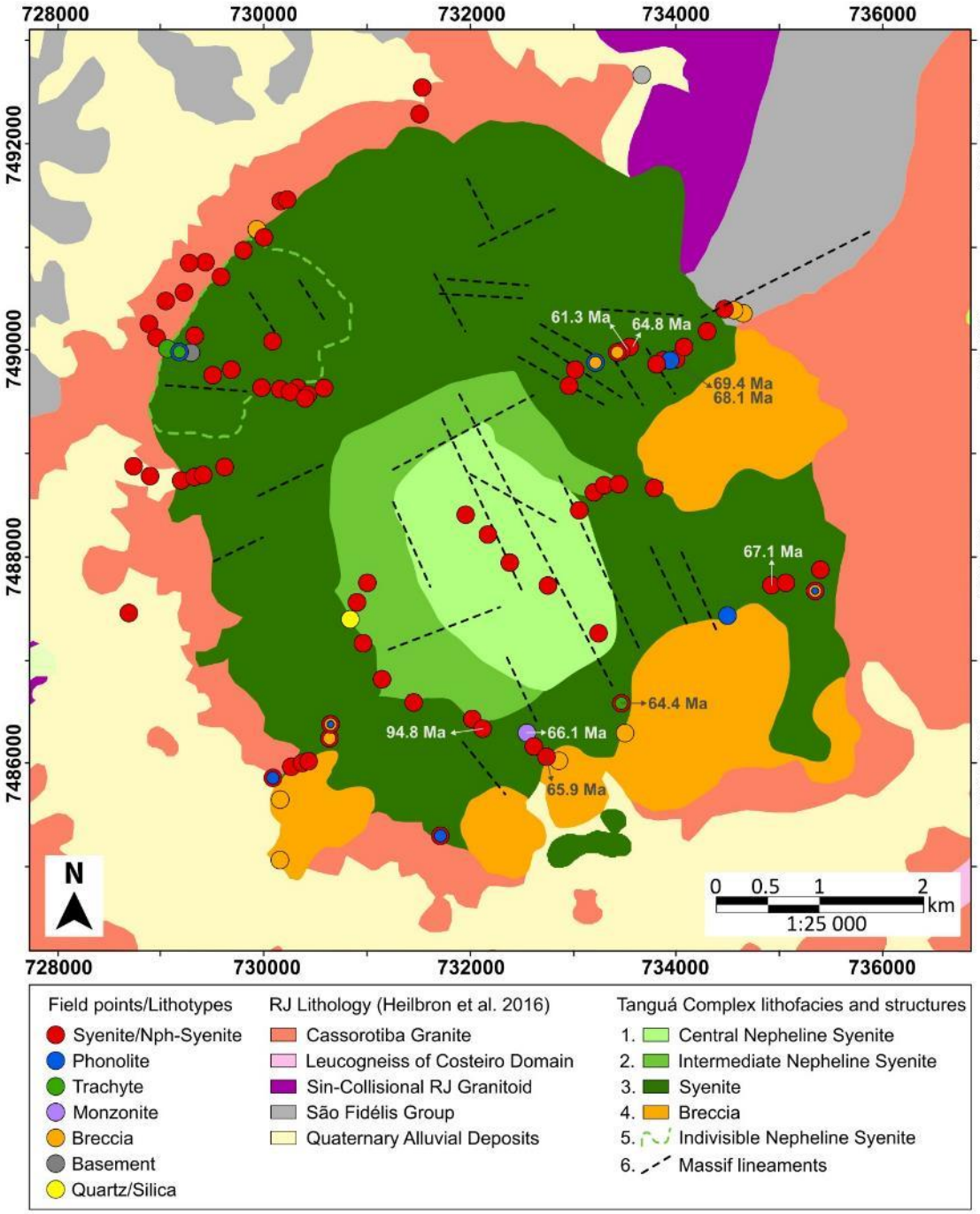

4.1.4.3 Petrography

4.1.4.3.1 Magmatic breccias

The breccias (Figure 18 – lithofacies 4) are yellowish ocher and weathered. It is matrix-supported, with polymictic clasts of different sizes and shapes, mainly rounded (Figure 19A-B). The breccias are fine-grained in the eastern region (Figure 19C) and locally show fractures and foliation fabric (Figure 19D). The rock matrix is fine and comprises ripiform K-feldspar, which can be altered to sericite. Coarse-grained feldspar and limonite/iron hydroxide also occur.

Figure 19 – Breccia lithotype images showing: A) breccia matrix supported sample with fragments (indicated by the write arrows); B) polymictic breccia fragment, with thick clasts (indicated by dashed lines and arrow) and supported matrix from the southern portion of the massif; C) altered breccia fragment with thin clasts and supported matrix from the east-northeast portion of the massif; D) outcrop of foliated polymict breccia, with thick clasts and matrix supported from the southern portion of the massif.

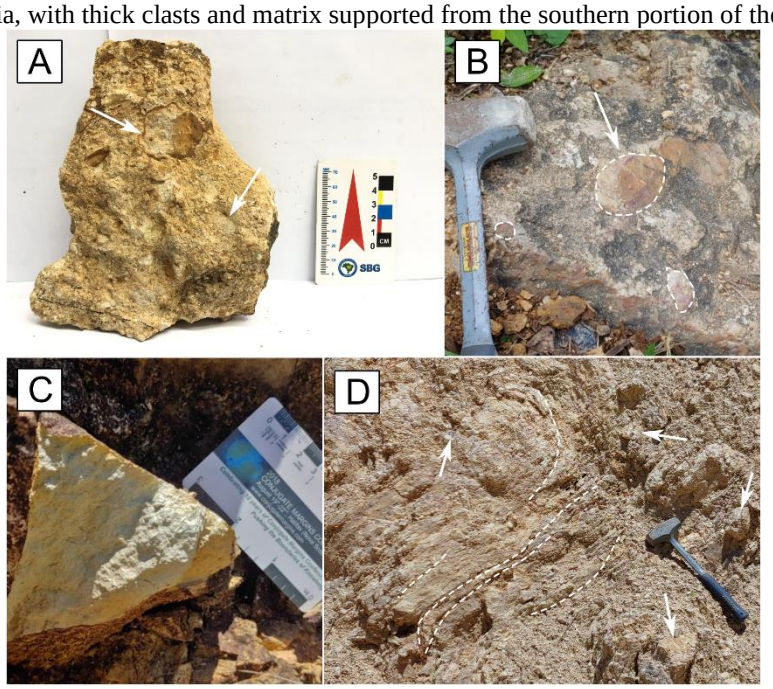

4.1.4.3.2 Phonolites

The lithotype occurs as dikes associated with massif lineaments (Figure 18 – structure 6), and it is commonly found as centimetric- to metric fragments (Figure 20A-C). The rock has a dark gray to black in color and an aphanitic to fine-grained phaneritic matrix with a porphyritic texture. It comprises K-feldspar as the main mineral in the matrix (Figure 20D and G), presenting phenocrysts of K-feldspar (Figure 20D and H), which can be altered to sericite, clinopyroxenes (Figure 20F and I), nepheline, titanite, amphibole (possible arfvedsonite - Figure 20E), sodalite, and opaques.

Figure 20 – Phonolite lithotype images showing: A) Fragment of phonolite with black color, fine grain, and presence of phenocrysts indicated by white arrows; B) Syenite fragment crosscut by a thin phonolite dike highlighted by a dashed white line; C) Syenite fragment in contact with phonolite highlighted by a dashed white line. Images between D and F are photomicrographs obtained from sample TG-16xx, and between G and I are photomicrographs obtained from sample TG-21. D) Rock with a feldspathic phaneritic matrix with crystal orientation and different phenocrysts. Under transmitted light (LT) and crossed lights (NC), 2.5x and scale: Basal section of clinoamphibole (possible arfvedsonite). Under LT and NP, 20x and scale: 100 µm; F) Clinopyroxene crystals (possible aegirine) skeletal poikilitic. Under LT and NP, 10x and scale: 250 µm; G) Detail in an aphanitic matrix with fine prismatic/ripiform crystals. Under LT and NC, 50x and scale: 50 µm; H) General view of the fine matrix with phenocrysts of different minerals. Under LT and NP, 5x and scale: 100 µm; I) Euhedral and zoned crystal of clinopyroxene (possible aegirine). The green anhedral nucleus of cpx has a growth twin showing reaction edges and a poikilitic texture. Under LT and NP, 20x and scale: 100 µm.

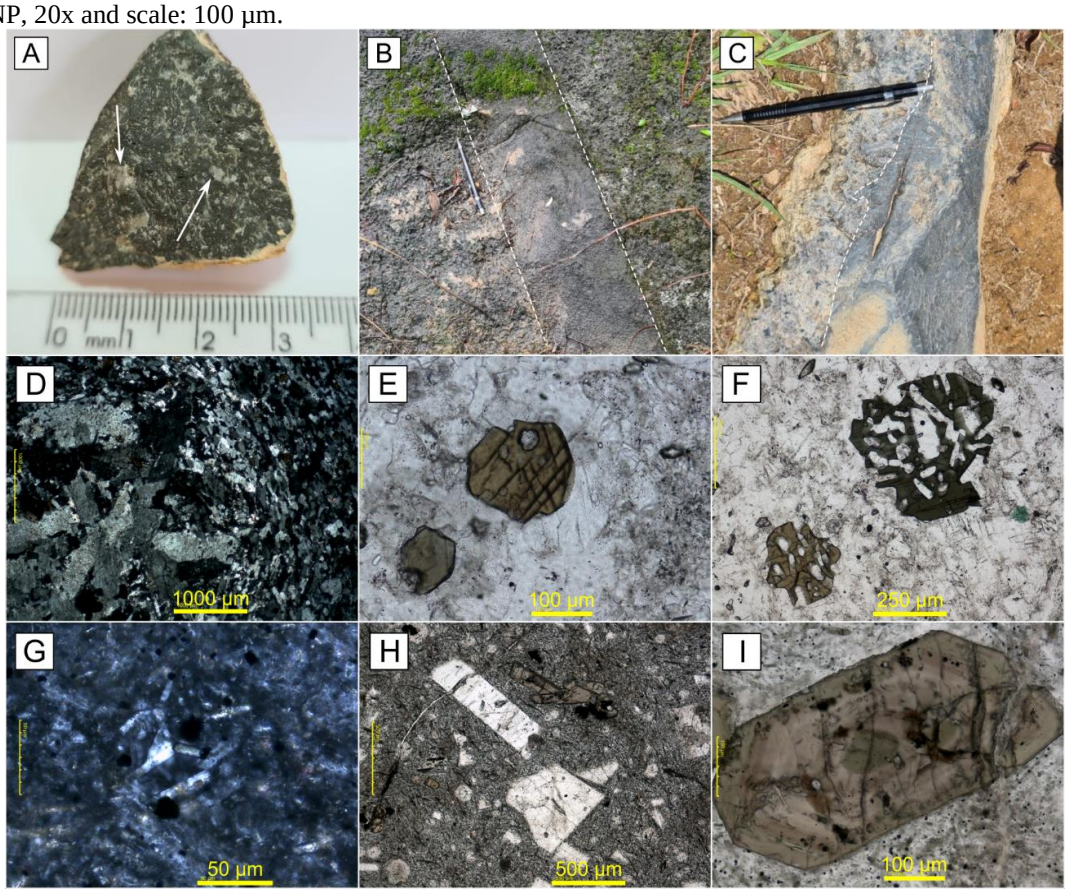

4.1.4.3.3 Trachyte

The leucocratic lithotype is rare and is observed in contact with syenite or phonolite. It is commonly weathered, has a beige color (Figure 21C), and is aphanitic with porphyritic texture. The rock mainly comprises K-feldspar as a fine matrix and large euhedral phenocrysts (Figure 21A-B). Microphenocrysts of feldspar or feldspathoid are observed, as well as carbonate (Figure 21C) and euhedral pyrite crystals (Figure 21D).

Figure 21 – Photomicrographs obtained from trachyte samples, showing: A) A General view of the rock with a fine and altered matrix with altered feldspar phenocrysts. Under transmitted light (LT) and parallel lights (NP), 5x and scale: 500 µm; B) Under LT light and crossed lights (NC), 5x and scale: 500 µm; C) A Portion with possible carbonate. Under LT and NC, 10x e scale: 250 µm; D) Detail of euhedral pyrite crystals. Under reflected light (LR) and NC, 10x and scale: 250 µm.

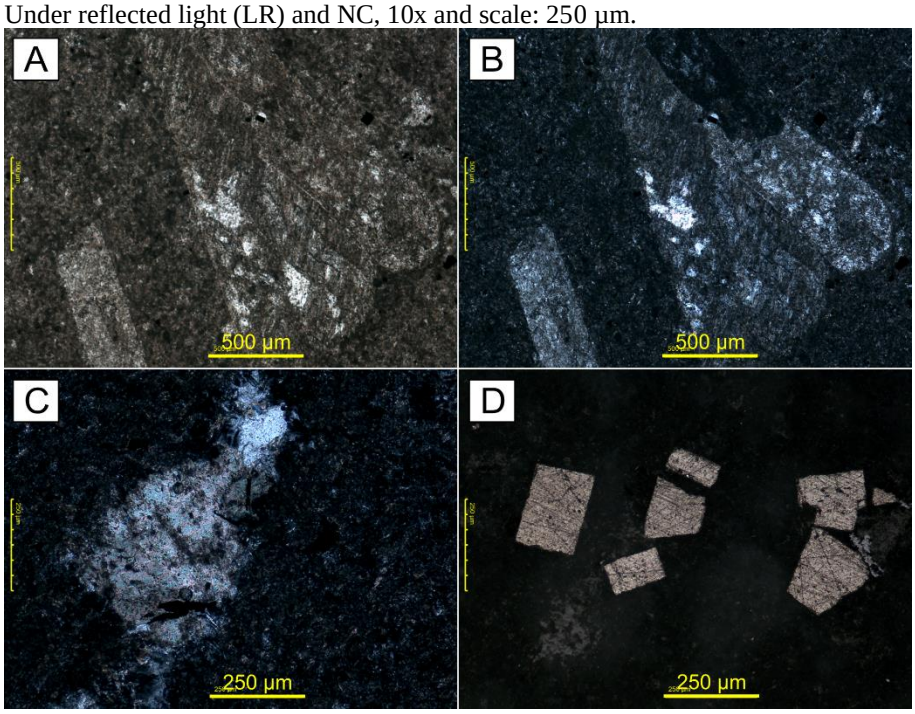

4.1.4.3.4Syenitic rocks

These rocks are the complex principal lithological constituent (Figure 18 – lithofacies 1, 2, 3 and 5), commonly as rounded fragments (Figure 22A), ranging from fine to coarse-grained, sometimes pegmatitic, and exhibit a white to medium-gray color (Figure 22B-F). The

rocks comprise feldspars (alkaline and plagioclase), nepheline, clinopyroxene, amphibole, and titanite as major minerals (Figure 23C-H), and biotite, sodalite, and leucite can also occur. The K-feldspar is the main mineral phase, with anhedral crystals, rarely euhedral, which can be altered to sericite and clay minerals (Figure 23A-B). The nepheline presence divides this group into 1) syenite and 2) nepheline syenite; however, here, they are grouped due to their similar features. The syenitic rocks are commonly crosscutted by millimeter- to centimeter-filled fractures (Figure 22D) and leucocratic aplites (Figure 22E), which coincide with general structures. Some fractures are filled by black or yellowish material, silica, and pyrite (Figure 22J and K, and Figure 23I), and this last one also occurs disseminated in the nearby rocks.

Figure 22 – Syenite lithotype images showing: A) Typical syenite rounded fragments; B) Detail of syenite granulation and typical texture; C) Contact between syenite and trachyte in a quarry outcrop ; D) Detail of leucocratic filled veins/fractures indicated by white arrows; E) Leucocratic aplite in syenite indicated by white dashed lines; F) Contact detail (dashed white line), between pegmatoid-grained syenite associated with fine syenite; G) Pinkish pseudoleucites in contact with a pinkish portion and granular texture; H) Detail in "euhedral" pseudoleucite with inclusions of biotite and magnetite; I) Pseudoleucite in fine syenite close to a river flow; J) Fractured portion filled with flint/quartz and pyrite; K) Pyrite detail.

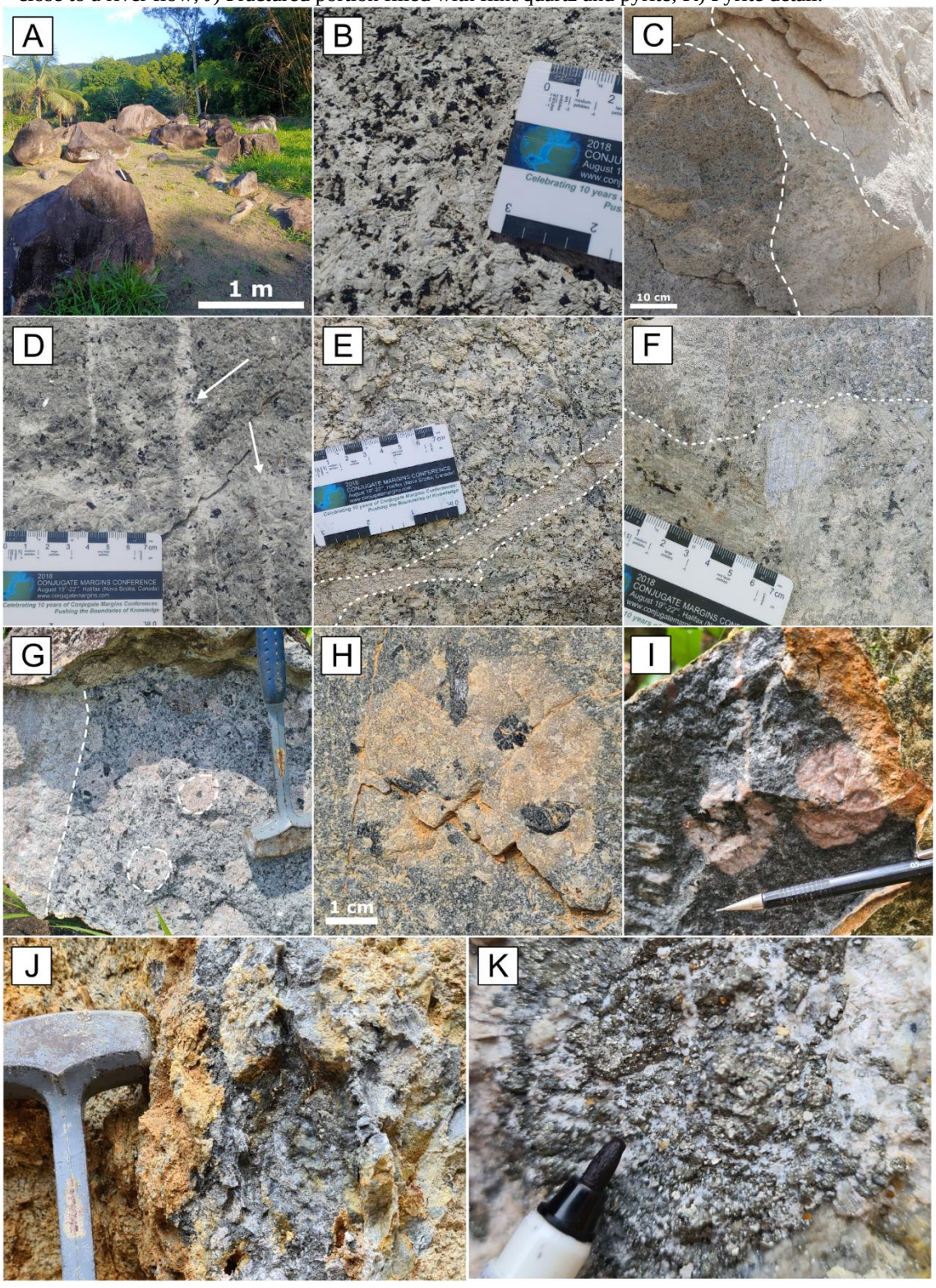

Figure 23 – Photomicrographs obtained from syenite samples, showing: A) General view of the rock with potassium feldspar (central portion), associated with plagioclase (polysynthetic extinction on the right), titanite, and biotite. The relationship between plagioclase and potassium feldspar may indicate an anti-rapakivi texture. Under LT and NC, 5x e scale: 500 µm; B) Detail of irregular contact between potassium feldspar crystals. Under LT and NC, 5x e scale: 500 µm; C) Nepheline detail (colorless crystal in the center of the image) associated with potassium feldspar. Under LT and NP, 5x e scale: 500 µm; D) Under LT and NC, 5x and scale: 500 µm; E) Hornblende crystal changing to biotite. Under LT and NP, 5x and 500 µm; F) Detail of clinopyroxene crystal associated with biotite and possible amphibole, indicating possible alteration between these minerals. Under LT and NP, 10x and 250 µm. G) Potassium feldspar associated with sodalite with total extinction (white arrows). Under LT and NP, 10X and scale: 250 µm; H) Detail of a portion with sodalite (white arrow) and possible leucite (yellow arrow). Under LT and NP, 20x e scale: 100 µm; I) Detail in anhedral pyrite crystal associated with dark gray mineral. Under LR and NP, 20x and 100 µm.

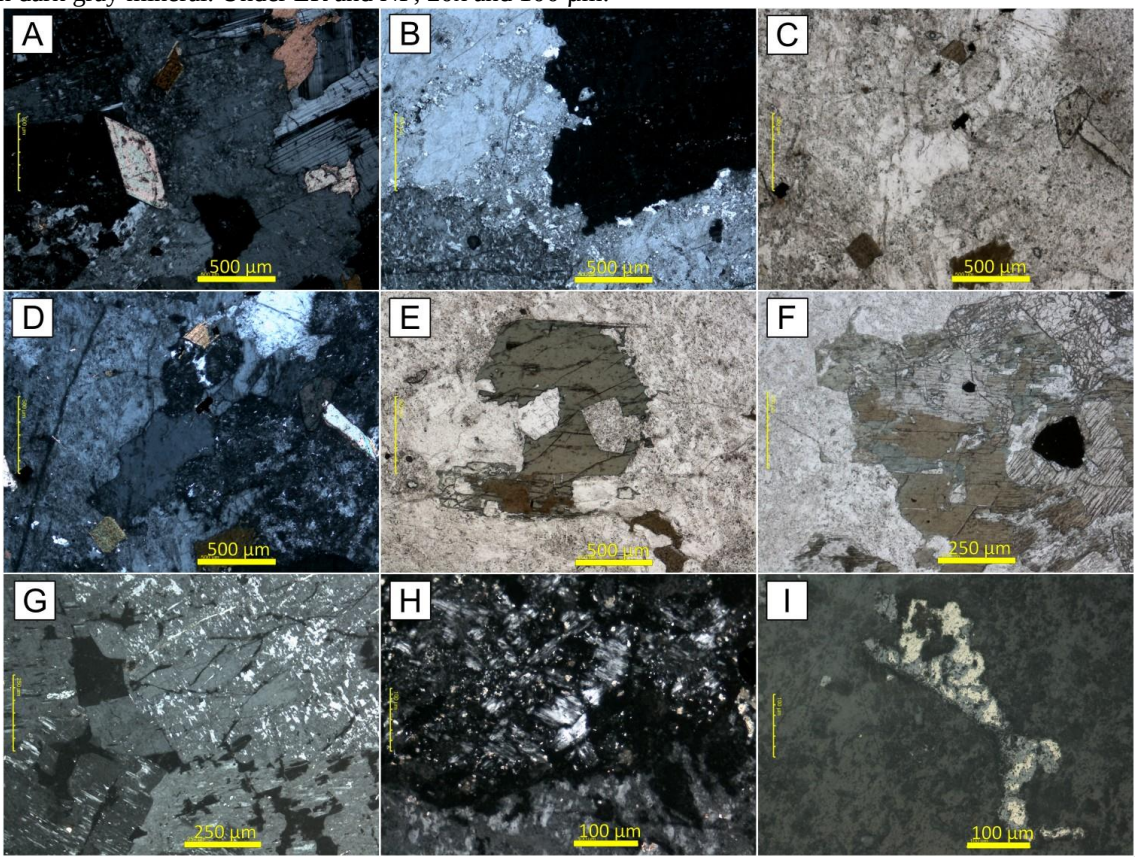

4.1.4.4 X-ray diffraction

X-ray diffraction analyses reveal that the syenitic rocks predominantly comprise feldspars, nepheline, and analcime. Based on these results, it was possible to differentiate this group, previously studied by petrography, into three facies, which was used to propose the new map (Figure 18): 1) central nepheline syenite, which comprises nepheline and analcime richer rocks; 2) intermediate nepheline syenite, with rocks mainly composed of nepheline and albite; and 3) syenite, which comprises rocks with nepheline absence. The phonolites can show three main features: i) high content of sanidine and nepheline, (ii) high content of

microcline and albite, or (iii) high albite content with no nepheline presence. However, this division was not followed due to the small number of samples. The trachyte, composed of feldspar and quartz, became the only rock with this characteristic. Monzonite was only identified based on the XRD results, was not studied using optical microscopy, and presents a similar syenitic facies mineralogy (Figure 18 – lithofacies 3) comprising albite, orthoclase, and microcline. This rock was not represented in the lithofaciological map due to its low representation (only one sample was identified). The detailed results can be found in the Supplementary Material.

4.1.4.5 Lithogeochemistry

The lithogeochemistry data will be presented following the identification based on petrography and X-ray diffractometer analyses. Thus, the lithotypes were split into syenite, nepheline-syenites, phonolites, trachytes, and monzonite. All obtained results and the ratios mentioned in this work are presented in the Supplementary Material.

4.1.4.5.1 Major and traces elements

Major and traces elements

The syenite rocks have SiO_2 contents ranging between 56.8 wt.% and 59.2 wt.%, while nepheline syenites vary between 54.9 wt.% and 59.1 wt.%. Phonolites show content between 50.5 wt.% and 59.8 wt.%, trachyte has 57.5 wt.% and 58.9 wt.%, and monzonite has 60.7 wt.%. All rocks can be classified as alkaline and of intermediate character (Figure 24), except for a phonolite sample (TG42B) that plots in the basalt field, with basic character and classified as sub-alkaline. According to the TAS diagram (LE BAS et al., 1986 - Figure 24), the rocks are classified as phonolite or trachyte, and based on the R1-R2 diagram (DE LA ROCHE et al., 1980 - Figure 25), the rocks plot mainly in the phonolite, trachy-phonolite, trachyte, or quartz-trachyte fields, this last associated with trachytes samples. The lithotypes are commonly metaluminous, but some samples show peraluminous character (Figure 26).

For the K_2O versus Na_2O binary diagram (Figure 27), the rocks fall mainly in the ultrapotassic series and less in the potassic series. It is important to highlight that these results plot near to the previous TC data, as well as to the Soarinho and Rio Bonito complexes.

Harker diagrams compare major oxides (Figure 28) and trace elements (Figure 29) with SiO_2. For the major oxides, nepheline syenites show positive correlations with Al_2O_3, K_2O, and Na_2O, while the others have a negative correlation. Except for CaO oxide, which has a discrete correlation, the data for syenite is scattered. Although the phonolite has less data, it shows correlations for P_2O_5 and K_2O.

For trace elements, these correlations are generally not straightforward, but nepheline syenites have negative correlations of Th, U, La, Ce, Eu, Hf, and Y, while phonolites suggest positive correlations for Th, La, Ce, Rb, Zr, and Nb. There is not enough data for the other lithotypes to establish these correlations. Compared to #Mg, syenites and phonolites have a negative correlation, while nepheline syenites do not show an obvious correlation (Figure 30).

The incompatible elements normalized by primitive mantle (Figure 31 - MCDONOUGH & SUN, 1995) show a decreasing tendency towards the most incompatible elements for all lithotypes. The Ba, P, and Ti anomalies are observed for all rocks, particularly negative ones, and Sr anomalies can be observed in all lithotypes except for nepheline syenites.

Figure 24 – TAS diagram (Total alkali versus SiO_2) by LE BAS et al. (1986) for the samples from the Tanguá Complex.

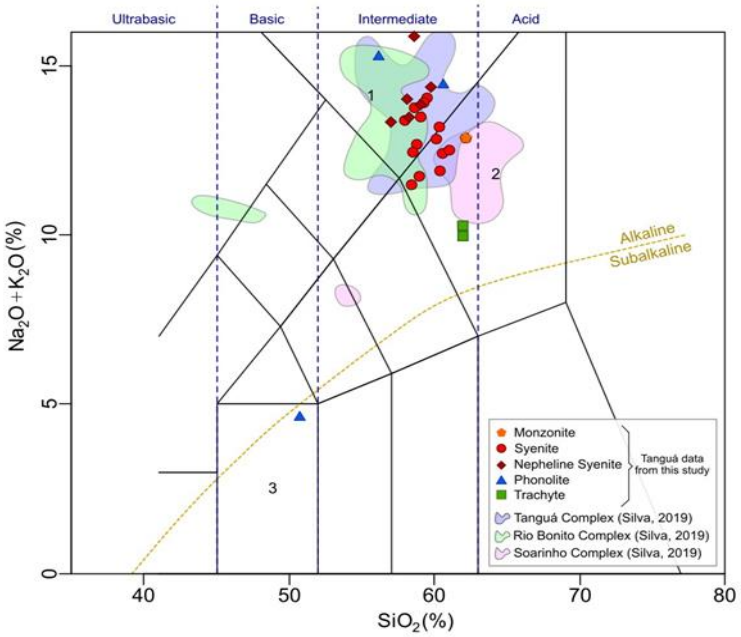

Legenda: 1 – phonolite; 2 – trachyte; 3 – basalt.

Figure 25 – R1-R2 diagram by DE LA ROCHE et al. (1980) for the samples from the Tanguá Complex.

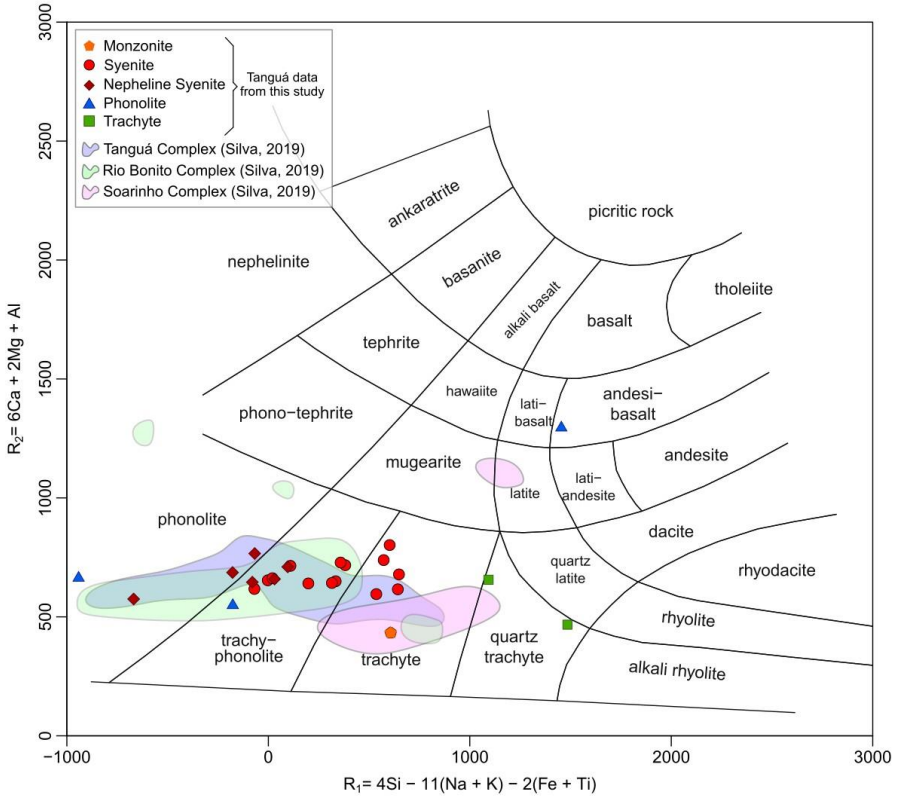

Figure 26 – A/NK versus A/CNK diagram by SHAND (1943) for the samples from the Tanguá Complex. The TG42A sample plots outside the diagram boundaries.

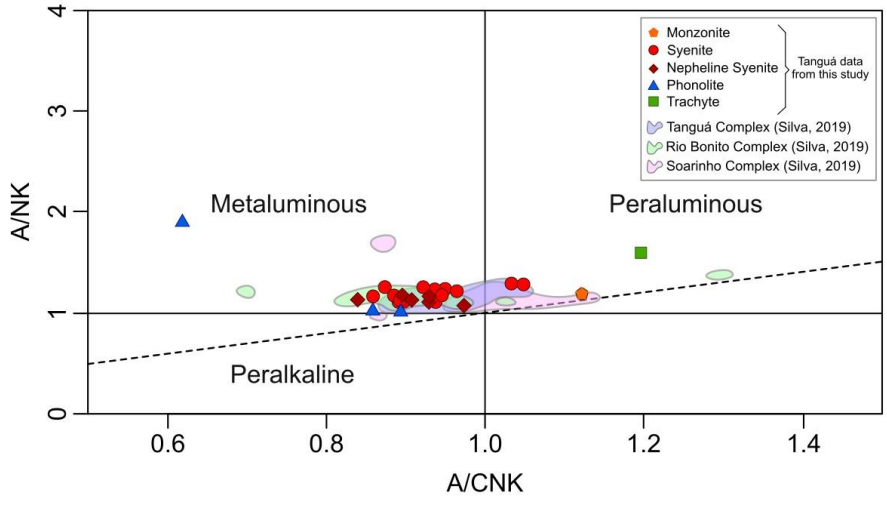

Figure 27 – K_2O versus Na_2O diagram by MIDDLEMOST (1975) for the samples from the Tanguá Complex

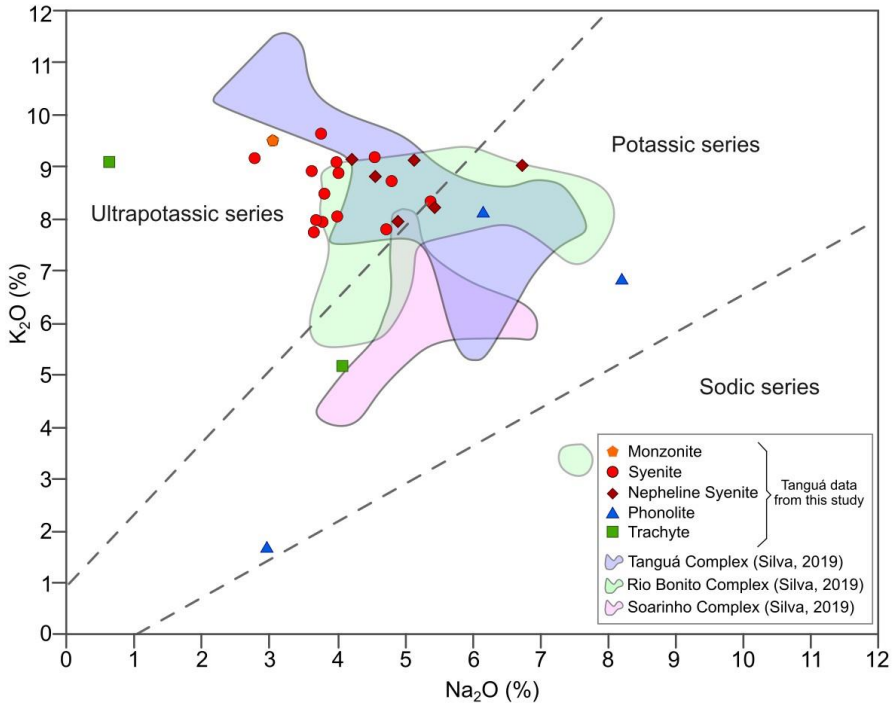

Figure 28 – Harker diagram for major elements (wt%) for the samples from the Tanguá Complex.

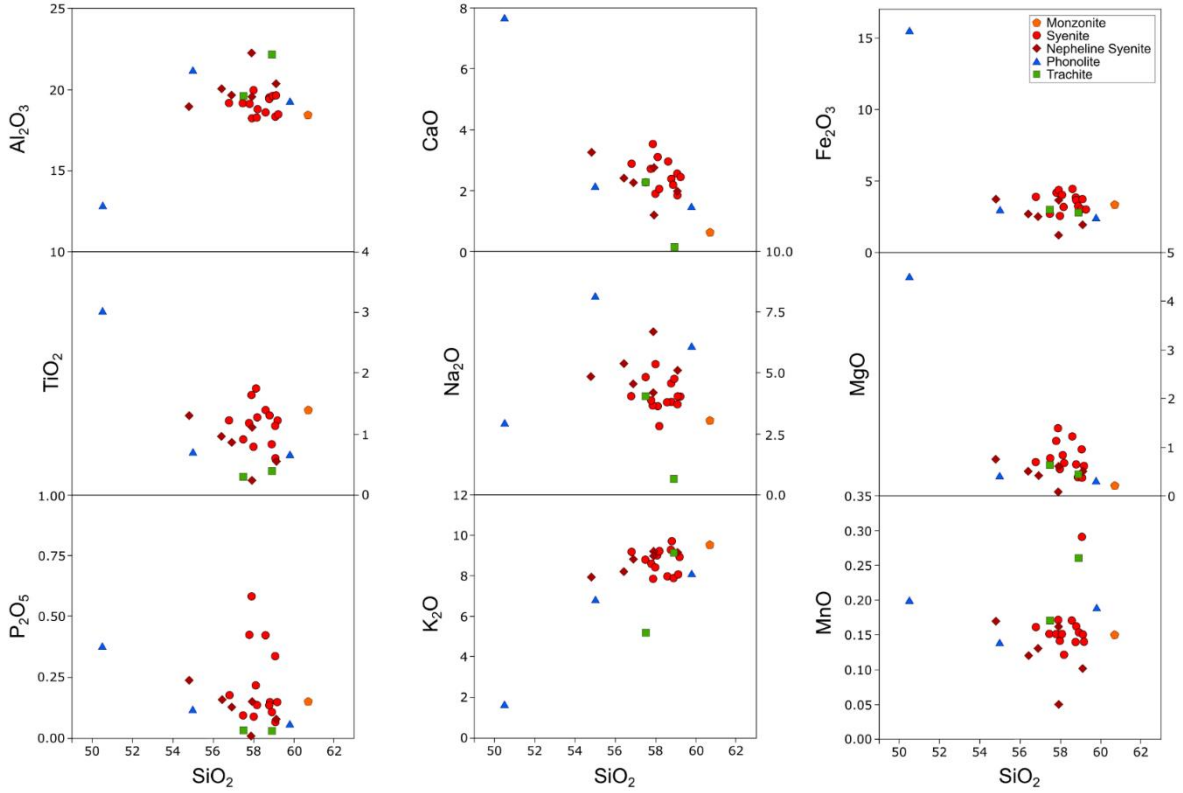

Figure 29 – Harker diagram for trace elements (ppm) for the samples from the Tanguá Complex.

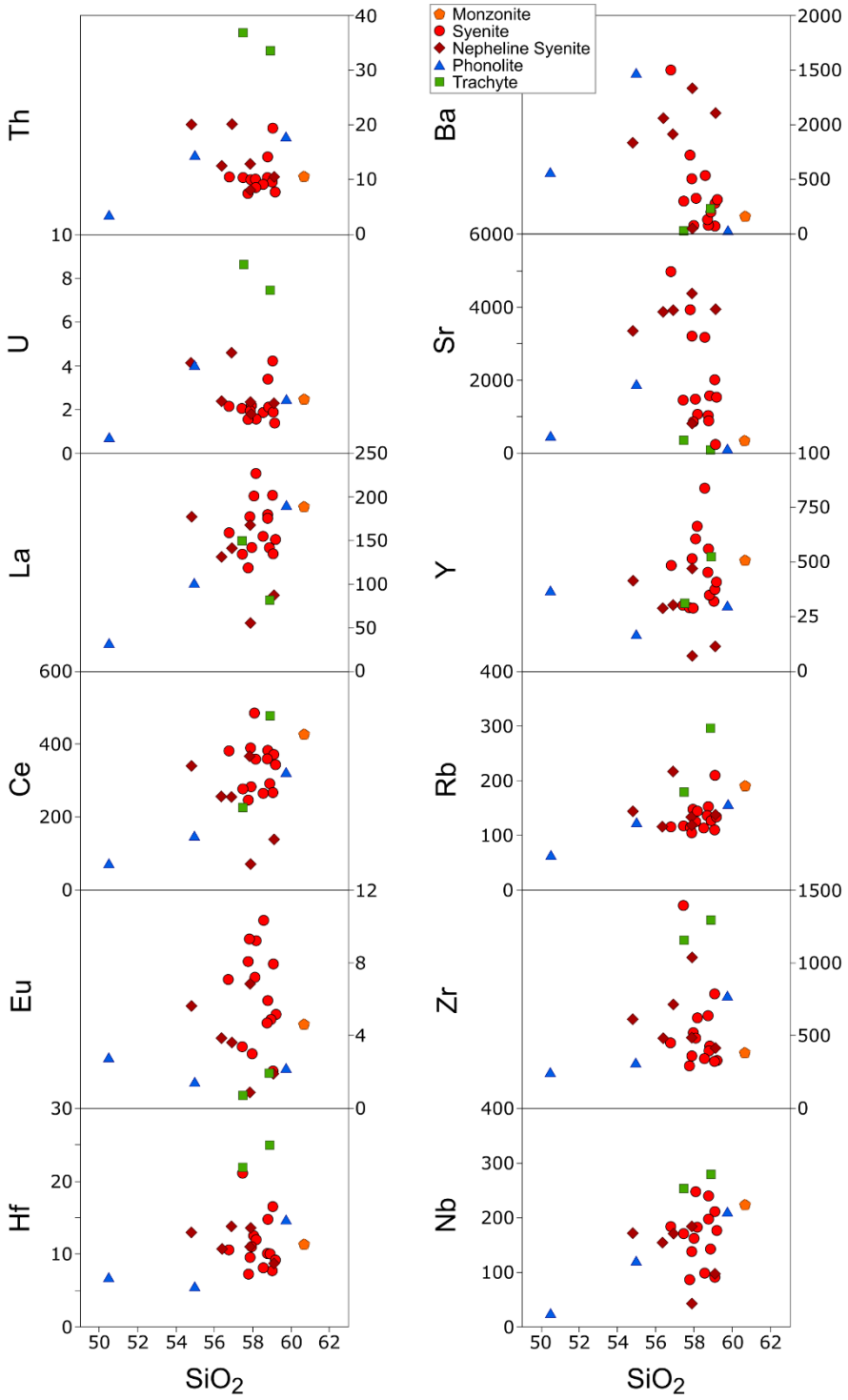

Figure 30 – Binary diagram of #Mg versus SiO_2 for the samples from the Tanguá Complex

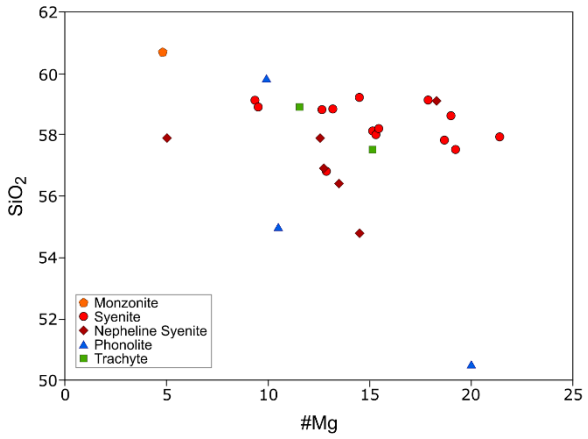

4.1.4.5.2 Rare Earth Elements

For REE normalized by primitive mantle diagrams (Figure 32 – McDonough & Sun, 1995), all lithotypes present descending patterns (La_N/Yb_N between 6.74 and 44.3) and are enriched than the primitive mantle. Syenites and nepheline syenites show mainly positive Eu anomalies (Eu/Eu* of 0.76 to 1.96 and 1.17 to 2.35, respectively) and trachytes negatives (0.43 and 0.73). The phonolites (0.82 to 1.11) and monzonite (0.89) show discrete Eu anomalies. The positive Ce anomaly of the trachyte is graphically visible and needs to be highlighted. Horizontalization of normalized HREE pattern occurs in phonolite, trachytes, and some nepheline syenites.

Figure 31 – Primitive Mantle normalized elements (MCDONOUGH AND SUN, 1995) for the samples from the Tanguá

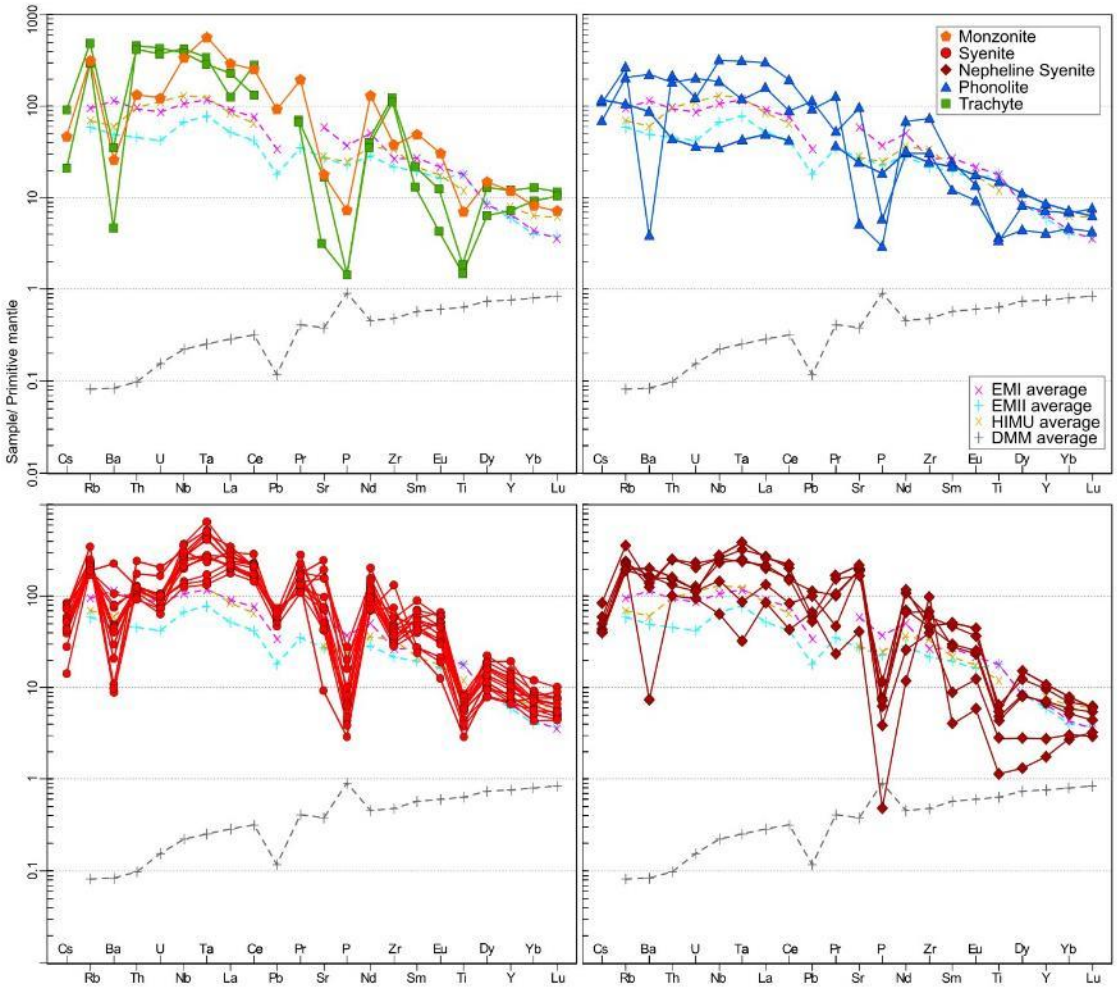

Fonte: Mantle sources average: DMM – WORKMAN & STANLEY (2005); EMI – SALTERS et al. (2011); EMII – WORKMAN et al. (2004); HIMU – CHAFFEY et al. (1989).

Figure 32 – Primitive mantle normalized rare earth elements (MCDONOUGH AND SUN, 1995)

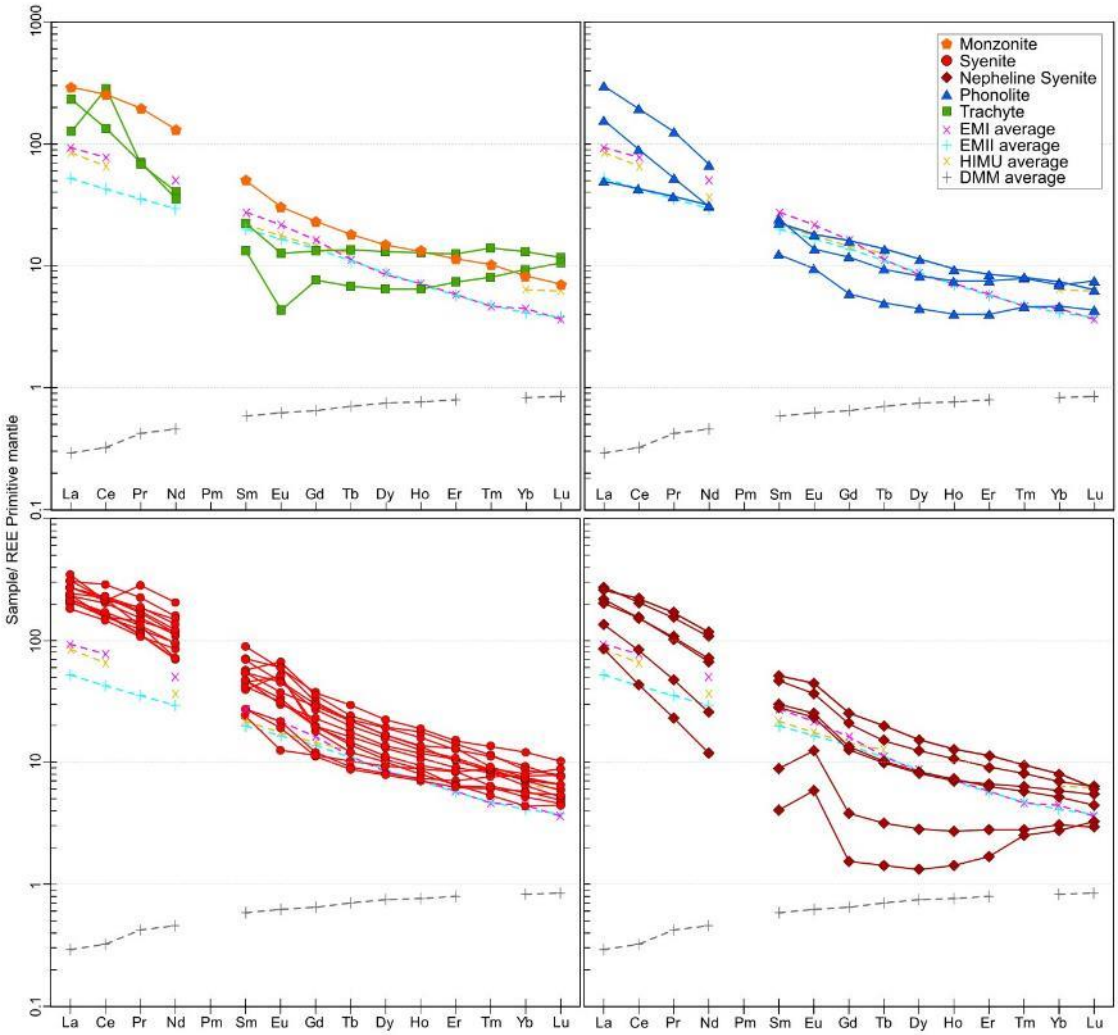

Fonte: Mantle sources average: DMM – WORKMAN & STANLEY (2005); EMI – SALTERS et al. (2011); EMII – WORKMAN et al. (2004); HIMU – CHAFFEY et al. (1989).

4.1.4.5.3CIPW norm

The CIPW norm exhibits that normative feldspars are the main minerals for the lithotypes, and the normative orthoclase (Or) is the most common. The results indicate that all nepheline syenites always show normative nepheline (Ne), while the syenites can show Ne, normative quartz (Q), or neither of these normative minerals. Trachytes show the highest Q content (19.4%), followed by a phonolite sample and monzonite. See the Supplementary Material for detailed results.

4.1.4.5.4 U-Pb geochronology

The obtained results are included in the Supplementary Material. Figure 33 displays the Tera-Wasserburg concordia diagrams, backscattered electron zircon images, and the positioning of LA-ICP-MS analyses in minerals. The U-Pb analyses and Lu-Hf analyses were conducted on five samples of syenite, one sample of nepheline syenite, monzonite, and phonolite.

The concordia diagram of syenite TG-02C yielded an age of 66.08 ± 0.47 Ma (11 grains), with an MSWD of 0.55 and a probability of agreement of 95%. The analyzed grains are anhedral to subhedral and mainly equidimensional, except for grain 4. For the syenite, TG-04D has obtained a concordia age of 64.40 ± 0.40 Ma (14 grains), with an MSWD of 1.6 and a probability of agreement of 2.9%. Except for grains 1, 5, and 10, which are subhedral and preferably prismatic, the others vary between anhedral and subhedral and tend to be more equidimensional. The concordia age of the syenite TG-18 yielded 64.82 ± 0.38 Ma (13 grains) with an MSWD of 0.44 and a probability of agreement of 99%. Some grains have subhedral and prismatic characteristics (2, 4, 8, and 11), while others are anhedral and subhedral and preferably equidimensional. The syenite TG-27 shows a concordia age of 67.06 ± 0.48 Ma (11 grains) with an MSDW of 0.89 and a probability of 60%. The grains are mainly anhedral and equidimensional. Finally, the syenite TG-03 has an older age than others, and the analyses yielded a concordia age of 94.82 ± 1.02 Ma (10 grains) with an MSWD of 0.29 and a probability of agreement of 100%. The zircon grains are more prismatic than other samples, although commonly anhedral or subhedral.

The nepheline-syenite (TG-19) analyses yielded an age 61.27 ± 0.48 Ma (7 grains) with an MSWD of 1.2 and a probability of 30%. The crystals are anhedral to subhedral with equidimensional features. For monzonite (TG-02), ten analyses were used to construct the concordia diagram, yielding an age of 65.89 ± 0.50 Ma with an MSWD of 0.49 and a probability of 97%. The grains are anhedral to euhedral with less prismatic shapes in the latter.

The phonolite sample TG-16 was analyzed twice because the first mount (TG-D) showed only six zircon grains large enough to carry out the analyses, while the second mount (TG-E) allowed for the analysis of 15 grains. For the first mount, the concordia age is 69.37 ± 0.58 Ma (5 grains) with an MSDW of 1.3 and a probability of 22%. The grains 2 and 4 are

more euhedral to subhedral and prismatic. The second sample presents a concordia age of 68.11 ± 1.38 Ma (15 grains) with an MSWD of 0.64 and a probability of 93%.

Figure 33 – Zircon U-Pb concordia diagram for the samples from Tanguá Complex and the analyzed zircon grains showing the area of analysis (red circle with 40 µm).

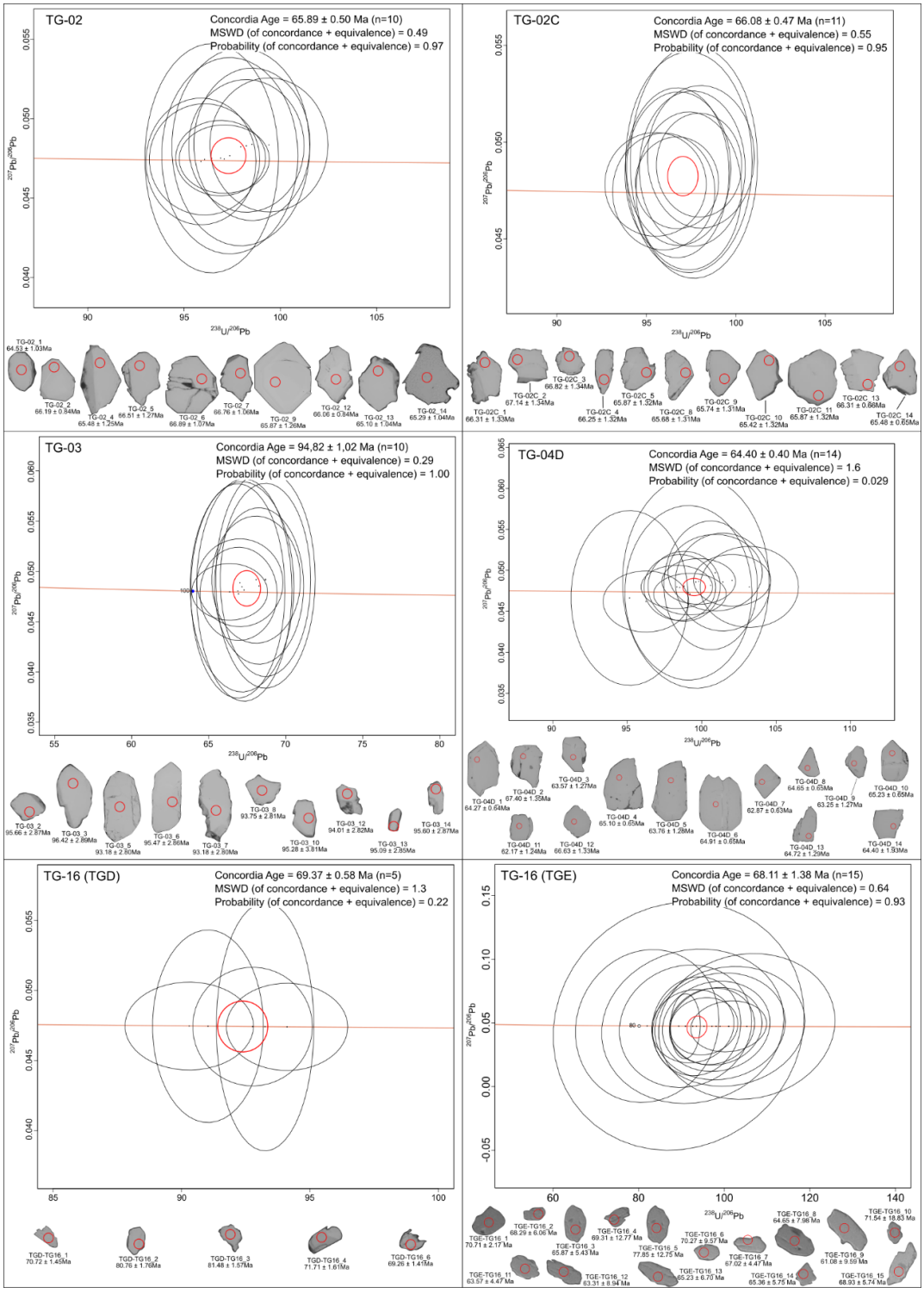

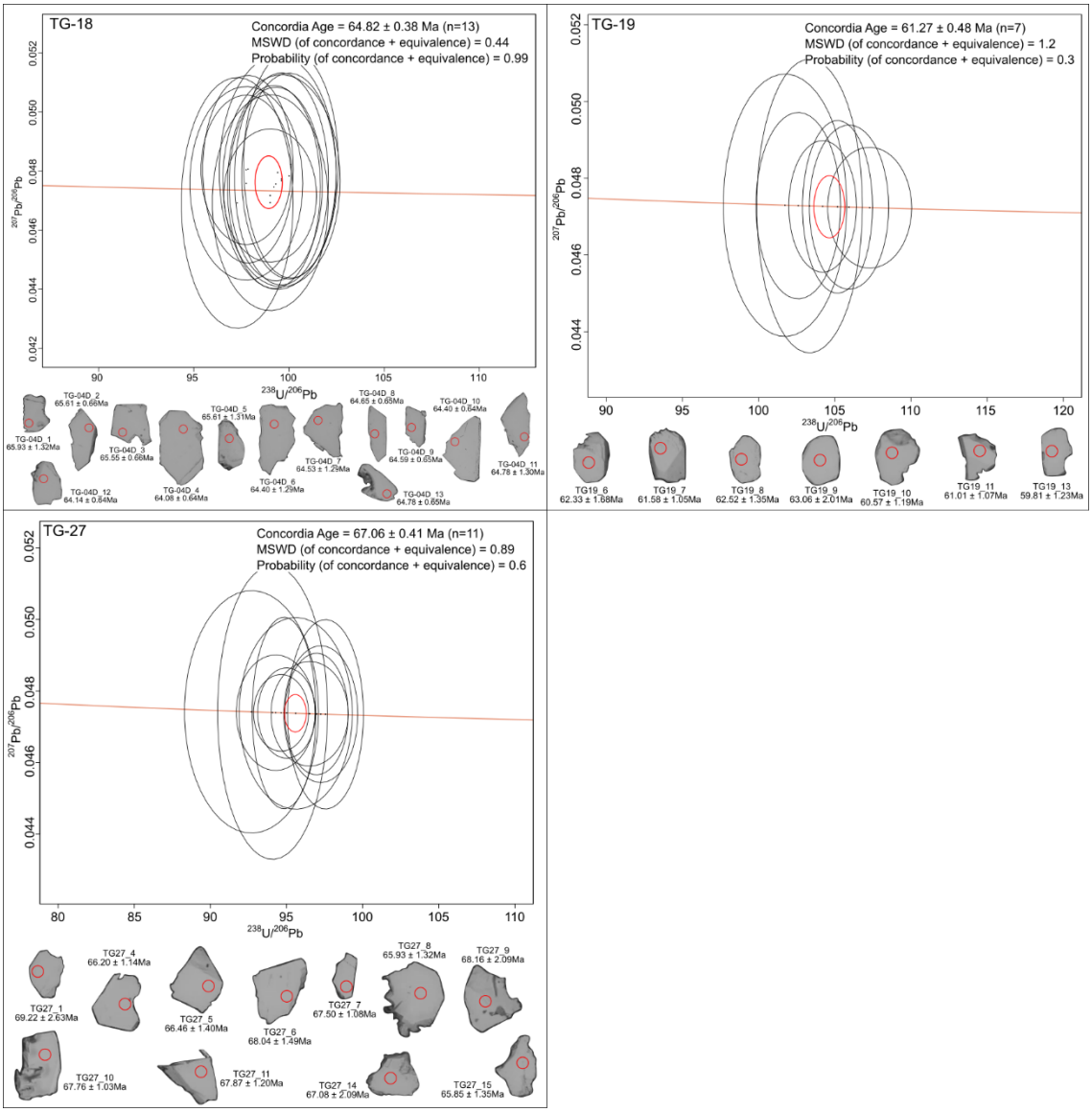

4.1.4.6 Lu-Hf isotopic geochemistry

The main results are presented in Table 7, and the complete results are in the Supplementary material. The $^{176}Hf/^{177}Hf_{(i)}$ and ε_{Hf} compared with the U-Pb ages are presented in Figure 34. The syenites exhibit $^{176}Hf/^{177}Hf_{(i)}$ ratios ranging from 0.282340 to 0.283050 and ε_{Hf} values varying between - 14.26 and + 11.49, with T_{DM} age between 282 and 1338 Ma. The nepheline syenite sample shows $^{176}Hf/^{177}Hf_{(i)}$ ratios varying from 0.282350 to 0.282680 and ε_{Hf} values between - 14.01 and - 2.36 with T_{DM} age between 820 and 1341 Ma. The monzonite exhibits $^{176}Hf/^{177}Hf_{(i)}$ ratios ranging from 0.282241 to 0.282786 and ε_{Hf} values between - 17.78 and + 1.51 with T_{DM} age from 665 to 1571 Ma. Finally, the phonolite shows

$^{176}Hf/^{177}Hf_{(i)}$ ratios varying between 0.282551 and 0.282942, and ε_{Hf} values between - 6.76 and + 7.30, and T_{DM} age between 430 and 976 Ma.

Table 7 – Isotopic geochemistry data using the Lu-Hf method by LA-ICP-MS on zircons of different samples from Tanguá Complex.

Sample	Lithotype	Data	$^{176}Hf/^{177}Hf$	$^{176}Hf/^{177}Hf_{(i)}$	ε_{Hf}	T_{DM}
TG-02	Monzonite	Minimum	0.282247	0.282241	-17.78	665
		Maximum	0.282789	0.282786	+1.51	1571
		Average	0.282444	0.282440	-10.75	1215
TG-02C	Syenite	Minimum	0.282594	0.282591	-5.41	376
		Maximum	0.282993	0.282990	+8.72	961
		Average	0.282786	0.282783	+1.38	681
TG-03	Syenite	Minimum	0.282535	0.282533	-6.80	282
		Maximum	0.283053	0.283050	+11.49	1001
		Average	0.282799	0.282796	+2.51	644
TG-04D	Syenite	Minimum	0.282357	0.282354	-13.80	754
		Maximum	0.282720	0.282718	-0.95	1287
		Average	0.282578	0.282575	-6.01	989
TG-18	Syenite	Minimum	0.282538	0.282535	-7.39	731
		Maximum	0.282750	0.282747	+0.09	1044
		Average	0.282640	0.282636	-3.85	916
TG-19	Nph-syenite	Minimum	0.282354	0.282350	-14.01	820
		Maximum	0.282682	0.282680	-2.36	1341
		Average	0.282548	0.282545	-7.14	1030
TG-27	Syenite	Minimum	0.282343	0.282340	-14.26	857
		Maximum	0.282655	0.282652	-3.20	1338
		Average	0.282541	0.282539	-7.22	1027
TG-16 (TGD)	Phonolite	Minimum	0.282552	0.282551	-6.73	812
		Maximum	0.282673	0.282672	-2.45	976
		Average	0.282610	0.282609	-4.69	901
TG-16 (TGE)	Phonolite	Minimum	0.282585	0.282584	-5.67	430
		Maximum	0.282943	0.282942	+7.30	938
		Average	0.282737	0.282735	-0.23	724

Figure 34 – ε_{Hf} and $^{176}Hf/^{177}Hf_{(i)}$ evolution diagrams for the samples from Tanguá Complex.

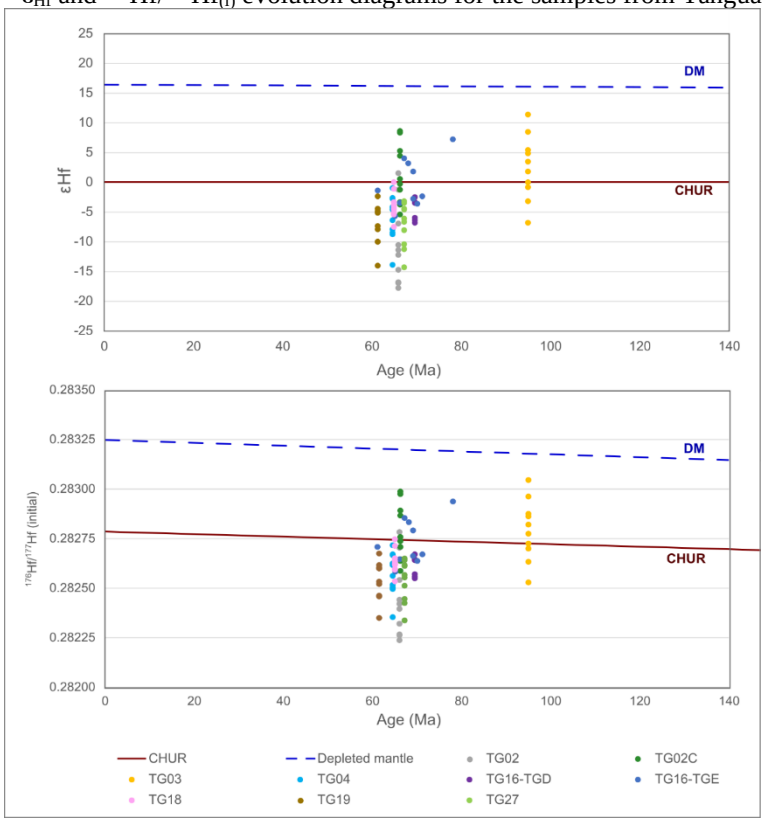

4.1.4.7 Sr-Nd isotopic geochemistry

Table 8 and Figure 35 show the results of isotopic analyses for Sr and Nd. The syenites exhibit $^{87}Sr/^{86}Sr_{(m)}$ varying between 0.705155 and 0.705478, $^{143}Nd/^{144}Nd_{(m)}$ ranging between 0.512429 and 0.512443, and ε_{Nd} values ranging from - 3.17 to - 2.62, whit T_{DM} ages between 772 and 862 Ma. The nepheline syenite has $^{87}Sr/^{86}Sr_{(m)}$ and $^{143}Nd/^{144}Nd_{(m)}$ of 0.705237 and 0.512467, respectively. The ε_{Nd} is - 2.31, and the T_{DM} model age is 677 Ma. Finally, for the phonolite, the ratios of $^{87}Sr/^{86}Sr_{(m)}$ and $^{143}Nd/^{144}Nd_{(m)}$ are 0.709476 and 0.512439, respectively. The ε_{Nd} value is - 2.77, and the T_{DM} model age is 725 Ma.

Figure 35 – ε_{Nd} plotted versus U-Pb age (Ma) diagram for samples from Tanguá Complex. The Model Ages (TDM) were calculated using GCDKit according to LIEW & HOFMANN (1988)

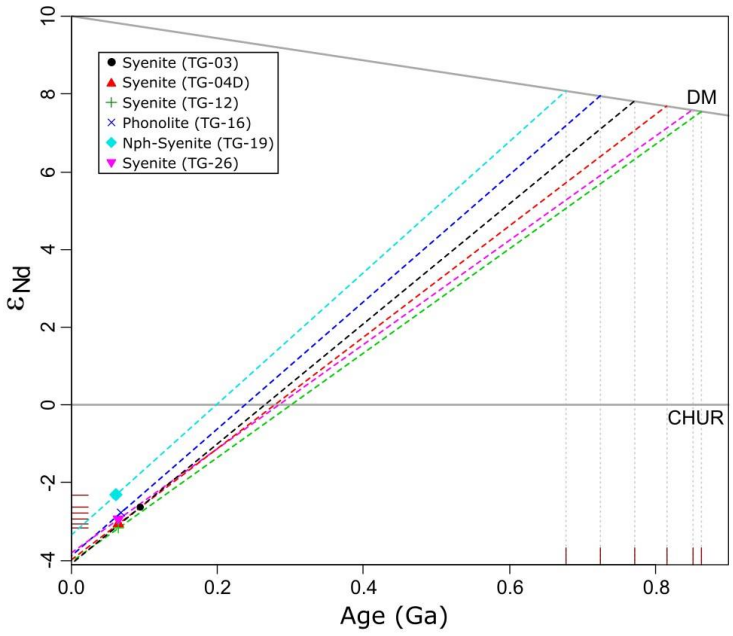

Table 8 – Sm-Nd isotopic geochemistry data for samples from Tanguá Complex

Sample	Lithotype	Sm (ppm)	Nd (ppm)	Rb (ppm)	Sr (ppm)	$^{143}Nd/^{144}Nd_{(m)}$	$^{147}Sm/^{144}Nd_{(m)}$	$^{143}Nd/^{144}Nd_{(i)}$	$\varepsilon_{Nd(i)}$	T_{DM} (Ma)	$^{87}Sr/^{86}Sr_{(m)}$	$^{87}Sr/^{86}Sr_{(i)}$	Age (Ma)
TG03	Syenite	10,6	83,5	116,5	1405,0	0,512429	0,0764	0.512382	-2.62	772	0.705155	0.704832	94.82
TG04D	Syenite	18,2	129,4	132,0	1475,0	0,512434	0,0850	0.512398	-3.06	816	0.705478	0.705241	64.40
TG12	Syenite	17,0	112,3	109,5	1965,0	0,512431	0,0916	0.512392	-3.17	862	0.705326	0.705177	65*
TG16	Phonolite	9,6	83,9	158,0	102,5	0,512439	0,0691	0.512408	-2.77	725	0.709476	0.705158	68.11
TG19	Nph-Syenite	1,5	13,7	133,0	821,0	0,512467	0,0649	0.512441	-2.31	677	0.705237	0.704829	61.27
TG26	Syenite	15,4	100,8	112,5	3910,0	0,512443	0,0923	0.512404	-2.94	852	0.705211	0.705134	65*

4.1.5 Discussions

4.1.5.1 Complex lithofaciological division and their features

As explained in section 2.2, the new lithofaciological map of the Tanguá Complex (Figure 18) displays three distinct syenitic units with a nearly concentric shape and an undivided zone in the NW portion of the Complex. The concentric units are formed, from the edge to the center, by syenite, intermediate nepheline syenite, and central nepheline syenite, while the NW portion consists of undivided nepheline syenite. A more unsaturated zone in the central position may indicate fewer interactions with the embedded rocks than the less unsaturated rocks (without nepheline) at the edges.

The nepheline syenite zone typically has more homogenous rocks and less leucocratic rocks than syenites, where it is easier to identify feldspar and mafic minerals. Based on the XRD studies, the central nepheline has analcime-rich rocks, whereas the intermediate nepheline syenite has albite-rich rocks with a low analcime content. According to DUMANSKA-SŁOWIK et al. (2023), the presence of analcime may be related to the alteration of feldspathoids, such as nepheline and sodalite, into nepheline syenites, suggesting a correlation between these more central zones of the massif. In contrast, the syenite unit consists of syenitic rocks without nepheline and cannot be divided. These mineralogical segregations and concentric formation suggest the process of crustal contamination, indicating a more significant interaction with the host rocks during the emplacement of the complex, increasing the silica content and decreasing that of nepheline. This crustal contamination is suggested by MOTOKI et al. (2015b).

The suggested NW zone comprises syenitic rocks with nepheline and analcime contents, similar to the nepheline zones, but it is not yet possible to indicate a segregation. Moreover, the U-Pb ages obtained for this work indicate that more than one intrusion occurred. One at *ca. 95* Ma, representing the syenite lithotype, and a second one at *ca*. 60-70 Ma composed of syenite, nepheline syenite, monzonite, and phonolite. This specific feature may be directly associated with the area in the NW portion, which shares similarities with the central part of the complex. This can indicate a distinct intrusion whose age is not defined but possibly syn- or post-genetic. Monzonite does not have a distinct characteristic structure in the massif to indicate a specific unit for this rock, and it was identified in the syenite zone.

The lithology's positioning in the syenitic zone, its higher SiO_2 content, and the presence of normative quartz may indicate potential crustal contamination for this sample.

The breccias are located on the complex edges, more specifically on the southern and eastern edges, as VALENÇA (1980) and HEINECK & RAPOSO (1981) suggested. According to MOTOKI et al. (2015a) and GERALDES et al. (2013), the breccias are associated with later subvolcanic conduits, which crosscut the basement and the alkaline stocks on the edges of the complex. Similar conduits have been identified in several PCCFA massifs, including Itatiaia, Mendanha, Itaúna, Tanguá, Morro dos Gatos, and Cabo Frio Island (MOTOKI et al., 2007b; MOTOKI & SICHEL, 2008; SICHEL et al., 2008). The breccia was found in the NW massif portion during the survey but could not be defined as a specific area. The breccias occur weathered, making identifying some features difficult; even so, foliation and fractures are observed, although we have not been able to subdivide them yet.

Trachyte outcrops in two locals on the Complex (NW and SE) suggest a lower occurrence. It is commonly associated with another lithotype and may exhibit an alteration zone at the contact (Figure 22C). The phonolite mainly occurs as dikes intruding on syenite. However, the presence of syenitic veins crosscutting the phonolite may indicate syn-genetic emplacement and the presence of different pulses in the massif. The differences observed in phonolite, based on mineralogy and grain size features, may suggest different magmatic processes during its emplacement (see Figure 20).

4.1.5.2 Tanguá Complex geochronology and its relationship with the PPCFA

The U-Pb ages obtained in this work suggest that the rocks of the Tanguá massif can be divided into two groups: 1) younger (ranging from 61.27 and 69.37 Ma), formed by different samples and lithotypes (nepheline syenite, syenite, monzonite, and phonolite); 2) older (94.82 ± 1.02 Ma), with one syenite sample (Figure 18). These results reinforce the presence of different pulses during the TC emplacement.

The ages of the first group are similar to the SILVA et al. (2023), which yielded an age of 65.5 ± 1 Ma (U-Pb age of nepheline syenite), and other studies using K-Ar and Rb-Sr methods, ranging from 66.8 to 70.5 Ma (BIONDI, 2005; MOTOKI et al., 2010; SONOKI & GARDA, 1988). This interval is typically associated with most previous studies, which would be interpreted as the primary emplacement period of the massif.

On the other hand, the second group is *ca.* 25 Ma older than the oldest rock from the first group. Based on the geochronological compilation carried out for this work, the Poços de Caldas – Cabo Frio Alignment has ages between 39.1 Ma (Tinguá Complex - SONOKI & GARDA, 1988) and 90.5 Ma (Itatiaia Complex - SONOKI & GARDA, 1988), massifs distant *ca.* 110 Km (Figure 16B), indicating this geochronological result of the Tanguá syenite as the oldest age in the entire Alignment.

4.1.5.3 Genetic models for the PCCFA

As previously mentioned, two model genesis are currently suggested for the Poços de Caldas – Cabo Frio Alignment: 1) magmatism linked to Trindade Mantle Plume with decreasing ages from west to east (GIBSON et al., 1995; HERZ, 1977; SADOWSKI & DIAS NETTO, 1981; THOMAZ FILHO et al., 2005; THOMPSON et al., 1998; VANDECAR et al., 1995); and 2) associated with the reactivation of regional geological structures generating partial melting, with random ages (ALMEIDA, 1991; ALVES et al, 2006; FERRARI, 2001; RICCOMINI et al., 2005; ZALÁN & OLIVEIRA, 2005). According to the plume model, the oldest ages of the alignment should be on the west side. However, the new geochronological data from Tanguá, related to a further east massif (Figure 16B-C), reinforces the absence of decreasing ages in the alignment and raises a question about the plume model. Several works, such as ALMEIDA (1991) and RICCOMINI et al. (2005), present similar understandings regarding the alignment ages.

Most of the geochronological results from previous studies and the current one yielded ages between 60 and 70 Ma for the Tanguá Complex, suggesting a main period of emplacement. The youngest age obtained for the nepheline syenite (61.27 ± 0.48 Ma) indicates that the massif presents more recent magmatic activity than previously documented. These ages are similar to those of the nearby Soarinho Massif (58 and 60 Ma, as suggested by SILVA et al., 2023). The phonolitic rocks that crosscut the syenitic rocks have the oldest ages of this period (68.11 Ma and 69.37 Ma). This confirms the syngenetic emplacement of these two rocks, as observed in the field mapping, and strengthens the idea of different magmatic pulses associated with the formation of the complex. The ages of the younger group, along with the oldest of the Tanguá massif (approximately 95 million years old), as well as the distribution of geochronological data from the other PCCFA massifs, which do not decrease

towards the east, suggest that the association of the genesis of this alignment with a conventional and stationary mantle plume is not supported.

4.1.5.4 Isotopic results and the Mantle sources components

The Lu-Hf and Sr-Nd pairs show similar behaviors during the mantle differentiation processes, allowing us to indicate which magma sources are involved in the rocks' emplacement. According to FAURE & MENSING (2005) and JONES et al. (2019), rocks with negative ε_{Nd} and ε_{Hf} values are associated with enriched mantle sources or derived from continental crust, while positive values are linked to depleted mantle sources.

Syenites and nepheline syenites isotopic ratios plotted between Depleted Mantle (DMM) and Enriched Mantle I (EMI) – DMM-EMI array – components in the $^{143}Nd/^{144}Nd$ versus $^{87}Sr/^{86}Sr$ diagram (Figure 36A), where these ratios have restricted variations. On the other hand, the phonolite sample presents different behavior and falls between DMM and Enriched Mantle II (EMII) – DMM-EMII array. These features indicate different emplacement processes and sources for these rocks. This behavior is similar to other massifs from the PCCFA, such as Poços de Caldas, Mendanha, Itatiaia, Morro Redondo, Soarinho, and Morro de São João (MOTA, 2012; ROSA, 2017; THOMPSON et al., 1998; ULBRICH et al., 2003). It could also suggest a mixture of different components for the TC rocks, similar to indicated for Brazilian alkaline bodies, such as the Soarinho Complex (SILVA et al. 2023) and Vitória Seamount (MAIA et al. 2021). However, Pb isotope data is required to confirm this mixture. For the $^{176}Hf/^{177}Hf$ versus $^{143}Nd/^{144}Nd_{(m)}$ diagram (Figure 36B), the samples fall close to the Enriched Mantle (EM) field, which reinforces the association of this magma component with the Tanguá Complex. The EMI sources could be linked with oceanic sediments associated with subducted slabs. This sediment's involvement is also suggested for the rocks of Vitória-Trindade Ridge (MAIA et al., 2021; QUARESMA et al., 2023). For MAIA et al. (2021), these characteristics would also indicate the presence of a mantle plume.

From the normalized diagrams by the primitive mantle, the rocks of the Tanguá Complex do not exhibit patterns similar to a single mantle source, thus reinforcing the possibility of a mixture of different sources. The normalized trace elements (Figure 31) present a P anomaly, similar to the enriched mantle sources. In contrast, the ascending pattern of the most incompatible elements observed in some rocks (trachyte, phonolite, and nepheline

syenite) is similar to the DMM. It is worth noting, however, that the Ba, P, and Ti anomalies are not observed in any mantle source and may indicate specific fractionation. For the REE normalized by the primitive mantle (Figure 32), most results have a similar pattern to the enriched sources, which have a descending pattern (LREE richest). On the other hand, some rocks (trachyte, phonolite, and nepheline syenite) show an ascending pattern for heavy REE, similar to DMM, with an ascending pattern (HREE richest).

All studied lithotypes (syenite and phonolite) show negative ε_{Nd} values, ranging from -3.17 to – 2.62, which associates these rocks with enriched mantle sources or continental crust. In contrast, the ε_{Hf} values vary between - 17.78 and + 11.4, with some lithotypes presenting negative and positive values and others only negative ones (Figure 37). This last behavior reinforces the component's participation already indicated by ε_{Nd} and suggests the involvement of depleted mantle sources. The Tanguá Complex rocks exhibit more restrictive ε_{Nd} values than ε_{Hf}, followed by the $^{143}Nd/^{144}Nd_{(m)}$ and $^{176}Hf/^{177}Hf$ ratios (Figure 37B). ZHANG et al. (2019) and DAHLQUIST et al. (2020) link these characteristics to inherited zircons from oceanic sediments associated with subducted slabs. The melt resulting from this process causes metasomatism, which leads to an increase in the $^{176}Hf/^{177}Hf$ ratio due to the retention of ^{177}Hf in the residual grains, generating decoupling from the $^{143}Nd/^{144}Nd$ ratio. According to CHAUVEL et al. (2008), zircon-rich detrital material could be associated with a low-ε_{Hf} reservoir and represent a component of continental crust (or Enriched Mantle source). The mantle recycling of subducted oceanic crust with sediment is also associated with the EMI end-member generation (MAIA et al., 2021). Soarinho Complex also has ε_{Hf} values ranging between – 32 and + 5.6, indicating the mixing of different magmas or crustal contaminations by host rocks (SILVA et al., 2023).

Model ages (T_{DM}) determine the time frame during which the magma originated from its source, which helps establish its geotectonic context. The Nd_{TDM} yielded ages between *ca*. 670 Ma and 860 Ma, which is coincident with Alignment model ages (*e.g.*, Itatiaia complex) and with the Brasiliano collisional events (COMIN-CHIARAMONTI et al., 2005; ROSA, 2017) and Neoproterozoic magmatic arc systems of the Ribeira Belt (860-595 Ma - HEILBRON et al., 2020). On the other hand, the Lu-Hf system presents model ages with a greater range (280-1570 Ma) in addition to ages older than these events. Based on the ages of the magmatic arcs, QUARESMA et al. (2023) suggest that oceanic slabs began their formation earlier and indicate that they may be older than 1.3 Ga. Furthermore, these last authors also suggest that the mantle source that originated the Paraná basalts and alkaline rocks on the edge of the Paraná Basin were metasomatized by slab-derived fluids associated

with the Brasiliano Event and have EMI affinity and similar Nd model age (between 0.8 Ga and 1.3 Ga). However, it is currently not possible to confirm the association between the Hf_{TDM} and the formation of Brasiliano oceanic slabs.

Figure 36 – A) Nd-Sr isotopic ratio correlation diagram. B) Correlation diagram of $^{143}Nd/^{144}Nd_{(m)}$ versus $^{176}Hf/^{177}Hf$.

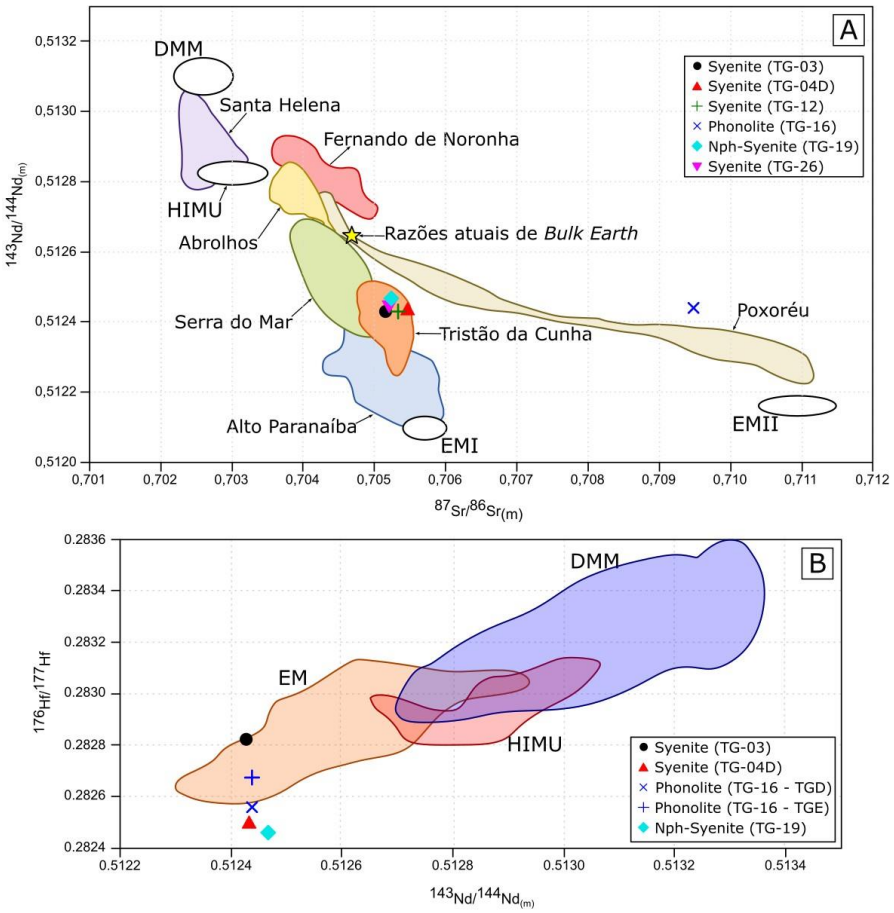

Fonte: A) The isotopic ratio data presented are: Abrolhos (FODOR et al., 1989), Alto Paranaíba (GIBSON et al., 1995), Alkaline rocks from Serra do Mar igneous complex (THOMPSON et al., 1998), Poxoréu (GIBSON et al., 1997), Fernando de Noronha (GERLACH et al., 1987), Tristan da Cunha (LE ROEX et al., 1990), and Santa Helena (CHAFFEY et al., 1989). Mantle components: Bulk Earth (ZINDLER AND HART, 1986), EMI (EISELE et al., 2002; HOFFMAN, 2014), DMM (ZINDLER AND HART, 1986; SALTERS AND STRACKE, 2004; WORKMAN AND HART, 2005), EMII (ZINDLER AND HART, 1986; HART, 1988) and HIMU (HART, 1988; JACKSON AND DASGUPTA, 2008). Modified from MAIA et al. 2021; B) Modified from STRACKE et al. 2012, from which the ranges of mantle components were determined.

Figure 37 – A) ε_{Hf} boxplot diagram for samples from Tanguá Complex. B) ε_{Hf} histogram diagram for samples from Tanguá Complex.

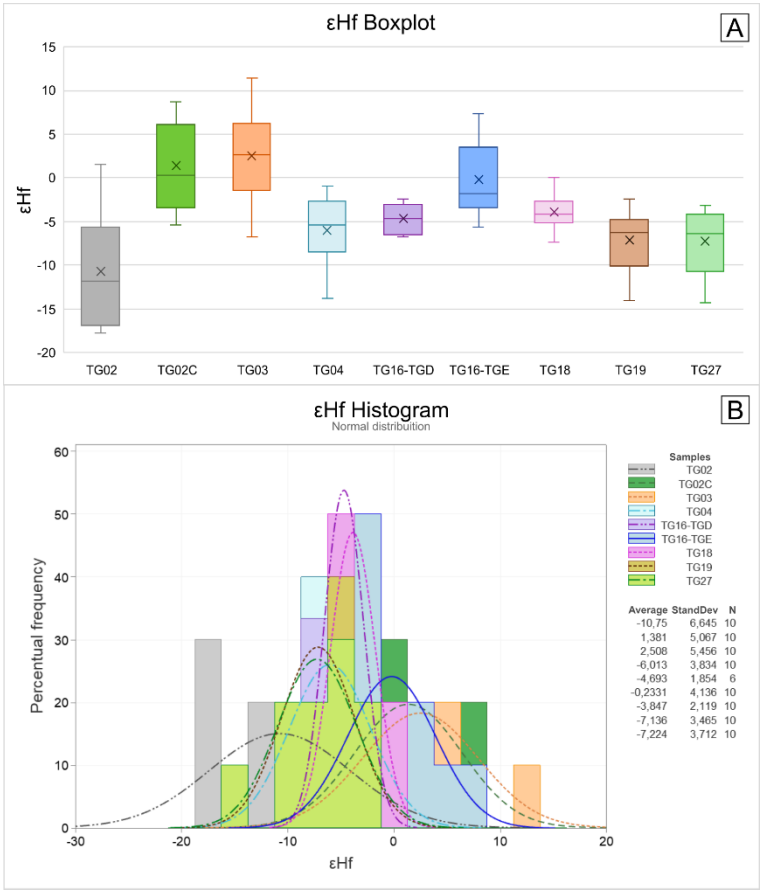

4.1.5.5 Fractional crystallization versus crustal assimilation

The previous results and discussions permit us to make some suggestions about the Tanguá Complex genesis. The Zr/TiO_2 ratio of the Tanguá Complex shows low values (< 0.5), which indicates a primitive magma associated with nepheline syenite magma (MOTOKI et al., 2015b). According to MOTOKI et al. (2010), the Silica Saturation Index (SSI) is used to understand the crystallization of nepheline or quartz. This parameter is calculated using the equation:

$$SSI = 1000 * \left(\frac{SiO_2}{60.0835} - \frac{Al_2O_3}{101.9601} - 5 * \left(\frac{Na_2O}{61.9785} + \frac{K_2O}{94.1956}\right) - \frac{CaO}{56.077} - \frac{MgO}{40.304} - \frac{MnO}{70.937} - \frac{FeO}{71.844} + 2 * \frac{Fe_2O_3}{159.687}\right) \#(1)$$

The TC nepheline syenites and phonolites (two samples) present negative SSI (Figure 38), indicating a nepheline crystallization, whereas syenites show negative and positive SSI,

suggesting different behavior with nepheline or quartz crystallization. Monzonite and phonolite (one sample) have the highest value (*ca*. 100) and are associated with quartz crystallization, which could indicate crustal contamination for undersaturated magmas (ANDERSEN & SORENSEN, 1993; MOTOKI et al., 2010; 2015b). These characteristics are confirmed by the lithogeochemical and CIPW norm, which show the highest SiO_2 content and quartz normative for syenite and monzonite. The Zr/TiO_2 versus SSI diagram (Figure 38) may indicate fractional crystallization (negative correlations) or crustal assimilation (positive correlations), and the syenites and nepheline syenites have negative correlations, reinforcing the importance of fractional crystallization.

Concave patterns in normalized REE (Figure 32) may indicate garnet fractionation (*e.g.*, KAY & GAST, 1973; HAWKESWORTH et al., 1979; TERAKADO, 1980) and are observed in nepheline syenite samples (TG-19 and TG-114), trachytes, and phonolites. Conversely, according to MOTOKI et al. 2015b crustal contamination leads to the ETR patterns becoming linear to convex. This phenomenon is observed in all syenites, monzonite, one sample of phonolite, and the remaining samples of nepheline syenite. The nepheline syenite samples (TG-19 and TG-114) mentioned also present the lowest values of REE sum and the lowest SSI, suggesting that they may be closer to the original magma's initial composition. According to ROSA (2018 and references therein), supersaturated alkaline rocks with crustal influence show ε_{Nd} decreasing according to the silica increasing. Similarly, the increase in the REE sum also indicates greater crustal assimilation (MOTOKI et al., 2015b). Both features are presented by the TC rocks (Figure 38).

According to AZZONE et al. (2018), for crustal assimilation contexts, the ratios $^{87}Sr/^{86}Sr_{(i)}$ and $^{143}Nd/^{144}Nd_{(i)}$ present broad values, together with an increase in the Ba/Sr, Rb/Sr ratios, and a decrease in the $(Ce/Pb)_N$ ratios. For the present studies, the ranges of $(Ce/Pb)_N$ vary between 0.65 and 5.42, Ba/Sr between 0.18 and 2.33, and Rb/Sr between 0.95 and 51.13. Regarding isotopes, the ratios $^{87}Sr/^{86}Sr_{(i)}$ are between 0.704832 and 0.705241 and $^{143}Nd/^{144}Nd_{(i)}$ 0.512382 and 0.512404. Although the ranges of isotopic results are more restricted than that observed by AZZONE et al. 2018, the other ratios reinforce the crustal assimilation importance, especially Ba/Sr and Rb/Sr.

Trachytes occur as later dikes, have a higher silica content and normative quartz than the other rocks, and include modal quartz as a constituent mineral, indicating that the magma was saturated with silica. Other massifs in the Alignment also contain rocks that are supersaturated in silica, such as Itatiaia (ROSA & RUBERTI, 2018) and Soarinho (SILVA et al., 2023). The presence of this rock type in these massifs is linked to the assimilation of

crustal rocks. According to ROSA (2017) and references, the transition from unsaturated to supersaturated rocks can occur in open systems through this process. The latter author states that the increase in crustal assimilation in the Itatiaia massif progressed to the point of breaking the thermal barrier. MOTOKI et al. (2015b) suggested values between 20% and 30% of crustal assimilation for rocks of the Tanguá Massif. However, isotopic studies are necessary for these rocks to confirm the source of the magma and its relationship with the other rocks.

4.1.5.6 Oceanic sediments and metasomatized melts

The relationship between the La/Yb vs La ratio allows us to determine whether fractional crystallization or partial melting has the greatest influence on the formation of the rocks being studied (DUMANSKA-SŁOWIK et al., 2023; GAO et al., 2007; YAN & JIANG, 2019). According to this analysis, the syenitic rocks display a nearly horizontal pattern in the La/Yb versus La diagram (see Figure 40A). This suggests that these rocks follow a trend of crystallization rather than partial melting, indicating a longer cooling time of the melt during the formation of this alkaline magma. On the other hand, the process associated with the phonolites' genesis follows a more partial melting trend, reinforcing these rocks' distinct origins. According to LAPORTE et al. (2014), phonolites and their plutonic equivalents (nepheline syenites) may have formed through fractional crystallization of basanites or alkaline basalts, or through the partial melting of the upper mantle. Isotopic data supports the second hypothesis, showing that phonolites plot in DMM-EMII array.

According to Riccomini et al. (2005), the Brazilian alkaline intrusions are mainly sourced from the lithospheric mantle, which is supported by isotopic data for the Tanguá Massif. In this context, LILE-bearing minerals are associated with volatile-bearing metasomatic minerals like phlogopite and amphibole. The presence of phlogopite in the source is confirmed by the Rb/Sr ratio (> 0.1), and the presence of amphibole is indicated by the Ba/Rb ratio (> 20) (YAN & JIANG, 2019). Although all lithologies show results indicating the presence of phlogopite, the ratios do not confirm the presence of amphibole. However, analysis of the Rb/Sr and Ba/Rb diagram (Figure 40B) reveals a clear correlation with phlogopite-rich sources and a subtle affinity with amphibole, as evidenced by some samples with Ba/Rb ratios close to 20. This main affinity is further supported by Figure 40C.

According to YAN & JIANG (2019), these minerals are linked to higher K and Ba contents, as observed in the Tanguá Complex. LAPORTE et al. (2014) also emphasize that in the context of the subcontinental lithospheric mantle, K enrichment is associated with the presence of these minerals. The presence of both minerals reinforces that the mantle source associated with the formation of these rocks was metasomatized (YAN & JIANG 2019 and references therein), as previously suggested using the isotopic results.

The enriched mantle components can be associated with recycled sediments in the mantle, with EMI being the oceanic type and EMII the continental type (CONDIE, 2016), and based on isotopic data, these mantle sources are associated with Tanguá Complex's rocks. The presence of isotopic decoupling further confirms the existence of these sediments (see Figure 37). According to WOODHEAD et al. (2001), high Th/Yb ratios are attributed to the melting of subducted sediments. PEARCE (2008) also reinforces that these high ratios can be linked to alkaline basalts with a recycled crustal component. From the Th/Yb–Nb/Yb graph, it is possible to verify ratios associated with the MORB-OIB array. Samples that plot above this trend indicate the interaction with the upper crustal interaction and mantle lithosphere with subduction component (PEARCE, 2008). The samples from the TC present high Th/Yb and Nb/Yb ratios, reinforcing the participation of enriched mantle sources (PEARCE, 2008) and, consequently, of subducted sediments. Although few samples are above the MORB-OIB array, according to the latter author, the participation of these sediments causes a smaller impact on enriched sources (high Th/Yb and high Nb/Yb).

According to DUMANSKA-SŁOWIK et al. (2023), metasomatism at the mantle source linked to subduction may involve plate-bound fluids or magmas from sediments. The Th/Yb versus Ba/La (Figure 40E) and U/Th versus Th (Figure 40F) diagrams suggest that the samples from the TC display distinct trends linked to sediments or sediment melts, highlighting their significant role in the mantle source. However, it's important to note that fluids rich in Cl- and/or F- that cause metasomatism at the source can create signatures similar to sediment melts, leading to potential overestimating of sediment presence. Additionally, the presence of sediments is also indicated by the Th/La vs Sm/La diagram (Figure 40G – Plank, 2005) and isotopic data (Figure 37).

Figure 38 – Zr/TiO_2 ratio versus SSI diagram (*Saturation Sílica Index* - MOTOKI et al. 2015b)

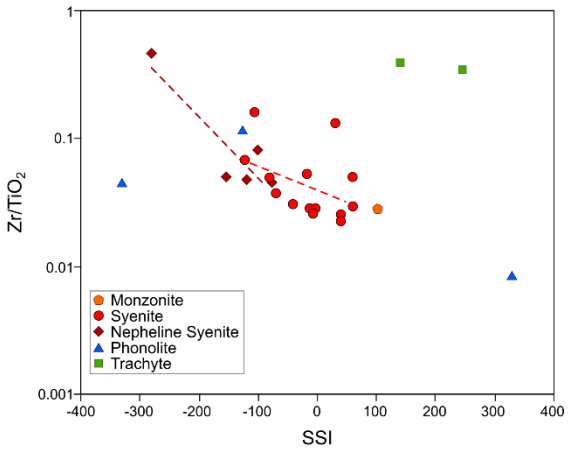

Figure 39 – SiO_2 versus ε_{Nd} (left) and REE sum versus ε_{Nd} (right) diagrams indicating negative correlations between the parameters.

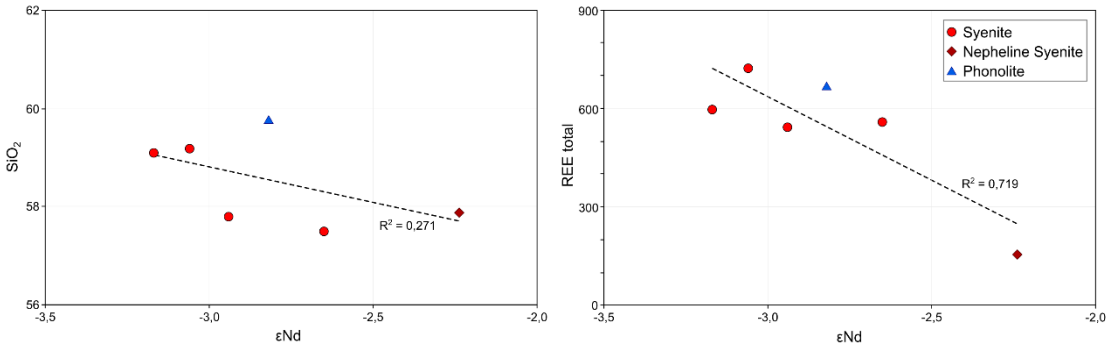

Figure 40 – Petrogenic diagrams for the rocks of Tanguá Complex. A) La/Yb versus La diagram; B) Rb/Sr versus Ba/Rb diagram; C) K/Rb versus Rb diagram; D) Th/Yb versus Nb/Yb diagram; E) Th/Yb versus Ba/La diagram; F) U/Th versus Th diagram; G) Th/La versus Sm/La diagram.

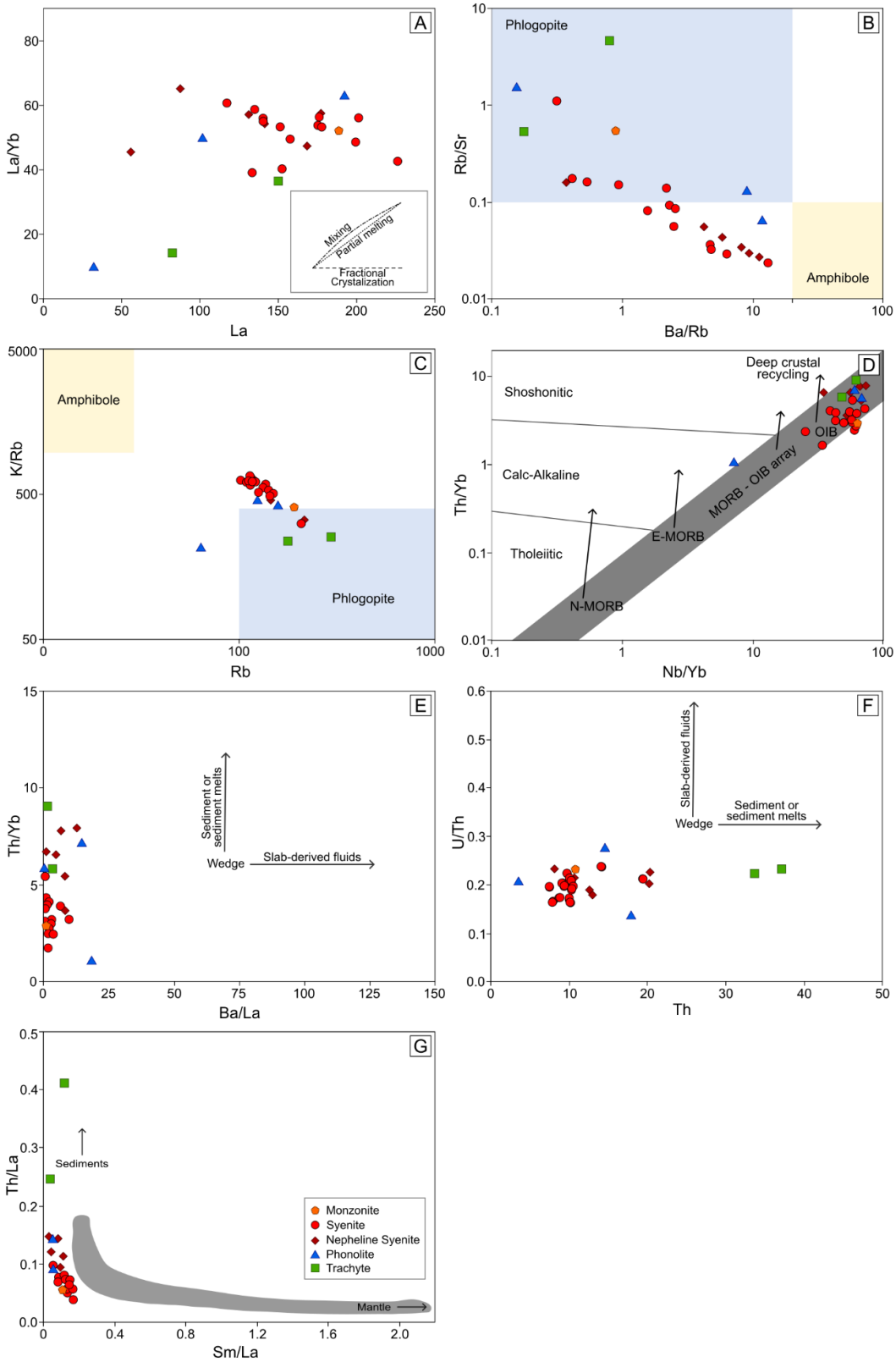

Fonte: The A-F diagrams were modified from YAN AND JIANG (2019 and references therein). The G diagram was modified from PLANK (2005 and references therein).

4.1.6 Concluding Remarks

Based on the results and discussions presented, it is possible to make some conclusions about the Tanguá Complex:

1. According to the fieldwork and petrography analyses, the TC comprises syenite, nepheline syenite, breccia, phonolite, and trachyte. The nepheline syenite is mostly located in the central portion, while the less undersaturated syenite is found in the outer portions, forming a roughly concentric structure. Nepheline syenites are divided into central (richer in analcime) and intermediate zones (richer in albite). However, an undivided nepheline syenite zone is also observed in the NW portion of the TC. The breccias are observed on the southern and eastern edges of the intrusion, and no further subdivisions have been observed yet. Phonolites and trachytes occur as dikes with centimetric- to metric-thickness and are associated with fractures, which are coincident with the regional lineaments.
2. Based on the field relationships and geochronological data, it is suggested that the intrusion of syenitic rocks and phonolites is syngenetic, presenting ages of 61.3 – 67.1 Ma and 68.1 – 69.4 Ma, respectively. In addition to the oldest age (ca. 95 Ma), these ages imply the occurrence of diverse magmatic pulses during the Complex's formation. We believe this pulse occurrence can account for the presence of nepheline syenite in the NW Complex portion. However, more information is required to confirm.
3. The Lu-Hf isotopic geochemistry data reveals that the rocks are linked with enriched and depleted mantle sources, as indicated by isotopic results. The lithotypes show distinct signatures suggesting different sources for them. The syenites and nepheline syenites display a similar behavior, implying a mixture between DMM and EMI. In contrast, phonolite exhibits a distinct behavior, indicating a mixture of DMM and EMII. The model's ages suggest that the rocks of the Tanguá Complex may be associated with the magmatic arcs formed during the development of the Ribeira Belt. This could be supported by the geochemical data, which indicate the presence of oceanic sediments linked to subducted slabs.
4. The geochemical and isotopic data suggest a restricted influence of fractional crystallization and important crustal assimilation, corroborating previous studies in the PCCFA complexes, including the Tanguá Complex. This is supported by the lithotype arrangement with more undersaturated rocks (nepheline syenites) in the alkaline

complex central zones, while the less undersaturated rocks (syenites) are in the outer portion. The results also suggest that the initial magma had a composition of nepheline syenite, although syenites (including nepheline syenites) and phonolites have different sources. Furthermore, these data also indicate that the TC was formed by the interaction of oceanic sediments with subducted slabs and metasomatized magmas in the source zone, homogenized before eruption.

5. Geochronological U-Pb data reveals that the TC was formed during two magmatic events during distinct periods: i) Cenomanian magmatism, of 94.82 Ma; ii) Danian-Maastrichtian magmatism, *ca*. 60-70 Ma. These data suggest that the TC intruded earlier than previously reported. Subsequently, the second pulse occurred in the Complex, forming nepheline syenites crosscut by phonolite and trachyte dikes. Based on MOTOKI et al. (2015a) and GERALDES et al. (2013), we estimate that the trachytes and breccias were formed during the last period or are younger than previous studies. However, new analyses are necessary to confirm this suggestion.
6. A syenite from the Tanguá Complex has 94.8 Ma, which makes it the oldest known age from the PCCFA and raises questions about the plume model, as the intrusion is in the eastern part of the alignment. Other authors have also questioned the plume model and propose that the formation of massifs is due to the partial melting of rocks caused by pre-existing fault reactivation (*e.g.*, RICCOMINI et al., 2005; AZZONE et al., 2018). Based on previous geochronological data and this new U-Pb age, we propose that the conventional plume concept does not align with the genesis of the PCCFA.

4.1.7 Acknowledgements

This paper was supported by CNPq (ProTrindade Program) [Process number. 557146/2009-7]; the MCT/CNPq project [number 26/2009]; and FAPERJ [Entidades Estaduais 2018 number 210.297/2018; APQ1 2019 number 210.179/2019; JCNE 2022 number 201.469/2022]. The corresponding author thanks Rio de Janeiro State University for supporting his research and FAPERJ for the doctoral fellowship. The authors thank the laboratories and collaborators of ISIPM (CIT SENAI), LGPA, LAGIR, and Multilab (all from UERJ) for the support offered during sample preparation, analysis, and data processing. The authors would like to take this opportunity to thank the journal's editors and reviewers for their critical review.

CONSIDERAÇÕES FINAIS

O Complexo Alcalino de Tanguá, localizado no estado do Rio de Janeiro, faz parte do Alinhamento Magmático Poços de Caldas – Cabo Frio. Este complexo é constituído principalmente por (álcali-feldspato) sienitos, nefelina sienitos e brechas magmáticas. Além dessas rochas, observa-se a ocorrência restrita de monzonito. Diques de fonolito e traquito, especialmente os primeiros, cortam as demais litologias.

O novo mapa litofaciológico do Complexo Tanguá mostra que o nefelina sienito ocorre predominantemente na porção central. Este litotipo é subdividido em dois tipos: central, com maior teor de analcima, e intermediário, com maior conteúdo de albita. O sienito, menos insaturado, é encontrado principalmente nas porções externas da intrusão, formando uma estrutura praticamente concêntrica. Essa disposição, associada aos dados analíticos, indica que os nefelina sienitos possuem composição próxima ao magma original do maciço. Adicionalmente, a interação deste magma com as rochas encaixantes possibilitou a assimilação de sílica e resultou na formação dos sienitos sem nefelina nas áreas externas.

Além da porção central do complexo, amostras de nefelina sienito também são encontradas na região NW do maciço, indicando a presença de uma zona distinta dentro do complexo. A relação dessas rochas com os sienitos e sua localização no maciço sugerem que sua gênese está associada a uma intrusão posterior à principal, que originou os nefelina sienitos e os sienitos. No entanto, a confirmação dessa hipótese depende de estudos adicionais, considerando as dificuldades de acesso e a limitada disponibilidade de dados. Essas intrusões também podem estar ligadas às estruturas circulares que podem ser observadas em outros locais do maciço, mas que não estão relacionadas às brechas magmáticas.

Fonolitos e traquitos ocorrem na forma de diques com escalas centimétricas a métricas e estão associados aos lineamentos regionais que são coincidentes com as direções das fraturas do maciço, reforçando a importância destas estruturas na formação do Complexo Tanguá. Já as brechas magmáticas são observadas majoritariamente nas bordas sul e leste da intrusão e não apresentam características suficientes para uma subdivisão. Estas rochas também são observadas de maneira bem restrita na porção norte do Complexo e conforme indicado por outros trabalhos como MOTOKI et al. (2008), tratam-se de rochas posteriores à formação principal do maciço. Apesar da identificação de monzonito em uma amostra na

porção SW do maciço a partir de análise por DRX, a rocha não tem representatividade suficiente para mapa.

Os resultados litogeoquímicos e suas diferentes classificações convergem em mostrar uma influência restrita de cristalização fracionada e importante de assimilação crustal, confirmando a indicação de alguns estudos prévios executados neste e em outros maciços do Alinhamento. Conforme previamente mencionado, a assimilação pode ser um dos fatores da ocorrência de rochas mais insaturadas, com nefelina, na porção central do Complexo, enquanto as menos insaturadas encontram-se na porção externa, além da presença pontual e restrita de monzonito no maciço. Adicionalmente, o traquito, única rocha do maciço com quartzo identificado por meio das análises mineralógicas, também pode ter sua gênese associada à assimilação crustal. No entanto, são necessários estudos adicionais para confirmar essa proposição.

Os dados geocronológicos de U-Pb, obtidos a partir de zircões de diferentes amostras do Complexo Tanguá, revelaram dois grupos distintos. O primeiro grupo, mais jovem, apresenta idade próxima a 65 Ma (Daniano-Maastrichtiano), em concordância com estudos anteriores. O segundo grupo, mais antigo, é formado por uma única amostra (TG-03) e apresenta idade de 94,8 Ma (Cenomaniano). Esses resultados geocronológicos, combinados com os dados de campo e informações de outros trabalhos, indicam que o Complexo Tanguá se formou a partir de diferentes pulsos magmáticos. Essa característica genética também é observada em outros maciços do Alinhamento, como Mendanha e Itatiaia (*e.g.* Mota et al. 2012 e Rosa, 2017).

O segundo grupo apresentado e que está associado à idade mais antiga do maciço, conforme mostrado no artigo 2, é também a idade mais antiga já obtida para o APCCF. A restrição desta idade pode indicar que estas rochas foram obliteradas por pulsos subsequentes e/ou que teve seus grãos de zircão resetados por estas intrusões mais juvenis. Esta idade, e por conseguinte a explicação anterior, sugerem que o modelo de pluma convencional, como o *hotspot* do Havaí, pode não explicar a formação do Alinhamento. Isso ocorre pois, o maciço mais antigo não está na porção oeste e consequentemente não se tem uma diminuição progressiva de oeste para leste. Essa característica também é apontada a partir da compilação de dados geocronológicos realizada a partir do artigo 1 apresentado por este trabalho.

Em contrapartida, o grupo de análises mais recentes pode ser associado à gênese principal do Complexo Tanguá, a qual pode ter suprimidos as rochas provenientes de intrusões mais velhas. Dentro deste grupo mais jovem, existe uma diferença de quase 10 Ma reforçando a presença de diferentes pulsos. Além disso, as idades mais antigas são

apresentadas pelos fonolitos e a mais jovem pelo sienito. Estes dados confirmam a origem singenética destas rochas, uma vez que os fonolitos ocorrem como diques cortando as rochas sieníticas (ou seja, mais jovens relativamente) e ainda ocorrem sendo cortados por estas, conforme observado nas campanhas de campo. Adicionalmente, os diques de fonolitos com aproximadamente 70 Ma reforçam a presença de rochas sieníticas no maciço mais antigas do que a intrusão principal, indicando, mais uma vez, a presença de pulsos magmáticos de diferentes idades neste Complexo.

Os dados de química isotópica por Sr-Nd do Complexo Tanguá apontam que os sienitos e os nefelina sienitos apresentam assinaturas semelhantes. Esses litotipos estão alinhados ao *trend* DMM-EM1, reforçando uma possível ligação genética entre eles. Por outro lado, o fonolito apresenta uma assinatura isotópica distinta. Essa rocha está relacionada ao *trend* DMM-EM2, sugerindo uma origem diferente dessas rochas no contexto do Complexo Tanguá. Estes resultados estão coerentes a estudos realizados em outros maciços reforçando, mais uma vez, uma gênese semelhante entre as intrusões do APCCF. A associação das rochas do Complexo Tanguá com fontes de manto enriquecido é confirmada pelos dados de Lu-Hf e de ε_{Nd}, sendo que os valores negativos deste último parâmetro ainda podem sugerir associação com rochas de crosta continental.

Dentre os dados isotópicos chama a atenção o comportamento distinto entre ε_{Nd} e ε_{Hf}, uma vez que o primeiro apresenta apenas valores negativos e o segundo valores negativos a positivos. Segundo as referências apresentadas no artigo 2, o desacoplamento entre as razões de $^{143}Nd/^{144}Nd$ and $^{176}Hf/^{177}Hf$ está ligada à presença de zircões herdados de sedimentos oceânicos associados a *slabs* de crosta subduzidas, causando também metassomatismo nos magmas. Além disso, estes zircões herdados podem representar os componentes crustais associados a uma fonte com baixa reserva de Hf. Esta associação com sedimentos para a fonte das rochas do Complexo Tanguá também é confirmada a partir de diferentes parâmetros químicos, bem como a presença de *melts* metassomatizados.

Em síntese, os resultados deste estudo indicam que o Complexo Tanguá se formou por meio de diferentes pulsos magmáticos, com idades distintas. É possível que algumas dessas rochas sejam ainda mais jovens do que os dados atualmente disponíveis. Outro ponto relevante é que as litologias estão associadas a fontes distintas, o que sugere uma dinâmica diferente para o maciço. Essa característica é semelhante à observada em outras intrusões alcalinas do APCCF. Cabe ressaltar ainda que a interação com as rochas encaixantes da Faixa Ribeira mostram uma aparente importância para a formação e a disposição das litologias. Essa interação resultou em uma estrutura praticamente concêntrica, com rochas menos insaturadas

localizadas nas bordas do complexo. É importante destacar também a semelhança deste com outros complexos do Alinhamento, como parâmetros litogeoquímicos e isotópicos, o que reforça uma gênese semelhante entre eles, o que também é sugerido por outros trabalhos (Guarino et al., 2019).

Os resultados geocronológicos apresentados não sustentam o modelo convencional de pluma para o APCCF, como indicado pela idade mais antiga do alinhamento (94,8 Ma). No entanto, alguns trabalhos apontam a presença de uma anomalia térmica abaixo da Cadeia Vitória-Trindade por meio de dados de tomografia, o que pode estar ligado à uma pluma na região da Ilha de Trindade (Celli et al., 2020; Quaresma et al., 2023). Além disso, trabalhos como Thompson et al. (1998) apontam que esta mesma pluma poderia estar associada à região *onshore* no período de formação dos maciços do alinhamento. Uma hipótese alternativa proposta neste trabalho é a presença de uma pluma não convencional, cuja cabeça poderia se dividir em múltiplos condutos, utilizando estruturas pré-existentes para o transporte do magma. Tal característica poderia explicar a presença de intrusões simultâneas em locais distintos do Alinhamento. Essa ideia reitera a importância dessas estruturas regionais e pode indicar que ambos os modelos apresentados pela literatura, pluma e reativação de falhas, podem estar associados à formação do Complexo Tanguá e do APCCF como um todo. No entanto, estudos litogeoquímicos, geocronológicos e isotópicos adicionais são necessários em outros complexos para trazer um melhor embasamento para esta sugestão.

REFERÊNCIAS

ALMEIDA, F. D. O sistema de riftes continentais que limitam a Bacia de Santos, Brasil. *Anais da Academia Brasileira de Ciências*, v. 48, p. 15-26, 1976.

ALMEIDA, F. F. M. de. Relações tectônicas das rochas alcalinas Mesozóicas da região meridional da Plataforma Sul-Americana. *Revista Brasileira de Geociências*, v. 13, p. 139–158, 1983. DOI: https://doi.org/10.25249/0375-7536.1983133139158.

ALMEIDA, F. F. M. de. Distribuição regional e relações tectônicas do magmatismo pós-paleozóico no Brasil. *Revista Brasileira de Geociências*, v. 16, p. 325–349, 1986.

ALMEIDA, F. F. M. de. O alinhamento magmático de Cabo Frio. In: SBG/Núcleos SP e RJ, 2° Simpósio de Geologia do Sudeste. *Atas*, p. 423–428, 1991.

ALMEIDA, F. F. M. de; CARNEIRO, C. D. R.; MIZUSAKI, A. M. P. Correlação do magmatismo das bacias da margem continental brasileira com o das áreas emersas adjacentes. *Brazilian Journal of Geology*, v. 26, p. 125–138, 1996. DOI: https://doi.org/10.25249/0375-7536.19963125138.

ALVES, E. da C.; MAIA, M.; SICHEL, S. E.; CAMPOS, C. M. P. de. Zona de fratura de Vitória-Trindade no Oceano Atlântico sudeste e suas implicações tectônicas. *Revista Brasileira de Geofísica*, v. 24, p. 117–127, 2006. DOI: https://doi.org/10.1590/S0102-261X2006000100009.

AMARAL, G.; BUSHEE, J.; CORDANI, U. G.; KAWASHITA, K.; REYNOLDS, J. H. Potassium-argon ages of alkaline rocks from southern Brazil. *Geochimica et Cosmochimica Acta*, v. 31, p. 117–142, 1967. DOI: https://doi.org/10.1016/S0016-7037(67)80041-3.

ANDERSEN, T.; SØRENSEN, H. Crystallization and metasomatism of nepheline syenite xenoliths in quartz-bearing intrusive rocks in the Permian Oslo rift, SE Norway. *Norsk geologisk tidsskrift*, v. 73, n. 4, p. 250-266, 1993.

ANDERSEN, T.; ERAMBERT, M.; LARSEN, A. O.; SELBEKK, R. S. Petrology of nepheline syenite pegmatites in the Oslo Rift, Norway: zirconium silicate mineral assemblages as indicators of alkalinity and volatile fugacity in mildly agpaitic magma. *Journal of Petrology*, v. 51, n. 11, p. 2303–2325, 2010. DOI: https://doi.org/10.1093/petrology/egq058.

ANDERSEN, T.; ELBURG, M.; ERAMBERT, M. Contrasting trends of agpaitic crystallization in nepheline syenite in the Pilanesberg Alkaline Complex, South Africa. *Lithos*, v. 312, p. 375–388, 2018.

ANDERSEN, T.; ELBURG, M.; ERAMBERT, M. The miaskitic-to-agpaitic transition in peralkaline nepheline syenite (white foyaite) from the Pilanesberg Complex, South Africa. *Chemical Geology*, v. 455, p. 166–181, 2017.

ARAÚJO, A. L. Geologia, geoquímica e petrologia das rochas alcalinas da ilha do Cabo Frio e das áreas continentais adjacentes, Arraial do Cabo-RJ. 1995. Dissertação (Mestrado) – Universidade Federal Fluminense, Niterói.

AVELAR, A. N. Caracterização dos minerais do grupo da apatita e carbonatos no minério sílico-carbonatado de Catalão, GO, e sua relevância no processo de flotação. 2018.

AZZONE, R. G.; RUBERTI, E.; DA SILVA, J. C. L.; DE BARROS GOMES, C.; ROJAS, G. E. E.; DE HOLLANDA, M. H. B. M.; TASSINARI, C. C. G. Upper Cretaceous weakly to strongly silica-undersaturated alkaline dike series of the Mantiqueira Range, Serra do Mar alkaline province: Crustal assimilation processes and mantle source signatures. *Brazilian Journal of Geology*, v. 48, p. 373–390, 2018. DOI: https://doi.org/10.1590/2317-4889201820170089.

BAS, M. L.; LE MAITRE, R.; STRECKEISEN, A.; ZANETTIN, B.; IUGS Subcommission on the Systematics of Igneous Rocks. A chemical classification of volcanic rocks based on the total alkali-silica diagram. *Journal of Petrology*, v. 27, n. 3, p. 745-750, 1986.

BEST, M. G. *Igneous and Metamorphic Petrology*. 2. ed. Brigham: Wiley-Blackwell, 2013.

BIONDI, J. C. Brazilian mineral deposits associated with alkaline and alkaline-carbonatite complexes. *Mesozoic to Cenozoic Alkaline Magmatism in the Brazilian Platform*. FAPESP, São Paulo, Brazil, p. 707–750, 2005. DOI: https://doi.org/10.2138/am.2007.485.

BRIGGS, R. M.; MCDONOUGH, W. F. Contemporaneous convergent margin and intraplate magmatism, North Island, New Zealand. *Journal of Petrology*, v. 31, n. 4, p. 813–851, 1990.

BROTZU, P.; BARBIERI, M.; BECCALUVA, L.; GARBARINO, C.; GOMES, C. B.; MACCIOTTA, G.; MELLUSO, L.; MORBIDELLI, L.; RUBERTI, E.; SIGOLO, J. B. Petrology and geochemistry of the Passa Quatro alkaline complex, southeastern Brazil. *Journal of South American Earth Sciences*, v. 6, p. 237–252, 1992. DOI: https://doi.org/10.1016/0895-9811(92)90044-Y.

BROTZU, P.; BECCALUVA, L.; CONTE, A. M.; FONSECA, M.; GARBARINO, C.; GOMES, C. B.; LEONG, R.; MACCIOTTA, G.; MANSUR, R. L.; MELLUSO, L.; MORBIDELLI, L.; RUBERTI, E.; SIGOLO, J. B.; TRAVERSA, G.; VALEN. Petrological and Geochemical Studies of Alkaline Rocks from Continental Brazil. 8. The Syenitic Intrusion of Morro Redondo, RJ. *Geochimica Brasiliensis*, v. 3, p. 63–80, 1989. DOI: https://doi.org/10.1016/S0024-4937(97)00007-8.

BROTZU, P.; MELLUSO, L.; BENNIO, L.; GOMES, C. B.; LUSTRINO, M.; MORBIDELLI, L.; MORRA, V.; RUBERTI, E.; TASSINARI, C.; D'ANTONIO, M. Petrogenesis of the Early Cenozoic potassic alkaline complex of Morro de São João, southeastern Brazil. *Journal of South American Earth Sciences*, v. 24, p. 93–115, 2007. DOI: https://doi.org/10.1016/j.jsames.2007.02.006.

BROTZU, P.; MELLUSO, L.; D'AMELIO, F.; LUSTRINO, M.; COMIN-CHIARAMONTI, P.; GOMES, C. B. Potassic dikes and intrusions of the Serra do Mar Igneous Province (SE Brazil). *Mesozoic to Cenozoic Alkaline Magmatism in the Brazilian Platform* (P. Comin-Chiaramonti & C. B. Gomes, eds.). Edusp/Fapesp, São Paulo, p. 443–472, 2005. DOI: https://doi.org/10.2138/am.2007.485.

BUSHEE, J. Geochronological and petrographic studies of alkaline rocks from Southern Brazil. I. Potassium-argon ages of some alkaline rocks from Southern Brazil. II. A geochronological study of the alkaline massif of Poços de Caldas, Brazil. III. Geology and petrography. Unpublished PhD Thesis, 143p., 1971.

CELLI, N. L.; LEBEDEV, S.; SCHAEFFER, A. J.; RAVENNA, M.; GAINA, C. The upper mantle beneath the South Atlantic Ocean, South America and Africa from waveform tomography with massive data sets. *Geophysical Journal International*, v. 221, n. 1, p. 178–204, 2020.

CEULENEER, G.; MONNEREAU, M.; RABINOWICZ, M.; ROSEMBERG, C. Thermal and petrological consequences of melt migration within mantle plumes. *Philosophical Transactions of the Royal Society of London. Series A: Physical and Engineering Sciences*, v. 342, p. 53–64, 1993. DOI: https://doi.org/10.1098/rsta.1993.0004.

CHAFFEY, D. J.; CLIFF, R. A.; WILSON, B. M. Characterization of the St. Helena source. In: Saunders, A. D.; Norry, M. J. (Eds.), *Magmatism in the Ocean Basins*, vol. 42. Geological Society, London, Special Publications, p. 257–276, 1989. DOI: https://doi.org/10.1144/GSL.SP.1989.042.01.16.

CHAKRABARTY, A.; MITCHELL, R. H.; REN, M.; SAHA, P. K.; PAL, S.; PRUSETH, K. L.; SEN, A. K. Magmatic, hydrothermal and subsolidus evolution of the agpaitic nepheline syenites of the Sushina Hill Complex, India: implications for the metamorphism of peralkaline syenites. *Mineralogical Magazine*, v. 80, n. 7, p. 1161–1193, 2016.

CHAUVEL, C.; LEWIN, E.; CARPENTIER, M.; ARNDT, N. T.; MARINI, J. C. Role of recycled oceanic basalt and sediment in generating the Hf–Nd mantle array. *Nature Geoscience*, v. 1, n. 1, p. 64–67, 2008.

CHIESSI, C. M. Tectônica cenozóica do Maciço Alcalino de Passa Quatro (SP-MG-RJ). *Dissertação (Mestrado)* – Instituto de Geociências, Universidade de São Paulo, São Paulo, 116 p., 2004. DOI: 10.11606/D.44.2004.tde-10042014-161924.

COMIN-CHIARAMONTI, P.; GOMES, C. B.; CENSI, P.; GASPARON, M.; VELÁZQUEZ, V. F. Alkaline complexes from the Alto Paraguay province at the border of Brazil (Mato Grosso do Sul State) and Paraguay. *Mesozoic to Cenozoic Alkaline Magmatism in the Brazilian Platform*. São Paulo: Edusp/Fapesp, p. 71–148, 2005.

CONDIE, K. C. *Earth as an Evolving Planetary System*. 3rd ed. [s.l.] Elsevier, 2016.

CONDIE, K. C. *Earth as an Evolving Planetary System*. Academic Press, 2021.

CORDANI, U. G.; TEIXEIRA, W. Comentários sobre as determinações geocronológicas existentes para as regiões das folhas Rio de Janeiro, Vitória e Iguape. *Folhas Rio de Janeiro/Vitória (Iguape SF23/24/SG 23. Carta Geológica do Brasil ao Milionésimo-Texto explicativo*. DNPM, Brasília, 1979.

COSTA, A. G. Rochas ornamentais. Disponível em: http://recursomineralmg.codemge.com.br/substancias-minerais/rochasornamentais/#sienito. Acesso em: 26 jul. 2021.

COURTILLOT, V.; DAVAILLE, A.; BESSE, J.; STOCK, J. Three distinct types of hotspots in the Earth's mantle. *Earth Planetary Science Letters*, v. 205, p. 295–308, 2003. DOI: https://doi.org/10.1016/S0012-821X(02)01048-8.

COURTNEY, R. C.; WHITE, R. S. Anomalous heat flow and geoid across the Cape Verde Rise: evidence for dynamic support from a thermal plume in the mantle. *Geophysical Journal International*, v. 87, p. 815–867, 1986. DOI: https://doi.org/10.1111/j.1365-246X.1986.tb01973.x.

DAHLQUIST, J. A.; GALINDO, C.; CÁMERA, M. M. M.; MORENO, J. A.; ALASINO, P. H.; BASEI, M. A.; GRANDE, M. M. A combined zircon Hf isotope and whole-rock Nd and Sr isotopes study of Carboniferous A-type granites, Sierras Pampeanas of Argentina. *Journal of South American Earth Sciences*, v. 100, 102545, 2020.

DE LA ROCHE, H. D.; LETERRIER, J. T.; GRANDCLAUDE, P.; MARCHAL, M. A classification of volcanic and plutonic rocks using R1R2-diagram and major-element analyses—its relationships with current nomenclature. *Chemical Geology*, v. 29, n. 1–4, p. 183-210, 1980.

DECKART, K.; FÉRAUD, G.; MARQUES, L. S.; BERTRAND, H. New time constraints on dyke swarms related to the Paraná-Etendeka magmatic province, and subsequent South Atlantic opening, southeastern Brazil. *Journal of Volcanology and Geothermal Research*, v. 80, p. 67–83, 1998. DOI: https://doi.org/10.1016/S0377-0273(97)00038-3.

DUMAŃSKA-SŁOWIK, M.; POWOLNY, T.; NGUYEN KHAC, G. Mineralogy and geochemistry of nepheline syenite from the Bang Phuc Massif of the Alkaline Cho Don Complex in North-Eastern Vietnam: Implications for magma evolution and fluid–rock interactions. *Journal of Petrology*, v. 64, n. 7, egad042, 2023. https://doi.org/10.1093/petrology/egad042.

DUTRA, C. V. Método chumbo-alfa e idades de zircões do maciço alcalino de Poços de Caldas, Minas Gerais. *Boletim do Instituto de Geologia*, EFMOP 1, 1966.

EISELE, J.; SHARMA, M.; GALER, S. J. G.; BLICHERT-TOFT, J.; DEVEY, C. W.; HOFMANN, A. W. The role of sediment recycling in EM-1 inferred from Os, Pb, Hf, Nd, Sr isotope and trace element systematics of the Pitcairn hotspot. *Earth and Planetary Science Letters*, v. 196, n. 1–2, p. 197–212, 2002. https://doi.org/10.1016/S0012-821X(01)00601-X.

ELTHON, D.; SCARFE, C. M. High-pressure phase equilibria of a high-magnesia basalt and the genesis of primary oceanic basalts. *American Mineralogist*, v. 69, n. 1–2, p. 1–15, 1984.

ENRICH, G. E. R.; AZZONE, R. G.; RUBERTI, E.; GOMES, C. B.; COMIN CHIARAMONTI, P. Itatiaia, Passa Quatro and São Sebastião Island, the major alkaline syenitic complexes from the Serra do Mar region. In: COMIN-CHIARAMONTI, P.; GOMES, C. B. (Eds.). *Mesozoic to Cenozoic Alkaline Magmatism in the Brazilian Platform*. Edusp/Fapesp, p. 443–472, 2005.

ERNST, R. E. *Large Igneous Provinces*. Cambridge: Cambridge University Press, 2014.

FAGUNDES, M. B. Caracterização petrográfica e geoquímica do Complexo Alcalino do Morro de São João, Casimiro de Abreu-RJ. Dissertação de mestrado, Universidade do Estado do Rio de Janeiro, 2020.

FAURE, G.; MENSING, T. M. *Principles and applications of geochemistry*. 2. ed. John Wiley & Sons, 2005.

FERRARI, A. L. Evolução tectônica do Graben da Guanabara. Tese de doutorado, Universidade de São Paulo, 2001.

FERREIRA, L. C. Processamento, integração e interpretação de dados de aeromagnetometria e aerogamaespectrometria do estado do Rio de Janeiro. Dissertação de mestrado, Universidade Federal Fluminense, 2018.

FODOR, R. V.; MCKEE, E. H.; ASMUS, H. E. K-Ar ages and the opening of the South Atlantic Ocean: basaltic rock from the Brazilian margin. *Marine Geology*, v. 54, M1–M8, 1983. https://doi.org/10.1016/0025-3227(83)90002-6.

GAO, Y.; HOU, Z.; KAMBER, B. S.; WEI, R.; MENG, X.; ZHAO, R. Adakite-like porphyries from the southern Tibetan continental collision zones: Evidence for slab melt metasomatism. *Contributions to Mineralogy and Petrology*, v. 153, n. 1, p. 105–120, 2007. https://doi.org/10.1007/s00410-006-0132-4.

GERALDES, M. C.; MOTOKI, A.; VARGAS, T.; IWANUCH, W.; BALMANT, A.; MOTOKI, K. F. Geology, petrography and emplacement mode of the Morro dos Gatos alkaline intrusive complex, state of Rio de Janeiro, Brazil. *Geociências*, v. 32, n. 4, p. 625–639, 2013.

GERALDES, M. C.; VARGAS, T. C.; EVANS, N.; NUMMER, A. R. Idades U-Th/He das mineralizações de fluorita da Intrusão Alcalina de Tanguá. In: Congresso Brasileiro de Geoquímica, 2009.

GERLACH, D. C.; STORMER, J. C.; MUELLER, P. A. Isotopic geochemistry of Fernando de Noronha. *Earth and Planetary Science Letters*, v. 85, n. 2–3, p. 129–144, 1987. https://doi.org/10.1016/0012-821X(87)90027-6.

GIBSON, S. A.; THOMPSON, R. N.; LEONARDOS, O. H.; DICKIN, A. P.; MITCHELL, J. G. The Late Cretaceous impact of the Trindade mantle plume: Evidence from large-volume, mafic, potassic magmatism in SE Brazil. *Journal of Petrology*, v. 36, n. 1, p. 189–229, 1995. https://doi.org/10.1093/petrology/36.1.189.

GIBSON, S. A.; THOMPSON, R. N.; WESKA, R. K.; DICKIN, A. P.; LEONARDOS, O. H. Late Cretaceous rift-related upwelling and melting of the Trindade starting mantle plume head beneath western Brazil. *Contributions to Mineralogy and Petrology*, v. 126, n. 3, p. 303–314, 1997. https://doi.org/10.1007/s004100050252.

GIEHL, C.; MARKS, M. A. W.; NOWAK, M. An experimental study on the influence of fluorine and chlorine on phase relations in peralkaline phonolitic melts. *Contributions to Mineralogy and Petrology*, v. 167, n. 3, p. 1–21, 2014. https://doi.org/10.1007/s00410-014-0977-7.

GOMES, C. B.; COMIN-CHIARAMONTI, P. An introduction to the alkaline and alkaline-carbonatitic magmatism in and around the Paraná Basin. In: *Mesozoic to Cenozoic Alkaline Magmatism in the Brazilian Platform*. FAPESP, p. 1–26, 2005.

GORDON, A. C.; SANTOS, A. C.; CAITANO, G. R.; STANTON, N.; MOHRIak, W. U. Magmatic cycles in Santos Basin (SE Brazil): Geochemical characterization and magmatic sources. *Journal of South American Earth Sciences*, v. 126, p. 104323, 2023. https://doi.org/10.1016/j.jsames.2023.104323.

GUARINO, V.; DE' GENNARO, R.; MELLUSO, L.; RUBERTI, E.; AZZONE, R. G. The transition from miaskitic to agpaitic rocks, as highlighted by the accessory phase assemblages in the Passa Quatro alkaline complex (Southeastern Brazil). *The Canadian Mineralogist*, v. 57, p. 339–361, 2019. https://doi.org/10.3749/canmin.1800073.

GUARINO, V.; LUSTRINO, M.; ZANETTI, A.; TASSINARI, C. C. G.; RUBERTI, E.; DE' GENNARO, R.; MELLUSO, L. Mineralogy and geochemistry of a giant agpaitic magma reservoir: The Late Cretaceous Poços de Caldas potassic alkaline complex (SE Brazil). *Lithos*, v. 398–399, p. 106330, 2021. https://doi.org/10.1016/j.lithos.2021.106330.

GUIMARÃES, A. R.; FITTON, J. G.; KIRSTEIN, L. A.; BARFOD, D. N. Contemporaneous intraplate magmatism on conjugate South Atlantic margins: A hotspot conundrum. *Earth and Planetary Science Letters*, v. 536, p. 116147, 2020.

HACKSPACHER, P. C.; GODOY, A. M. Vertical displacement during late-collisional escape tectonics (Brasiliano Orogeny) in the Ribeira Belt, São Paulo State, Brazil. *Journal of African Earth Sciences*, v. 29, p. 25–32, 1999. https://doi.org/10.1016/S0899-5362(99)00077-9.

HART, S. R.; HAURI, E. H.; OSCHMANN, L. A.; WHITEHEAD, J. A. Mantle plumes and entrainment: isotopic evidence. *Science*, v. 256, n. 5056, p. 517–520, 1992.

HART, S. R. Heterogeneous mantle domains: signatures, genesis and mixing chronologies. *Earth and Planetary Science Letters*, v. 90, p. 272–296, 1988. https://doi.org/10.1016/0012-821X(88)90131-8.

HASUI, Y.; CARNEIRO, C. D. R.; COIMBRA, A. M. The Ribeira Fold Belt. *Revista Brasileira de Geociências*, v. 5, p. 257–267, 1975.

HAWKESWORTH, C. J.; O'NIONS, R. K.; ARCULUS, R. J. Nd and Sr isotope geochemistry of island arc volcanics, Grenada, Lesser Antilles. *Earth and Planetary Science Letters*, v. 45, n. 2, p. 237–248, 1979. https://doi.org/10.1016/0012-821X(79)90126-2.

HEILBRON, M.; DE MORISSON VALERIANO, C.; PEIXOTO, C.; TUPINAMBÁ, M.; NEUBAUER, F.; DUSSIN, I.; CORRALES, F.; BRUNO, H.; LOBATO, M.; ALMEIDA, J. C. H.; EIRADO SILVA, L. G. Neoproterozoic magmatic arc systems of the central Ribeira belt, SE-Brazil, in the context of the West-Gondwana pre-collisional history: A review. *Journal of South American Earth Sciences*, v. 103, p. 102710, 2020. https://doi.org/10.1016/j.jsames.2020.102710.

HEILBRON, M.; EIRADO, L. G.; ALMEIDA, J. *Mapa geológico e de recursos minerais do estado do Rio de Janeiro*. CPRM, 2016.

HEILBRON, M.; MOHRIAK, W.; VALERIANO, C. M.; MILANI, E.; ALMEIDA, J. C. H.; TUPINAMBÁ, M. From collision to extension: The roots of the South-eastern continental margin of Brazil. In: TALWANI, A.; MOHRIAK, W. (Eds.). *Atlantic Rifts and Continental Margin*. AGU Geophysical Monograph Series, v. 115, p. 1–36, 2000. https://doi.org/10.1029/GM115p0001.

HEILBRON, M.; PEDROSA-SOARES, A. C.; CAMPOS NETO, M.; SILVA, L. C.; TROUW, R. A. J.; JANASI, V. C. A Província Mantiqueira. In: MANTESSO-NETO, V.; BARTORELLI, A.; CARNEIRO, C. D. R.; BRITO NEVES, B. B. (Eds.). *O desvendar de um continente: A moderna geologia da América do Sul e o legado da obra de Fernando Flávio Marques de Almeida*. Beca Produções, p. 203–234, 2004.

HEILBRON, M.; RIBEIRO, A.; VALERIANO, C. M.; PACIULLO, F. V.; ALMEIDA, J. C. H.; TROUW, R. J. A.; TUPINAMBÁ, M.; EIRADO SILVA, L. G. The Ribeira Belt. In: HEILBRON, M.; VASCONCELOS, C. L.; ALMEIDA, M. B. (Eds.). *São Francisco Craton, Eastern Brazil: Tectonic Genealogy of a Miniature Continent*. Springer, p. 277–302, 2017. https://doi.org/10.1007/978-3-319-01715-0_15.

HEILBRON, M.; TUPINAMBÁ, M.; VALERIANO, C. M.; ARMSTRONG, R.; EIRADO, L. G. S.; MELO, R. S.; SIMONETTI, A.; SOARES, A. C. P.; MACHADO, N. The Serra da Bolívia Complex: the record of a new Neoproterozoic arc-related unit at Ribeira belt. *Precambrian Research*, v. 238, p. 158–175, 2013. https://doi.org/10.1016/j.precamres.2013.09.014.

HEILBRON, M.; VALERIANO, C. M.; TASSINARI, C. C. G.; ALMEIDA, J. C. H.; TUPINAMBÁ, M.; SIGA, O.; TROUW, R. Correlation of Neoproterozoic terranes between the Ribeira Belt, SE Brazil and its African counterpart: Comparative tectonic evolution and open questions. *Geological Society of London, Special Publications*, v. 294, p. 211–237, 2008. https://doi.org/10.1144/SP294.11.

HEINECK, C. A.; RAPOSO, F. O. *Projeto Fluorita*. CPRM, 1981.

HERZ, N. Timing of spreading in the South Atlantic: Information from Brazilian alkalic rocks. *Geological Society of America Bulletin*, v. 88, p. 101–112, 1977. https://doi.org/10.1130/0016-7606(1977)88<101

>2.0.CO;2.

HOFFMAN, A. W. Sampling mantle heterogeneity through oceanic basalts: Isotopes and trace elements. In: HOLLAND, H. D.; TUREKIAN, K. K. (Eds.). *Treatise on Geochemistry*. 2. ed. Elsevier, v. 3, p. 67–101, 2014. https://doi.org/10.1016/B978-0-08-095975-7.00203-5.

JACKSON, M. G.; DBASGUPTA, R. Compositions of HIMU, EM1, and EM2 from global trends between radiogenic isotopes and major elements in ocean island basalts. *Earth and Planetary Science Letters*, v. 276, p. 175–186, 2008. https://doi.org/10.1016/j.epsl.2008.09.023.

JACKSON, S. E.; PEARSON, N. J.; GRIFFIN, W. L.; BELOUSOVA, E. A. The application of laser ablation-inductively coupled plasma-mass spectrometry to in situ U–Pb zircon geochronology. *Chemical Geology*, v. 211, n. 1-2, p. 47–69, 2004. https://doi.org/10.1016/j.chemgeo.2004.06.017.

JIANG, Y.; JIANG, S.; LING, H.; DAI, B. Low-degree melting of a metasomatized lithospheric mantle for the origin of Cenozoic Yulong monzogranite-porphyry, east Tibet: Geochemical and Sr–Nd–Pb–Hf isotopic constraints. *Earth and Planetary Science Letters*, v. 241, n. 3–4, p. 617–633, 2006. https://doi.org/10.1016/j.epsl.2005.11.023.

JONES, R. E.; VAN KEKEN, P. E.; HAURI, E. H.; TUCKER, J. M.; VERVOORT, J.; BALLENTINE, C. J. Origins of the terrestrial Hf-Nd mantle array: evidence from a combined geodynamical-geochemical approach. *Earth and Planetary Science Letters*, v. 518, p. 26–39, 2019.

JOURDAN, F.; RENNE, P. R. Age calibration of the Fish Canyon sanidine $^{40}Ar/^{39}Ar$ dating standard using primary K–Ar standards. *Geochimica et Cosmochimica Acta*, v. 71, n. 2, p. 387–402, 2007. https://doi.org/10.1016/j.gca.2006.09.002.

KAY, R. W.; GAST, P. W. The rare earth content and origin of alkali-rich basalts. *The Journal of Geology*, v. 81, n. 6, p. 653–682, 1973. https://doi.org/10.1086/627919.

KELEMEN, P. B.; HIRTH, G.; SHIMIZU, N.; SPIEGELMAN, M.; DICK, H. J. A review of melt migration processes in the adiabatically upwelling mantle beneath oceanic spreading ridges. *Philosophical Transactions of the Royal Society of London. Series A: Mathematical, Physical and Engineering Sciences*, v. 355, n. 1723, p. 283–318, 1997.

KHOMIAKOV, A. P. Mineralogy of hyperagpaitic alkaline rocks. Oxford: Oxford University Press, 1995.

KOPPERS, A. A. ArArCALC—software for $^{40}Ar/^{39}Ar$ age calculations. *Computers & Geosciences*, v. 28, n. 5, p. 605–619, 2002. https://doi.org/10.1016/S0098-3004(01)00095-4.

KUSHIRO, I. Partial melting experiments on peridotite and origin of mid-ocean ridge basalt. *Annual Review of Earth and Planetary Sciences*, v. 29, n. 1, p. 71–107, 2001. Disponível em: http://www.annualreviews.org/doi/10.1146/annurev.earth.29.1.71.

LAPORTE, D.; LAMBART, S.; SCHIANO, P.; OTTOLINI, L. Experimental derivation of nepheline syenite and phonolite liquids by partial melting of upper mantle peridotites. *Earth and Planetary Science Letters*, v. 404, p. 319–331, 2014.

LAZNICKA, P. Giant metallic deposits: Future sources of industrial metals. [s.l.]: Springer Science & Business Media, 2006.

LE BAS, M.; MAITRE, R. L.; STRECKEISEN, A.; ZANETTIN, B.; IUGS SUBCOMMISSION ON THE SYSTEMATICS OF IGNEOUS ROCKS. A chemical classification of volcanic rocks based on the total alkali-silica diagram. *Journal of Petrology*, v. 27, n. 3, p. 745–750, 1986.

LE MAITRE, R. W.; STRECKEISEN, A.; ZANETTIN, B.; LE BAS, M. J.; BONIN, B.; BATEMAN, P. *Igneous rocks: a classification and glossary of terms: recommendations of the International Union of Geological Sciences Subcommission on the Systematics of Igneous Rocks*. [s.l.] Cambridge University Press, 2005.

LE MAITRE, R. W.; STRECKEISEN, A.; ZANETTIN, B.; LE BAS, M. J.; BONIN, B.; BATEMAN, P.; BELLENI, A.; DUDEK, S.; EFREMOVA, J.; KELLER, J.; LAMEYRE, P. A.; SABINE, R.; SCHMID, H.; SØRENSEN, H.; WOOLLEY, A. R. *Igneous rocks: a classification and glossary of terms: recommendations of the International Union of Geological Sciences Subcommission on the Systematics of Igneous Rocks*. Cambridge University Press, Cambridge, 2002.

LE ROEX, A. P.; CLASS, C.; O'CONNOR, J.; JOKAT, W. Shona and Discovery aseismic ridge systems, South Atlantic: trace element evidence for enriched mantle sources. *Journal of Petrology*, v. 51, p. 2089–2120, 2010. https://doi.org/10.1093/petrology/egq050.

LIEW, T. C.; HOFMANN, A. W. Precambrian crustal components, plutonic associations, plate environment of the Hercynian Fold Belt of central Europe: indications from a Nd and Sr isotopic study. *Contributions to Mineralogy and Petrology*, v. 98, p. 129–138, 1988.

LUDWIG, K. R. User's manual for IsoPlot 3.0. A geochronological toolkit for Microsoft Excel, 2003. 71 p.

MACEDO, B. N.; PETERNEL, R.; SANTOS, A. C. D.; SIMAS, M. P. Resende lamprophyres: new petrological and structural interpretations for a regional Upper Cretaceous alkaline mafic dyke swarm. *Brazilian Journal of Geology*, v. 52, e20210043, 2022.

MACHADO, N.; VALLADARES, C.; HEILBRON, M.; VALERIANO, C. U-Pb geochronology of the central Ribeira belt (Brazil) and implications for the evolution of the Brazilian Orogeny. *Precambrian Research*, v. 79, p. 347–361, 1996. https://doi.org/10.1016/0301-9268(95)00103-4.

MAIA, T. M.; DOS SANTOS, A. C.; ROCHA-JÚNIOR, E. R. V.; VALERIANO, C. de M.; MENDES, J. C.; JECK, I. K.; DOS SANTOS, W. H.; DE OLIVEIRA, A. L.; MOHRIAK, W. U. First petrologic data for Vitória Seamount, Vitória-Trindade Ridge, South Atlantic: a contribution to the Trindade mantle plume evolution. *Journal of South American Earth Sciences*, v. 109, 2021. https://doi.org/10.1016/j.jsames.2021.103304.

MARKS, M. A. W.; MARKL, G. A global review on agpaitic rocks. *Earth-Science Reviews*, v. 173, p. 229–258, 2017. https://doi.org/10.1016/j.earscirev.2017.06.002.

MARKS, M. A.; HETTMANN, K.; SCHILLING, J.; FROST, B. R.; MARKL, G. The mineralogical diversity of alkaline igneous rocks: critical factors for the transition from miaskitic to agpaitic phase assemblages. *Journal of Petrology*, v. 52, n. 3, p. 439–455, 2011. https://doi.org/10.1093/petrology/egq086.

MCDONOUGH, W. F.; SUN, S. S. The composition of the Earth. *Chemical Geology*, v. 120, n. 3-4, p. 223–253, 1995. https://doi.org/10.1016/0009-2541(94)00140-4.

MELLUSO, L.; GUARINO, V.; LUSTRINO, M.; MORRA, V.; DE' GENNARO, R. The REE- and HFSE-bearing phases in the Itatiaia alkaline complex (Brazil) and geochemical evolution of feldspar-rich felsic melts. *Mineral Magazine*, v. 81, p. 217–250, 2017. https://doi.org/10.1180/minmag.2016.080.122.

MIDDLEMOST, E. A. The basalt clan. *Earth-Science Reviews*, v. 11, n. 4, p. 337–364, 1975.

MILANI, E. J. Evolução tectono-estratigráfica da Bacia do Paraná e seu relacionamento com a geodinâmica fanerozóica do Gondwana sul-ocidental. Tese (Doutorado) — Universidade Federal do Rio Grande do Sul, 1997.

MJELDE, R.; WESSEL, P.; MÜLLER, R. D. Global pulsations of intraplate magmatism through the Cenozoic. *Lithosphere*, v. 2, n. 5, p. 361–376, 2010.

MONTEIRO, L. G. P. Petrogênese do Maciço Alcalino de Morro dos Gatos: implicações da tectônica do embasamento e seu potencial econômico. 2021.

MONTES-LAUAR, C. R.; PACCA, I. G.; MELFI, A. J.; KAWASHITA, K. Late Cretaceous alkaline complexes, southeastern Brazil: paleomagnetism and geochronology. *Earth and Planetary Science Letters*, v. 134, p. 425–440, 1995. https://doi.org/10.1016/0012-821X(95)00135-Y.

MONTES-LAUAR, C. R.; PACCA, I. I. G. Estudo paleomagnético dos maciços alcalinos de Poços de Caldas, Passa Quatro e Itatiaia.

MORAES, L. C. de; SEER, H. J. Terras Raras. Disponível em: http://recursomineralmg.codemge.com.br/substancias-minerais/terras-raras/. Acesso em: 25 jul. 2021.

MOTA, C. E. M. Petrogênese e geocronologia das intrusões alcalinas de Morro Redondo, Mendanha e Morro de São João: caracterização do magmatismo alcalino no estado do Rio de Janeiro e implicações geodinâmicas. Tese (Doutorado) — Universidade do Estado do Rio de Janeiro, 2012.

MOTA, C. E. M.; GERALDES, M. C.; HORTA DE ALMEIDA, J. C.; VARGAS, T.; MARINHO DE SOUZA, D.; PIMENTEL DA SILVA, A. Características isotópicas (Nd e Sr), geoquímicas e

petrográficas da intrusão alcalina do Morro de São João: implicações geodinâmicas e sobre a composição do manto sublitosférico. 2009. https://doi.org/10.5327/Z1519-874X2009000100006.

MOTOKI, A.; ARAÚJO, A. L.; SICHEL, S. E.; GERALDES, M. C.; JOURDAN, F.; MOTOKI, K. F.; DA SILVA, S. Nepheline syenite magma differentiation with continental crustal assimilation for the Cabo Frio Island intrusive complex, State of Rio de Janeiro, Brazil. *Geociências*, v. 32, p. 195–218, 2013.

MOTOKI, A.; SICHEL, S. E.; SILVA, S. da; MOTOKI, K. F. Morphologic characteristics and erosive resistance of felsic alkaline intrusive massif of Tanguá, State of Rio de Janeiro, Brazil, based on the ASTER GDEM. *Geosciences= Geociências*, v. 34, p. 19–31, 2015a.

MOTOKI, A.; SICHEL, S. E.; SOARES, R.; AIRES, J. R.; SAVI, C.; PETRAKIS, G. H.; MOTOKI, K. F. Rochas piroclásticas de preenchimento de condutos subvulcânicos do Mendanha, Itaúna e Ilha de Cabo Frio, RJ, e seu processo de formação com base no modelo de implosão de conduto. *Geociencias*, v. 27, p. 451–467, 2008.

MOTOKI, A.; SICHEL, S. E.; VARGAS, T.; AIRES, J. R.; IWANUCH, W.; MELLO, S. L. M.; MOTOKI, K. F.; DA SILVA, S.; BALMANT, A.; GONÇALVES, J. Geochemical evolution of the felsic alkaline rocks of Tanguá and Rio Bonito intrusive bodies, State of Rio de Janeiro, Brazil. *Geociencias*, v. 29, p. 291–310, 2010.

MOTOKI, A.; SICHEL, S. E.; VARGAS, T.; MELO, D. P.; MOTOKI, K. F. Geochemical behaviour of trace elements during fractional crystallization and crustal assimilation of the felsic alkaline magmas of the State of Rio de Janeiro, Brazil. *Anais da Academia Brasileira de Ciências*, v. 87, p. 1959–1979, 2015b. https://doi.org/10.1590/0001-3765201520130385.

NETTO, A. M.; GERALDES, M. C.; VIGNOL-LELARGE, M. L. Idade traço de fissão em apatita do maciço alcalino do Mendanha: implicações sobre o magmatismo cretáceo no Estado do Rio de Janeiro. *Simpósio de Geologia do Sudeste*, 9, 2005.

OUABID, M.; GARRIDO, C. J.; OUALI, H.; HARVEY, J.; HIDAS, K.; MARCHESI, C.; ACOSTA-VIGIL, A.; DAUTRIA, J. M.; MESSBAHI, H.; ROMÁN-ALPISTE, M. J. Late Cadomian rifting of the NW Gondwana margin and the reworking of Precambrian crust: evidence from bimodal magmatism in the early Paleozoic Moroccan Meseta. *International Geology Review*, v. 63, n. 16, p. 2013–2036, 2021.

PEARCE, J. A. Geochemical fingerprinting of oceanic basalts with applications to ophiolite classification and the search for Archean oceanic crust. *Lithos*, v. 100, n. 1-4, p. 14–48, 2008.

PLANK, T. Constraints from thorium/lanthanum on sediment recycling at subduction zones and the evolution of the continents. *Journal of Petrology*, v. 46, n. 5, p. 921–944, 2005. https://doi.org/10.1093/petrology/egi005.

QUARESMA, G. D. O. A.; DOS SANTOS, A. C.; ROCHA-JÚNIOR, E. R. V.; BONIFÁCIO, J.; REGO, C. A. Q.; MATA, J.; VALERIANO, C. de M.; JOURDAN, F.; MATTIELLI, N.; GERALDES, M. C. Isotopic constraints on Davis bank, Vitória-Trindade Ridge: A revised petrogenetic model. *Journal of South American Earth Sciences*, v. 122, p. 104099, 2023.

RENNE, P. R.; BALCO, G.; LUDWIG, K. R.; MUNDIL, R.; MIN, K. Response to the comment by WH Schwarz et al. on "Joint determination of 40K decay constants and 40Ar*/40K for the Fish Canyon sanidine standard, and improved accuracy for $^{40}Ar/^{39}Ar$ geochronology" by PR Renne et al. (2010). *Geochimica et Cosmochimica Acta*, v. 75, n. 17, p. 5097–5100, 2011. https://doi.org/10.1016/j.gca.2011.06.021.

RIBEIRO FILHO, E.; CORDANI, U. G. Contemporaneidade das intrusões de rochas alcalinas do Itatiaia, Passa Quatro e Morro Redondo. *Publicação*, n. 62-63, 1966.

RICCOMINI, C.; VELÁZQUEZ, V. F.; GOMES, C. B. Tectonic controls of the Mesozoic and Cenozoic alkaline magmatism in central-southeastern Brazilian Platform. In: COMIN-CHIARAMONTI, P.; GOMES, C. de B. (Eds.). *Mesozoic to Cenozoic Alkaline Magmatism in the Brazilian Platform*. Edusp, p. 31–56, 2005. https://doi.org/10.2138/am.2007.485.

ROCHA-JÚNIOR, E. R. V.; MARQUES, L. S.; BABINSKI, M.; MACHADO, F. B.; PETRONILHO, L. A.; NARDY, A. J. R. A telltale signature of Archean lithospheric mantle in the Paraná continental flood basalts genesis. *Lithos*, v. 364, p. 105519, 2020. https://doi.org/10.1016/j.lithos.2020.105519.

ROCIO, M. A. R.; SILVA, M. M. D.; CARVALHO, P. S. L. D.; CARDOSO, J. G. D. R. Terras-raras: situação atual e perspectivas. *BNDES Setorial*, n. 35, p. 369–420, mar. 2012.

ROSA, P. A. da S.; RUBERTI, E. Nepheline syenites to syenites and granitic rocks of the Itatiaia Alkaline Massif, Southeastern Brazil: new geological insights into a migratory ring complex. *Brazilian Journal of Geology*, v. 48, p. 347–372, 2018. https://doi.org/10.1590/2317-4889201820170092.

ROSA, P. A. S. Geologia e evolução petrogenética do maciço alcalino de Itatiaia, MG-RJ. Dissertação (Mestrado) — Universidade de São Paulo, São Paulo, 2017.

SADOWSKI, G. R.; DIAS NETTO, C. de M. O Lineamento Sismotectônico de Cabo Frio. *Revista Brasileira de Geociências*, v. 11, n. 4, p. 209–212, 1981.

SALTERS, V. J.; MALLICK, S.; HART, S. R.; LANGMUIR, C. E.; STRACKE, A. Domains of depleted mantle: New evidence from hafnium and neodymium isotopes. *Geochemistry, Geophysics, Geosystems*, v. 12, n. 8, 2011.

SALTERS, V. J. M.; STRACKE, A. Composition of the depleted mantle. *G-Cubed*, v. 5, Q05B07, 2004. https://doi.org/10.1029/2003GC000597.

SAMPAIO, J. A.; FRANÇA, S. C. A.; BRAGA, P. F. A. Rochas e minerais industriais: nefelina sienito. *Cent. Tecnol. Min.*, 2. ed. Rio de Janeiro, Brasil, 2008.

SANTOS, A. C. dos; HACKSPACHER, P. C. Meso-Cenozoic Brazilian Offshore Magmatism: Geochemistry, Petrology, and Tectonics. Academic Press, 2021.

SCHILLING, J.; MARKS, M. A.; WENZEL, T.; MARKL, G. Reconstruction of magmatic to subsolidus processes in an agpaitic system using eudialyte textures and composition: a case study from Tamazeght, Morocco. *The Canadian Mineralogist*, v. 47, n. 2, p. 351–365, 2009. https://doi.org/10.3749/canmin.47.2.351.

SCHORSCHER, H. D.; SHEA, M. E. The regional geology of the Poços de Caldas alkaline complex: mineralogy and geochemistry of selected nepheline syenites and phonolites. *Journal of Geochemical Exploration*, v. 45, p. 25–51, 1992. https://doi.org/10.1016/0375-6742(92)90121-N.

SHAND, S. J. *Eruptive rocks. Their genesis composition, classification, and their relation to ore-deposits with a chapter on meteorite*. New York: John Wiley & Sons, 1943.

SHEA, M. E. Isotopic geochemical characterization of selected nepheline syenites and phonolites from the Poços de Caldas alkaline complex, Minas Gerais, Brazil. *Journal of Geochemical Exploration*, v. 45, p. 173–214, 1992. https://doi.org/10.1016/0375-6742(92)90125-R.

SICHEL, S. E.; MOTOKI, A.; IWANUCH, W.; VARGAS, T.; AIRES, J. R.; DE MELO, D. P.; MOTOKI, K. F.; BALMANT, A.; RODRIGUES, J. G. Cristalização fracionada e assimilação da crosta continental pelos magmas de rochas alcalinas félsicas do estado do Rio de Janeiro. *Anuário do Instituto de Geociências*, v. 35, n. 2, p. 84-104, 2012. http://dx.doi.org/10.11137/2012_2_84_104.

SICHEL, S. E.; MOTOKI, A.; SAVI, D. C.; SOARES, R. Subvolcanic vent-filling welded tuff breccia of Cabo Frio Island, State of Rio de Janeiro, Brazil. *Rem: Revista Escola de Minas*, v. 61, p. 423–432, 2008. https://doi.org/10.1590/S0370-44672008000400004.

SILVA, D. A. da; POTRATZ, G. L.; GERALDES, M. C. Geochemistry and geochronology (U-Pb and Lu-Hf) of the Soarinho Alkaline Massif (Brazil): Implications on mantle versus crustal signature of syenitic magma. *Minerals*, v. 13, n. 7, p. 904, 2023.

SILVA, D. A. da. Geoquímica e geocronologia (U-Pb e Lu-Hf) das intrusões alcalinas félsicas de Soarinho, Tanguá, Rio Bonito e Tinguá: implicações sobre as fontes do magmatismo alcalino no Estado do Rio de Janeiro. Tese (Doutorado) — Universidade do Estado do Rio de Janeiro, 2019. https://doi.org/10.1017/CBO9781107415324.004.

SILVA, D. A. da; GERALDES, M. C.; VARGAS, T.; JOURDAN, F.; NOGUEIRA, C. C. $^{40}Ar/^{39}Ar$ age, lithogeochemistry and petrographic studies of the Cretaceous Alkaline Marapicu Intrusion, Rio de Janeiro, Brazil. *Boletim do Museu Paraense Emílio Goeldi - Ciências Naturais*, v. 10, p. 399–422, 2015. https://doi.org/10.46357/bcnaturais.v10i3.474.

SILVA, D. A. da; MOTOKI, A.; SANTOS, A. C. dos; MENDES, J.; JOURDAN, F.; GERALDES, M. C.; LANA, C. de C. Multiple processes of geochemical evolution for the alkaline rocks of Rio Bonito intrusive complex, Rio de Janeiro State, Brazil: $^{40}Ar/^{39}Ar$ and U-Pb ages and Lu-Hf isotopes on zircon and constraints on crustal signature. *Geologia USP. Série Científica*, v. 20, p. 213–234, 2020. https://doi.org/10.11606/issn.2316-9095.v20-151049.

SILVA, D. A. da; GERALDES, M. C.; RODRIGUES, S. W. O.; MCMASTER, M.; EVANS, N.; NUMMER, A. R.; VARGAS, T. (U-Th)/He ages from the fluorite mineralization of the Tanguá alkaline intrusion. *Anuário do Instituto de Geociências - UFRJ*, v. 41, p. 14–21, 2018. https://doi.org/10.11137/2018_2_14_21.

SILVEIRA, L. S.; DUTRA, T.; VALENTE, S. C.; RAGATKY, D. C. Modelos eruptivos preliminares para o Complexo Vulcânico de Nova Iguaçu, RJ. In: *Simpósio de Vulcanismo e Ambientes Associados*, 3, 2005, p. 333–337.

SJÖQVIST, A. S. Agpaitic rocks of the Norra Kärr alkaline complex. Projet de fin d'études, 2015.

SMITH, P.E., EVENSEN, N.M., YORK, D., SZATMARI, P., CONCEICAO, J.C.J., DESTRO, N., 1999. Getting it on track: Ar-Ar geochronology of alkali intrusions of the Serra do Mar province, Brazil. Eos (Transactions, American Geophysical Union) 80, F1134–F1135.

SMITH, P. E.; EVENSEN, N. M.; YORK, D.; SZATMARI, P.; DE OLIVEIRA, D. C. Single-crystal 40Ar-39Ar dating of pyrite: No fool's clock. *Geology*, v. 29, n. 5, p. 403-406, 2001.

SONOKI, I. K.; GARDA, G. M. Idades K-Ar de rochas alcalinas do Brasil Meridional e Paraguai Oriental: compilação e adaptação às novas constantes de decaimento. *Boletim IG - USP, Série Científica*, v. 19, p. 63–85, 1988. https://doi.org/10.11606/issn.2316-8986.v19i0p63-85.

SØRENSEN, H. The alkaline rocks. 1974.

SØRENSEN, H. Agpaitic nepheline syenites: a potential source of rare elements. *Applied Geochemistry*, v. 7, n. 5, p. 417–427, 1992.

SØRENSEN, H. The agpaitic rocks - an overview. *Mineralogical Magazine*, v. 61, n. 407, p. 485–498, 1997. https://doi.org/10.1180/minmag.1997.061.407.02.

SOUZA, I. C. de A.; SCHNEIDER, C. L. Avaliação da rocha nefelina sienito para aplicação na rochagem, extração de potássio a partir de um agente alcalino, 2015.

STRACKE, A. Earth's heterogeneous mantle: a product of convection-driven interaction between crust and mantle. *Chemical Geology*, v. 330, p. 274–299, 2012. https://doi.org/10.1016/j.chemgeo.2012.08.007.

STRACKE, A.; HOFMANN, A. W.; HART, S. R. FOZO, HIMU, and the rest of the mantle zoo. *Geochemistry, Geophysics, Geosystems*, v. 6, n. 5, p. 20, 2005. Disponível em: http://doi.wiley.com/10.1029/2004GC000824.

TAKENAKA, L. B. Refinamento do método de datação U-Pb in situ via LA-Q-ICP-MS: aplicação no Complexo Alcalino Poços de Caldas - MG. 2014. Dissertação (Mestrado) — Universidade Federal de Ouro Preto.

TANAKA, T.; TOGASHI, S.; KAMIOCA, H. JNd-1: a Neodymium isotopic reference in consistency with La Jolla Neodymium. *Chemical Geology*, v. 168, p. 279–281, 2000. https://doi.org/10.1016/S0009-2541(00)00198-4.

TERA, F.; WASSERBURG, G. J. U-Th-Pb systematics in three Apollo 14 basalts and the problem of initial Pb in lunar rocks. *Earth and Planetary Science Letters*, v. 14, n. 3, p. 281–304, 1972.

TERAKADO, Y. Fine structures of rare earth element patterns of Tahitian rocks. *Geochemical Journal*, v. 14, n. 4, p. 155–166, 1980. https://doi.org/10.2343/geochemj.14.155.

THOMAZ FILHO, A.; DE CESERO, P.; MIZUSAKI, A. M.; LEÃO, J. G. Hot spot volcanic tracks and their implications for South American plate motion, Campos basin (Rio de Janeiro state), Brazil. *Journal of South American Earth Sciences*, v. 18, p. 383–389, 2005. https://doi.org/10.1016/j.jsames.2004.11.006.

THOMAZ FILHO, A.; RODRIGUES, A. L. O alinhamento de rochas alcalinas Poços de Caldas-Cabo Frio (RJ) e sua continuidade na Cadeia Vitória-Trindade. *Revista Brasileira de Geociências*, v. 29, p. 189–194, 1999. https://doi.org/10.25249/0375-7536.199929189194.

THOMPSON, R. N.; GIBSON, S. A.; MITCHELL, J. G.; DICKIN, A. P.; LEONARDOS, O. H.; BROD, J. A.; GREENWOOD, J. C. Migrating Cretaceous-Eocene magmatism in the Serra do Mar Alkaline Province, SE Brazil: melts from the deflected Trindade mantle plume? *Journal of Petrology*, v. 39, p. 1493–1526, 1998. https://doi.org/10.1093/petroj/39.8.1493.

TORRES, J. D. P. O potencial mineral das rochas alcalinas: estudo de caso no batólito sienítico Itarantim, província alcalina do sul do Estado da Bahia. 2017.

TROUW, R. A. J.; HEILBRON, M.; RIBEIRO, A.; PACIULLO, F. V. P.; VALERIANO, C. M.; ALMEIDA, J. C. H.; TUPINAMBÁ, M.; ANDREIS, R. R. The central segment of the Ribeira belt. In: CORDANI, U. G.; MILANI, E. J.; THOMAZ FILHO, A.; CAMPOS, D. A. (Eds.). *Tectonic Evolution of South America*, 31th International Geological Congress, Rio de Janeiro, Brazil, p. 287–310, 2000.

TSEKHMISTRENKO, M.; SIGLOCH, K.; HOSSEINI, K.; BARRUOL, G. A tree of Indo-African mantle plumes imaged by seismic tomography. *Nature Geoscience*, v. 14, n. 8, p. 612–619, 2021.

TSUKADA, K.; YAMAMOTO, K.; GANTUMUR, O.; NURAMKHAAN, M. Early Paleozoic subduction initiation volcanism of the Iwatsubodani formation, Hida Gaien belt, Southwest Japan. *International Journal of Earth Sciences*, v. 106, p. 1429–1451, 2017.

ULBRICH, H.; DEMAIFFE, D.; VLACH, S. R. F.; ULBRICH, M. N. C. Geochemical and Sr, Nd and Pb isotope signatures of phonolites and nepheline syenites from the Poços de Caldas alkaline massif, southeastern Brazil. In: *South American Symposium of Isotope Geology*, p. 698–701, 2003.

ULBRICH, H.; VLACH, S. R. F.; DEMAIFFE, D.; ULBRICH, M. N. C. Structure and origin of the Poços de Caldas alkaline massif, SE Brazil. In: *Mesozoic to Cenozoic Alkaline Magmatism in the Brazilian Plataform*. São Paulo: Edusp/Fapesp, p. 367–418, 2005. https://doi.org/10.2138/am.2007.485.

ULBRICH, H.; GOMES, C. de B. Alkaline rocks from continental Brazil. *Earth-Science Reviews*, v. 17, n. 1–2, p. 135–154, 1981.

ULBRICH, H. H. G. J.; VLACH, S. R. F.; ULBRICH, M. N. C.; KAWASHITA, K. Penecontemporaneous syenitic-phonolitic and basic-ultrabasic-carbonatitic rocks at the Poços de Caldas Alkaline Massif, SE Brazil: geologic and geochronologic evidence. *Revista Brasileira de Geociências*, v. 32, p. 15–26, 2002. https://doi.org/10.25249/0375-7536.20023211526.

USSING, N. V. *Geology of the country around Julianehaab, Greenland*. [s.l.]: I commission hos CA Reitzel, 1912.

VALENÇA, J.; REIS, A. P.; CARVALHO FILHO, C. A.; SOARES FILHO, J. R. S.; BRAUN, P. V. C. B. Geologia do complexo ígneo alcalino do Morro Redondo (Município de Resende, Estado do Rio de Janeiro). *Anais da Academia Brasileira de Ciências*, v. 55, p. 135-136, 1983.

VALENÇA, J. G. Geology, petrography and petrogenesis of some alkaline igneous complexes of Rio de Janeiro State, Brazil. Tese (Doutorado) — West Ontario University, 1980.

VALERIANO, C. M.; RAGATKY, D.; GERALDES, M. C.; HEILBRON, M.; VALLADARES, C. S.; SCHMITT, R.; TUPINAMBÁ, M.; PALERMO, N.; ALMEIDA, J. C. H.; DUARTE, B. P.; MARTINS JR., E. C.; NOGUEIRA, J. R. A new TIMS laboratory under construction in Rio de Janeiro, Brazil. In: *Symposium on Isotope Geology*, 2003.

VAN DECAR, J. C.; JAMES, D. E.; ASSUMPÇÃO, M. Seismic evidence for a fossil mantle plume beneath South America and implications for plate driving forces. *Nature*, v. 378, p. 25–31, 1995. https://doi.org/10.1038/378025a0.

VERMEESCH, P. IsoplotR: a free and open toolbox for geochronology. *Geoscience Frontiers*, v. 9, n. 5, p. 1479-1493, 2018. https://doi.org/10.1016/j.gsf.2018.04.001.

VLACH, S. R. F.; VILALVA, F. C. J.; ULBRICH, M. N. C.; ULBRICH, H. H. G. J.; VASCONCELOS, P. M. Phlogopite from carbonatitic veins associated with the Poços de Caldas Alkaline Massif, SE Brazil: mineralogy and $^{40}Ar/^{39}Ar$ dating by the laser step heating method. 2003.

WANG, J. Y.; SANTOSH, M.; YANG, C. X.; NAKAGAWA, M.; DONG, Y. Ancient crustal recycling in modern island arcs: a tale of the world's youngest charnockite from SW Japan. *Lithos*, v. 354, 105360, 2020.

WATSON, S.; MCKENZIE, D. Melt generation by plumes: a study of Hawaiian volcanism. *Journal of Petrology*, v. 32, p. 501–537, 1991. https://doi.org/10.1093/petrology/32.3.501.

WIEDENBECK, M. A. P. C.; ALLE, P.; CORFU, F. Y.; GRIFFIN, W. L.; MEIER, M.; OBERLI, F. V.; VON QUADT, A.; RODDICK, J. C.; SPIEGEL, W. Three natural zircon standards for U-Th-Pb, Lu-Hf, trace element and REE analyses. *Geostandards Newsletter*, v. 19, n. 1, p. 1-23, 1995. https://doi.org/10.1111/j.1751-908X.1995.tb00147.x.

WILLBOLD, M.; STRACKE, A. Formation of enriched mantle components by recycling of upper and lower continental crust. *Chemical Geology*, v. 276, n. 3-4, p. 188-197, 2010.

WILSON, M. Magmatism and the geodynamics of basin formation. *Sedimentary Geology*, v. 86, n. 1–2, p. 5–29, 1993.

WINTER, J. D. *An introduction to igneous and metamorphic petrology*. 2001.

WORKMAN, R. K.; HART, S. R. Major and trace element composition of the depleted MORB mantle (DMM). *Earth and Planetary Science Letters*, v. 231, n. 1-2, p. 53-72, 2005. https://doi.org/10.1016/j.epsl.2004.12.005.

WORKMAN, R. K.; HART, S. R.; JACKSON, M.; REGULOUS, M.; FARLEY, K. A.; BLUSZTAJN, J.; STAUDIGEL, H. Recycled metasomatized lithosphere as the origin of the Enriched Mantle II (EM2) end-member: evidence from the Samoan Volcanic Chain. *Geochemistry, Geophysics, Geosystems*, v. 5, n. 4, 2004.

YAN, X.; JIANG, S. Y. Petrogenesis and tectonic implications of Early Cretaceous shoshonitic syenites in the northern Wuyi Mt Range, Southeast China. *Journal of Asian Earth Sciences*, v. 180, 103877, 2019. https://doi.org/10.1016/j.jseaes.2019.103877.

YARMOLYUK, V. V.; KUZMIN, M. I.; ERNST, R. E. Intraplate geodynamics and magmatism in the evolution of the Central Asian Orogenic Belt. *Journal of Asian Earth Sciences*, v. 93, p. 158-179, 2014.

ZALÁN, P. V.; OLIVEIRA, J. A. B. Origem e evolução estrutural do Sistema de Riftes Cenozóicos do Sudeste do Brasil. *Boletim de Geociências da PETROBRAS*, v. 13, p. 269–300, 2005.

ZARASVANDI, A.; REZAEI, M.; LENTZ, D.; POURKASEB, H.; KAREVANI, M. The Kasian volcanic rocks, Khorramabad, Iran: evidence for a Jurassic intra-oceanic island arc in Neo-Tethys ocean. *Iranian Journal of Science and Technology*, v. 39, n. A2, p. 165, 2015.

ZHANG, C.; SANTOSH, M.; LUO, Q.; JIANG, S.; LIU, L.; LIU, D. Impact of residual zircon on Nd-Hf isotope decoupling during sediment recycling in subduction zone. *Geoscience Frontiers*, v. 10, n. 1, p. 241-251, 2019.

ZINDLER, A.; HART, S. R. Chemical geodynamics. *Annual Review of Earth and Planetary Sciences*, v. 14, p. 493–571, 1986. https://doi.org/10.1146/annurev.ea.14.050186.002425.

APÊNDICE A – Tabela de pontos levantados em campo

Datum: WGS 1984 (GPS)

Sistema de coordenadas: UTM (Zona: 23K)

Ponto	X	Y	Z	Litologia
Embasamento	733665.8	7492658.3	37.6	Gnaisse alterado
TG01	732850.6	7486029.0	39.5	Brecha alterada
TG02A	732736.3	7486066.2	75.6	Nefelina sienito alterado
TG02B	732612.2	7486176.3	99.4	Sienito
TG02C	732556.7	7486292.0	132.6	Sienito com titanita
TG03	732122.1	7486345.4	202.5	Sienito com titanita
TG04	733470.8	7486588.3	64.8	Sienito/Traquito
TG05	733246.6	7487269.7	224.8	Sienito
TG06	732758.9	7487731.8	261.8	Sienito
TG07	732383.8	7487955.6	307.3	Sienito
TG08	732172.6	7488217.9	337.3	Sienito
TG09	731954.8	7488416.0	385.9	Sienito
TG10	734636.9	7490357.4	95.1	Brecha fina
TG10B	734555.7	7490394.0	102.8	Brecha fina
TG11	734468.4	7490399.3	109.7	Sienito Leucocrático porfirítico
TG12	734309.2	7490196.1	159.9	Sienito
TG13	734078.7	7490035.3	253.9	Sienito
TG14	729423.4	7490855.1	52.3	Sienito
TG14A	729276.5	7490847.2	35.5	Sienito
TG15	733985.1	7489919.2	272.2	Sienito
TG16	733935.7	7489909.3	283.7	Fonolito
TG17	733875.4	7489912.0	299.1	Sienito
TG17B	733827.6	7489878.5	315.7	Sienito
TG18	733543.1	7490027.0	392.8	Sienito
TG19	733455.4	7489998.8	414.7	Sienito
TG20	733427.3	7489977.0	433.0	Brecha próxima a sienito
TG21	733206.6	7489898.1	460.6	Fonolito
TG22	733026.7	7489814.5	453.6	Sienito com biotita
TG23	732959.0	7489666.3	473.3	Sienito grosso
TG24	735403.8	7487885.4	88.1	Sienito
TG25	735340.7	7487667.9	95.1	Sienito/Brecha/Fonolito
TG26	735068.3	7487763.9	89.3	Sienito com aplitos
TG27	734928.0	7487727.8	88.3	Sienito

Ponto	X	Y	Z	Litologia
TG28	734498.8	7487437.5	78.2	Fonolito
TG29	733505.5	7486294.5	62.1	Brecha
TG30A	731504.8	7492290.4	50.1	Sienito
TG30B	731531.9	7492554.2	36.9	Sienito
TG32	729042.5	7490488.1	42.9	Sienito
TG33	729220.7	7490567.8	65.0	Sienito com venulação
TG34	729584.3	7490723.5	113.8	Sienito porfirítico
TG35	729795.3	7490970.0	118.9	Sienito
TG36	729992.0	7491102.4	134.5	Sienito
TG37	729938.7	7491175.0	124.1	Brecha
TG38	730176.8	7491458.9	114.5	Sienito
TG38B	730215.9	7491472.5	125.6	Sienito
TG39	728881.6	7490259.3	53.5	Sienito
TG40	728954.1	7490131.9	83.5	Sienito
TG41	729059.1	7490022.0	117.7	Traquito
TG42	729166.9	7489991.5	169.3	Traquito/Fonolito
TG43	729328.8	7490147.3	194.1	Sienito
TG44	729290.6	7489993.9	204.2	Embasamento
TG45	729507.8	7489766.2	286.1	Sienito
TG46	729679.0	7489823.2	321.2	Rocha alterada (sienito) com sílex
TG47	730090.1	7490095.7	395.0	Sienito
TG48	730151.3	7485068.7	3.3	Brecha
TG49	730163.9	7485660.0	24.9	Brecha
TG50B	730088.3	7485871.2	34.7	Sienito/Fonolito
TG51	730405.7	7486018.9	62.1	Sienito
TG52	730636.7	7486240.8	115.0	Brecha/Sienito
TG53	730647.1	7486393.2	145.5	Brecha/Sienito/Fonolito
TG54	731143.6	7486825.3	225.6	Sienito
TG55	730957.5	7487185.6	301.7	Sienito
TG56	730834.5	7487407.9	367.8	Veio de quartzo
TG57	730903.1	7487587.3	390.7	Sienito
TG58	731000.2	7487760.0	411.1	Sienito
TG59	731444.6	7486620.3	252.7	Sienito
TG60	732019.3	7486454.6	242.1	Sienito
TG61	729199.6	7488754.5	71.5	Sienito
TG62	729323.1	7488787.0	82.8	Sienito com pseudoleucita
TG63	729408.2	7488819.2	104.7	Sienito com pseudoleucita
TG64	729612.8	7488889.7	127.5	Sienito com pseudoleucita

Ponto	X	Y	Z	Litologia
TG65	729966.6	7489642.8	249.8	Sienito com pseudoleucita
TG66	730148.4	7489621.6	304.1	Sienito com pseudoleucita
TG67	730270.6	7489608.7	372.2	Sienito com pseudoleucita
TG68	730316.3	7489643.4	384.7	Sienito
TG69	730400.0	7489542.9	447.1	Sienito com pseudoleucita
TG70	730420.6	7489573.8	456.5	Sienito
TG71	730580.5	7489640.0	501.0	Sienito
TGC72	728398.0	7488967.1	-12.4	Sienito
TGC73	728739.7	7488887.0	39.3	Sienito
TGC74	728895.6	7488801.9	52.3	Sienito
TGC75	728683.5	7487458.8	22.2	Sienito
TG76	730265.3	7485970.8	50.6	Sienito
TG77	730370.1	7486003.3	57.6	Sienito
TG78	731710.0	7485317.9	78.2	Sienito/Fonolito
TG110	733783.0	7488677.0		Sienito
TG111	733442.0	7488713.0		Sienito
TG112	733302.0	7488696.0		Sienito
TG113	733202.0	7488634.0		Sienito
TG114	733055.0	7488461.0		Sienito

APÊNDICE B – Tabela de resultados de análises químicas

Amostra	TG-02	TG-02B	TG-02C	TG-03	TG-04D	TG-06	TG-09	TG-12	TG-16
Analito	Litologia								
	Monzonito	Sienito	Sienito	Sienito	Sienito	Nefelina sienito	Nefelina sienito	Sienito	Fonolito
SiO_2	60,70	58,20	58,10	57,50	59,20	56,40	56,90	59,10	59,80
Al_2O_3	18,45	18,70	18,20	19,15	18,40	20,10	19,70	18,30	19,35
Fe_2O_3	3,42	3,12	3,96	2,72	3,06	2,77	2,55	3,73	2,51
CaO	0,62	2,02	3,09	2,25	2,42	2,44	2,29	2,55	1,50
MgO	0,20	0,66	0,82	0,75	0,60	0,50	0,43	0,94	0,32
Na_2O	3,05	2,77	3,61	4,80	4,00	5,42	4,54	3,66	6,14
K_2O	9,53	9,16	8,93	8,72	8,91	8,20	8,82	7,99	8,13
Cr_2O_3	0,00	<0,002	<0,002	<0,002	<0,002	<0,002	<0,002	<0,002	<0,002
TiO_2	1,40	1,25	1,73	0,90	1,19	0,97	0,88	1,11	0,67
MnO	0,15	0,12	0,15	0,15	0,14	0,12	0,13	0,15	0,19
P_2O_5	0,15	0,13	0,21	0,09	0,14	0,16	0,13	0,33	0,06
SrO	0,04	0,12	0,17	0,16	0,17	0,46	0,44	0,24	0,01
BaO	0,02	0,03	0,03	0,03	0,03	0,12	0,10	0,03	<0,01
LOI	2,30	2,61	1,41	1,53	2,00	2,50	2,82	1,89	0,96
Total	100,03	98,89	100,41	98,75	100,26	100,16	99,73	100,02	99,64
Ba	169,5	310	319	297	305	1075	918	268	24,1
Ce	428	355	484	273	340	258	255	261	325
Cr	20	10	20	10	10	10	10	10	10
Cs	0,99	1,7	0,59	0,3	0,84	0,92	1,78	1,7	2,31
Dy	10	15,1	12,85	5,44	8,75	5,61	5,46	7,11	5,52
Er	4,94	6,59	5,56	3,09	3,94	2,76	2,9	2,79	3,29
Eu	4,66	9,13	7,11	3,32	5,16	3,9	3,61	7,83	2,11
Ga	23,2	21,6	21	23	20,7	24,9	26,2	21,6	24,4
Gd	12,45	20,3	16,2	6,56	10,75	7,28	6,86	10,7	6,36
Hf	11,4	12	12,3	21	9,1	10,8	13,8	7,7	14,8
Ho	1,95	2,82	2,37	1,09	1,61	1,08	1,04	1,3	1,11
La	188,5	226	199,5	133	151	131	141	134,5	192,5
Lu	0,48	0,69	0,51	0,53	0,35	0,3	0,37	0,31	0,51
Nb	225	182	247	169	175,5	154,5	170,5	90,1	211
Nd	163	255	198,5	87,9	137,5	88,9	83,1	118,5	84,8
Pr	49,5	72,2	56,9	28,3	39,1	27	25,9	31,3	32
Rb	191	141,5	124	116,5	132	115,5	218	109,5	158
Sm	20,3	36,4	27,9	11,15	18,9	12,1	11,35	18,55	9,81
Sn	4	4	4	3	3	2	2	2	3
Sr	349	1015	1430	1405	1475	3890	3900	1965	102,5
Ta	21,2	17,9	24,4	10,3	16,1	9,4	8,9	5,5	11,6
Tb	1,79	2,91	2,22	0,9	1,6	1	0,98	1,37	0,92

Amostra	TG-02	TG-02B	TG-02C	TG-03	TG-04D	TG-06	TG-09	TG-12	TG-16
Analito	Litologia								
	Monzonito	Sienito	Sienito	Sienito	Sienito	Nefelina sienito	Nefelina sienito	Sienito	Fonolito
Th	10,7	8,71	10,1	10,2	7,73	12,5	20,3	9,37	17,8
Tm	0,69	0,92	0,76	0,52	0,56	0,39	0,43	0,42	0,53
U	2,49	1,49	1,66	1,95	1,27	2,37	4,61	1,85	2,48
V	60	49	60	42	47	52	44	31	31
W	10	5	10	4	6	3	4	2	6
Y	51,1	65,9	60,2	30	40,6	29,1	30,5	32	30,6
Yb	3,6	5,3	4,1	3,39	2,83	2,29	2,59	2,28	3,04
Zr	392	613	483	1390	331	487	718	325	780
Ag	<0,5	<0,5	<0,5	<0,5	<0,5	<0,5	<0,5	<0,5	<0,5
As	12	<5	<5	5	6	<5	<5	<5	7
Cd	<0,5	<0,5	<0,5	<0,5	<0,5	<0,5	<0,5	<0,5	<0,5
Co	2	2	3	2	2	2	2	1	2
Cu	1	1	1	1	1	1	2	1	1
Li	20	10		10	10	10	10	10	10
Mo	7	4	8	6	7	3	7	1	5
Ni	1	<1	<1	1	<1	<1	1	<1	<1
Pb	14	10	8	11	8	8	17	10	14
Sc	1	1	1	1	1	1	1	2	1
Tl	10	10	10	<10	10	<10	10	<10	10
Zn	84	78	98	81	84	76	81	94	109
Mg	0,12	0,40	0,49	0,45	0,36	0,30	0,26	0,57	0,19
Fe	2,39	2,18	2,77	1,90	2,14	1,94	1,78	2,61	1,76

Amostra	TG-18	TG-19	TG-21	TG-24	TG-26	TG-27	TG-113	TG-114	TG04C
Analito	Litologia								
	Sienito	Nefelina sienito	Fonolito	Sienito	Sienito	Sienito	Nefelina sienito	Nefelina sienito	Traquito
SiO_2	58,00	57,90	55,00	58,60	57,80	57,90	54,80	59,10	57,5
Al_2O_3	19,90	22,30	21,30	18,50	19,05	18,15	18,95	20,40	19,6
Fe_2O_3	2,50	1,31	3,10	4,45	4,13	4,35	3,83	1,97	3,01
CaO	1,88	1,19	2,17	2,95	2,70	3,53	3,28	2,00	2,25
MgO	0,52	0,08	0,42	1,21	1,10	1,37	0,75	0,51	0,62
Na_2O	5,35	6,72	8,20	3,75	3,80	3,63	4,87	5,13	4,07
K_2O	8,35	8,99	6,84	7,93	8,50	7,77	7,96	9,12	5,17
Cr_2O_3	<0,002	<0,002	0,01	<0,002	<0,002	<0,002	<0,002	<0,002	0,002
TiO_2	0,76	0,23	0,71	1,37	1,16	1,62	1,30	0,56	0,3
MnO	0,14	0,05	0,14	0,17	0,15	0,17	0,17	0,10	0,17
P_2O_5	0,08	0,01	0,12	0,42	0,42	0,58	0,24	0,08	0,03
SrO	0,10	0,10	0,22	0,38	0,47	0,38	0,41	0,46	0,03
BaO	0,01	<0,01	0,16	0,06	0,07	0,05	0,09	0,12	<0,01
LOI	1,88	1,19	1,60	1,67	1,39	2,19	1,19	1,56	6,59
Total	99,47	100,07	99,99	101,46	100,74	101,69	97,84	101,11	99,34
Ba	59,2	48,8	1475	532	708	492	842	1110	31,1
Ce	277	72,4	149	260	244	385	342	139,5	224
Cr	10	10	10	10	10	10	10	10	7
Cs	1,23	0,84	1,46	1,56	0,83	1,16	1,25	1,05	0,44
Dy	5,31	0,89	2,97	13	6,75	11,15	8,36	1,9	4,34
Er	2,74	0,73	1,74	6,15	2,85	4,48	3,98	1,22	3,24
Eu	2,94	0,9	1,44	10,3	8,07	9,26	5,62	1,92	0,67
Ga	24	24,3	23,2	21,7	21	21,5	24,7	23,2	28,9
Gd	6,04	0,83	3,2	19,15	9,76	17	11,3	2,07	4,15
Hf	10,8	13,6	5,6	8	7,2	9,5	13,1	8,8	21,9
Ho	1,04	0,21	0,59	2,64	1,18	1,99	1,59	0,4	0,96
La	140,5	55,1	101,5	152,5	117	175,5	177	87,3	150
Lu	0,33	0,22	0,29	0,53	0,3	0,4	0,43	0,2	0,72
Nb	161	41,8	122,5	96,7	83,4	134,5	171,5	98	254
Nd	88,9	14,8	38,1	146,5	106,5	187	135	32,3	44,1
Pr	28,5	5,87	13,15	36,6	27,5	46,6	39,2	12	17,9
Rb	144	133	124	113	112,5	102,5	146	137,5	179,5
Sm	11,1	1,64	4,94	23,3	16,1	28,7	19,05	3,59	5,38
Sn	3	1	1	2	3	3	3	1	2,8
Sr	841	821	1905	3140	3910	3180	3360	3950	337
Ta	10,1	1,2	4,4	6,4	5	10,4	12,1	3,2	10,6
Tb	0,86	0,14	0,49	2,38	1,19	2,18	1,49	0,31	0,67
Th	9,65	8,11	14,55	9,11	7,46	9,89	20,2	10,6	37,1
Tm	0,41	0,17	0,31	0,78	0,36	0,58	0,55	0,19	0,55
U	2,14	1,89	4,02	1,83	1,45	1,67	4,09	2,28	8,63

Amostra	TG-18	TG-19	TG-21	TG-24	TG-26	TG-27	TG-113	TG-114	TG04C
Analito	Litologia								
	Sienito	Nefelina sienito	Fonolito	Sienito	Sienito	Sienito	Nefelina sienito	Nefelina sienito	Traquito
V	42	28	53	41	45	42	81	36	9
W	8	3	3	2	3	2	5	3	8
Y	28,6	7,5	17,4	83,9	29,1	51,3	41,8	11,9	28,6
Yb	2,55	1,21	2,03	3,81	1,93	3,11	3,07	1,34	2,55
Zr	517	1040	320	342	298	358	617	417	517
Ag	<0,5	<0,5	<0,5	<0,5	<0,5	<0,5	<0,5	<0,5	<0,5
As	<5	<5	<5	<5	<5	5	9	8	<5
Cd	<0,5	<0,5	<0,5	<0,5	<0,5	<0,5	<0,5	<0,5	<0,5
Co	2	<1	4	4	2	4	3	1	2
Cu	1	<1	3		2	1	1	1	1
Li	10	<10	10	10	10	10	10	10	10
Mo	11	2	2	1	1	2	9	2	11
Ni	<1	<1	1	<1	1	<1	<2	<3	<1
Pb	11	10	17	9	7	9	9	15	11
Sc	<1	<1	<1	2	2	2	1	1	<1
Tl	<10	<10	<10	<10	<10	<10	10	10	<10
Zn	97	36	81	95	84	97	113	59	97
Mg	0,31	0,05	0,25	0,73	0,66	0,83	0,45	0,31	0,31
Fe	1,75	0,92	2,17	3,11	2,89	3,04	2,68	1,38	1,75

Amostra	TG42A	TG42B	TG62A	TG64A	TG71	TG76	TG77A	TG78A
Analito	Litologia							
	Traquito	Fonolito	Sienito	Nefelina sienito	Sienito	Sienito	Sienito	Sienito
SiO_2	58,9	50,5	58,8	57,9	58,8	58,9	56,8	59,1
Al_2O_3	22,2	12,8	19,35	19,6	19,45	19,55	19,15	19,55
Fe_2O_3	2,85	15,65	3,75	3,69	3,53	3,21	3,87	2,94
CaO	0,15	7,72	2,35	2,76	2,16	2,21	2,86	1,82
MgO	0,43	4,54	0,63	0,61	0,62	0,39	0,66	0,35
Na_2O	0,63	2,95	4,55	4,21	3,76	4,73	3,98	4,01
K_2O	9,13	1,68	9,22	9,18	9,66	7,82	9,13	8,08
Cr_2O_3	<0,002	0,01	<0,002	<0,002	<0,002	<0,002	0,002	<0,002
TiO_2	0,38	3,05	1,28	1,11	1,28	0,81	1,2	0,59
MnO	0,26	0,2	0,16	0,16	0,14	0,15	0,16	0,29
P_2O_5	0,03	0,38	0,14	0,15	0,13	0,1	0,17	0,06
SrO	<0,01	0,05	0,11	0,48	0,08	0,17	0,54	0,02
BaO	0,03	0,06	0,01	0,14	0,01	0,02	0,16	0,01
LOI	4,87	1,02	1,16	0,89	1,74	1,99	0,96	4,15
Total	99,86	100,61	101,51	100,88	101,36	100,05	99,64	100,97
Ba	235	576	138,5	1335	72,9	196	1500	65,1
Ce	477	71,4	379	373	356	289	378	370
Cr	<5	73	6	7	6	5	7	5
Cs	1,92	2,47	1,59	0,86	0,96	1,1	0,91	1,53
Dy	8,79	7,62	9,3	10,25	11,35	7,71	10,8	6,36
Er	5,5	3,71	4,72	4,93	5,77	3,74	4,8	3,68
Eu	1,94	2,78	4,63	6,85	5,86	4,86	7,06	1,96
Ga	36,6	25,3	21,9	22,5	20,7	25,9	21,2	26,1
Gd	7,23	8,68	12,55	13,75	15,8	10,8	14,8	6,25
Hf	25	6,79	14,5	11,05	9,84	9,77	10,45	16,4
Ho	1,91	1,38	1,77	1,89	2,06	1,42	1,9	1,33
La	82,1	32	175	168	177,5	140	157,5	201
Lu	0,79	0,43	0,45	0,41	0,45	0,37	0,45	0,61
Nb	281	23,3	237	184,5	195,5	139	182	208
Nd	50,5	39,1	144	147	170,5	119,5	153,5	90,9
Pr	17,2	9,36	43,1	43,3	48,3	34,1	44,7	33,9
Rb	297	64,2	149,5	119,5	136,5	126	114	209
Sm	9,04	9,02	19,25	20,9	22,4	17,15	22,3	9,88
Sn	3,6	2,2	3,3	2,7	3,3	3,4	2,7	3,4
Sr	63,6	488	1005	4370	854	1525	4950	187
Ta	12,8	1,6	19,6	14,3	18,8	9,7	15,2	8,7
Tb	1,34	1,35	1,77	1,96	2,18	1,47	1,99	1,02
Th	33,7	3,5	14,05	12,95	10,3	9,98	10,2	19,4
Tm	0,95	0,54	0,57	0,64	0,63	0,44	0,6	0,61
U	7,49	0,73	3,33	2,31	2,02	2,09	2,11	4,13

Amostra	TG42A	TG42B	TG62A	TG64A	TG71	TG76	TG77A	TG78A
Analito	Litologia							
	Traquito	Fonolito	Sienito	Nefelina sienito	Sienito	Sienito	Sienito	Sienito
V	24	465	44	52	43	31	56	13
W	3,4	1,5	4,9	3,6	7,2	1,8	3,9	2,4
Y	52,6	37,5	45,2	47	55,6	34,9	47,9	37,6
Yb	5,78	3,23	3,25	3,53	3,32	2,49	3,18	3,58
Zr	1300	256	632	493	386	417	454	780
Ag	-	-	-	-	-	-	-	-
As	-	-	-	-	-	-	-	-
Cd	-	-	-	-	-	-	-	-
Co	-	-	-	-	-	-	-	-
Cu	-	-	-	-	-	-	-	-
Li	-	-	-	-	-	-	-	-
Mo	-	-	-	-	-	-	-	-
Ni	-	-	-	-	-	-	-	-
Pb	-	-	-	-	-	-	-	-
Sc	<0,5	35,4	2	1,3	1,7	1,2	1,8	0,7
Tl	-	-	-	-	-	-	-	-
Zn	-	-	-	-	-	-	-	-
Mg	0,26	2,74	0,38	0,37	0,37	0,24	0,40	0,21
Fe	1,99	10,95	2,62	2,58	2,47	2,25	2,71	2,06

APÊNDICE C – Tabela com resultados semiquantificados das fases por Difratometria de Raios X

Amostra	TG-32C	TG-56	TG-02	TG-04C	TG-41	TG-42A	TG-21	TG-14	TG-113	TG-06	TG-09	TG-19	TG-114
Analito	Litologia												
	Embasam.	Embasam.	Monzonito	Traquito	Traquito	Traquito	Nefelina sienito	Nefelina sienito	Nefelina sienito	Nefelina sienito	Nefelina sienito	Nefelina sienito	Nefelina sienito
Quartzo	56.0	86.7		11.8	0.5	24.0							
Ortoclásio		5.6	27.4	2.3			9.8	22.0	16.9	12.8	11.1	13.0	8.1
Microclina			14.9	14.3		35.3	49.1	37.9	43.3	44.3	49.2	43.3	49.8
Sanidina						6.7							
Albita			47.2	59.8	99.5	5.5	24.2	23.1	12.3	12.4	11.8	12.1	10.5
Labradorita	31.3												
Andesina													
Nefelina			5.2				5.8	8.4	13.4	9.8	10.1	25.5	19.4
Sodalita												0.3	
Analcima							2.2	1.4	4.3	13.7	12.4	2.8	8.1
Muscovita			3.2	8.2		14.3							
Biotita	12.6							0.4		1.6			
Flogopita													
Goethita			1.1										
Magnetita							1.3	0.7	1.3				
Calcita			0.6	1.5		2.7							
Anatásio			0.2										
Titanita							4.3	3.6	5.1	3.1	3.1	2.1	2.1
F-Arfvedsonita							3.4	2.5	3.3	2.3	2.3		2.0
Hornblenda												0.9	
Aegerina													
Pirita				2.1									
Caulinita		7.7				11.5							
Dolomita													
Hedenbergita													
Riebeckita													
Ferrotschermakita	0.1												
Zircão													

Amostra	TG-36	TG-47	TG-37	TG-63D	TG-64A	TG-65A	TG-65B	TG-04D	TG-18	TG-24	TG-26	TG-02C	TG-12
Analito	Litologia												
	Nefelina sienito	Nefelina sienito	Nefelina sienito	Nefelina sienito	Nefelina sienito	Nefelina sienito	Nefelina sienito	Sienito	Sienito	Sienito	Sienito	Sienito	Sienito
Quartzo													
Ortoclásio	60.1	82.3	56.1					11.7	14.6	28.9	45.5	13.6	18.9
Microclina								49.1	47.6	45.6	30.6	62.9	35.0
Sanidina				81.5	85.4	84.6	85.7						
Albita	24.5		29.7					23.6	28.3	10.4	13.7	15.7	39.1
Labradorita													
Andesina													
Nefelina	5.3	12.3	2.3	11.3	13.0	12.2	12.3						
Sodalita				3.6									
Analcima	2.9				1.5	2.2	1.2	7.7	3.7	4.1	3.2	3.9	0.1
Muscovita													
Biotita	3.6	5.4	4.1	3.5					2.7	5.2	4.1	0.2	5.7
Flogopita													
Goethita													
Magnetita								1.2					
Calcita			4.0										
Anatásio			0.3										
Titanita								3.9	2.4	3.2	2.5	3.6	0.4
F-Arfvedsonita								2.7	0.8	2.5		0.2	
Hornblenda	3.5										0.4		0.7
Aegerina													
Pirita													
Caulinita													
Dolomita													
Hedenbergita													
Riebeckita					0.1	0.9	0.8						
Ferrotschermakita													
Zircão			3.6										

Amostra	TG-27	TG-62A	TG-68	TG-71	TG-76	TG-77A	TG-77B	TG-78A	TG-78B	TG-16	TG-21	TG-28	TG-42B
Analito	Litologia												
	Sienito	Sienito	Sienito	Sienito	Sienito	Sienito	Sienito	Sienito	Sienito	Fonolito	Fonolito	Fonolito	Fonolito
Quartzo													
Ortoclásio	7.8				42.7								
Microclina	36.8	68.8			12.1	23.1	65.2	35.6	37.0	53.5		3.0	2.4
Sanidina			60.0	68.2		65.3				3.8	54.6	49.5	12.2
Albita	46.6	28.3	37.6	24.1	32.7		29.9	55.9	50.0	28.0	1.6	3.6	57.3
Labradorita													
Andesina								1.8	9.5				
Nefelina										4.7	38.0	33.9	
Sodalita		0.8								1.7		1.8	
Analcima		1.4	1.1	0.7	7.3		4.0			2.6	5.5	4.7	
Muscovita													
Biotita	4.0								3.7				5.2
Flogopita								1.7					
Goethita													
Magnetita												1.9	
Calcita													
Anatásio													
Titanita	2.6									3.3	0.3	0.8	8.9
F-Arfvedsonita										2.1			
Hornblenda	2.2		1.3	7.0	4.0	7.4							14.0
Aegerina					1.1					0.8		0.7	
Pirita													
Caulinita													
Dolomita						4.2		3.2					
Hedenbergita								1.7					
Riebeckita		0.7					0.9						
Ferrotschermakita													
Zircão													

APÊNDICE D – Imagens dos difratogramas das amostras com os minerais indicados

Embasamento

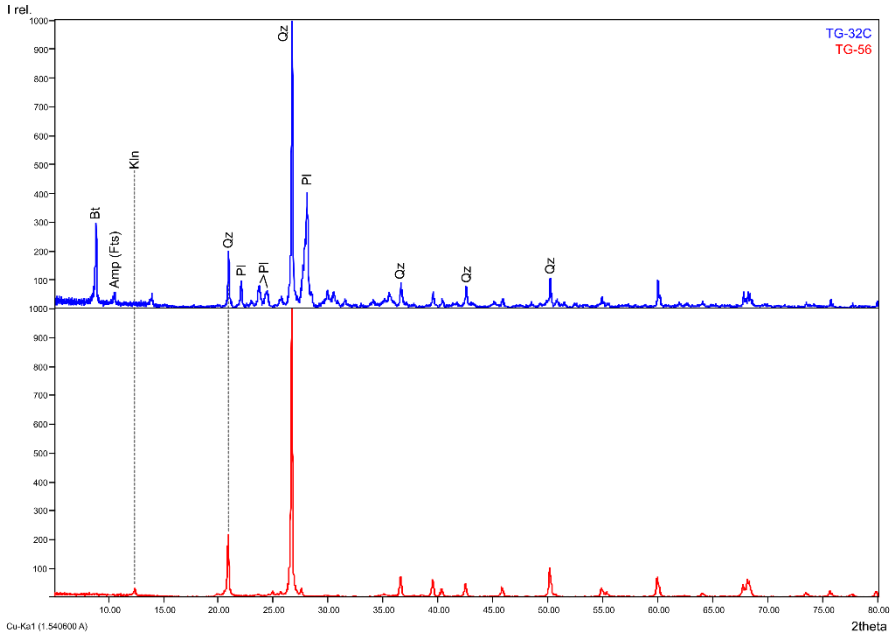

Amp – anfibólio; Bt - biotita; Fts - ferro-tschermakita; Pl - plagioclásio; Qz – quartzo (Warr, 2021).

Monzonito

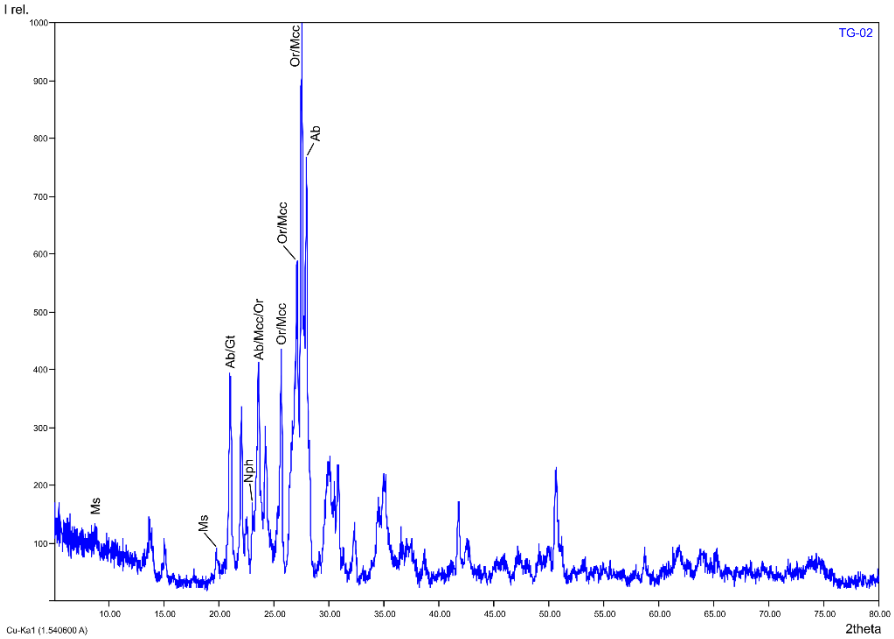

Ab - albita; Gt - goethita; Mcc - microclina; Ms - muscovita; Nph – nefelina; Or – ortoclásio (Warr, 2021)

Fonolito

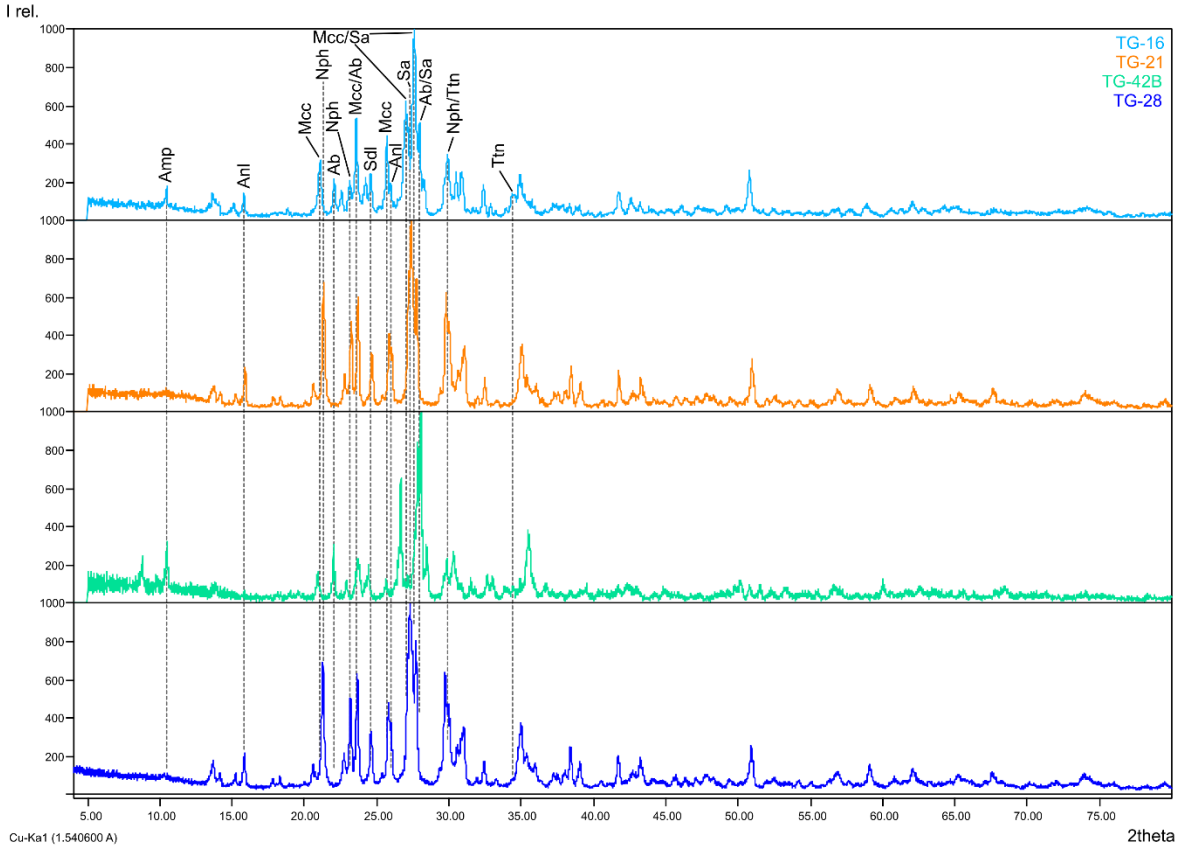

Ab - albita; Amp - anfibólio; Anl - analcima; Mcc - microclina; Nph - nefelina; Sa - sanidina; Sdl - sodalita; Ttn - titanita (Warr, 2021)

Nefelina sienito

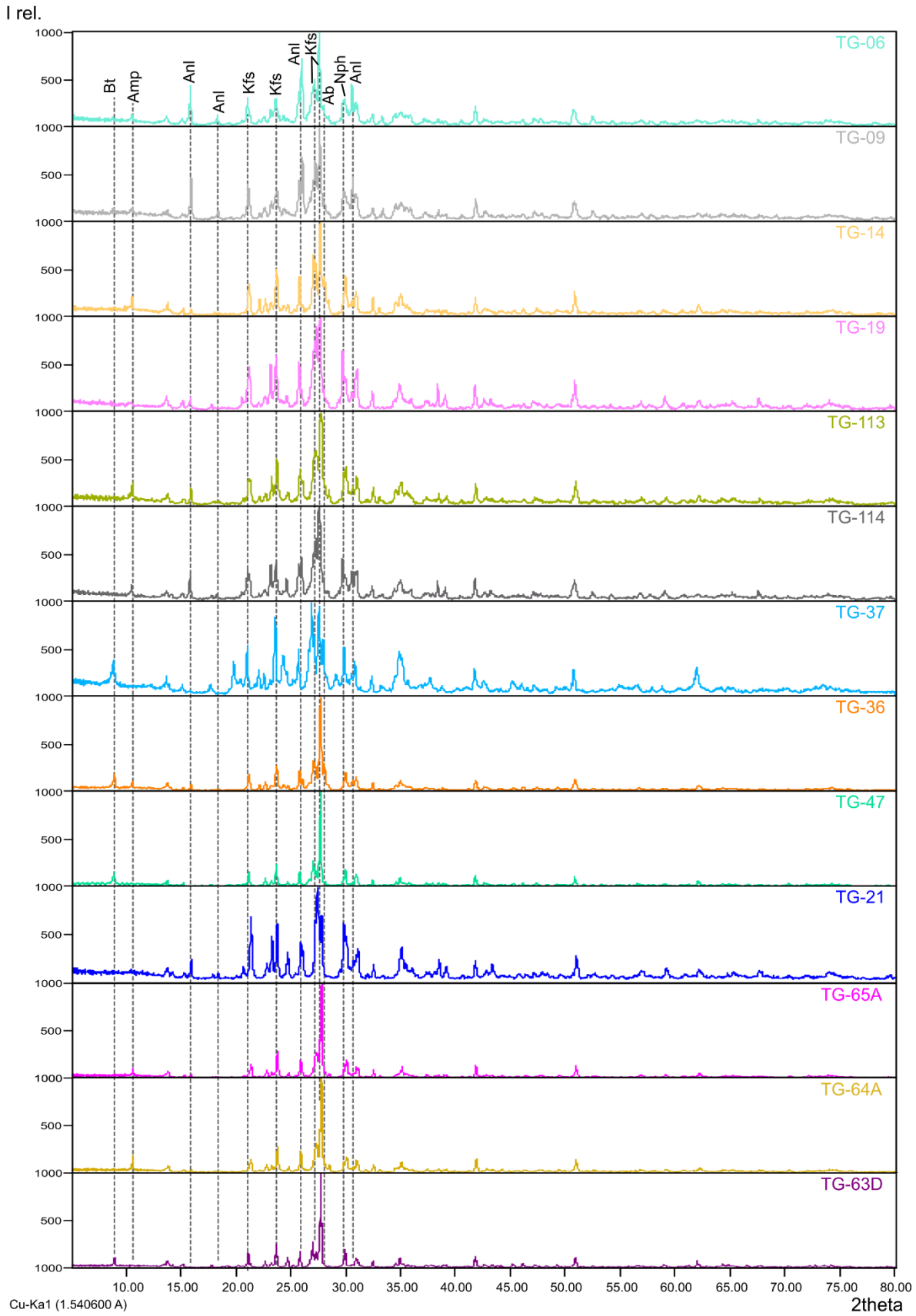

Ab - albita; Amp - anfibólio; Anl - analcima; Bt - biotita; Kfs - K-feldspato (microclina e/ou ortoclásio); Nph – nefelina (Warr, 2021).

(Alcali-feldspato) Sienito

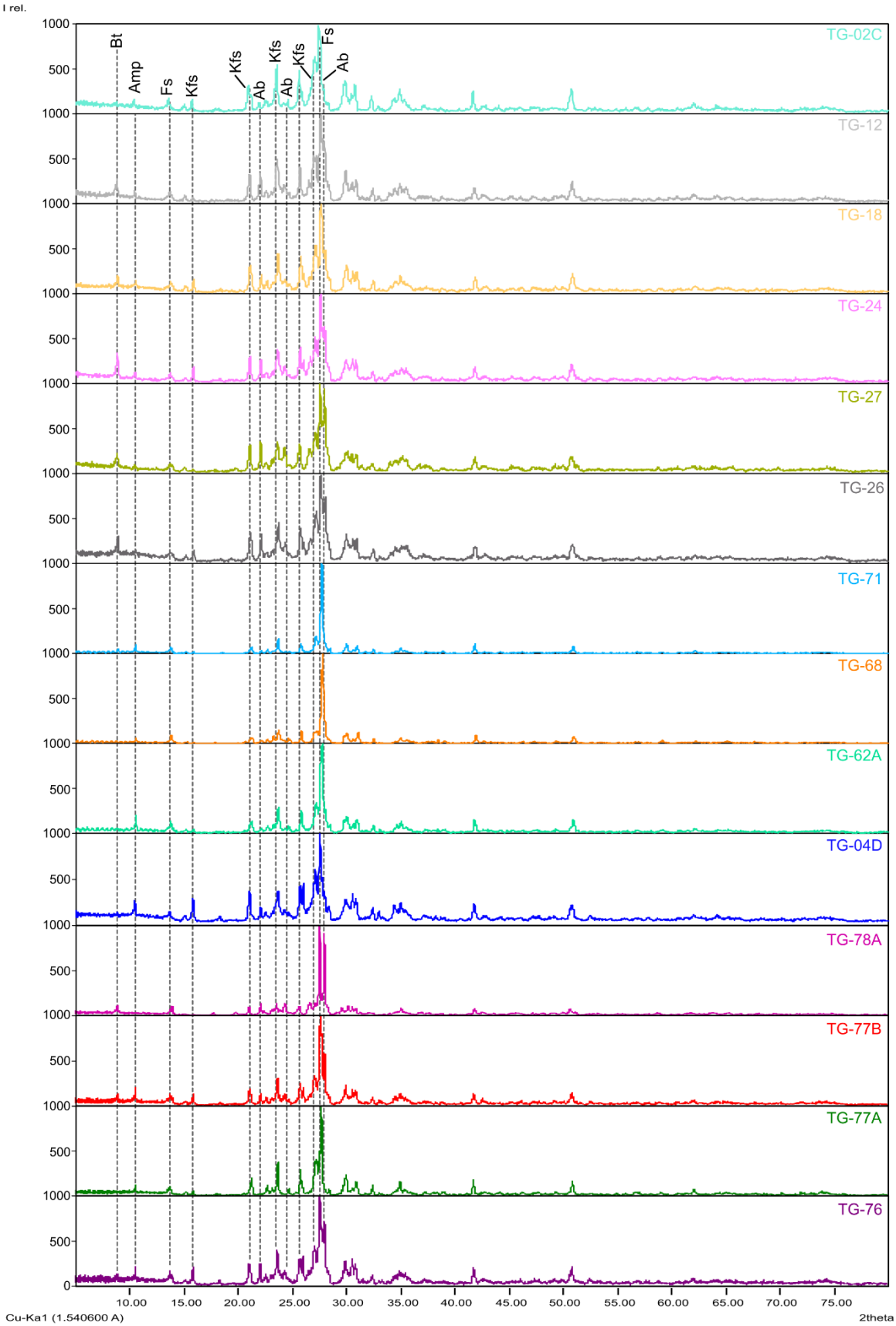

Ab - albita; Amp - anfibólio; Anl - analcima; Bt - biotita; Fsp – feldspato (Kfs e Ab) Kfs - K-feldspato (microclina, sanidina e/ou ortoclásio); Nph – nefelina (Warr, 2021).

APÊNDICE E – Geoquímica Isotópica de Sr-Sm-Nd

Amostra	Sm_{ID} (ppm)	Nd_{ID} (ppm)	$^{143}Nd/^{144}Nd(m)$	Std. Err. Abs (2s)	$^{147}Sm/^{144}Nd(m)$	$^{87}Sr/^{86}Sr(m)$	Std. Err. Abs (2s)
TG03	10.6	83.5	0.512429	0.000007	0.0764	0.705155	0.000016
TG04D	18.2	129.4	0.512434	0.000003	0.085	0.705478	0.000018
TG12	17	112.3	0.512431	0.000004	0.0916	0.705326	0.000009
TG16	9.6	83.9	0.512439	0.000002	0.0691	0.709476	0.000008
TG19	1.5	13.7	0.512467	0.000003	0.0649	0.705237	0.000011
TG26	15.4	100.8	0.512443	0.000002	0.0923	0.705211	0.00001

APÊNDICE F – U-Pb em Zircão por LA-ICP-MS

Amostra	Litotipo	Análise	Razões							Idades					
			$^{207}Pb/^{206}Pb$	2s%	$^{207}Pb/^{235}U$	2s%	$^{206}Pb/^{238}U$	2s%	Rho	$^{207}Pb/^{206}Pb$	2s%	$^{207}Pb/^{235}U$	2s%	$^{206}Pb/^{238}U$	2s%
TG-02	Monzonito	TG02_1	0.046970151	12.57867009	0.065151019	57.3433221	0.01006	55.94670365	0.975644619	115.454082	176	65.88400513	5	64.52689785	2
		TG02_2	0.047247371	3.178345998	0.067229305	10.81390626	0.01032	10.33628005	0.955832222	74.43840355	106	66.40871726	3	66.1860587	1
		~~TG02_3~~	~~0.044561678~~	~~25.86857478~~	~~0.06402219~~	~~107.013434~~	~~0.01042~~	~~103.8397414~~	~~0.970343045~~	~~54.80677154~~	~~403~~	~~66.49869988~~	~~11~~	~~66.8240838~~	~~3~~
		TG02_4	0.045646218	23.90321374	0.064258683	106.5100382	0.01021	103.7931819	0.974492017	109.0972298	255	66.66073242	7	65.48415815	2
		TG02_5	0.045025761	23.98028436	0.064378535	102.91594	0.01037	100.0831488	0.972474709	73.93794323	298	66.70652638	8	66.50507914	2
		TG02_6	0.045757296	14.64544837	0.065803037	63.85855629	0.01043	62.15646429	0.973345905	63.89663143	171	66.80660252	5	66.88788283	2
		TG02_7	0.046410759	9.738806523	0.066614792	42.04431173	0.01041	40.90085324	0.972803491	70.43045094	152	66.86001875	4	66.76028413	2
		~~TG02_8~~	~~0.043748339~~	~~39.77475976~~	~~0.062853659~~	~~159.2627818~~	~~0.01042~~	~~154.2160891~~	~~0.968312166~~	~~77.93736796~~	~~667~~	~~67.12701842~~	~~18~~	~~66.8240838~~	~~4~~
		TG02_9	0.045855666	17.36092102	0.064932889	75.36913492	0.01027	73.34238147	0.973108973	81.92708832	257	66.29927705	7	65.86702247	2
		~~TG02_10~~	~~0.044088245~~	~~40.58073459~~	~~0.061335972~~	~~176.455028~~	~~0.01009~~	~~171.7253065~~	~~0.973195881~~	~~112.523211~~	~~436~~	~~65.99480202~~	~~12~~	~~64.71836128~~	~~2~~
		~~TG02_11~~	~~0.044469314~~	~~26.42850633~~	~~0.06431869~~	~~111.2101044~~	~~0.01049~~	~~108.0241704~~	~~0.971352117~~	~~56.32523732~~	~~316~~	~~66.97226887~~	~~9~~	~~67.2706638~~	~~2~~
		TG02_12	0.04726239	2.609509805	0.067120344	7.762817356	0.0103	7.311073237	0.941806679	71.43335498	98	66.2030727	3	66.0584461	1
		TG02_13	0.046570663	16.55384529	0.065174805	75.1518392	0.01015	73.30599662	0.975438491	117.4050903	197	66.50778687	5	65.10127109	2
		TG02_14	0.046765566	13.86186562	0.065641008	62.78908313	0.01018	61.23983705	0.975326187	112.523211	174	66.56457543	5	65.29271746	2
TG-02C	Sienito	TG02(C)_1	0.0484	7.68595	0.069003	7.685957	0.01034	2.417795	0.314573	118.8668	181	67.75277	5	66.31367	2
		TG02(C)_2	0.0478	5.104603	0.069004	5.104613	0.01047	2.387775	0.467768	89.38181	121	67.75408	3	67.14307	2
		TG02(C)_3	0.04743	5.650432	0.068143	5.650442	0.01042	2.399232	0.42461	70.93198	134	66.93583	4	66.82408	2
		TG02(C)_4	0.04861	6.994446	0.069235	6.994453	0.01033	2.420136	0.346008	129.0626	165	67.97346	5	66.24986	2
		TG02(C)_5	0.04894	9.807928	0.0693	9.807933	0.01027	2.92113	0.297833	144.9575	230	68.03533	6	65.86702	2
		~~TG02(C)_6~~	~~0.05067~~	~~4.499704~~	~~0.069934~~	~~4.499715~~	~~0.01001~~	~~1.998002~~	~~0.444029~~	~~225.8459~~	~~104~~	~~68.63649~~	~~3~~	~~64.20778~~	~~1~~
		~~TG02(C)_7~~	~~0.04724~~	~~9.144793~~	~~0.069043~~	~~9.144799~~	~~0.0106~~	~~2.830189~~	~~0.309486~~	~~61.3767~~	~~218~~	~~67.79049~~	~~6~~	~~67.97237~~	~~2~~
		TG02(C)_8	0.04895	10.29622	0.069112	10.29623	0.01024	2.929688	0.28454	145.4368	242	67.85649	7	65.67559	2
		TG02(C)_9	0.04861	7.076733	0.068699	7.076741	0.01025	2.439024	0.344654	129.0626	166	67.46415	5	65.7394	2
		TG02(C)_10	0.04922	6.501422	0.069222	6.50143	0.0102	2.45098	0.376991	158.3241	152	67.96072	4	65.42035	2
		TG02(C)_11	0.04746	7.332491	0.067205	7.332498	0.01027	2.434275	0.331984	72.43565	174	66.04333	5	65.86702	2
		~~TG02(C)_12~~	~~0.04707~~	~~18.61058~~	~~0.068924~~	~~18.61058~~	~~0.01062~~	~~3.295669~~	~~0.177086~~	~~52.77997~~	~~444~~	~~67.67778~~	~~12~~	~~68.09994~~	~~2~~
		TG02(C)_13	0.04788	4.427736	0.068262	4.427748	0.01034	1.934236	0.436844	93.34388	105	67.04836	3	66.31367	1
		TG02(C)_14	0.04879	4.837057	0.068684	4.837068	0.01021	1.958864	0.404969	137.7517	114	67.45019	3	65.48416	1
TG-03	Sienito	~~TG03_1~~	~~0.124029813~~	~~27.27534438~~	~~0.282512329~~	~~191.7650751~~	~~0.01652~~	~~189.8154356~~	~~0.989833188~~	~~2312.367807~~	~~296~~	~~293.4050728~~	~~45~~	~~105.6246849~~	~~6~~
		TG03_2	0.04458819	33.69330159	0.091909904	101.8688489	0.01495	96.13544505	0.943717791	101.2394504	431	95.87607323	17	95.66059756	3
		TG03_3	0.047335184	6.112581141	0.098355488	18.12058811	0.01507	17.05848954	0.941387191	96.80286314	132	96.43750157	5	96.42272769	3
		~~TG03_4~~	~~0.043653164~~	~~51.63392919~~	~~0.089019505~~	~~154.2520592~~	~~0.01479~~	~~145.3534834~~	~~0.942311462~~	~~143.5188713~~	~~651~~	~~96.53583579~~	~~26~~	~~94.64428387~~	~~4~~
		TG03_5	0.0459873	29.20080879	0.092321014	92.85039399	0.01456	88.13914244	0.949259757	154.5161707	377	95.52957367	15	93.18305218	3
		TG03_6	0.047780731	10.02153589	0.098293067	31.03476534	0.01492	29.37218885	0.946428579	140.6378152	186	97.23107111	7	95.47005095	3
		TG03_7	0.044762141	41.59567463	0.089861467	130.9469033	0.01456	124.1647749	0.948207035	157.8485535	424	95.65944204	17	93.18305218	3
		TG03_8	0.046039823	23.37484359	0.092997771	73.86031036	0.01465	70.06398599	0.948601294	125.1859895	314	94.9542043	12	93.75487794	3
		~~TG03_9~~	~~0.04288333~~	~~50.36814261~~	~~0.089341706~~	~~141.6833499~~	~~0.01511~~	~~132.4281762~~	~~0.934677055~~	~~81.92708832~~	~~811~~	~~96.1045153~~	~~32~~	~~96.67675105~~	~~5~~
		TG03_10	0.044630691	36.62754266	0.091628291	112.0508182	0.01489	105.8952736	0.945064707	121.3001562	420	96.28649341	17	95.2794987	4
		~~TG03_11~~	~~0.043929687~~	~~48.59331723~~	~~0.089038271~~	~~143.7574738~~	~~0.0147~~	~~135.2956052~~	~~0.941137888~~	~~137.2701626~~	~~747~~	~~95.73186142~~	~~29~~	~~94.072537~~	~~4~~
		TG03_12	0.046948389	19.99695901	0.095091953	64.44590976	0.01469	61.26497299	0.950641759	155.4689732	255	96.38070426	10	94.00900644	3
		TG03_13	0.044549576	34.91706212	0.091277484	106.0463052	0.01486	100.1329997	0.944238458	105.6640797	446	95.49560025	17	95.08894083	3
		TG03_14	0.046101779	15.59031399	0.094966309	48.78247762	0.01494	46.22415205	0.947556465	86.90065949	199	95.26277661	8	95.59708265	3

Amostra	Litotipo	Análise	Razões							Idades					
			$^{207}Pb/^{206}Pb$	2s%	$^{207}Pb/^{235}U$	2s%	$^{206}Pb/^{238}U$	2s%	Rho	$^{207}Pb/^{206}Pb$	2s%	$^{207}Pb/^{235}U$	2s%	$^{206}Pb/^{238}U$	2s%
TG-04D	Sienito	TG04D_1	0.047943785	6.412917597	0.066237101	28.89741014	0.01002	28.17684867	0.975064842	130.0303602	118	66.0247525	3	64.27160443	1
		TG04D_2	0.042375096	44.09994092	0.061406548	178.4391873	0.01051	172.9038426	0.968979097	29.29081012	448	66.36558519	12	67.3982524	2
		TG04D_3	0.047988716	14.85371053	0.065571341	70.68347324	0.00991	69.10514216	0.977670437	180.5179662	186	66.70083666	5	63.56949539	2
		TG04D_4	0.046387517	14.00319944	0.064918495	63.39100044	0.01015	61.82498962	0.975296007	93.83846487	166	65.86874583	4	65.10127109	1
		TG04D_5	0.043943382	40.43201484	0.0602256	180.3771878	0.00994	175.7873206	0.974554059	106.6457129	316	64.8878253	8	63.76098726	2
		TG04D_6	0.04627064	16.37800061	0.064563534	74.61250073	0.01012	72.79276311	0.975610821	101.2394504	175	65.87941293	5	64.90981903	1
		TG04D_7	0.048177279	5.708073532	0.065098295	25.06174851	0.0098	24.40305585	0.973717211	136.3067027	131	64.7876124	4	62.86730986	1
		TG04D_8	0.046677121	4.381940411	0.064873282	17.55310765	0.01008	16.99735822	0.968338972	53.28690443	114	64.35649217	3	64.65454077	1
		TG04D_9	0.045814519	25.18499678	0.062284693	117.033626	0.00986	114.2916688	0.976571202	126.15601	240	64.89990797	6	63.25032963	2
		TG04D_10	0.047195657	7.186968947	0.066179619	32.16447779	0.01017	31.35125371	0.974716702	97.29640969	114	66.0877991	3	65.22890263	1
		TG04D_11	0.046514267	13.71112473	0.062145722	63.71907955	0.00969	62.22641045	0.976574221	97.29640969	205	63.06345308	5	62.16504785	2
		TG04D_12	0.045487137	7.476011096	0.065163653	29.84816403	0.01039	28.89674988	0.968124869	7.026951736	167	65.04530901	4	66.6326829	2
		TG04D_13	0.042615117	47.07230885	0.059286543	199.6895277	0.01009	194.0621168	0.971819199	61.3767005	440	64.63045654	12	64.71836128	2
		TG04D_14	0.043226581	52.19242767	0.059839214	224.5774712	0.01004	218.4284575	0.972619633	126.15601	514	66.04697537	14	64.39925241	3
TGD_TG-16	Fonolito	TGD_16_001	0.065489086	5.201812579	0.099611077	5.597393941	0.011031573	2.0668732	0.36925634	790.0880988	14	96.41733296	5	70.72469811	2
		TGD_16_002	0.147466786	3.748924318	0.256326216	4.341046221	0.012606587	2.18866369	0.50417885	2316.756902	3	231.7019634	4	80.7592961	2
		TGD_16_003	0.172420266	4.135927889	0.302380703	4.5696961	0.012719337	1.943250611	0.425247231	2581.276272	3	268.2579848	4	81.47704133	2
		TGD_16_004	0.055152915	4.576025637	0.085063058	5.099630926	0.011185908	2.250827615	0.441370689	418.4273021	25	82.89395905	5	71.70867592	2
		~~TGD_16_005~~	~~0.05067483~~	~~3.688229082~~	~~0.070747032~~	~~4.072670962~~	~~0.010125457~~	~~1.72731439~~	~~0.424123237~~	~~226.066259~~	~~39~~	~~69.40805267~~	~~4~~	~~64.94464601~~	~~2~~
		TGD_16_006	0.060500333	4.139668422	0.090109779	4.620257224	0.010802217	2.051809486	0.444089882	621.5164045	15	87.60566236	5	69.26213987	2
TGE_TG-16	Fonolito	TGE_16_001	0.04724	21.76121931	0.071843367	21.97845504	0.01110721	3.082502267	0.14025109	61.3767005	1037	70.44721415	30	70.71467003	2
		TGE_16_002	0.04748	32.89806234	0.069720677	33.09099071	0.01065	3.568075117	0.10782618	73.43733059	1564	68.43434477	45	68.29130192	6
		TGE_16_003	0.04743	25.46911238	0.067162189	25.68337685	0.01027	3.310613437	0.128901019	70.93197939	1212	66.0029096	33	65.86702247	5
		TGE_16_004	0.04756	51.30361648	0.070887362	51.83463397	0.01081	7.400555042	0.142772399	77.43797148	2437	69.54116367	71	69.31177848	13
		TGE_16_005	0.04749	50.87386818	0.079557243	51.29818992	0.01215	6.58436214	0.128354668	73.93794323	2419	77.72858456	79	77.85193377	13
		TGE_16_006	0.04781	40.49362058	0.072248789	40.86199871	0.01096	5.474452555	0.133974175	89.87759291	1919	70.8312079	57	70.26832856	10
		TGE_16_007	0.04743	19.10183428	0.068339326	19.28884122	0.01045	2.679425837	0.138910669	70.93197939	909	67.1223139	25	67.01547901	4
		TGE_16_008	0.044103452	48.62246439	0.061296319	139.7768895	0.01008	131.0474525	0.937547351	60.36764701	1706	64.54191102	46	64.65454077	8
		TGE_16_009	0.0471	48.91719745	0.061824289	49.32153665	0.00952	6.302521008	0.12778436	54.30030499	2334	60.91126179	60	61.07958332	10
		TGE_16_010	0.04785	81.88087774	0.073628747	82.5607446	0.01116	10.5734767	0.128069057	91.85922271	3880	72.13714109	121	71.54350792	19
		TGE_16_011	0.046173792	20.93707084	0.063091445	57.86117888	0.00991	53.94029186	0.932236309	71.43335498	808	63.77342153	21	63.56949539	4
		TGE_16_012	0.047009225	40.44099206	0.063973707	44.96641283	0.00987	19.65971628	0.437208909	71.93457781	1896	63.53687752	50	63.31416405	9
		TGE_16_013	0.044889801	42.86637471	0.062946257	134.1427943	0.01017	127.1092569	0.947566789	98.77615989	1406	66.12782104	39	65.22890263	7
		TGE_16_014	0.04742	25.89624631	0.066624967	26.13612024	0.01019	3.532875368	0.135172142	70.43045094	1232	65.49162527	33	65.35653165	6
		TGE_16_015	0.04782	24.21580928	0.070879282	24.44627027	0.01075	3.348837209	0.136987654	90.3732245	1148	69.53350265	33	68.9291187	6
TG-18	Sienito	TG18_1	0.0469	7.675906	0.066476	7.675913	0.01028	2.431907	0.316823	44.13814	183	65.35015	5	65.93083	2
		TG18_2	0.04802	4.664723	0.067733	4.664734	0.01023	1.955034	0.419109	100.2546	110	66.54569	3	65.61178	1
		TG18_3	0.04804	5.661948	0.067695	5.661958	0.01022	1.956947	0.345631	101.2395	134	66.50953	4	65.54797	1
		TG18_4	0.0482	6.721992	0.066392	6.721999	0.00999	2.002002	0.297828	109.0972	159	65.26954	4	64.08013	1
		TG18_5	0.04756	6.055509	0.067084	6.055517	0.01023	2.443793	0.403565	77.43797	144	65.92848	4	65.61178	2
		TG18_6	0.04765	6.547744	0.065963	6.547752	0.01004	2.49004	0.380289	81.92709	155	64.8609	4	64.39925	2
		TG18_7	0.04793	7.093678	0.066482	7.093685	0.01006	2.485089	0.350324	95.81532	168	65.3559	5	64.5269	2
		TG18_8	0.04744	6.155143	0.065934	6.155152	0.01008	1.984127	0.322352	71.43335	146	64.83322	4	64.65454	1
		TG18_9	0.04754	5.889777	0.066007	5.889786	0.01007	1.986097	0.33721	76.43872	140	64.90317	4	64.59072	1
		TG18_10	0.04771	6.37183	0.066046	6.371838	0.01004	1.992032	0.312631	84.91304	151	64.94002	4	64.39925	1
		TG18_11	0.04691	6.736304	0.065326	6.736311	0.0101	2.475248	0.367449	44.64774	161	64.2546	4	64.78218	2
		TG18_12	0.04781	6.191173	0.06592	6.191181	0.01	2	0.32304	89.87759	147	64.82071	4	64.14395	1
		TG18_13	0.04715	4.326617	0.065661	4.326629	0.0101	1.980198	0.457677	56.83108	103	64.5731	3	64.78218	1
		~~TG18_14~~	~~0.04882~~	~~5.981155~~	~~0.06664~~	~~5.981163~~	~~0.0099~~	~~2.020202~~	~~0.337761~~	~~139.1954~~	~~140~~	~~65.50583~~	~~4~~	~~63.50566~~	~~1~~

Amostra	Litotipo	Análise	Razões							Idades					
			$^{207}Pb/^{206}Pb$	2s%	$^{207}Pb/^{235}U$	2s%	$^{206}Pb/^{238}U$	2s%	Rho	$^{207}Pb/^{206}Pb$	2s%	$^{207}Pb/^{235}U$	2s%	$^{206}Pb/^{238}U$	2s%
TG-19	Nefelina sienito	~~TGC_19_001~~	~~0.057765821~~	~~10.42867583~~	~~0.085905911~~	~~11.30017252~~	~~0.010785762~~	~~4.35162261~~	~~0.385093467~~	~~520.8912357~~	~~47~~	~~83.68238308~~	~~11~~	~~69.15719771~~	~~4~~
		~~TGC_19_002~~	~~0.04710834~~	~~11.44333065~~	~~0.068051357~~	~~13.02268531~~	~~0.010477019~~	~~6.216149642~~	~~0.477332401~~	~~54.72268334~~	~~545~~	~~66.84852602~~	~~13~~	~~67.18784873~~	~~6~~
		~~TGC_19_003~~	~~0.047272026~~	~~4.295591409~~	~~0.06632591~~	~~4.99827394~~	~~0.010176015~~	~~2.555511069~~	~~0.511278713~~	~~62.99119344~~	~~168~~	~~65.20683153~~	~~5~~	~~65.26728556~~	~~3~~
		~~TGC_19_004~~	~~0.047288407~~	~~2.846473028~~	~~0.066259847~~	~~3.189215474~~	~~0.010162358~~	~~1.43829296~~	~~0.450986449~~	~~63.81638655~~	~~108~~	~~65.14392255~~	~~3~~	~~65.18013206~~	~~1~~
		~~TGC_19_005~~	~~0.047202882~~	~~2.381355189~~	~~0.065495867~~	~~3.000206307~~	~~0.010063385~~	~~1.824934342~~	~~0.608269617~~	~~59.50348324~~	~~97~~	~~64.41613178~~	~~3~~	~~64.54850402~~	~~2~~
		TGC_19_006	0.051536755	5.976840656	0.069043333	6.563099195	0.009716356	2.711392044	0.413126781	264.9104975	54	67.79115145	6	62.33331449	3
		TGC_19_007	0.047296308	2.917526233	0.062588827	3.38455461	0.009597725	1.715590448	0.506888098	64.21428404	111	61.64201938	3	61.57588517	2
		TGC_19_008	0.047183298	4.143103502	0.063405434	4.678910853	0.009746236	2.174143542	0.464668725	58.51431923	174	62.42205174	5	62.52407684	2
		TGC_19_009	0.047215212	5.830201744	0.063992796	6.652822257	0.009829872	3.204495531	0.481674605	60.12597511	241	62.98273663	7	63.05800583	3
		TGC_19_010	0.047156345	3.652663757	0.0613763	4.153112453	0.009439724	1.976459088	0.475898284	57.15194926	157	60.48269311	4	60.56694993	2
		TGC_19_011	0.047312591	3.827573019	0.062029074	4.211414699	0.009508616	1.756615652	0.417108211	65.03394379	144	61.10699066	4	61.00688554	2
		~~TGC_19_012~~	~~0.049639798~~	~~2.410847532~~	~~0.063097247~~	~~2.983688865~~	~~0.0092189~~	~~1.757900287~~	~~0.589170107~~	~~178.1617162~~	~~32~~	~~62.12773841~~	~~3~~	~~59.15658809~~	~~2~~
		TGC_19_013	0.047251261	2.684670915	0.060728094	3.38786924	0.009321268	2.06644624	0.609954545	61.94455126	105	59.8623842	3	59.81042778	2
		~~TGC_19_014~~	~~0.047301684~~	~~3.201881523~~	~~0.060228849~~	~~4.630896575~~	~~0.009234783~~	~~3.3456177~~	~~0.722455716~~	~~64.4849146~~	~~121~~	~~59.38436698~~	~~5~~	~~59.25803641~~	~~3~~
		~~TGC_19_015~~	~~0.047133231~~	~~4.861693131~~	~~0.058774664~~	~~5.977918584~~	~~0.009044023~~	~~3.478426441~~	~~0.581879193~~	~~55.98272602~~	~~215~~	~~57.99073024~~	~~6~~	~~58.03945798~~	~~3~~
TG-27	Sienito	TGC_27_001	0.048130783	5.668472321	0.071637894	6.838346476	0.0107949	3.825101837	0.559360636	105.7025463	132	70.25250485	7	69.21547481	4
		~~TGC_27_002~~	~~0.047404557~~	~~2.379583539~~	~~0.071031992~~	~~2.944497526~~	~~0.010867575~~	~~1.73425715~~	~~0.588982376~~	~~69.6556203~~	~~83~~	~~69.67824441~~	~~3~~	~~69.67894858~~	~~2~~
		~~TGC_27_003~~	~~0.048293288~~	~~1.709163336~~	~~0.072349451~~	~~2.296279404~~	~~0.010865437~~	~~1.533512241~~	~~0.66782476~~	~~113.6613854~~	~~36~~	~~70.92648792~~	~~2~~	~~69.66531555~~	~~2~~
		TGC_27_004	0.048285075	2.831735074	0.068718283	3.317823008	0.010321864	1.728937819	0.521106103	113.2601027	60	67.48236929	3	66.19794884	2
		TGC_27_005	0.047552902	2.475836138	0.067946898	3.255741144	0.010363139	2.114257745	0.649393687	77.08338891	78	66.74921271	3	66.46130582	2
		TGC_27_006	0.047730863	2.721939935	0.069824826	3.504556491	0.010609851	2.207478016	0.629887982	85.9500429	77	68.53315017	3	68.03520927	2
		TGC_27_007	0.04736054	2.144572636	0.068735653	2.678445376	0.010526019	1.604642591	0.59909476	67.4452176	77	67.49887214	3	67.5004408	2
		TGC_27_008	0.047078713	3.269345903	0.066728671	3.836066617	0.010279846	2.006684942	0.523110035	53.22165554	150	65.59028017	4	65.92984973	2
		TGC_27_009	0.047422716	6.965352656	0.069504514	7.618800684	0.010629805	3.087067581	0.405190752	70.56666455	247	68.22909091	7	68.16248939	3
		TGC_27_010	0.047390004	1.820640439	0.069042358	2.380841813	0.010566413	1.534169525	0.644381125	68.92512455	64	67.79022592	2	67.75812447	2
		TGC_27_011	0.051354514	4.197338924	0.074945358	4.560556273	0.010584366	1.783541274	0.391079765	256.7745266	39	73.38153337	4	67.87264116	2
		~~TGC_27_012~~	~~0.047260572~~	~~2.227755262~~	~~0.06447773~~	~~2.798413283~~	~~0.009894856~~	~~1.693583006~~	~~0.605194028~~	~~62.41397824~~	~~86~~	~~63.44541243~~	~~3~~	~~63.47282915~~	~~2~~
		~~TGC_27_013~~	~~0.047249915~~	~~2.726530326~~	~~0.063743492~~	~~3.220199254~~	~~0.009784385~~	~~1.713393013~~	~~0.532076707~~	~~61.87672948~~	~~107~~	~~62.74479406~~	~~3~~	~~62.76762636~~	~~2~~
		TGC_27_014	0.047356808	4.554022762	0.068298812	5.524647512	0.010459946	3.127715909	0.566138546	67.25767269	167	67.08375196	5	67.07893216	3
		TGC_27_015	0.049091412	4.341964497	0.069495995	4.803722263	0.010267222	2.055016275	0.427796647	152.1991368	69	68.221003	5	65.84929923	2

APÊNDICE G – Lu-Hf em Zircão por LA-ICP-MS

Amostra	Análise	U/Pb Age (Ma)	$^{176}Hf/^{177}Hf$	$^{176}Hf/^{177}Hf_{(t)}$	ε_{Hf}	T_{DM}
TG-02	TG02_1	65.89	0.28279	0.28279	1.5	665
	TG02_2	65.89	0.28245	0.28244	-10.6	1227
	TG02_4	65.89	0.28227	0.28226	-17.0	1438
	TG02_5	65.89	0.28240	0.28240	-12.3	1264
	TG02_6	65.89	0.28227	0.28227	-16.8	1495
	TG02_7	65.89	0.28233	0.28232	-14.8	1423
	TG02_9	65.89	0.28255	0.28254	-7.0	1028
	TG02_12	65.89	0.28225	0.28224	-17.8	1571
	TG02_13	65.89	0.28243	0.28242	-11.4	1200
	TG02_14	65.89	0.28271	0.28271	-1.3	843
TG-02C	TG02C_1	66.08	0.28271	0.28271	-1.2	753
	TG02C_2	66.08	0.28259	0.28259	-5.4	961
	TG02C_4	66.08	0.28277	0.28276	0.6	770
	TG02C_5	66.08	0.28265	0.28265	-3.3	874
	TG02C_8	66.08	0.28264	0.28264	-3.7	852
	TG02C_9	66.08	0.28299	0.28299	8.7	376
	TG02C_10	66.08	0.28290	0.28289	5.3	516
	TG02C_11	66.08	0.28274	0.28274	-0.2	742
	TG02C_13	66.08	0.28298	0.28298	8.4	391
	TG02C_14	66.08	0.28288	0.28287	4.5	579
TG-03	TG03_2	94.82	0.28283	0.28282	3.5	596
	TG03_3	94.82	0.28279	0.28278	1.9	726
	TG03_5	94.82	0.28253	0.28253	-6.8	1001
	TG03_6	94.82	0.28305	0.28305	11.5	282
	TG03_7	94.82	0.28271	0.28270	-0.8	767
	TG03_8	94.82	0.28288	0.28288	5.4	545
	TG03_10	94.82	0.28264	0.28264	-3.1	844
	TG03_12	94.82	0.28273	0.28273	0.1	739
	TG03_13	94.82	0.28287	0.28286	4.9	542
	TG03_14	94.82	0.28297	0.28297	8.5	399
TG-04D	TG04D_1	64.4	0.28250	0.28250	-8.7	1103
	TG04D_2	64.4	0.28272	0.28272	-0.9	754
	TG04D_3	64.4	0.28262	0.28262	-4.5	889
	TG04D_4	64.4	0.28267	0.28267	-2.6	845
	TG04D_5	64.4	0.28256	0.28256	-6.4	959
	TG04D_6	64.4	0.28251	0.28251	-8.5	1114
	TG04D_7	64.4	0.28236	0.28235	-13.8	1287
	TG04D_8	64.4	0.28267	0.28267	-2.7	855
	TG04D_9	64.4	0.28263	0.28263	-4.1	975
	TG04D_10	64.4	0.28253	0.28252	-7.9	1113
TGD_TG-16	TGD_16_001	69.37	0.28256	0.28256	-6.4	958
	TGD_16_002	69.37	0.28265	0.28265	-3.4	851
	TGD_16_003	69.37	0.28267	0.28267	-2.5	812
	TGD_16_004	69.37	0.28265	0.28265	-3.3	855
	TGD_16_005	69.37	0.28258	0.28257	-5.9	953
	TGD_16_006	69.37	0.28255	0.28255	-6.7	976

Amostra	Análise	U/Pb Age (Ma)	$^{176}Hf/^{177}Hf$	$^{176}Hf/^{177}Hf_{(t)}$	ε_{Hf}	T_{DM}
TGE_TG-16	TG_16_001	71	0.28270	0.28270	-2.0	819
	TG_16_002	68	0.28280	0.28280	3.0	583
	TG_16_003	66	0.28260	0.28260	-3.0	848
	TG_16_004	69	0.28280	0.28280	2.0	657
	TG_16_005	78	0.28290	0.28290	7.0	430
	TG_16_006	70	0.28260	0.28260	-4.0	850
	TG_16_007	67	0.28290	0.28290	4.0	550
	TG_16_009	61	0.28270	0.28270	-1.0	756
	TG_16_014	65	0.28260	0.28260	-6.0	938
	TG_16_015	69	0.28270	0.28270	-3.0	811
TG-18	TG18_2	64.82	0.28272	0.28271	-1.1	782
	TG18_3	64.82	0.28264	0.28264	-3.7	950
	TG18_4	64.82	0.28254	0.28254	-7.4	1044
	TG18_5	64.82	0.28275	0.28275	0.1	731
	TG18_6	64.82	0.28261	0.28260	-5.1	997
	TG18_7	64.82	0.28262	0.28262	-4.4	936
	TG18_8	64.82	0.28263	0.28262	-4.3	931
	TG18_10	64.82	0.28264	0.28263	-4.0	921
	TG18_11	64.82	0.28260	0.28260	-5.3	981
	TG18_12	64.82	0.28266	0.28265	-3.2	889
TG-19	TGC_19_003	61.27	0.28247	0.28246	-10.0	1136
	TGC_19_005	61.27	0.28261	0.28261	-4.9	925
	TGC_19_007	61.27	0.28261	0.28260	-5.1	941
	TGC_19_008	61.27	0.28268	0.28268	-2.4	820
	TGC_19_009	61.27	0.28254	0.28254	-7.4	1074
	TGC_19_010	61.27	0.28260	0.28260	-5.2	939
	TGC_19_011	61.27	0.28235	0.28235	-14.0	1341
	TGC_19_012	61.27	0.28262	0.28262	-4.4	878
	TGC_19_013	61.27	0.28247	0.28246	-10.1	1170
	TGC_19_014	61.27	0.28253	0.28252	-7.9	1074
TG-27	TGC_27_001	67.06	0.28262	0.28262	-4.5	909
	TGC_27_002	67.06	0.28252	0.28252	-8.1	1069
	TGC_27_003	67.06	0.28265	0.28264	-3.5	857
	TGC_27_004	67.06	0.28257	0.28257	-6.1	966
	TGC_27_005	67.06	0.28262	0.28262	-4.3	889
	TGC_27_006	67.06	0.28243	0.28243	-11.2	1185
	TGC_27_007	67.06	0.28245	0.28245	-10.5	1183
	TGC_27_010	67.06	0.28266	0.28265	-3.2	857
	TGC_27_012	67.06	0.28256	0.28256	-6.6	1016
	TGC_27_015	67.06	0.28234	0.28234	-14.3	1338